

Efforts Towards C–C Bond Formations: From Ni Catalysis to Transition-Metal Free Electrolysis

Thesis by
Wendy Zhang

In Partial Fulfillment of the Requirements for the
Degree of
Doctor of Philosophy in Chemistry

The logo for the California Institute of Technology (Caltech), featuring the word "Caltech" in a bold, orange, sans-serif font.

CALIFORNIA INSTITUTE OF TECHNOLOGY
Pasadena, California

2024
Defended July 19, 2023

© 2024

Wendy Zhang

ORCID: 0000-0002-6895-9598

All rights reserved except where otherwise noted

ACKNOWLEDGEMENTS

Professor Kimberly See. I am so lucky to work in your lab, Kim! You have been an awesome advisor for me, and I am truly grateful for all your advice and encouragement. When I first joined the lab, you told me that you will treat me like a postdoc and you entrusted me with leading multiple projects. The gesture meant the world to me, considering the self-doubt I was struggling with at the time. Over the past two years, I have had the opportunity to delve into electrochemistry and surface chemistry, things that I never imagined I would learn. I really enjoy studying the metal sacrificial anode. The confidence and the feeling of ownership I now have over my project is amazing, and I owe it to your support and guidance. I am also extremely thankful for your genuine care for my career development. When I was confused about my future and career goals, you invited me for a chat, and discussed everything over a beer. Thanks to you, I now have a lot of clarity on what I aspire to achieve after completing my PhD. Your mentorship has been transformative for my PhD, and I am forever grateful for your investment in my personal and professional success.

Professor Brian Stoltz. Thank you so much for being on my committee! You have always been exceptionally kind and supportive as a professor, not only to me but to so many other students. When I was lost during my PhD, I didn't hesitate to reach out to you for help. You are the professor I can wholeheartedly trust to provide guidance while always keeping my best interest at heart. Without your encouragement, I would most likely have given up chemistry two years ago. Thank you so much for giving me the courage to keep going!

Professor Sarah Reisman. Thank you for being the chair of my committee! You've been there the entire time, from all the yearly meetings, to the propositions exam, to now, finally, the thesis defense. All the advice and guidance you gave me are extremely helpful, and I'm sure I will continue to benefit from them for the rest of my chemistry career. When I was considering the possibility of joining the See group, you proactively reached out to Kim on my behalf. I really appreciate that! Thank you so much for everything!

Brian Lee. Making the first close friend in a new lab is not an easy task, but you and I quickly bonded over shared Asian trauma. It is always a lot of fun to discuss anything with you when we are working together in the glovebox, and filter is not

necessary for our conversations. I love all the food adventures we had over the years! Sharing food culture has always been the activity I enjoy the most, and I can never forget our reactions when we realized how different the definition of “Korean cold noodle” is for us. You tried very hard to show me sports, a concept that is quite foreign to me for anyone who knows me well. Despite that, I had the most fun at my first baseball game and hockey game. You also introduced me to D&D and DM’ed my very first campaign. Your DM sound effects are very memorable and diverse, including “rrrrrahhhhh”, “rah,” “rah!,” rraaahh~.” There are too many memories to include in this short acknowledgement. All I can say is I am very lucky to have had you as my friend during graduate school!

Skyler Ware. Without a doubt you are one of my best friends! Before I joined the See lab, I was getting used to an environment without many women and slowly persuaded myself that it does not matter if I don’t have female friends. How wrong was I! I am so much happier with you in my life! Thanks to CSOE, we started working together ever since I joined the lab. In lab, we solve scientific challenges together and help each other through hard times. Outside of lab, we have drinking parties, have Skyline chili, play Star Wars Family Feud, start a women’s D&D session, and have food adventure at Dollar Hits. I greatly admire the way in which you discover your passion and your determination in the pursuit of your dreams. It is something I am still working on, and I can’t be more grateful to have you as my role model. I am sure that we will stay close after Caltech. For now, I will end the acknowledgement with a sound effect that we both find hilarious, “druuuuuueeeHeeeeeHEEHEEHEEHEE!”

Steven Stradley. If anyone made me spend more money during graduate school, you are definitely on the list. I was aware of thrifting before, but after seeing your passion and ability to thrift, I was inspired! As a result, I spend a lot more of my precious free time in Goodwill, Savers, and antique stores, looking for my next big find. It doesn’t help when you are incredibly skillful at thrifting and seem to have a big find every other day! We are also each other’s mental support when life is hard in lab. Whenever I need someone to take a coffee break with, you are always there. I tend to stress out very often, but you always tell me that “you got this!” You are also my food adventure/D&D buddy, and we have spent a lot of fun time together. Thank you for everything! Graduate school is so hard, but it is not impossible because of friends like you.

Jake Evans. Thank you so much for being the savior of my projects! I can’t think

of a better person as the GLA of the XPS. Kratos is a very intimidating instrument, and it has its own personality. I really appreciate how patient you are when training me. Every time I am panicking and yelling, “JAKE, HELP!”, you are always there. I remember you told me that “you are not a true XPS expert until you drop a sample holder in the chamber.” I can proudly say that I haven’t dropped a single sample in the XPS chamber yet, and I am super okay with not being an expert. Not just the savior of my projects, you are also an incredible friend. I enjoy all the time we spend hanging out together, whether it’s watching random YouTube videos, having Korean BBQ, or just chatting over a drink. Barbaro will always be the best bard in my mind!

Chaoxuan Gu. Thank you Chaoxuan for being such an amazing collaborator! Our scientific background is so different, and I always learn something new from you during our biweekly meetings. You are always so patient explaining to me concepts about computational chemistry that I am not familiar with. It is just super fun to bounce ideas off together. I also had a great time hanging out with you in Pasadena when you and your friends were traveling in LA. Having a collaborator who is not only exceptionally competent as a scientist, but also a pleasure to work with, and an incredible friend is not as easy as many people might assume. I cannot be more grateful for having the chance to work with you during my PhD!

Jeremy Tran. I miss you so much Jeremy! Ever since you left Pasadena, I am afraid of going to any of the Cantonese restaurants, because I don’t need anyone to judge my Mandarin lol. I am very grateful to have met you at the beginning of my graduate school. I have lots of chaotic memories about hanging out with you. Things like cheesy Chinese New Year music on YouTube playing on repeat at your party, burning the dumplings I made at my party, pregame for some other parties. . . It was too much food and alcohol, the things I desperately needed in graduate school. You have always been supportive with every step I took, and I am so grateful to have a friend like you!

Bradley Paul-Gorsline. You are the person in lab with whom I felt comfortable to discuss nickel catalysis mechanism without being judged. You are the person who would watch every new episode of “Worth It” with me. You are the person who, when I asked, “What is God doing?,” responded with a simple yet profound answer: “I don’t know. Chilling.” You are the person who told me to figure out what I want in life when I was struggling the most in graduate school. You are the person who, when you got married and walked down the aisle, made me cry like a baby. I miss

you so much, Bradley! And I miss your daily pistachio even more!

Larry Henling. Thank you so much for helping me with all the single crystal XRD! Calling my samples “single crystals” is a bit too generous. Most of the time they are just some dubious looking solid that I desperately want to believe is the nickel intermediate I need. 90% of the time they were just LiBr coordinated to DME. Despite that, you were always incredibly patient and tried to fish out whatever you could from the sludge I gave you. You were also extremely accommodating to my complete inability to find the XRD room (after years). At the beginning, you would give me a call, and tell me to meet you at a certain door of BI, and I failed to find the right door every single time. Eventually, you just came over to my lab to pick up the sample, which I appreciate a lot. The nickel mechanism project was an extremely challenging one, and I couldn't have gotten as far as I did without all your help!

Joe Drew. Thank you so much for doing everything you did for the CCE division! Whenever we need to get something done in lab, either fixing the AC or installing a new glovebox, we always CC you in the email, because we know we can count on you! One of the running jokes among the graduate students is “Joe Drew should run for President of America, because he gets things done.” On top of that, the thing I appreciate the most is you always checked on me and asked me if I was happy after I switched lab. Knowing that someone cares about my happiness instead of just my science is a huge comfort when things get hard. Thank you so much!

Professor William McNamara. Thank you for being my first advisor and introducing me to the world of chemistry! I still remember sending you the first email asking if I can work in your lab as a freshman in undergrad. At the time I was contacting both your lab and a biology lab. The moment you replied yes, my career path changed forever. You continued to support me throughout my graduate school. Over the years, you were not only just a mentor, but also a good friend. I share with you all the big events of my life. When I was thinking about making the hard decision of switching lab, you were the first person I contacted. Your kind words encouraged me to keep fighting for what I deserved and reminded me why I chose chemistry in the first place. I would definitely not have gotten this far without you. Thank you so much for everything!

Alice Sogomonian. Thank you so much for taking care of me throughout my PhD! You are such a kind and caring person, and you make every appointment and conversation positive and enjoyable. I have been missing you dearly ever since your retirement in 2021. I hope you are enjoying the new chapter of your life and you

will always be one of the people I remember most fondly at Caltech!

Dr. Maria Oh. Thank you so much for taking care of my mental health for over 2 years! While I know it is your job to do counseling, there are moments when I feel a bit sad that you became acquainted with me during the period when I was gradually slipping into the darkest time of my PhD. I want you to know that I am doing so much better now, and I've accomplished so much. I would not have been able to get to where I am today without all your help! Thank you so much!

Dr. Evelyn Novello. Thank you so much for taking care of my metal health for the past two years! You helped me with adjusting to a new lab environment, dealing with anxiety, processing trauma, and balancing work and life. But most importantly, you helped me to understand more about my strengths and weaknesses. With that self-awareness, even when life gets bad again in the future, I can deal with it with more ease. Thank you so much for all your help!

Loren and Pat McFarland. Thank you for making me feel like a member of the McFarland family! Being an international student in the US for ten years, I almost forget what it feels like to have family support. You really took me in and took care of me like parents would. All the big decisions Zak and I made, switching lab, adopting a puppy, getting married, buying a house, you were always there to support and guide us. I spent many relaxing weekends at your house in Santa Barbara. It is a place where I can breathe when things get too intense in Pasadena. I love hanging out at the fire pit and gazing at the stars. I love all the wine tasting. I love how excited you were for me when I took my hiking and camping adventure. I love cooking with the whole family in the kitchen. I love all the Christmas and Thanksgiving family gatherings. Thank you for everything, and I love you guys so much!

Zak McFarland. If I were to attempt to describe the feeling of meeting you, it would be "as if I just woke up." From the very beginning, you have shown me how to live and enjoy life. Throughout this absurd journey of graduate school, you have been my anchor, steering me away from toxicity and depression, and infusing each day instead with happiness and joy. You opened up a world of new experiences for me, introducing me to my first video game (*Zelda: Breath of the Wild*), taking me on coffee/wine tasting, exploring estate sales in LA, driving together to the beach in a convertible. . . You encourage me to embrace happiness, even if it means pursuing activities that may seem crazy at times. We would search all the thrift stores in town just for a secondhand picture frame, or buy six chairs at a yard sale with frozen groceries still in the car, or stress-make dumplings right before a deadline.

The year 2021 is extremely special for us. In between moving in together and me leaving a toxic lab, we welcomed Kiki into our lives in June, got engaged in August and married in October. Moving into 2022, we started an exciting new journey of homeownership. We've been together for 5 years, and every moment with you has been a sweet memory. Life is so much more colorful after I met you, and I am looking forward to spending the rest of my life with you! Thank you for all the love and support! I love you today, tomorrow, always, and forever!

Skyler Mendoza. Where do I even start?! We met during the visitation weekend, and we both quickly made the “mistake” of coming to Caltech, lol. Looking back, that encounter was incredibly lucky as I can't imagine navigating the challenges of the past few years without your unwavering support. Remember the “pacman” problem set that kept us up all night? Remember the cold chicken wings we had when we finally made it to the grading session at 10 pm? Remember the midnight chicken tenders and tofu nuggets? Remember the rotavap water bath extraction you helped me with? Remember me murmuring “it's turning green it's turning green,” in front of the glovebox and you thinking I was delusional? Remember the “no pain no gain” hot pot we had together? Remember the trash bags in the closet? We also adopted two beautiful kittens during grad school! I am always amazed by the way you take pictures of the cats. It is more accurate to call them frames of a movie than pictures. You were also very protective of me when I first started dating Zak. It took about two years for you to say, “yeah, Zak is a good man,” and you eventually officiated our wedding. You are an integral part of my life, my confidant, and chosen family. Our graduate school experience was filled with laughter, tears, and countless cherished memories that I could never fully capture without adding a few hundred more pages to this acknowledgement. As a token of appreciation for the quotes you collected in your thesis acknowledgement, I want to share a few of your memorable phrases: Boat! They invented boat!", "Shit, I reinvented boat!", "Wait for me, wait for me!!!", "We made ass chicken.", "W-W-W-Wendy, she's pooping by the sea. W-W-W-Wendy, she's pooping next to me.", and "Carbo baby, Carbo baby baby boy."

Carbo and Nickel. When Skyler Mendoza and I first moved off campus in the summer of 2018, we agreed on adopting two cats at the end of that year. But we quickly made the mistake to visit the Pet Food Express on Lake Ave to check all the cats available for adoption a week after we moved in. It must have been kitten season because the staff members ran out of ideas and named all the cats with elements of

the periodic table. I immediately picked the five-month-old kitten named Nickel, since I was working on nickel “cat”alysis. Skyler picked out a three-month-old kitten which he later named Carbo, short for carbo”cat”ion. Nickel has extremely poor coordination as a cat. He is always falling off the couch, the bed, and the coffee table. When he jumped onto the kitchen counter for the first time after spending a year with us, Skyler and I were cheering so hard. Carbo is the opposite of Nickel. He has been jumping off the walls like Spiderman ever since the day we took him home. Carbo and Nickel helped Skyler and I survive the pandemic shut down. The difficult time was more bearable when we had them sleeping in our arms. Thank you so much for being our baby boys, and we love you!

Kiki. Kiki is the puppy that makes me believe “meant-to-be.” She was born in Mexico in Feb 2021. When the Real Bark rescued her from the street, she was a one-month-old baby covered by hundreds of ticks. She was then transferred to the US for treatment and getting her ready to be adopted. While she was getting the treatment, I was struggling through my most difficult time during graduate school. It was a dark time, and I was praying for a puppy that would love me and give me the mental support that I desperately needed. We found Kiki’s information online in June 2021, and very quickly the Real Bark arranged our first meeting. It was love at first sight. We fell in love with Kiki as soon as they brought her to us. She was just a tiny 6-lbs little bean. She fell in love with us immediately as well. As soon as she saw me, she ran as fast as she could towards me, stood on her back legs with her paws resting on my knees, and kept licking my hands. She became a part of the family ever since. I’d like to think that it was always meant to be that Kiki and I would save each other’s lives. She is now a spoiled princess. And I am so swamped by her love that I never suffered from a bad depression episode ever since. I wouldn’t have survived graduate school without her and there’s not enough I can say to express how much I love her. She is my motivation, and I will work hard to give my little princess the best life ever!

Restaurants. While LA area is known for its notoriously high living cost, the food here is the absolute best! Anything you crave, LA has it to offer. Here is a not complete list of the restaurants that comfort my soul when science is not behaving. There are also a few restaurants at the end of the list that are no longer in business. But they should still be mentioned because of how amazing they were!

Takuya, Mediterranean Cafe, The Reyn, Swami’s Cafe, Dollar Hits, Roma Deli, Wild Oak Cafe, Bistro 45, Bone Kettle, Colette, Union, The Cellar Wine Library,

The 1894 Wine Bar, The Edison, RT Rogers Brewing Co, Stone Brewing Tap Room, Lucky Baldwin's Pub, Jones Coffee, Dog Haus, Flour + Tea, Tpumps, Grand Central Market (Sari Sari Store, Sticky Rice, Tacos Tumboras a Tomas, The Oyster Gourmet), The Counter, Nine & Nine Thai Kitchen, Ramen Tatsunoya, Aikan Sushi, Sugarfish, Sushi Stop, Gyu-Kaku, King's Row, Noodle Street, Boiling Point, Meet Qin Noodle, Chengdu Taste, Mian, Dulan's, Capital Seafood Restaurant, Tea Spots, Ding's Garden, Din Tai Fung, Shenyang Restaurant, Tokyo Shabu Shabu, Abricott, Shandong Dumpling, Du-par's, White Horse, Pacific Seafood Grill, Delicatessen by Osawa, Paul Martin's.

Games. How can you survive the pandemic without playing the board game Pandemic! Here is a list of video games and board games I enjoyed during the shutdown and afterwards!

Zelda: Breath of the Wild, Hades, Animal Crossing: New Horizon, Pandemic (Legacy), Betrayal at the House on the Hill, Forbidden Island/Desert, Five Crowns, Star Wars Family Feud, D&D.

I also want to express my gratitude to the following people for all their help during graduate school: Professor Song Lin, Professor Yue Qi, Yi Wang, Weiyang Guan, Lingxiang Lu, and Wen Zhang, for being amazing collaborators; Dr. Mariel Tourani, and Dr. Ashwini Lal, for taking care of my mental health; Laura Flower Kim, for answering all my questions with regard to immigration status and providing me assistance when I was in great need; Roxana Amiri, for helping me with immigration; Chi Ma and Bruce Brunschwig, for helping me with SEM/EDS and XPS; Paul Oyala, David Vander Velde, and Scott Virgil, for helping me with EPR, NMR, and all kinds of chromatography techniques. Ricardo Zarazua and Nathan Hart, for making the electrochemical cell parts; Alison Ross, Julianne Just, and Sadie Rubalcava, Beth Marshall, for their help when I am trying to schedule meetings and all the logistics; Felix Schneck and Dan Tong, for being supportive friends; Sam Engle for being an amazing friend and answering all my questions when I am freaking out about Kiki's health; Andreas Butler and Tim Csernica, for being fun D&D buddies; Zac Iton, Michelle Qian, Christopher Povinelli, Colin Morrell, Tori Davis, and all the other See lab members, for being the best lab mates I can ever ask for.

ABSTRACT

The selective construction of C–C bonds has been a critical challenge in modern synthetic organic chemistry. Among the numerous methodologies developed, cross-coupling remains an attractive strategy for direct C–C bond formation. Herein, a diverse range of cross-coupling reactions for C–C bond formations are investigated from different perspectives. First, the mechanism of a Ni/cyano-box-catalyzed asymmetric Suzuki alkylation is studied. The existing data is consistent with a radical chain pathway that is previously proposed for other Ni-catalyzed enantioselective cross-coupling reactions. Next, moving on from the traditional electrophile-nucleophile cross-couplings, we explore Ni-catalyzed reductive coupling of alkyl halides with internal olefins in the presence of a hydrosilane. With judicious choice of the directing group, hydroalkylation of internal olefins can be achieved with high regio- and enantioselectivity. Following that, an electrochemically driven, transition-metal free cross-electrophile coupling reaction is explored as a greener alternative to constructive $C(sp^3)$ – $C(sp^3)$ bonds. Specifically, we focus on improving the Mg sacrificial anode performance in these electroreductive systems. By carefully choosing the electrolyte composition, we are able to manipulate the metal electrode interfaces for a more effective counter electrode. Finally, Al stripping in ethereal solvents is investigated for its application as a sacrificial anode in reductive electrosynthesis. Inspired by Al corrosion chemistry, we are able to achieve bulk Al stripping in THF-based electrolyte by incorporating halide co-supporting electrolytes.

PUBLISHED CONTENT AND CONTRIBUTIONS

Zhang, W., C. Gu, Y. Wang, S. D. Ware, L. Lu, S. Lin, Y. Qi, K. A. See (2023). “Improving the Mg Sacrificial Anode in Tetrahydrofuran for Synthetic Electrochemistry by Tailoring Electrolyte Composition”. In: *JACS Au*, 8, pp. 2280–2290. DOI: 10.1021/jacsau.3c00305.

W.Z. conceived the idea, performed the electrochemistry and surface characterization experiments, prepared the data, and wrote the manuscript.

TABLE OF CONTENTS

Acknowledgements	iii
Abstract	xi
Published Content and Contributions	xii
Table of Contents	xii
Nomenclature	xiv
Chapter I: A Mechanistic Investigation of Nickel/Cyano-Box-Catalyzed Asymmetric Suzuki Alkynylation	1
1.1 Introduction	2
1.2 Results and Discussion	8
1.3 Conclusion	24
1.4 Supporting Information	25
Chapter II: Nickel-Catalyzed Regioselective and Enantioselective Coupling of Alkyl Halides with Internal Olefins	51
2.1 Introduction	52
2.2 Results and Discussion	53
2.3 Conclusion	60
2.4 Supporting Information	61
Chapter III: Improving the Mg Sacrificial Anode in Tetrahydrofuran for Synthetic Electrochemistry by Tailoring Electrolyte Composition	138
3.1 Introduction	139
3.2 Results and Discussion	142
3.3 Conclusions	155
3.4 Methods	155
3.5 Supporting Information	159
Chapter IV: Enabling Al Sacrificial Anodes in Tetrahydrofuran Electrolytes for Reductive Electrosynthesis	178
4.1 Introduction	179
4.2 Results and Discussion	181
4.3 Conclusions	192
4.4 Methods	192
4.5 Supporting Information	197
Bibliography	208

NOMENCLATURE

- Ac.** acetyl.
- Ar.** aryl.
- BE.** binding energy.
- Bn.** benzyl.
- Boc.** *tert*-butyloxycarbonyl.
- box.** bis(oxazoline).
- Bpin.** pinacolborane.
- Bu.** butyl.
- Bz.** benzoyl.
- CE.** counter electrode.
- cod.** 1,5-cyclooctadiene.
- Cy.** cyclohexane.
- DCM.** dichloromethane.
- DG.** directing group.
- DMA.** dimethylacetamide.
- DMAP.** 4-dimethylaminopyridine.
- DME.** dimethoxyethane.
- DMF.** N,N-dimethylformamide.
- EDC.** 1-ethyl-3-(3-dimethylaminopropyl)carbodiimide.
- EDL.** electrical double layer.
- EDS.** energy-dispersive X-ray spectroscopy.
- ee.** enantiomeric excess.
- EIS.** electrochemical impedance spectroscopy.
- EPR.** electron paramagnetic resonance.
- Et.** ethyl.

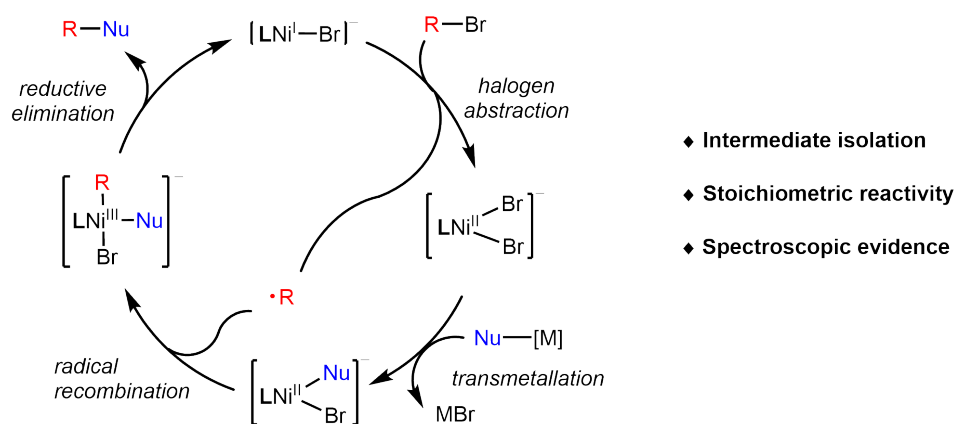
- Fc/Fc⁺**. ferrocene/ferrocenium.
- GC**. gas chromatography.
- hex.** hexyl.
- HMDS**. hexamethyldisilazane.
- HPLC**. high-performance liquid chromatography.
- KE**. kinetic energy.
- LC**. liquid chromatography.
- LMCT**. ligand-to-metal charge-transfer.
- LSV**. linear sweep voltammetry.
- MD**. molecular dynamics.
- Me.** methyl.
- NMR**. nuclear magnetic resonance.
- NPhth**. phthalimide.
- OCV**. open-circuit voltage.
- OTf**. triflate.
- OTs**. tosylate.
- pent.** pentyl.
- Ph.** phenyl.
- PMHS**. polymethylhydrosiloxane.
- Pr.** propyl.
- pybox**. pyridine bis(oxazoline).
- RE**. reference electrode.
- SE**. supporting electrolyte.
- SEI**. solid electrolyte interphase.
- SEM**. scanning electron microscopy.
- SFC**. supercritical fluid chromatography.
- SOMO**. singly occupied molecular orbital.

- TBA.** tetrabutylammonium.
- TBME.** methyl *tert*-butyl ether.
- TBS.** *tert*-butyldimethylsilyl.
- td-DFT.** time-dependent density-functional theory.
- terpy.** terpyridine.
- terpy’.** 4,4’,4’’tri-*tert*-butylterpyridine.
- TFSI.** bis(trifluoromethanesulfonyl)imide.
- THF.** tetrahydrofuran.
- TIPS.** triisopropylsilane.
- TM.** transmetallation.
- WE.** working electrode.
- XPS.** X-ray photoelectron spectroscopy.

Chapter 1

A MECHANISTIC INVESTIGATION OF
NICKEL/CYANO-BOX-CATALYZED ASYMMETRIC SUZUKI
ALKYNYLATION

Abstract: Nickel-catalyzed cross-coupling is a powerful tool for the selective formation of C–C bonds. Although tremendous progress has been made in method development, the mechanisms of these catalytic reactions are less well-understood. Researchers have investigated the catalytic pathways for systems utilizing tridentate ligands. However, systems with bidentate ligands are rarely studied due to instability of the nickel intermediates. Here, we examine the pathway for an asymmetric Suzuki alkynylation of α -bromo- α -trifluoromethyl electrophiles catalyzed by a nickel/cyano-box catalyst. To test the feasibility of each proposed elementary step, we synthesize the proposed intermediates for the catalytic reaction and test their stoichiometric reactivity. The spectroscopic/stoichiometric evidence strongly supports a nickel(II) complex, $[\text{LNi}^{\text{II}}\text{BrNu}]\text{Li}$, being the predominant resting state of the catalytic reaction. The existing data is consistent with a radical chain pathway, which has been previously proposed for nickel-catalyzed enantioselective Negishi arylation and Kumada arylation reactions.



1.1 Introduction

Over the past decade, tremendous progress has been made in nickel-catalyzed asymmetric cross-coupling reactions.^{1,2} Despite the progress, the mechanisms of these catalytic reactions are less well-understood. Various ligands (terpyridine, bis(oxazoline), bipyridine, etc.) have been employed in nickel-catalyzed cross-coupling reactions, leading to additional challenge in systematic mechanistic investigations.^{1,2} However, since many of these ligands share similar structural and electronic properties, the mechanism of nickel-catalyzed cross-coupling reactions supported by these ligand systems might be similar to one another.³ In fact, preliminary mechanistic studies on catalytic reactions involving different ligands have revealed several common aspects of their catalytic pathways.

Firstly, evidence strongly supports that the activation of alkyl halides occurs *via* a radical pathway. Gonzalez-Bobes *et al.* reported a nickel/amino-alcohol catalyzed Suzuki coupling of an alkyl bromide bearing a pendant olefin.⁴ Under the catalytic conditions, the reaction yields the cyclization/cross-coupling product with diastereoselectivity identical to that of the same product resulting from direct Bu_3SnH reduction (Figure 1.1). The observation is consistent with an initial generation of a secondary radical intermediate, followed by a 5-exo-trig cyclization prior to the reaction with the nucleophile. Additionally, researchers have developed a wide range of asymmetric nickel-catalyzed cross-coupling reactions that proceed by stereoconvergence instead of kinetic resolution.⁵ The success of these catalytic reactions indicates that a carbon-centered radical is formed as the key intermediate.

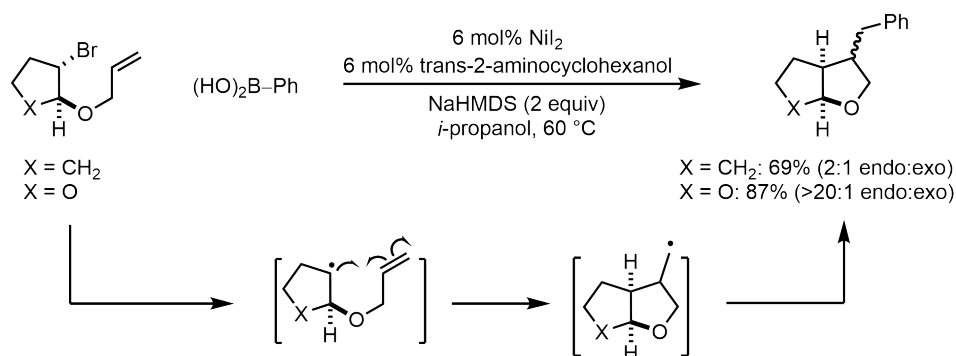


Figure 1.1: Mechanistic pathway for the nickel-catalyzed cyclization/cross-coupling reaction.

Secondly, both experimental and computational studies suggest that a nickel(I)/(III) mechanism is more likely than a nickel(0)/(II) mechanism. In 2005, Jones *et al.* synthesized several nickel/terpy' complexes and utilized them to probe the catalytic

intermediates in a Negishi cross-coupling reaction.⁶ The reaction of (terpy')Ni^{II}MeI with 5 equivalents of heptylzinc bromide only gives 8% yield of the cross-coupling product. This result argues against a reductive elimination from nickel(II)-dialkyl mechanism. On the contrary, the reaction of (terpy')Ni^IMe with 5 equivalents of heptyl bromide furnishes 90% yield of the cross-coupling product, supporting a possible nickel(I) to nickel(III) redox pathway. Additionally, Li *et al.* reported a computational study on a nickel/diamine catalyzed Suzuki cross-coupling system.⁷ They conclude that the nickel(0)/(II) pathway is not favored due to the high activation barriers of reductive elimination from the nickel(II)-dialkyl intermediate (+37.7 and +57.5 kcal/mol for singlet and triplet, respectively). In comparison, the activation barrier of reductive elimination from the nickel(III) intermediate is only +11.5 kcal/mol, which is a more kinetically favorable process. Other than nickel/diamine catalyst, computational studies suggest that nickel catalysts supported by bipyridine and pybox ligands also proceed by a nickel(I)/(III) pathway for C–C bond formation.^{8,9}

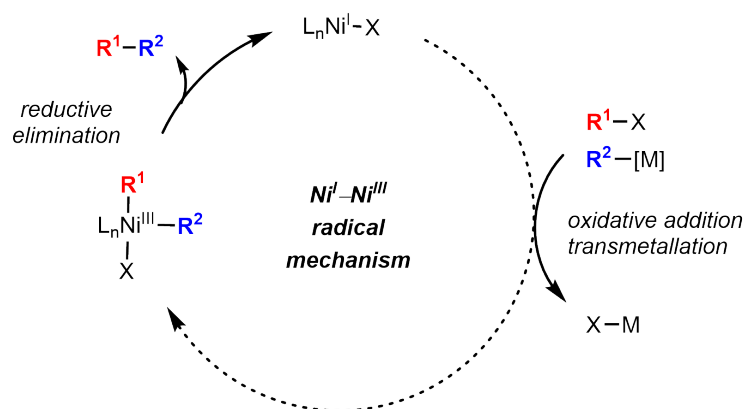


Figure 1.2: A general catalytic cycle for nickel-catalyzed cross-coupling reactions.

Based on the key aspects of the mechanism discussed above, we are able to construct a general catalytic cycle for nickel-catalyzed cross-coupling reactions (Figure 1.2). The catalytic cycle starts from a nickel(I) intermediate, $L_n Ni^I X$. It can undergo oxidative addition and transmetalation with the electrophile and the nucleophile, respectively, yielding a nickel(III) intermediate. Finally, the nickel(III) intermediate reductively eliminates to yield the cross-coupling product and regenerate the nickel(I) intermediate. This general catalytic cycle does not specify the reaction pathway of oxidative addition and transmetalation. In fact, researchers have shown that these two elementary steps can take place in very different pathways depending on the ligand system and reaction condition.

In 2005, Jones *et al.* investigated the mechanism of a nickel/terpy-catalyzed Negishi alkylation reaction and proposed a transmetallation-first mechanism (Figure 1.3).¹⁰ In the proposed catalytic pathway, (terpy)Ni^IX first undergoes transmetallation with alkylzinc, generating (terpy)Ni^IR². (terpy)Ni^IR² then undergoes oxidative addition with alkyl halide, forming (terpy)Ni^{II}R²X and an alkyl radical, ·R¹. (terpy)Ni^{II}R²X and ·R¹ subsequently recombine to generate the nickel(III) intermediate, which reductively eliminates to afford the cross-coupling product and regenerate the nickel(I) halide intermediate. The transmetallation-first mechanism is supported by the stoichiometric reactivity of nickel(I) alkyl complex and computational study.¹¹

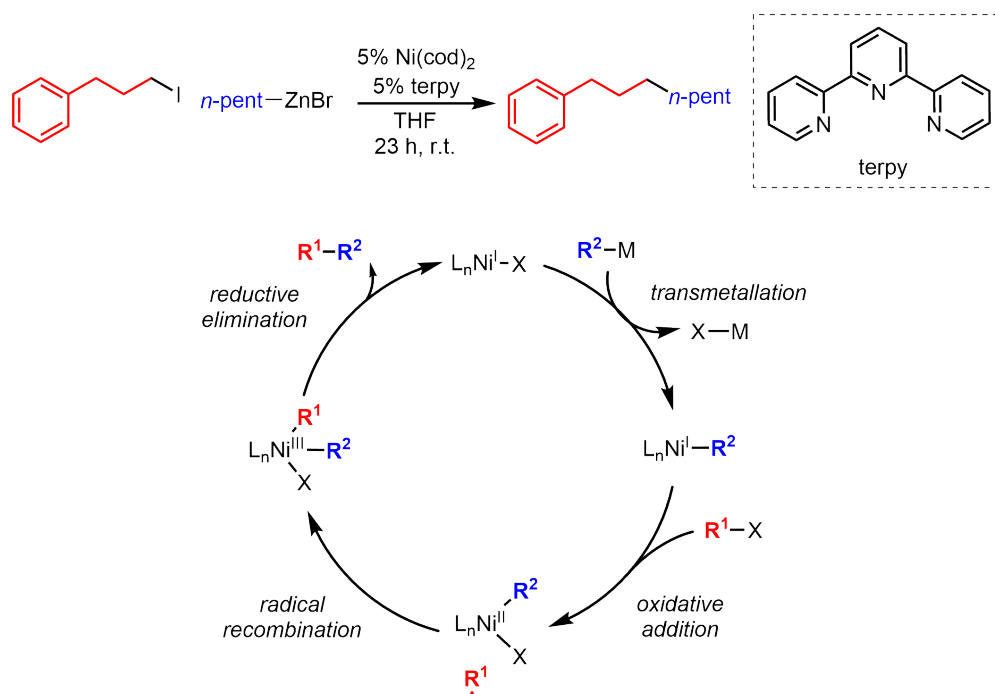


Figure 1.3: Transmetallation-first mechanism proposed for the nickel/terpy-catalyzed Negishi alkylation reaction.

In 2013, Breitenfeld *et al.* investigated the mechanism of a nickel/pincer-catalyzed Kumada alkylation reaction and proposed a bimetallic oxidative addition mechanism (Figure 1.4).¹² In this mechanism, the activation of alkyl halide (R¹-X) involves two nickel centers. The key intermediate for the activation of alkyl halide is the [(pincer)Ni^{II}R²](R²-MgCl) complex, which results from transmetallation of [(pincer)Ni^{II}X](R²-MgCl) with R²-MgCl. Once formed, [(pincer)Ni^{II}R²](R²-MgCl) reacts with R¹-X via an inner sphere single electron transfer, giving rise to ·R¹. ·R¹ then escapes from the solvent cage and recombine with another (pincer)Ni^{II}R² complex, forming (pincer)Ni^{III}R¹R² which reductively eliminates to produce the

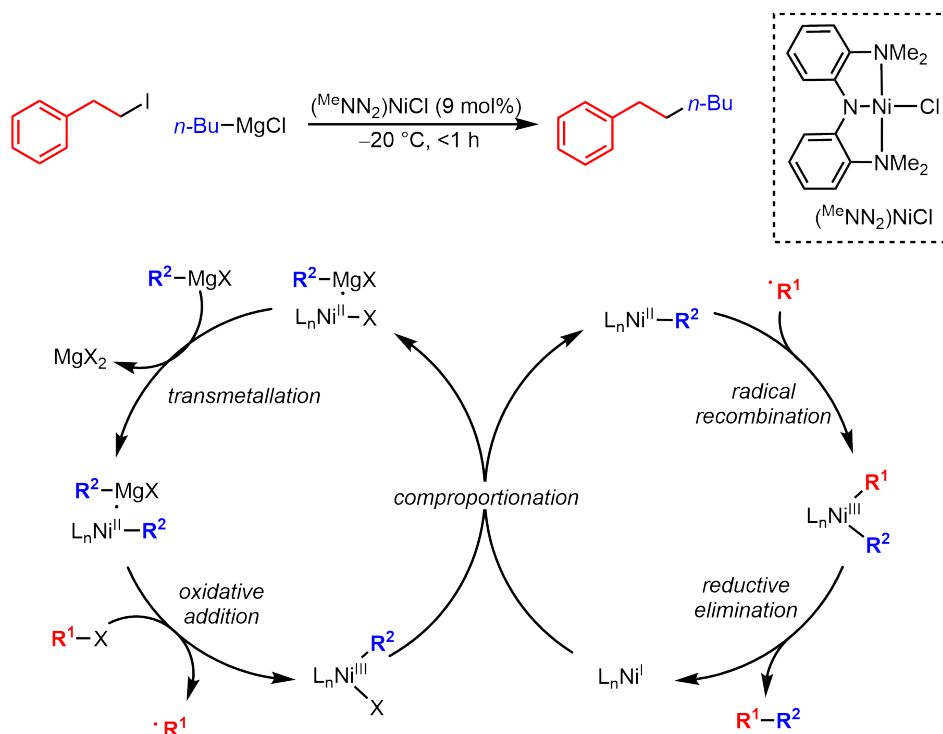


Figure 1.4: Bimetallic oxidative addition mechanism proposed for the nickel/pincer-catalyzed Kumada alkylation reaction.

cross-coupling product.

In 2014, Schley *et al.* investigated the mechanism of a nickel/(-)-*i*-Pr-pybox-catalyzed enantioselective Negishi arylation reaction and proposed a radical chain transfer mechanism (Figure 1.5).¹³ In the radical chain transfer mechanism, propargylic bromide undergoes oxidative addition with (pybox)Ni^IBr, yielding a free propargylic radical and (pybox)Ni^{II}Br₂. (pybox)Ni^{II}Br₂ reacts with the arylzinc reagent to give [(pybox)Ni^{II}Ar]Br. [(pybox)Ni^{II}Ar]Br then combines with the free propargylic radical to generate the nickel(III) intermediate, which reductively eliminates to yield the cross-coupling product and regenerate (pybox)Ni^IBr. The mechanism is supported by spectroscopic and stoichiometric evidence. [(pybox)Ni^{II}Ph]BARF₄ is crystallographically characterized. Analysis of the catalytic reaction *via* UV-vis is consistent with the rapid formation of [(pybox)Ni^{II}Ph]⁺ as the predominant resting state of nickel. The stoichiometric reaction of [(pybox)Ni^{II}Ph]BARF₄ with propargylic bromide under the catalytic conditions furnishes comparable yield and % ee compared to the standard catalytic reaction, supporting [(pybox)Ni^{II}Ph]⁺ as the key intermediate of the proposed mechanism.

In 2019, Yin *et al.* reported a mechanistic investigation of another enantioselective

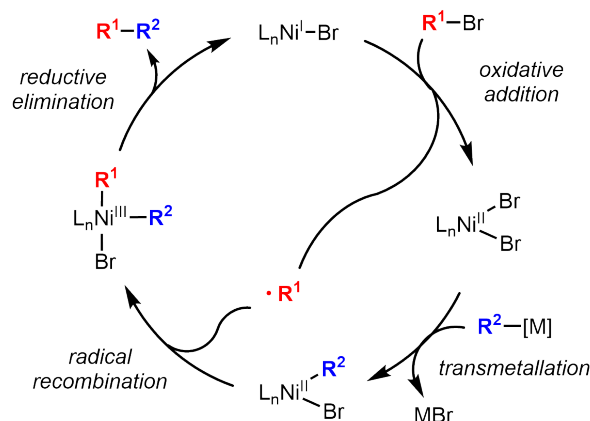
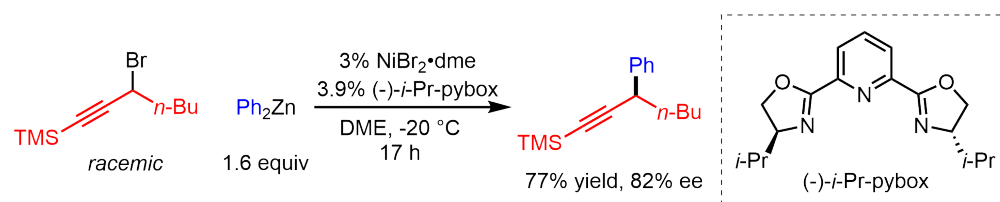


Figure 1.5: Radical chain transfer mechanism proposed for the nickel/pybox-catalyzed Negishi arylation reaction.

cross-coupling reaction, nickel/*(S,S)*-Ph-box-catalyzed Kumada arylation.¹⁴ Both spectroscopic and stoichiometric evidence point towards an organonickel(II) complex, (box)Ni^{II}ArBr, being the predominant resting state of the catalyst. The paper also reported the isolation of (box)Ni^IBr, which serves as the chain-carrying radical for the proposed mechanism. Interestingly, the radical chain transfer pathway proposed in this work is consistent with the mechanism proposed for the nickel/pybox-catalyzed Negishi arylation.

In summary, previous work on the mechanisms of nickel-catalyzed cross-couplings demonstrates the effect of ligand on the reaction pathway. While the terpy, pincer, and pybox ligands are all tridentate ligands, they support different mechanisms for the nickel-catalyzed cross-coupling reactions. On the other hand, ligands that share similar structural motifs can afford the same catalytic cycle despite the differences in reaction conditions. The enantioselective nickel/pybox-catalyzed Negishi coupling and nickel/box-catalyzed Kumada coupling both proceed *via* a radical chain transfer pathway. Both pybox and box ligands contain bis(oxazoline), which may correlate with the mechanisms of the nickel-catalyzed reactions they supported.

Figure 1.6 categorizes the commonly used ligands to four classes: neutral tridentate, neutral bidentate, anionic tridentate, and anionic bidentate ligands.³ To the

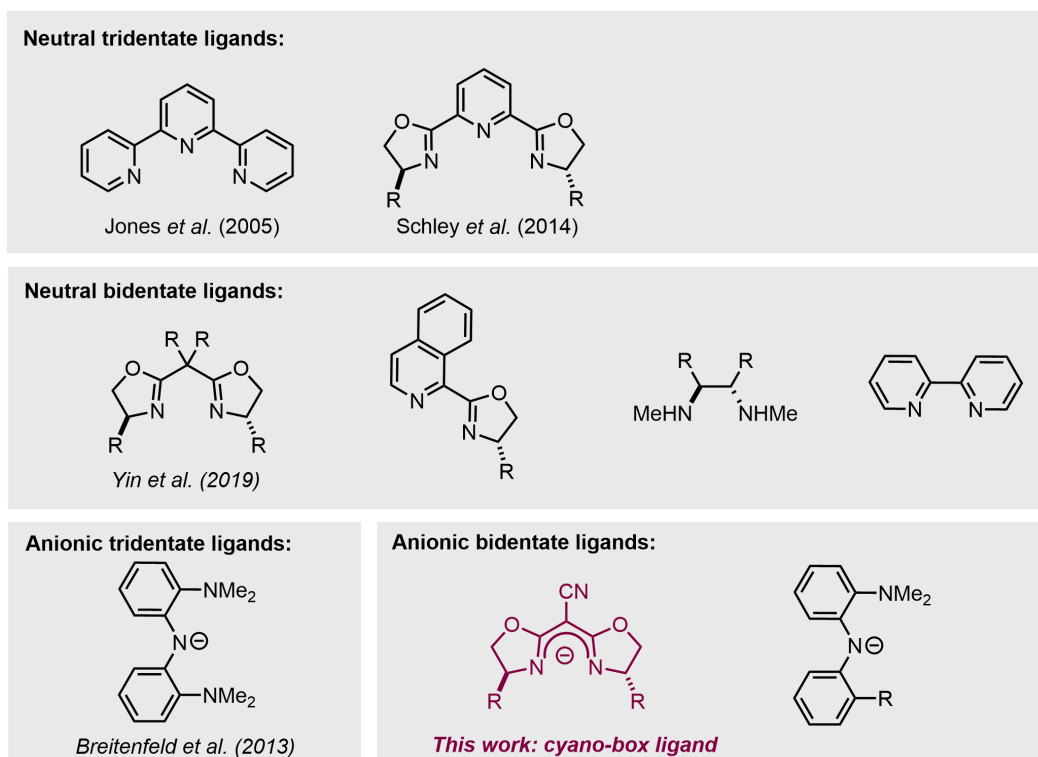


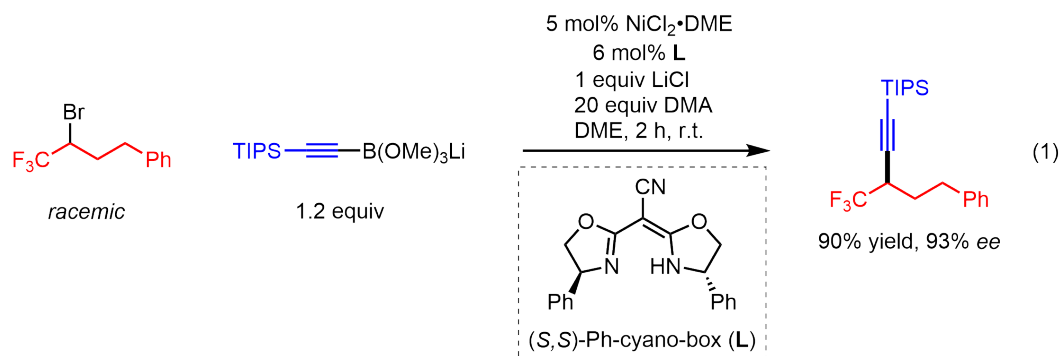
Figure 1.6: Various ligand classes that have been employed in nickel-catalyzed cross-coupling reactions.

best of our knowledge, there have been no systematic mechanistic investigations of a nickel-catalyzed, enantioselective cross-coupling reaction employing an anionic, bidentate ligand. Here, we examine the pathway of a nickel/cyano-box-catalyzed enantioselective Suzuki alkynylation of α -bromo- α -trifluoromethyl electrophiles. The cyano-box ligand (**L**) also contains bis(oxazoline). Therefore, we are interested in comparing the mechanism to that of the nickel/pybox- and nickel/box-catalyzed reactions. To elucidate the mechanism of the Suzuki alkynylation reaction, we prepare the proposed intermediates for the catalytic reaction and test their stoichiometric reactivity. In particular, we provided spectroscopic and stoichiometric evidence supporting a nickel(II) complex $[\text{LNi}^{\text{II}}\text{BrNu}]\text{Li}$ being the predominant resting state of the catalytic reaction. The existing data is consistent with a radical chain pathway that has been proposed for the nickel-catalyzed enantioselective Negishi arylation and Kumada arylation reactions.

1.2 Results and Discussion

Modifying the Catalytic System for the Mechanistic Investigation

To study the mechanism of cyano-box supported nickel-catalyzed cross-couplings, we choose an asymmetric Suzuki alkylation of α -bromo- α -trifluoromethyl electrophiles as the system (eq 1).¹⁵ The reaction employs a $\text{NiCl}_2\cdot\text{DME}/(S,S)\text{-Ph-cyano-box (L)}$ catalyst to enable C–C bond formation and induce enantioselectivity. LiCl and DMA additives are employed to achieve high yield and enantioselectivity. While the catalytic condition affords the desired cross-coupling products with a broad functional group tolerance, it is not ideal for a mechanistic study. Firstly, the reaction is heterogeneous. Secondly, the system involves both Br (from the alkyl bromide electrophile) and Cl (from the nickel pre-catalyst and LiCl additive), which will inevitably complicate the spectroscopy results. In order to reduce the halogen combinatorial complexity, we attempt to unify the halogens to Cl, Br, or I (Table 1.S1). To our delight, simply replacing $\text{NiCl}_2\cdot\text{DME}$ and LiCl with $\text{NiBr}_2\cdot\text{DME}$ and LiBr can avoid the halogen combinatorial problem while still afford 81% yield and 90% ee for the cross-coupling product. LiBr also has higher solubility than LiCl , which gives rise to a homogeneous reaction system that is more convenient for spectroscopic studies.



In the original Suzuki alkylation reaction condition, the active catalyst is formed *in situ* by stirring the nickel pre-catalyst and **L** (1:1.2) in the solvent at room temperature for 10 min. While this approach is convenient and sufficient for methodology development, we prefer a well-defined nickel complex for the mechanistic study to minimize the variables in the system. Based on previous studies on nickel-catalyzed cross-coupling systems,^{13,14} we hypothesize that $[\text{LNi}^{\text{II}}\text{Br}_2]^-$ is an active intermediate in the catalytic cycle that can serve as a stable, well-defined nickel catalyst for the Suzuki alkylation reaction. Additionally, it may also serve as a precursor

for the syntheses of other nickel complexes that are potential active intermediates. However, the synthesis of $[\text{LNi}^{\text{II}}\text{Br}_2]^-$ is particularly not straightforward due to the chemical reactivity of **L**.

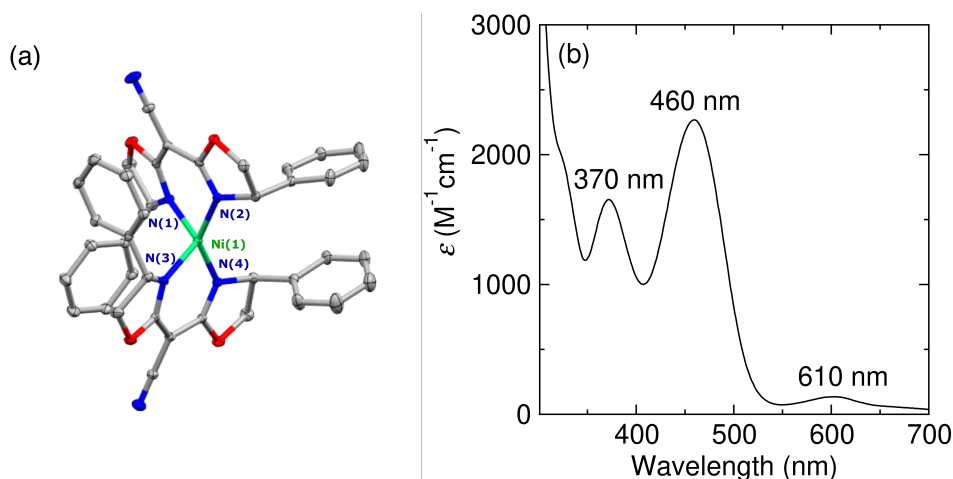
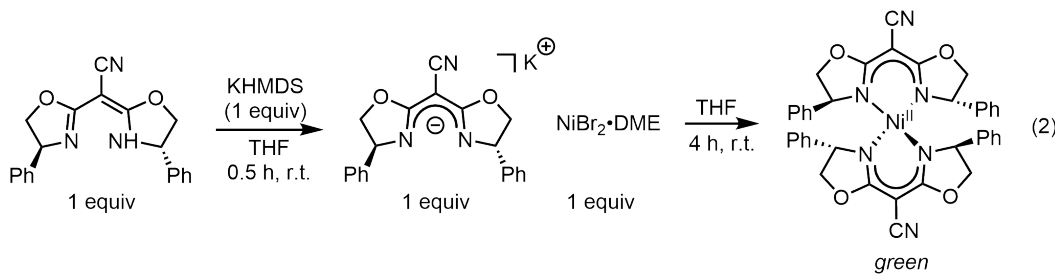


Figure 1.7: (a) X-ray crystal structure of $\text{L}_2\text{Ni}^{\text{II}}$ (ellipsoids shown at 30% probability; hydrogens, and additional solvent molecules in the asymmetric unit are omitted for clarity). (b) UV-vis spectrum of $\text{L}_2\text{Ni}^{\text{II}}$ in THF at r.t.

We first attempt to synthesize $[\text{LNi}^{\text{II}}\text{Br}_2]^-$ by reacting the deprotonated **L** with 1 equivalent of $\text{NiBr}_2\cdot\text{DME}$ (eq 2). However, the only product obtained from this reaction is the bis-ligand complex, $\text{L}_2\text{Ni}^{\text{II}}$. The crystal structure reveals its tetrahedral configuration. The strong absorbance at 370 nm and 460 nm give $\text{L}_2\text{Ni}^{\text{II}}$ a characteristic green color (Figure 1.7). $\text{L}_2\text{Ni}^{\text{II}}$ is not an active catalyst for the Suzuki alkynylation reaction. Using $\text{L}_2\text{Ni}^{\text{II}}$ as the catalyst for the model reaction gives 0% yield of the cross-coupling product.

Despite numerous variations of the reaction conditions (lower/higher temperature, different solvents, etc.), $\text{L}_2\text{Ni}^{\text{II}}$ remains as the only product indicated by UV-vis. The deprotonated **L** is a strong LX type ligand with an open chelation site. Therefore, we hypothesize that the deprotonated **L** may quickly replace both the DME and bromide

of $\text{NiBr}_2 \cdot \text{DME}$, making the formation of $\text{L}_2\text{Ni}^{\text{II}}$ a kinetically favorable process. Based on these observations, pre-deprotonation of **L** is most likely detrimental to the isolation of $[\text{LNi}^{\text{II}}\text{Br}_2]^-$.

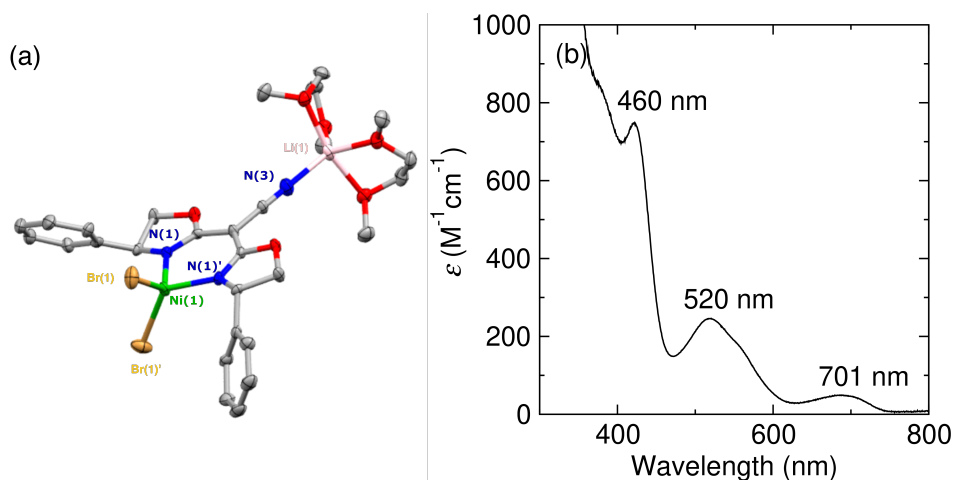
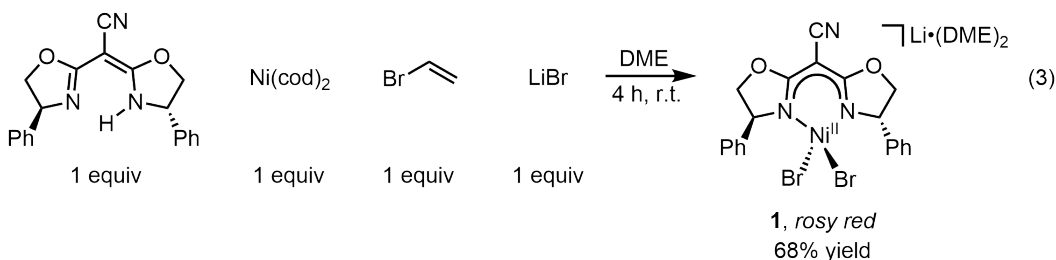


Figure 1.8: (a) X-ray crystal structure of **1** (ellipsoids shown at 30% probability; hydrogens, and additional solvent molecules in the asymmetric unit are omitted for clarity). (b) UV-vis spectrum of **1** in DME/DMA at r.t.

We then attempt to synthesize $[\text{LNi}^{\text{II}}\text{Br}_2]\text{Li}$ by reacting **L** with $\text{Ni}(\text{cod})_2$ in the presence of vinyl bromide and LiBr in DME (eq 3). We hypothesize that vinyl bromide first oxidatively adds to $\text{Ni}(\text{cod})_2$, generating a nickel(II) vinyl bromide intermediate. In the presence of **L**, the vinyl group presumably undergoes protodemetalation, forming $\text{LNi}^{\text{II}}\text{Br}$ and ethylene gas. Br^- from LiBr then fills the vacant site in $\text{LNi}^{\text{II}}\text{Br}$, affording the desired product $[\text{LNi}^{\text{II}}\text{Br}_2]\text{Li}$ (Figure 1.9). The reaction successfully yields the desired product with 68% yield. The isolated rosy red solid is crystallographically characterized as $[\text{LNi}^{\text{II}}\text{Br}_2]\text{Li} \cdot (\text{DME})_2$ (**1**), adopting a tetrahedral geometry. The Li counter cation coordinates to the cyano group in **L**, with two DME solvent molecules chelated (Figure 1.8). In DME/DMA, **1** exhibits three distinct absorptions at 460 nm, 520 nm, and 701 nm. We assign these

absorptions to LMCT, LMCT, and $d \rightarrow d$ transitions, respectively, with the aid of td-DFT calculation (Figure 1.S12).

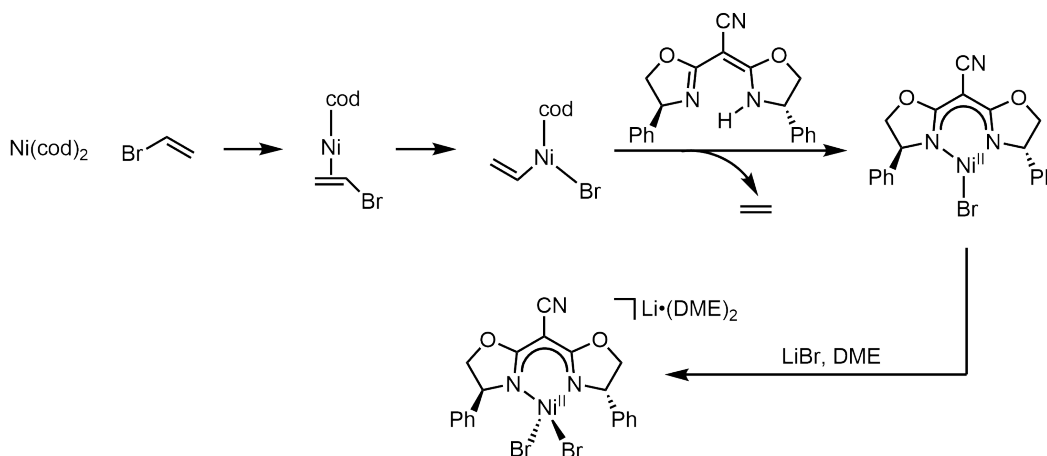


Figure 1.9: Hypothesized chemical events for the synthesis of $[\text{LNi}^{\text{II}}\text{Br}_2]\text{Li}$.

Using **1** as the catalyst for the Suzuki alkylation reaction furnishes 80% yield and 95% ee of the cross-coupling product, comparable to the original reaction condition (eq 4). Unfortunately, even with a well-defined **1** as the catalyst, both LiBr and DMA are required to ensure high yield of the reaction (Table 1.S1). Additionally, without LiBr or DMA, there are no distinct absorption features in the UV-vis spectra, making mechanistic study more challenging (Figure 1.S5-1.S6). Therefore, the final model system retains LiBr and DMA additives. The modified reaction avoids halogen combinatorial complexity, uses a well-defined nickel complex as the catalyst, and remains homogeneous throughout the entire reaction. With the model reaction in hand, we proceed to investigate the resting state of the nickel catalyst for the Suzuki alkylation reaction.



Probing the Resting State of the Catalytic Reaction

EPR analysis of the catalytic reaction progression reveals that the reaction is EPR silent, indicating a nickel(0) or nickel(II) catalytic resting state (Figure 1.S1). With the aid of *in situ* UV-vis spectroscopy, we are able to observe the formation of a distinct nickel species during the catalytic reaction with a strong absorption at

420 nm, a weaker absorption at 510 nm, and a very weak absorption at around 700 nm (Figure 1.10). The absorption at 700 nm is consistent with a $d \rightarrow d$ transition, indicating the predominant nickel species during the catalytic reaction is a nickel(II) complex. The nickel(II) complex is not **1**, as the UV-vis spectrum of **1** is drastically different from that of the catalytic resting state.

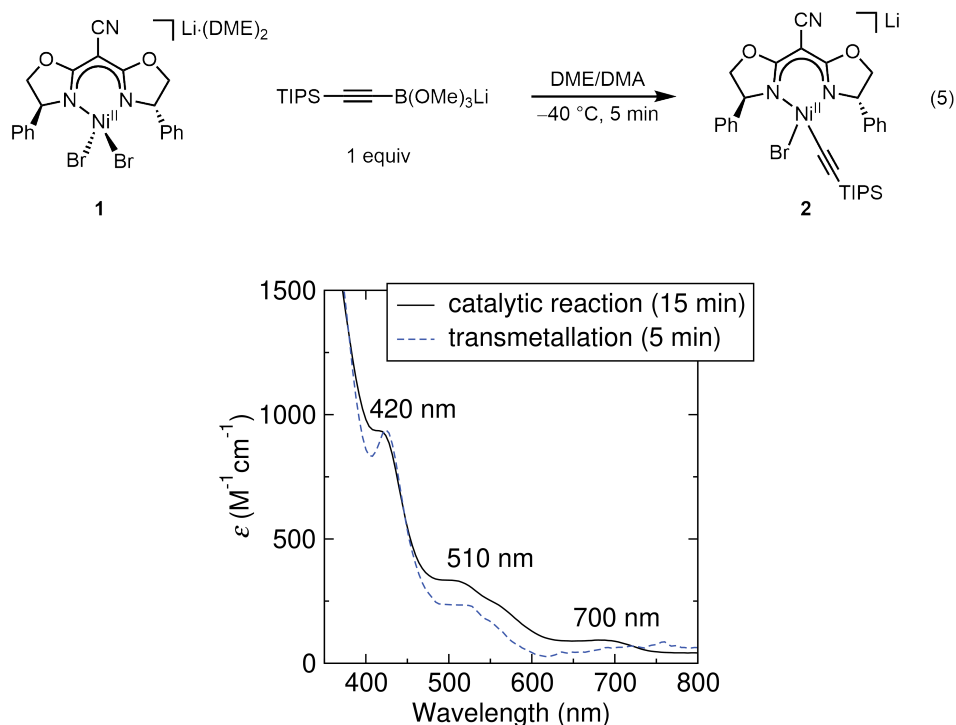


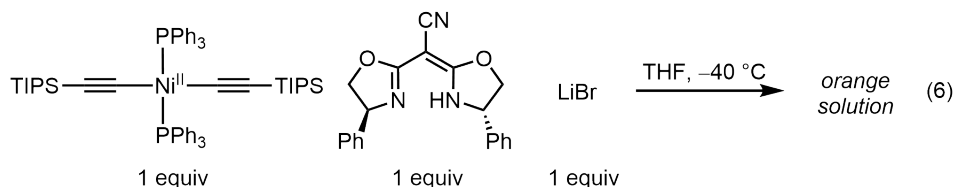
Figure 1.10: UV-vis of the catalytic reaction resting state and the transmetallation reaction of **1** with the nucleophile.

$[\text{LNi}^{\text{II}}\text{Br}(\text{C}\equiv\text{C}-\text{TFSI})]^-$ is another nickel(II) species that is likely the resting state of the catalytic reaction (for the rest of the discussion, we will use "Nu" to represent $-\text{C}\equiv\text{C}-\text{TFSI}$). To test this hypothesis, we react **1** with the nucleophile at $-40\text{ }^\circ\text{C}$ and monitor the reaction with UV-vis. The goal of carrying the reaction at low temperature is to prevent the decomposition of the transmetallation product. The transmetallation reaction yields a UV-vis spectrum that is consistent with the spectrum of the catalytic reaction in progression (Figure 1.10). This observation supports the EPR silent species $[\text{LNi}^{\text{II}}\text{BrNu}]\text{Li}$ (**2**) being the resting state of the catalytic reaction.

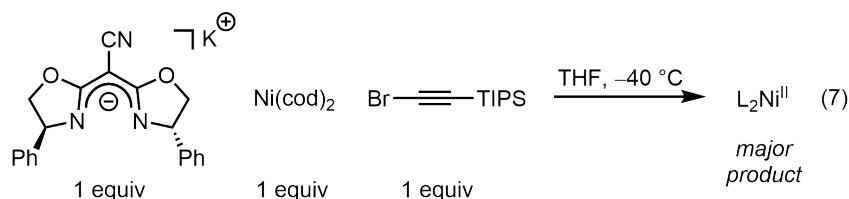
In view of **2** as the potential intermediate in the cross-coupling reaction, we are motivated to isolate **2** and examine its stoichiometric reactivity towards the α -bromo- α -trifluoromethyl electrophile. While the transmetallation reaction can yield

the desired product, monitoring the reaction progression with UV-vis reveals that **2** does not remain stable under the transmetalation reaction condition even at $-40\text{ }^{\circ}\text{C}$ (Figure 1.S3). Therefore, we explored other synthetic strategies for the isolation of **2**.

There are a few alkynyl nickel(II) complexes reported in the literature, all supported by phosphine ligands.^{16–18} Inspired by the success of **1** synthesis *via* protodemetalation, we attempt the synthesis of **2** using a dialkynyl nickel(II) bis-phosphine complex as the precursor (eq 6). We hypothesize that in the presence of **L**, one of the alkynyl groups undergoes protodemetalation, forming the $\text{LNi}^{\text{II}}\text{Nu}$ intermediate. $\text{LNi}^{\text{II}}\text{Nu}$ can then react with LiBr to generate **2**. Unfortunately, the UV-vis of the ligand exchange reaction in progression does not match that of the catalytic reaction resting state (Figure 1.S7). Additionally, we are unable to detect the elimination of (TIPS)acetylene, indicating the ligand exchange does not take place as expected. Therefore, the ligand exchange reaction is not an effective approach to synthesize **2**.



Following the unsuccessful protodemetalation, we attempt to synthesize **2** *via* oxidative addition. For the mechanistic investigation of nickel/box-catalyzed Kumada coupling, (box) $\text{Ni}^{\text{II}}\text{PhBr}$ is synthesized by oxidative addition of phenylbormide to (box) Ni^0 .¹⁴ Additionally, previous work has demonstrated that alkynylbromide can oxidatively add to a nickel(0) source, yielding alkynylbromide nickel(II) complex.^{17,18} Inspired by these results, we attempt an oxidative addition reaction shown in eq 7. To eliminate the potential complication from the proton of **L**, we deprotonate **L** with KHMDS in THF. However, the oxidative addition reaction only yield $\text{L}_2\text{Ni}^{\text{II}}$ as the major product indicated by UV-vis. We suspect that the deprotonated **L** (L^-) is a strong enough ligand to replace both cod ligands in the nickel(0) precursor, forming $[\text{L}_2\text{Ni}^0]^{2-}$, which is then oxidized by the alkynylbromide to form $\text{L}_2\text{Ni}^{\text{II}}$.



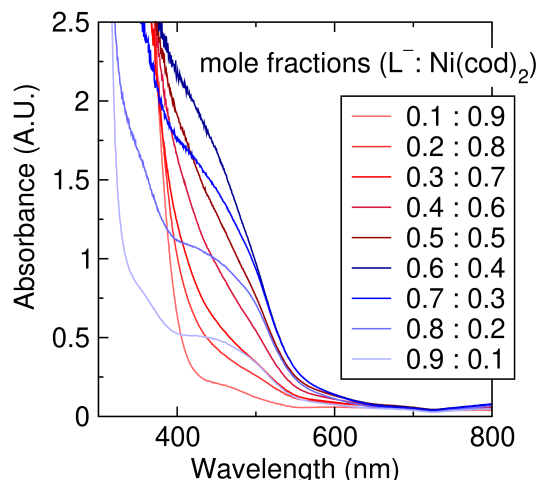
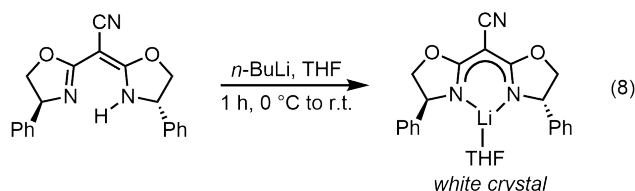


Figure 1.11: UV-vis of the complexation reaction of $\text{Ni}(\text{cod})_2$ with various equivalence of deprotonated L^- in THF.

To test the hypothesis, we use Job's method to determine the stoichiometry of L^- binding to $\text{Ni}(\text{cod})_2$. Figure 1.11 shows the UV-vis spectra of different mole fractions of L^- and $\text{Ni}(\text{cod})_2$ in THF. As the mole fraction of L^- to $\text{Ni}(\text{cod})_2$ increases from 0.1:0.9 to 0.5:0.5, there's a consistent increase in the UV-vis absorbance without any distinct peak resolved. When the mole fraction of L^- to $\text{Ni}(\text{cod})_2$ increases to 0.6:0.4, the solution reaches the highest absorbance. As the mole fraction increases further, the UV-vis absorbance decreases, and a broad absorbance peak at ~ 450 nm is resolved. The spectra obtained for 0.1:0.9 to 0.4:0.6 do not overlap with those for 0.9:0.1 to 0.6:0.4, indicating different speciation at those mole fractions. We hypothesize that at low L^- mole fractions, $[\text{LNi}^0]^-$ is the predominant species. But at high L^- , $[\text{L}_2\text{Ni}^0]^{2-}$ becomes the main nickel complex. The change in speciation can explain the different UV-vis spectra observed at different mole fractions. When the mole fraction of L^- to $\text{Ni}(\text{cod})_2$ is 0.5:0.5, $[\text{LNi}^0]^-$ and $[\text{L}_2\text{Ni}^0]^{2-}$ likely both exist in the solution as L^- is a strong LX type ligand. If we want to synthesize **2** via oxidative addition illustrated in eq 7, it is important to generate $[\text{LNi}^0]^-$ cleanly. As the Job's method indicates a mixture of mono- and bis-ligand nickel(0) complexes in a 1:1 L^- and $\text{Ni}(\text{cod})_2$ reaction mixture, it is unlikely to synthesize **2** using the reaction condition in eq 7.



To prevent the formation of $[\mathbf{L}_2\text{Ni}^0]^{2-}$, we use *n*-BuLi to deprotonate **L** in THF (eq 8). The crystal structure of $[\mathbf{L}]\text{Li}\cdot\text{THF}$ shows the coordination of **L** to Li^+ in a bidentate fashion, which prevents the formation of an open chelation site that would be problematic for the oxidative addition reaction. We envision that an alkynyl bromide can oxidatively add to $\text{Ni}(\text{cod})_2$, forming the nickel(II) alkynyl bromide intermediate. The nickel(II) intermediate then undergoes ligand exchange with the lithiated **L**, generating LiBr and a nickel(II) alkynyl intermediate. LiBr can then fill the vacant site of the nickel(II) alkynyl intermediate, giving rise to the desired product **2** (Figure 1.12).

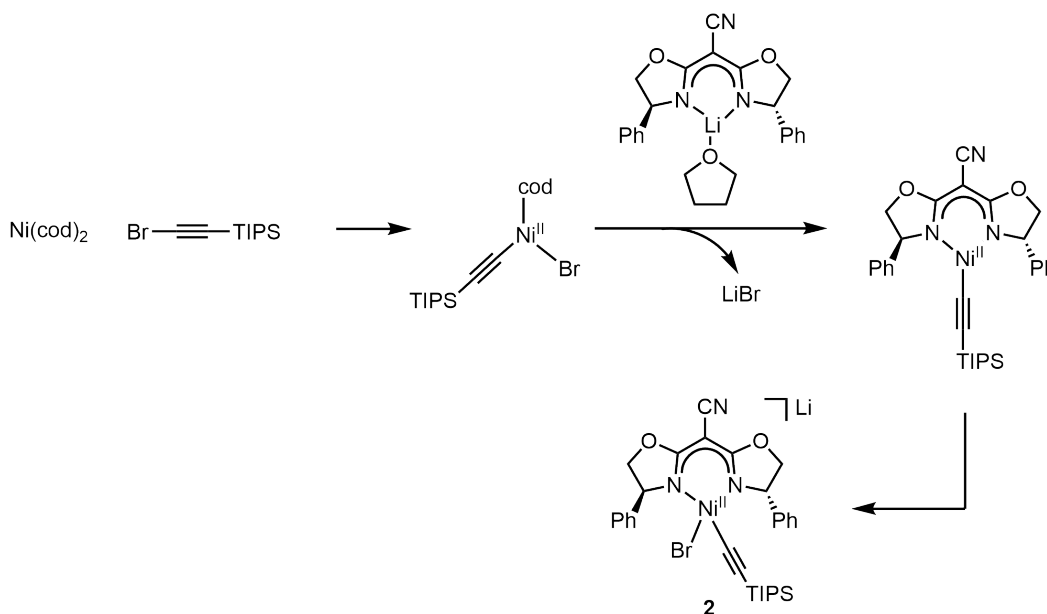


Figure 1.12: Hypothesized chemical events for the synthesis of $[\text{LNi}^{\text{II}}\text{BrNu}]\text{Li}$.

We first carry out the oxidative addition reaction with lithiated **L** in DME at room temperature (eq 9). The reaction yields a green solution. Monitoring the reaction progression with UV-vis reveals a strong absorption at 452 nm (Figure 1.13a), which does not match that of the resting state, or $\text{L}_2\text{Ni}^{\text{II}}$. Surprisingly, the reaction also generates diyne as a major product. We suspect that the oxidative addition reaction can access the desired product **2**. However, due to the low steric hinderance from the ligands, **2** generated *in situ* can undergo ligand exchange with another **2**, forming a bis-alkynyl nickel(II) intermediate, which reductively eliminates to yield diyne as the product (Figure 1.14). The detection of EPR signal (Figure 1.S10) during the oxidative addition reaction further supports our hypothesis, as reductive elimination will generate nickel(0) species that can undergo comproportionation with any nickel(II) complexes in the reaction mixture to yield nickel(I) complexes.

Monitoring the oxidative addition reaction with GC reveals diyne formation from the very beginning of the reaction, indicating that **2** does not remain stable at room temperature if formed (Figure 1.13b).

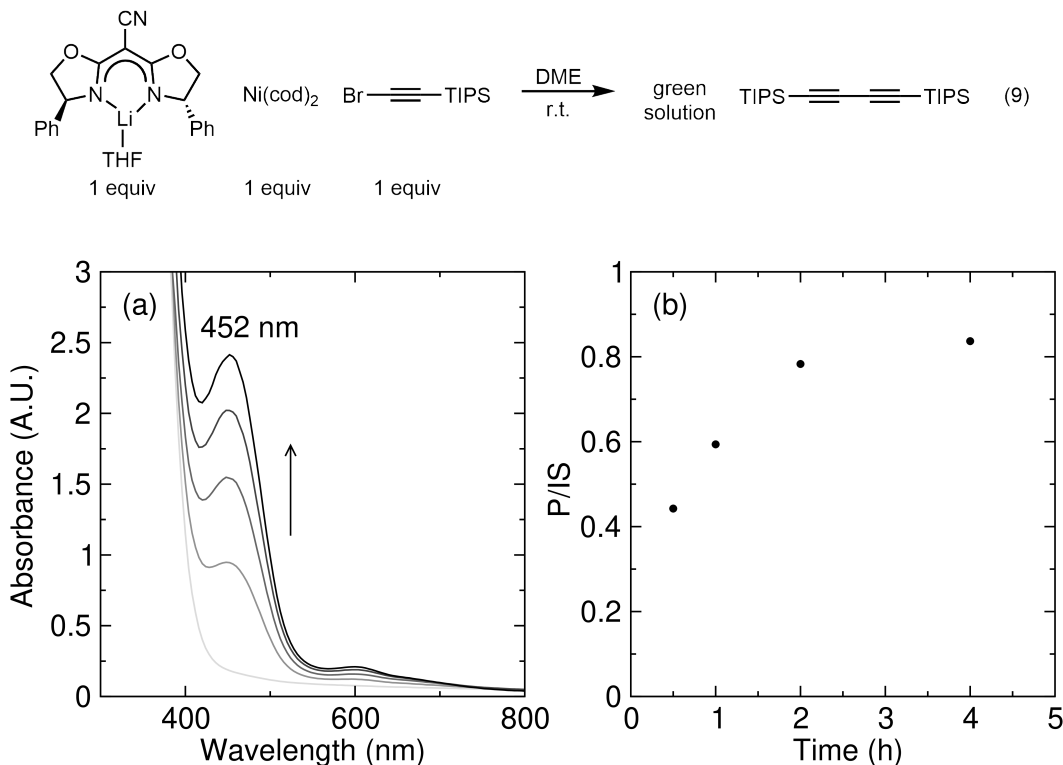


Figure 1.13: (a) UV-vis of the oxidative addition reaction progression (0-2 h). Spectra were collected every 30 min. (b) Monitor the formation of diyne with GC with hexadecane as the internal standard.

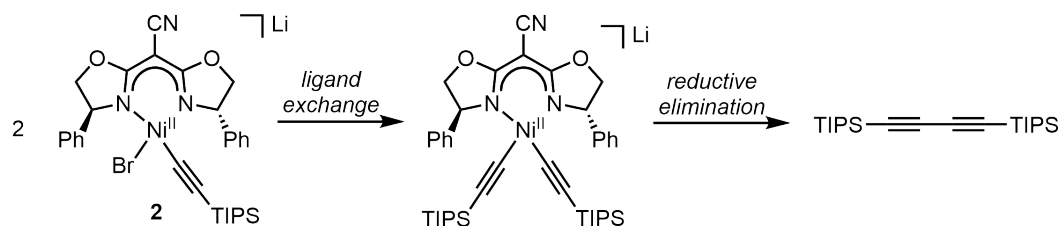


Figure 1.14: Hypothesized chemical events of the decomposition of $[\text{LNi}^{\text{II}}\text{BrNu}]\text{Li}$.

To prevent the ligand exchange decomposition pathway, we attempt to increase the bulkiness of **L** (Figure 1.15) in hopes of isolating an analog of **2**.¹⁴ Additionally, we tested various substituents (e.g., -Ph, $-(\text{CH}_2)_2\text{Ph}$) on the alkynyl bromide for the oxidative addition reaction (eq 10). The stability of the alkynyl bromide nickel(II) complex and the solubility of lithiated cyano-box ligands are the main challenges. At room temperature, the ligand exchange takes place as indicated by the formation

of diyne. At low temperature, the solubility of lithiated cyano-box ligands decrease significantly, leading to ligand crystallization from the reaction mixtures. Therefore, despite numerous attempts with various reaction conditions, the isolation of **2** or its analog remain elusive.

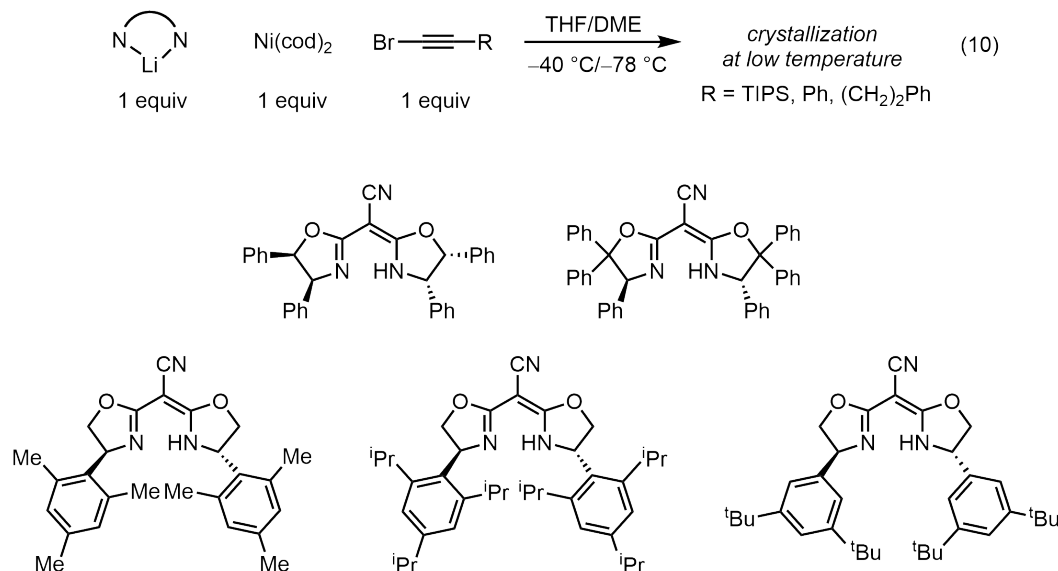
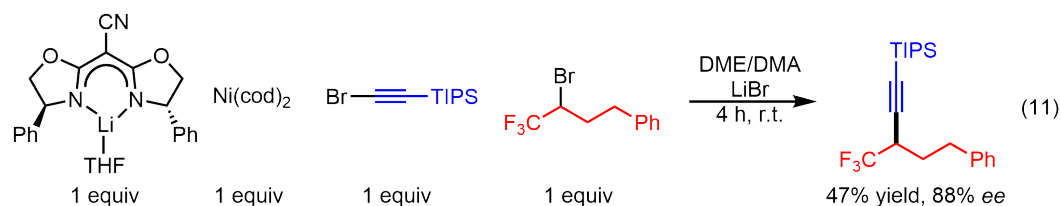


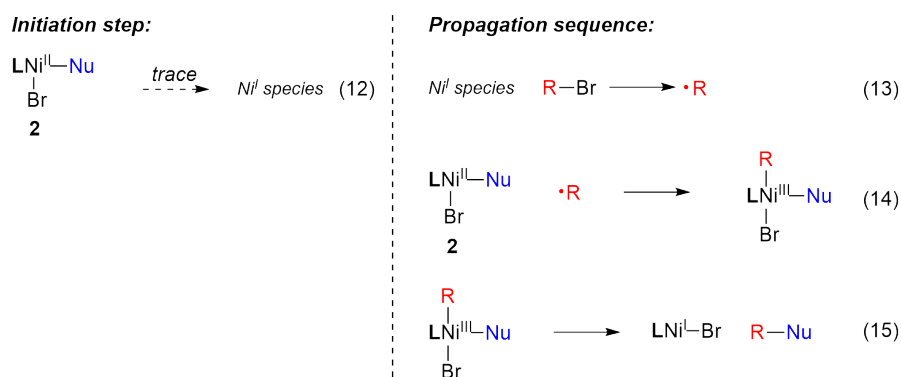
Figure 1.15: Various bulky Ar-cyano-box ligands.

Given the challenges associated with **2** isolation, we seek to generate **2** and test its reactivity *in situ*. As indicated by Figure 1.13b, the formation and decomposition of **2** takes place in the time span of 2 hours at room temperature. Therefore, it is possible to intercept **2** before it decomposes *via* ligand exchange, and test its stoichiometric reactivity towards α -bromo- α -trifluoromethyl electrophiles at room temperature. To generate **2** *in situ*, we add alkynyl bromide to a solution of lithiated **L**, Ni(cod)₂, and LiBr in DME/DMA at room temperature. The reaction is immediately followed by the addition of the α -bromo- α -trifluoromethyl electrophile (eq 11). After 4 h at room temperature, the reaction affords the cross-coupling product with 47% yield and 88% ee.



Despite the low yield of the stoichiometric reaction, the enantioselectivity obtained is rather comparable to the standard catalytic reaction (93% ee). The comparable

enantioselectivity suggests that the stoichiometric reaction and the catalytic reaction can access the same transition state for reductive elimination to forge the C–C bond. We postulate that during the *in situ* stoichiometric reaction, **2** is first generated *via* the oxidative addition mechanism proposed in eq 11. **2** then decomposes at room temperature to generate trace amounts of nickel(I) species (eq 12). The nickel(I) species can initiate the reaction by abstracting the halogen from the electrophile (eq 13). The resulting organic radical is captured by **2** to form $[\text{LNi}^{\text{III}}\text{BrNuR}]\text{Li}$ (eq 14), which reductively eliminates to afford the cross-coupling product with high enantioselectivity (eq 15). This result, together with the spectroscopic evidence, strongly supports **2** being an active intermediate of this catalytic reaction.



Synthesis of $[\text{LNi}^{\text{I}}\text{Br}]^-$

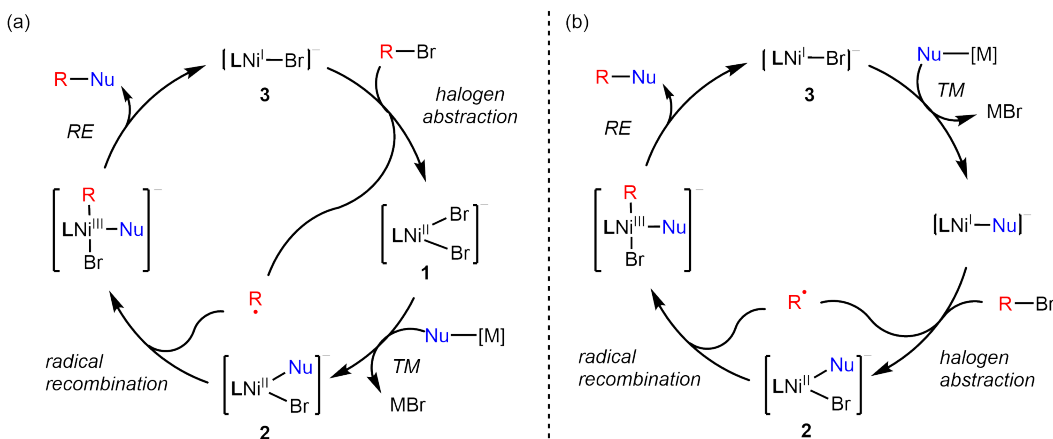
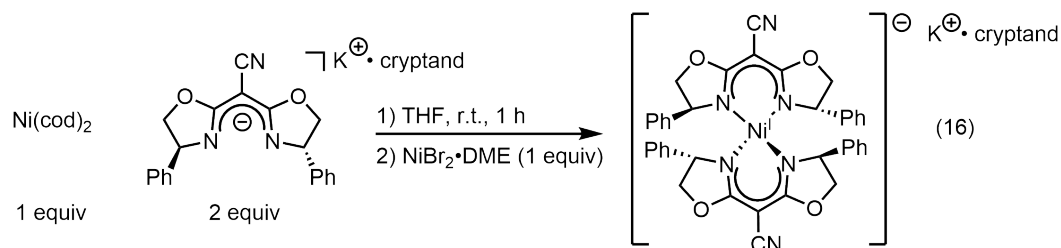


Figure 1.16: Working catalytic pathways with **2** as the resting state of the catalytic cycle (TM = transmetalation; RE = reductive elimination).

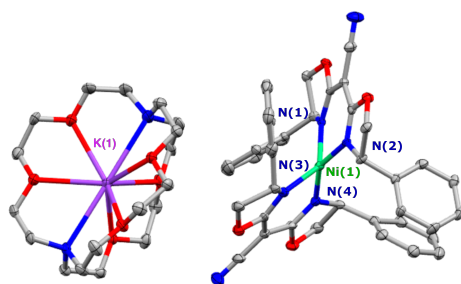
Based on the knowledge of **2** being an active intermediate, we construct two possible catalytic cycles for the Suzuki alkynylation reaction. For the oxidative addition-first radical chain pathway, the reaction of $[\text{LNi}^{\text{I}}\text{Br}]^-$ (**3**) with the electrophile generates **1** and an organic radical. **1** undergoes transmetalation to afford the resting

state **2**, which reacts with the organic radical to give the nickel(III) intermediate (Figure 1.16a). Alternatively, **3** can undergo transmetalation first to generate $[\text{LNi}^{\text{I}}\text{Nu}]^-$, which can then react with the electrophile to afford the resting state **2** (Figure 1.16b). In order to distinguish between the two possible pathways, we decided to isolate **3** and compare the rate constant for the oxidative addition of the electrophile to **3** and the rate constant for the transmetalation of the nucleophile to **3**.

There are two crystallographically characterized bis(oxazoline)-supported nickel(I) bromide complexes reported in literature.^{13,14} Both complexes are synthesized *via* a comproportionation reaction between nickel(0) and nickel(II) in the presence of the ligand of interest. Inspired by these synthesis, we conduct a series of comproportionation reactions in attempt to access **3**.



(a)



(b)

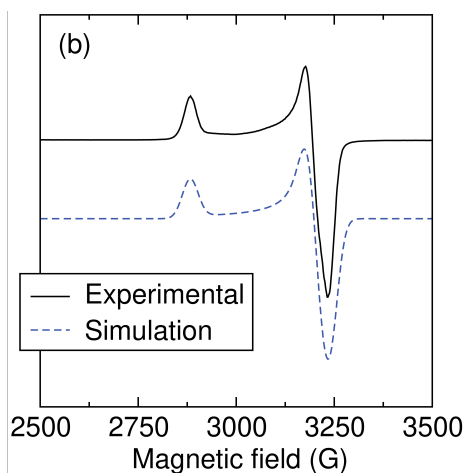


Figure 1.17: (a) X-ray crystal structure of $[\text{L}_2\text{Ni}^{\text{I}}]\text{K}(\text{cryptand})$ (ellipsoids are shown at 30% probability; hydrogens and additional solvent molecules in the asymmetric unit are omitted for clarity). (b) X-band EPR spectrum and the simulation of $[\text{L}_2\text{Ni}^{\text{I}}]\text{K}(\text{cryptand})$ collected at 77 K in a THF/2-MeTHF (1:1) glass at $\nu = 9.404$ GHz at 2.036 mW power and a modulation amplitude of 2.00 G.

We first attempt to react $\text{Ni}(\text{cod})_2$ with $\text{NiBr}_2 \cdot \text{DME}$ in the presence of L^- (eq 16). By trapping K^+ with 2.2.2-cryptand, the reaction furnishes $[\text{L}_2\text{Ni}^{\text{I}}]\text{K}(\text{cryptand})$ as

the major product (Figure 1.17a). The EPR spectrum of $[\text{L}_2\text{Ni}^{\text{I}}]\text{K}(\text{cryptand})$ depicts an axial signal without any resolved N hyperfine couplings (Figure 1.17b, simulation parameters: $g_x = 2.3300$, $g_y = 2.0730$, $g_z = 2.1000$). Using $[\text{L}_2\text{Ni}^{\text{I}}]\text{K}(\text{cryptand})$ as the catalyst for the Suzuki alkynylation reaction gives 0% yield of the cross-coupling product, indicating $[\text{L}_2\text{Ni}^{\text{I}}]^-$ not being an active nickel intermediate for the catalytic reaction.

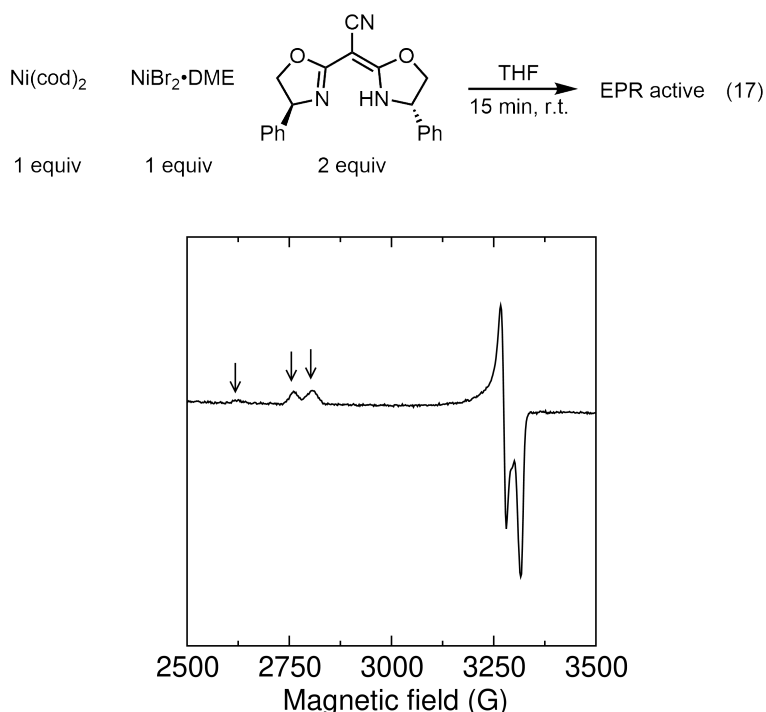


Figure 1.18: X-band EPR spectrum of the filtrate of the comproportionation reaction shown in eq 17. The spectrum was collected at 77 K in frozen THF at $\nu = 9.403$ GHz at 2.036 mW power and a modulation amplitude of 2.00 G.

To avoid the formation of $[\text{L}_2\text{Ni}^{\text{I}}]^-$ formation, we perform the comproportionation reaction without deprotonating **L** (eq 17). The reaction mixture is filtered after stirring at room temperature for 15 min. Analyzing the filtrate with EPR reveals three new nickel(I) species, indicated by the arrows in Figure 1.18. It is not immediately obvious which signal represents the desired product **3**. We hypothesize that the filtrate may contain a mixture of **3** and $\text{LNi}^{\text{I}}(\text{cod})$.

To observe $\text{LNi}^{\text{I}}(\text{cod})$ separately without the complication from bromide, we oxidize $\text{Ni}(\text{cod})_2$ using FcPF_6 in the presence of **L** (eq 18). Analyzing the reaction mixture with EPR reveals two axial signals that are consistent with the major products observed in the comproportionation reaction (Figure 1.19). The signals are assigned as $\text{LNi}^{\text{I}}(\eta^4\text{-cod})$ and $\text{LNi}^{\text{I}}(\eta^2\text{-cod})$. This orthogonal approach to reproduce the

nickel(I) signals observed in Figure 1.18 confirms that the comproportionation reaction shown in eq 17 does not yield **3** as the major product.

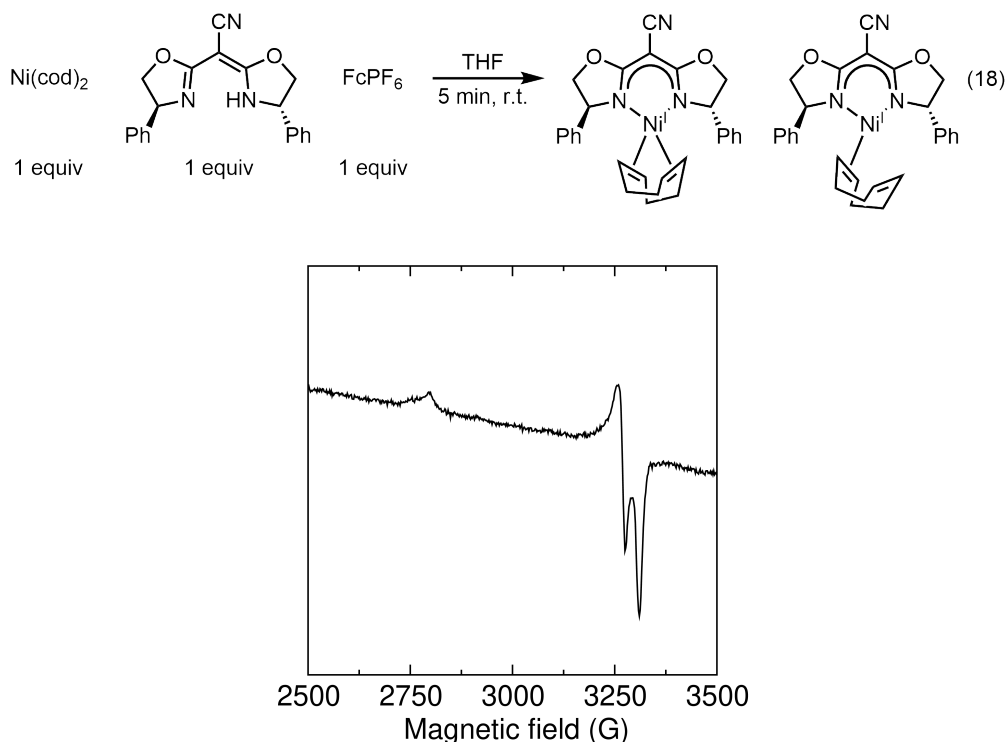


Figure 1.19: X-band EPR spectrum of the filtrate of the oxidation reaction shown in eq 18. The spectrum was collected at 77 K in frozen THF at $\nu = 9.393$ GHz at 2.036 mW power and a modulation amplitude of 2.00 G.

Our third approach to comproportionation is carried out between $\text{Ni}(\text{cod})_2$ and $\text{NiBr}_2 \cdot \text{DME}$ in the presence of **L** and LiBr (eq 19). We hypothesize that the excess Br^- can displace cod on $\text{LNi}^{\text{I}}(\text{cod})$, leading to the formation of **3**. The EPR of the comproportionation reaction reveals a new axial signal that is likely **3** (Figure 1.20).

To further confirm the identify of the nickel(I) species, we attempt to obtain the same EPR signal through an alternative synthetic route. Jones *et al.* reported the synthesis of $(\text{terpy})\text{Ni}^{\text{I}}$ *via* oxidation of $\text{Ni}(\text{cod})_2$ by a single electron oxidant Me-I or Et-I .⁶ Thus, we carry out a similar oxidation of $\text{Ni}(\text{cod})_2$ using benzyl bromide in the presence of **L** (eq 20). Although in much lower yield, this orthogonal synthetic route generates the same axial EPR signal observed in the comproportionation reaction (Figure 1.S8). This experiment provides strong evidence that the EPR signal observed in Figure 1.20) corresponds to **3**.

Despite the success of identifying the EPR signal of **3**, isolating the nickel(I) complex is not straightforward. As indicated by the weak EPR signals detected, neither the

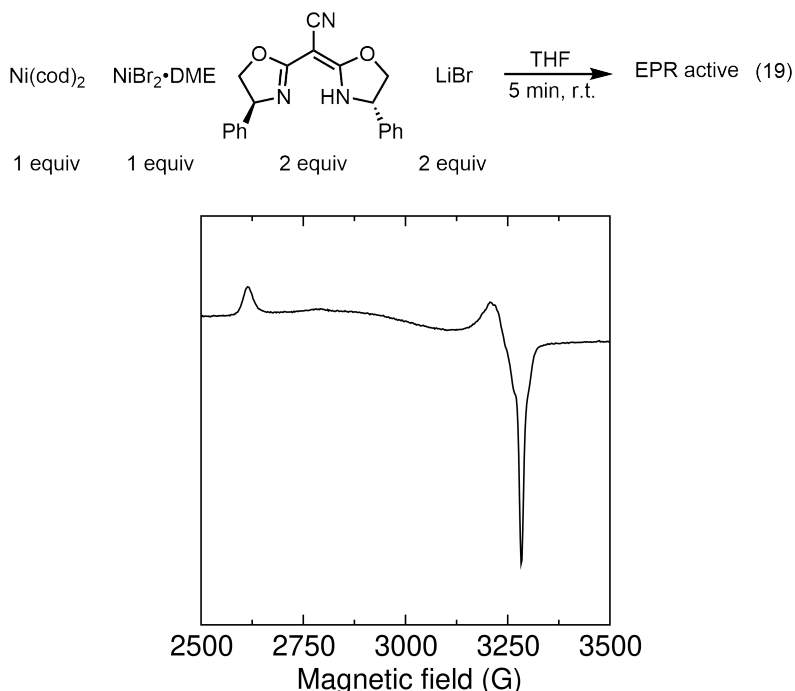
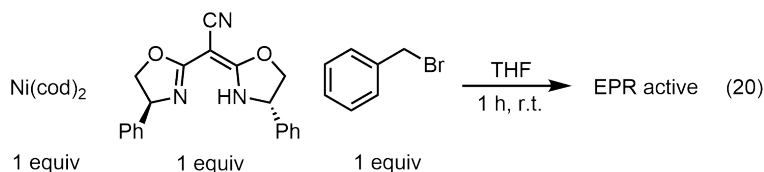


Figure 1.20: X-band EPR spectrum of the filtrate of the comproportionation reaction shown in eq 19. The spectrum was collected at 77 K in frozen THF at $\nu = 9.367$ GHz at 2.031 mW power and a modulation amplitude of 2.00 G.



comproportionation route (eq 19) nor the oxidation route (eq 20) are able to generate **3** with high yield. Additionally, the $\text{LNi}^{\text{I}}(\text{cod})$ signals are present in both EPR spectra. The mixed nickel(I) species adds additional challenge to the isolation of **3**.

To isolate **3**, it is important to develop an alternative synthetic route that can access **3** with high yield. After extensive reaction condition screening, we are able to generate **3** via a different comproportionation route. As shown in eq 21, the reaction involves the comproportionation between $\text{Ni}(\text{cod})_2$ and $\text{NiBr}_2 \cdot \text{DME}$ in the presence of **L**. The reaction quickly generates a light brown solution with precipitation of nickel black. The EPR spectrum of the reaction filtrate depicts a high resolution signal consist with that of **3** with small N hyperfine coupling (Figure 1.21b, simulation parameters: $g_x = 2.5618$, $g_y = 2.0681$, $g_z = 2.0400$; for one N atom, $A_x(^{14}\text{N}) = 18$ MHz, $A_y(^{14}\text{N}) = 44$ MHz, $A_z(^{14}\text{N}) = 16$ MHz; for one N atom, $A_x(^{14}\text{N}) = 33$ MHz, $A_y(^{14}\text{N}) = 49$ MHz, $A_z(^{14}\text{N}) = 12$ MHz; $lw = 1.35$, $g\text{Strain}$, $W_x = 0.01$,

$W_y = 0.01$, $W_z = 0.01$). The isodensity representation of the SOMO of **3** shows that the unpaired electron is delocalized over the cyano-box ligand, which explains the observed N hyperfine coupling. (Figure 1.21a). With quantitative EPR, we are able to calculate the yield of the comproportionation reaction to be 70%.

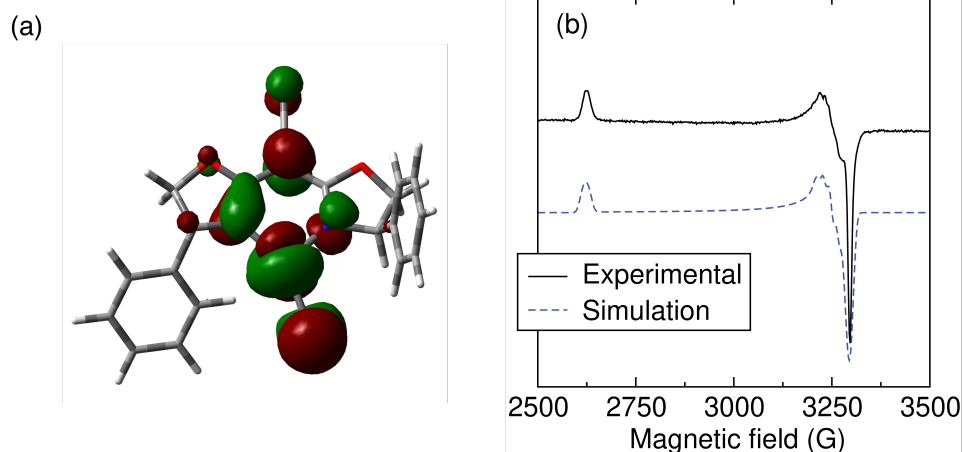
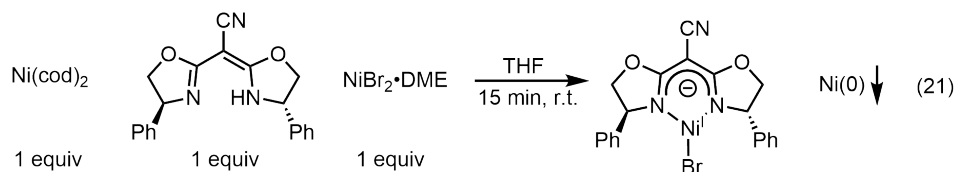
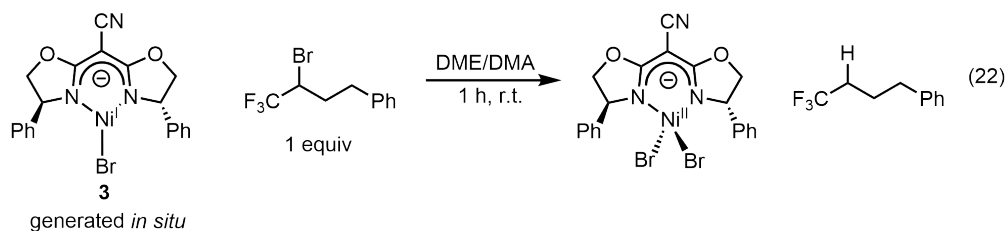


Figure 1.21: (a) The isodensity representation of the SOMO of **3**. (b) X-band EPR spectrum and the simulation of the filtrate of the comproportionation reaction shown in eq 21. The spectrum was collected at 77 K in a THF/2-MeTHF (1:1) glass at $\nu = 9.403$ GHz at 2.021 mW power and a modulation amplitude of 2.00 G.

Unfortunately, the isolation of **3** remains elusive even with the new comproportionation condition. The challenges of crystallizing **3** is similar to those encountered during the attempted isolation of **2**. At room temperature, the nickel(I) complex decomposes indicated by the decreased EPR signal intensity as a function of time. At low temperature, the solubility of **L** and NiBr₂·DME decrease, resulting in the starting materials crashing out of the reaction mixture. However, we are able to test the reactivity of *in situ* generated **3** without isolation. As shown in eq 22, *in situ* generated **3** can react with the α -bromo- α -trifluoromethyl electrophile, generating **2** (Figure 1.S4) and the hydrodehalogenation product. This reaction demonstrate the ability of **3** to activate the electrophile in the catalytic reaction condition, supporting the oxidative addition elementary step in the proposed mechanism shown in Figure 1.16.



1.3 Conclusion

In summary, our study aims to elucidate the mechanism of an enantioselective nickel/cyano-box-catalyzed Suzuki alkynylation of α -bromo- α -trifluoromethyl electrophile. Specifically, we focus on isolating the three potential intermediates ($[\text{LNi}^{\text{II}}\text{Br}_2]^-$, $[\text{LNi}^{\text{II}}\text{BrNu}]^-$, and $[\text{LNi}^{\text{I}}\text{Br}]^-$) and evaluating their stoichiometric reactivity. In particular, we provided spectroscopic/stoichiometric evidence supporting $[\text{LNi}^{\text{II}}\text{BrNu}]^-$ being the predominant resting state of the catalytic reaction. The existing data is consistent with a radical chain pathway. However, to unambiguously distinguish between the oxidative-addition-first and transmetalation-first mechanisms shown in Figure 1.16, we need to isolate $[\text{LNi}^{\text{I}}\text{Br}]^-$ and compare its reactivity with the electrophile and the nucleophile in the future. The research presented here demonstrates the challenges of isolating anionic bidentate ligand supported nickel complexes. We hope the strategies shown here can inform future efforts to synthesize similar metal complexes.

1.4 Supporting Information

I. General Information

Materials. The following reagents were purchased from commercial suppliers and used as received: Ni(cod)₂ (98+%, Strem), NiBr₂·DME (99+%, Alfa Aesar), *n*-BuLi (2.5 M in hexanes, Sigma-Aldrich). DME, THF, Et₂O, DCM, and *n*-pentane were sparged with dry argon and dried *via* a solvent purification system comprised of columns packed with neutral alumina. The α -bromo- α -trifluoromethyl electrophile and **L** were synthesized according to reported procedures.¹⁵ Unless noted otherwise, all reagents were purchased from commercial vendors and used without further purification.

Crystallographic details. X-ray diffraction studies were carried out at the Beckman Institute Crystallography Facility on a Bruker KAPPA four-circle diffractometer. The crystals were mounted in a nylon loop with Paratone-N oil. Data was collected at 100 K using Mo-K α ($\lambda = 0.71073 \text{ \AA}$) radiation. Using Olex 2,¹⁹ the structure was solved using Direct Methods and refined with the ShelXL²⁰ refinement package using Least Squares minimization. X-ray quality crystals were grown as described in the experimental procedures.

Spectroscopy. X-band continuous-wave EPR measurements were conducted on a Bruker EMX spectrometer with the sample in a frozen solvent at 77 K. Simulation of EPR spectra was accomplished using the EasySpin package.

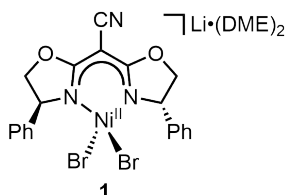
UV-vis spectra were collected on a Cary 50 UV-vis spectrometer using a 10 nm path-length quartz cuvette equipped with a puncturable screw cap. Variable-temperature measurements employed a Unisoku CoolSpek cryostat.

¹H and ¹⁹F NMR were collected on a Varian 300 MHz spectrometer at ambient temperature. ¹H spectra were referenced to residual solvent resonances. ¹⁹F spectra were referenced to external α,α,α -trifluorotoluene ($\delta = -63.72$).

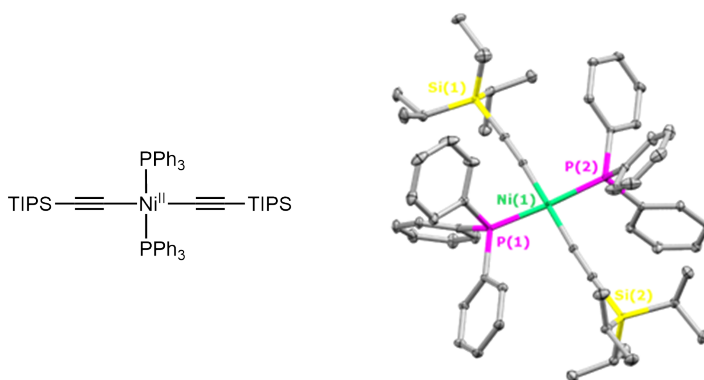
Chromatography. GC data were collected on an Agilent 6890N GC system with an FID detector. *n*-hexadecane was used as an internal standard. Analysis of enantio-enriched organic compounds was conducted on an Agilent 1100 series system with Daicel CHIRALPAK or Daicel CHIRALCEL columns (internal diameter 4.6 mm, column length 250 mm, particle size 5 μ m).

II. Synthesis

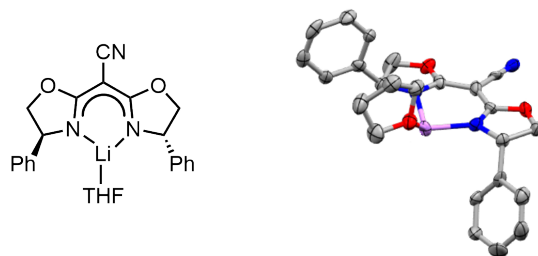
These yields have not been optimized. All manipulations were carried out using standard Schlenk or glovebox techniques under a N₂ atmosphere.



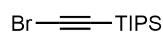
[LNi^{II}Br₂]Li·DME₂ (**1**) To an oven-dried 20 mL vial equipped with a stir bar, Ni(cod)₂ (0.15 mmol), **L** (0.15 mmol), LiBr (0.15 mmol) and DME (10 mL) were added. The mixture was stirred vigorously for 10 min at room temperature until all starting materials had dissolved. Vinyl bromide (0.15 mmol) was then added to the reaction mixture *via* a microsyringe. The reaction mixture was stirred for 4 h at room temperature to yield a red solution. Layer diffusion of *n*-pentane into the red solution at room temperature furnished **1** as a rosy red crystal (68% yield).



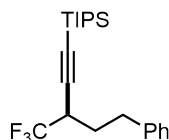
Ni^{II}(PPh₃)₂(C≡C-TIPS)₂ An oven-dried 20 mL vial equipped with a stir bar was charged with Ni(PPh₃)₂Br₂ (0.13 mmol) (triisopropylsilane)acetylene (0.75 mmol) and CuI (0.018 mmol). To the solid mixture benzene (5 mL) was added. The mixture was cooled to 0 °C and diethylamine (1.6 mmol) was added. The reaction mixture was allowed to slowly warm to room temperature and stirred overnight. The resulting solution was concentrated and re-dissolved in DCM. Layer diffusion of *n*-pentane into the DCM solution at room temperature furnished the desired product as a yellow crystal (2% yield). The product was stored in a glovebox.



[L]Li·THF To an oven-dried 20 mL vial equipped with a stir bar, **L** (0.15 mmol) and THF (2 mL) were added. The solutions was cooled to 0 °C for 10 min. To the stirred solution of ligand was added *n*-BuLi (2.5 M, 0.16 mmol). The reaction was stirred at 0 °C for 30 min followed by another 30 min stirring at room temperature. Layer diffusion of *n*-pentane into the reaction solution at room temperature furnished **[L]Li·THF** as a white crystal.



(Bromoethynyl)triisopropylsilane An oven-dried 40 mL vial equipped with a stir bar was charged with ethynyltriisopropylsilane (5.0 mmol), N-bromosuccinimide (6.0 mmol), and AgNO₃ (0.5 mmol). To the solid mixture, acetone was added. The reaction mixture was stirred at room temperature overnight without exposing to light. The reaction mixture was then filtered through a celite plug and concentrated under reduced pressure. The crude was purified by chromatography on silica gel (100% hexanes), which furnished a colorless oil as the desired product.



Triisopropyl(5-phenyl-3-(trifluoromethyl)pent-1-yn-1-yl)silane. The title compound was synthesized from (±)-(3-bromo-4,4,4-trifluorobutyl)benzene and the corresponding alkynylboron reagent using the catalytic cross-coupling procedure described in the next section. The characterization data are consistent with the previous report.¹⁵

III. Catalytic Reaction

Preparation of alkynylboron reagents (0.47 M). An oven-dried 4 mL vial equipped with a stir bar was charged with the alkyne (0.5 mmol) and DME (0.5 mL). The vial was closed with a PTFE septum cap. A solution of *n*-BuLi (2.45 M; 0.20 mL, 2.0 mmol; 1.0 equiv) was added over 1 min to the 4 mL vial, which had been cooled to 0 °C for 10 min. The mixture was allowed to stir at 0 °C for another 5 min and then warmed to room temperature. After stirring at room temperature for 10 min, DME was added to produce a total volume of 1 mL (0.5 M). Next B(OMe)₃ (0.062 mL; 2.2 mmol; 1.1 equiv) was added to the alkynyllithium solution to provide an alkynylboron solution (0.47 M). The mixture was allowed to stir for 30 min at room temperature and used directly in the cross-coupling reactions.

Modify the catalytic reaction condition for the mechanistic study. An oven-dried 4 mL vial equipped with a stir bar was charged with nickel catalyst (0.005 mmol) and LiX additive (0.10 mmol). Solvent (0.74 mL, DME or DME/DMA 5.3:1 v/v) was added to the vial and the mixture was vigorously stirred at room temperature for 30 min. The electrophile (R-X, 0.10 mmol) was then added to the vial and the vial was sealed with a PTFE septum cap and wrapped with electrical tape. To the vigorously stirred solution of catalyst and electrophile was added a solution of the alkynylboron reagent (0.12 mmol; 1.2 equiv) over 1 min. The mixture was stirred at room temperature for 5 h, then MeOH (0.2 mL) was added to quench the reaction. The resulting mixture was then diluted with Et₂O (3 mL) and washed with deionized water (3 mL × 3). The organic layer was dried over MgSO₄, filtered, and then concentrated. The crude was analyzed with ¹⁹F NMR spectroscopy and chiral HPLC. The condition variations and the yield and %ee of the cross-coupling product are tabulated in Table 1.S1.

General procedure for the model nickel-catalyzed asymmetric alkylation. An oven-dried 4 mL vial equipped with a stir bar was charged with **1** (0.005 mmol) and LiBr (0.10 mmol). DME/DMA (5.3:1 v/v) (0.74 mL) was added to the vial and the mixture was vigorously stirred at room temperature for 30 min. The electrophile (R-Br, 0.10 mmol) was then added to the vial and the vial was sealed with a PTFE septum cap and wrapped with electrical tape. To the vigorously stirred solution of catalyst and electrophile was added a solution of the alkynylboron reagent (0.12 mmol; 1.2 equiv) over 1 min. The mixture was stirred at room temperature for 5 h, then MeOH (0.2 mL) was added to quench the reaction. The resulting mixture was then diluted with Et₂O (3 mL) and washed with deionized water (3 mL × 3).

The organic layer was dried over MgSO_4 , filtered, and then concentrated. The crude was analyzed with ^{19}F NMR spectroscopy and chiral HPLC.

Table 1.S1: Attempt to unify the halogens and remove additives in catalytic reaction condition.

Ni catalyst	LiX	R-X	Yield (%)	% ee
$\text{NiCl}_2 \cdot \text{DME} + \mathbf{L}$ (1.2 equiv)	LiCl	Cl	0	–
$\text{NiBr}_2 \cdot \text{DME} + \mathbf{L}$ (1.2 equiv)	LiBr	Br	81	90
$[\text{LNi}^{\text{II}}\text{I}_2]\text{NBu}_4^a$	LiI	I	26	60
$[\text{LNi}^{\text{II}}\text{Br}_2]\text{Li} \cdot \text{DME}_2$	LiBr	Br	80	95
$[\text{LNi}^{\text{II}}\text{Br}_2]\text{Li} \cdot \text{DME}_2^b$	LiBr	Br	76	95
$[\text{LNi}^{\text{II}}\text{Br}_2]\text{Li} \cdot \text{DME}_2^b$	–	Br	62	96

^asynthesized by oxidizing $\text{Ni}(\text{cod})_2$ with vinyl iodide (1 equiv) in the presence of \mathbf{L} (1 equiv) and TBAI (1 equiv) in THF. ^bThe reaction was performed without DMA additive.

Monitoring the model catalytic reaction with EPR spectroscopy. In a nitrogen-filled glovebox, an oven-dried 20 mL vial equipped with a stir bar was charged with $\text{NiBr}_2 \cdot \text{DME}$ (0.025 mmol), **L** (0.03 mmol), and LiBr (0.50 mmol). DME/DMA (5.3:1 v/v, 3.8 mL) was added to the vial and the mixture was vigorously stirred at room temperature for 30 min. The electrophile (0.50 mmol) was then added to the vial and the vial was sealed with a PTFE septum cap. To the vigorously stirred solution of catalyst and electrophile was added the solution of the alkynylboron reagent (0.60 mmol; 1.2 equiv) over 1 min. At each indicated time point, an aliquot (0.3 mL) of the reaction mixture was transferred *via* syringe to an EPR tube equipped with a rubber septum in the glovebox. The EPR tube was then transferred out of the glovebox and then promptly frozen with liquid nitrogen and subjected to EPR analysis at 77 K.

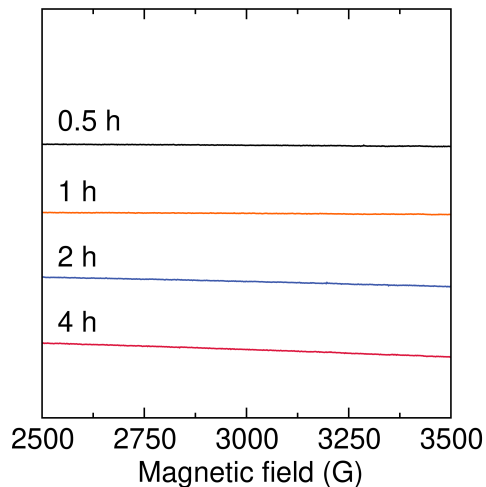


Figure 1.S1: X-band EPR spectra of the model catalytic reaction at different time points. The spectra were collected at 77 K in frozen DME/DMA at $\nu = 9.389$ GHz at 2.031 mW power and a modulation amplitude of 2.00 G.

Monitoring the model catalytic reaction with UV-vis spectroscopy. In a nitrogen-filled glovebox, a quartz cuvette equipped with a stir bar was charged with **1** (0.005 mmol), and LiBr (0.10 mmol). DME/DMA (5.3:1 v/v, 3.8 mL) was added to the cuvette and the mixture was stirred at room temperature to obtain a homogeneous solution. The electrophile (0.10 mmol) was then added to the cuvette and the cuvette was sealed with a puncturable screw cap and transferred out of the glovebox. To the stirred solution was added the solution of the alkynylboron reagent (0.12 mmol) over 1 min. The reaction was monitored *via* UV-vis spectroscopy.

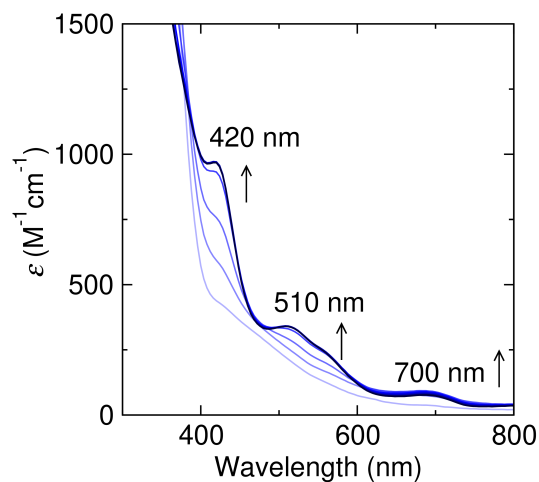


Figure 1.S2: UV-vis spectra of the model catalytic reaction from 1 min to 40 min. Spectrum was collected every 5 min. Starting from 15 min, the UV-vis absorption features no longer changes.

IV. Stoichiometric Reactivity

Transmetallation between 1 and the nucleophile. In a nitrogen-filled glovebox, a solution of **1** (0.0025 mmol) in DME/DMA (5.3:1 v/v, 3.9 mL) was added to a quartz cuvette. The cuvette was then sealed with a puncturable screw cap and cooled to $-40\text{ }^{\circ}\text{C}$, and a solution of the nucleophile (0.005 mmol) was added *via* syringe over 10 s with stirring. The reaction was monitored *via* UV-vis spectroscopy.

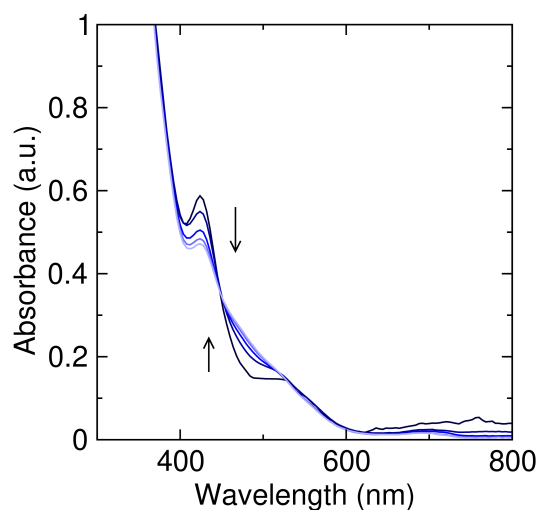
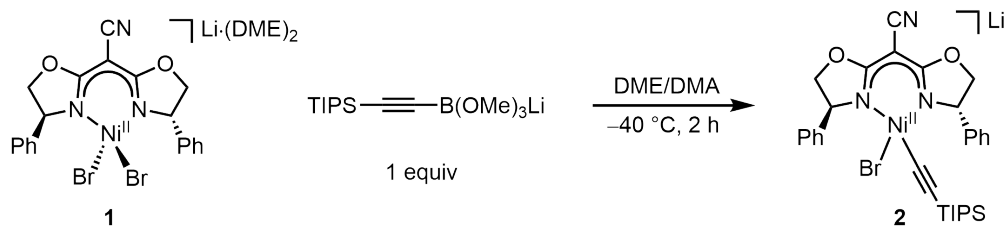
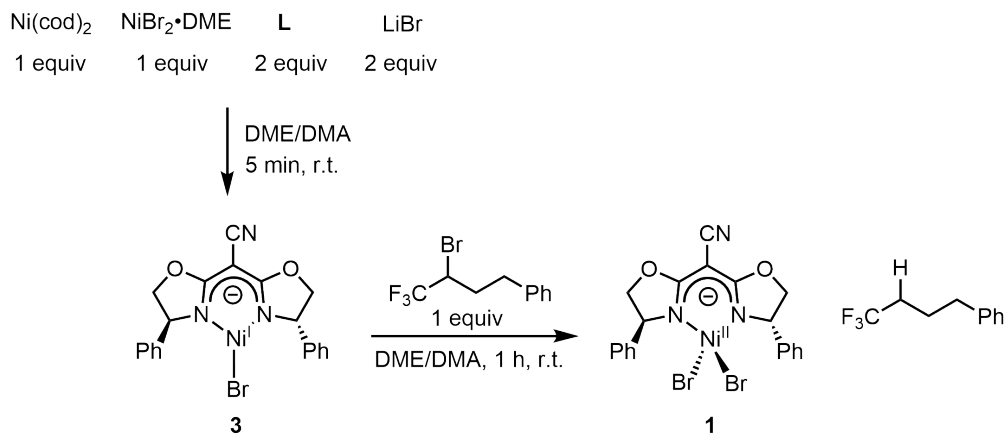


Figure 1.S3: UV-vis spectra of the transmetallation reaction. The spectra were collected at 5 min, 30 min, 1 h, 1.5 h, and 2 h after the addition of nucleophile. The UV-vis absorption features at 420 nm, 510 nm disappeared during the 2 h time span, indicating decomposition of the transmetallation product.

Intercept the *in situ* generated 2 with the electrophile (eq 11). In a nitrogen-filled glovebox, an oven-dried 2 mL vial equipped with a stir bar was charged with [L]Li·THF (0.025 mmol), Ni(cod)₂ (0.025 mmol), and LiBr (0.1 mmol). DMA (0.19 mL) and DME (1.81 mL) were added to the vial and the mixture was stirred at room temperature to obtain a homogeneous solution. The electrophile (0.025 mmol) and alkynyl bromide (0.025 mmol) were then added *via* microsyringe. The reaction mixture was stirred at room temperature for 12 h. After 12 h, MeOH (0.2 mL) was then added to quench the reaction. The resulting mixture was then diluted with Et₂O (3 mL) and washed with deionized water (3 mL × 3). The organic layer was dried over MgSO₄, filtered, and then concentrated. The crude was analyzed with ¹⁹F NMR spectroscopy and chiral HPLC. The reaction yielded the cross-coupling product with 47% yield and 88 %ee.

Halogen abstraction from the electrophile by *in situ* generated 3. In a nitrogen-filled glovebox, a quartz cuvette equipped with a stir bar was charged with L (0.03 mmol), Ni(cod)₂ (0.015 mmol), NiBr₂·DME (0.015 mmol), and LiBr (0.03 mmol). DMA (0.2 mL) and DME (3.8 mL) were then added to dissolve the solid reactants. The cuvette was sealed with a puncturable screw cap and transferred out of the glovebox. UV-vis spectrum was collected after the reaction was stirred at room temperature for 5 min. The electrophile was then added *via* microsyringe, and the resulting reaction mixture was stirred at room temperature for 1 h. Another UV-vis spectrum was collected 1 h after the electrophile addition. MeOH (0.2 mL) was then added to quench the reaction. The resulting mixture was then diluted with Et₂O (3 mL) and washed with deionized water (3 mL × 3). The organic layer was dried over MgSO₄, filtered, and then concentrated. The crude was analyzed with ¹⁹F NMR spectroscopy.



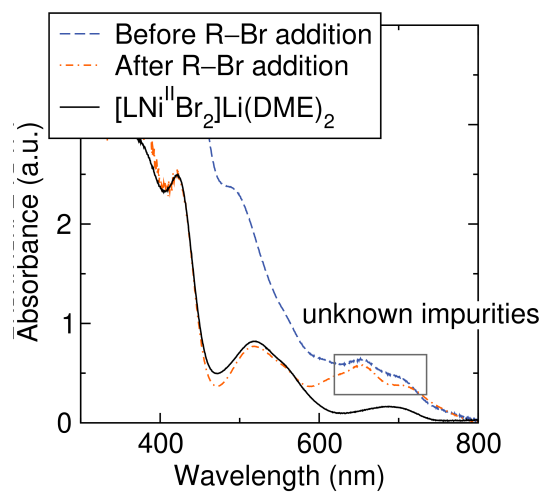


Figure 1.S4: UV-vis spectra of the comproportionation reaction before and after the electrophile (R-Br) addition. The spectra were compared to that of **1** in DME/DMA.

V. UV-vis Data

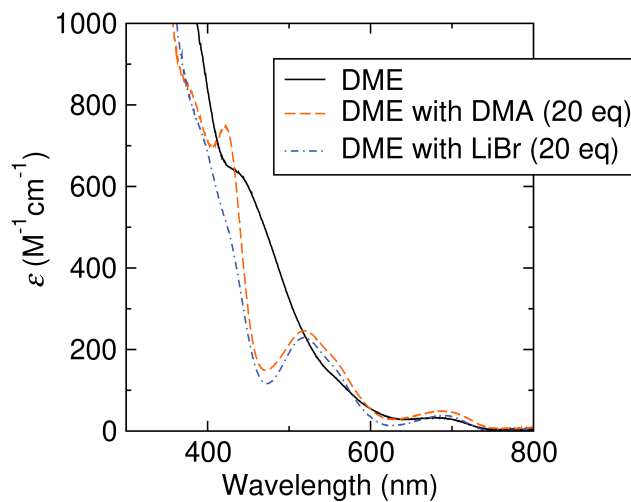


Figure 1.S5: UV-vis spectra of **1** (1 equiv) in DME, DME with DMA additive, and DME with LiBr additive at room temperature. Additives are required to observe the absorption at 520 nm and 460 nm.

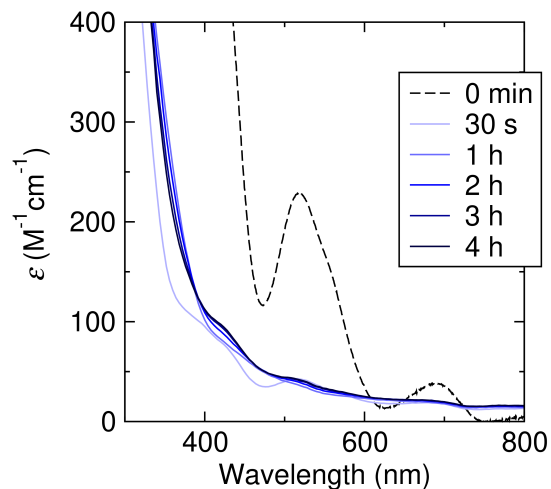
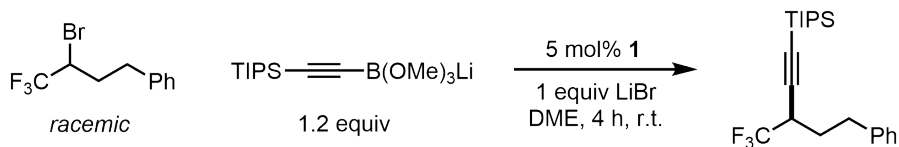


Figure 1.S6: UV-vis spectra of the catalytic reaction without DMA additive. The time point was calculated from the addition of nucleophile. There are no distinct absorption features in the spectra without DMA additive.

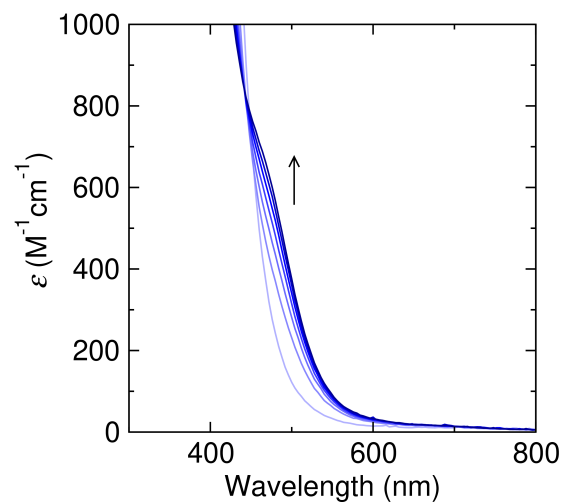


Figure 1.S7: UV-vis spectra of the ligand exchange reaction shown in eq 6. Spectra were collected at $-40\text{ }^{\circ}\text{C}$ every 10 min. The spectra do not match that of the resting state.

VI. EPR Data

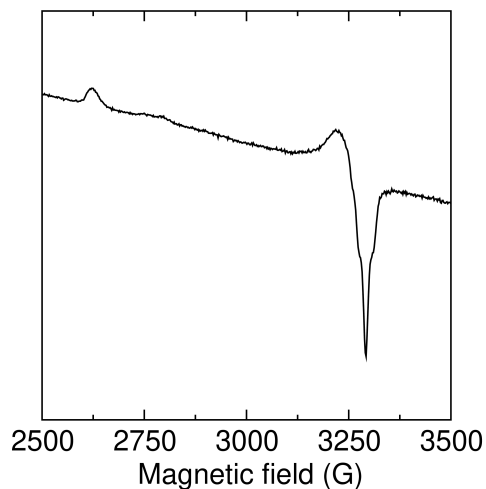


Figure 1.S8: X-band EPR spectrum of the filtrate of the oxidation reaction shown in eq 20. The spectrum was collected at 77 K in frozen DME/DMA at $\nu = 9.418$ GHz at 2.041 mW power and a modulation amplitude of 2.00 G.

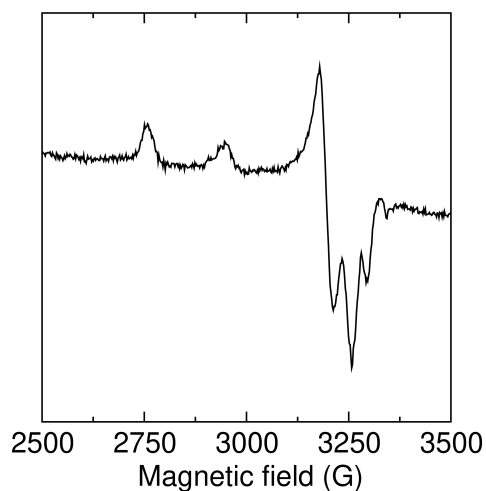


Figure 1.S9: X-band EPR spectrum of the transmetalation reaction above. The spectrum was collected at 77 K in frozen DME/DMA at $\nu = 9.368$ GHz at 2.041 mW power and a modulation amplitude of 2.00 G.

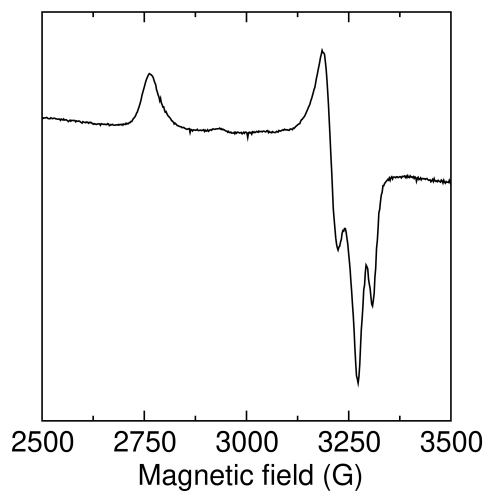
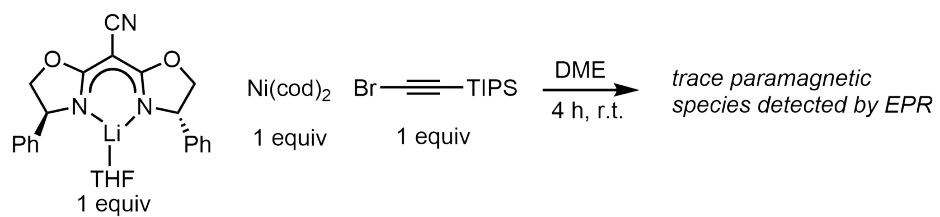


Figure 1.S10: X-band EPR spectrum of the oxidative addition reaction above. The spectrum was collected at 77 K in frozen DME at $\nu = 9.385$ GHz at 2.021 mW power and a modulation amplitude of 2.00 G.

VII. X-Ray Crystallographic Data

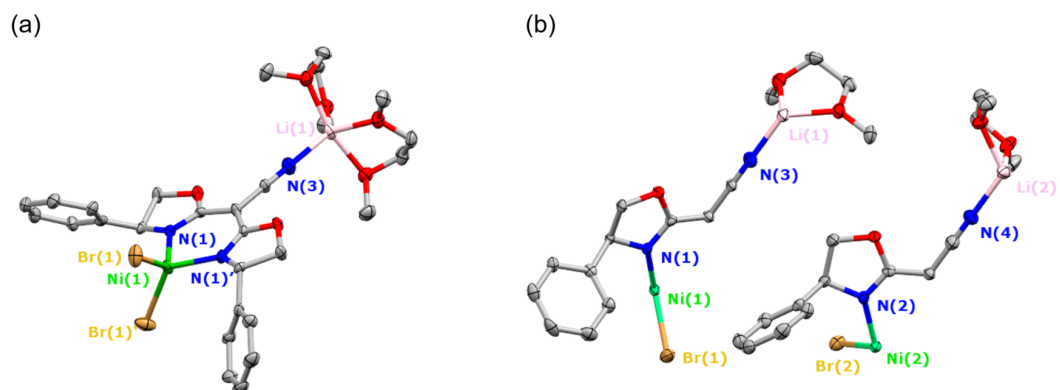


Figure 1.S11: (a) The crystal structure of **1**. (b) The asymmetric unit cell of the crystal. The thermal ellipsoids were plotted at the 30% probability level. Hydrogens were omitted for clarity.

Table 1.S2: Crystal data and structure refinement for **1**.

Identification code	[LNi ^{II} Br ₂]Li·DME ₂
Empirical formula	C ₂₈ H ₃₅ Br ₂ LiN ₃ NiO ₆
Formula weight	735.05
Temperature/K	100.02
Crystal system	monoclinic
Space group	C2
a/Å	19.9347(10)
b/Å	14.2673(7)
c/Å	14.7244(7)
α/°	90
β/°	130.2970(10)
γ/°	90
Volume/Å ³	3194.1(3)
Z	4
ρ _{calc} /g/cm ³	1.5284
μ/mm ⁻¹	3.152
F(000)	1491.8
Crystal size/mm ³	0.32 × 0.3 × 0.25
Radiation	Mo Kα (λ = 0.71073)
2θ range for data collection/°	5.36 to 55.08
Index ranges	-25 ≤ h ≤ 25, -18 ≤ k ≤ 18, -19 ≤ l ≤ 19
Reflections collected	39311
Independent reflections	7324 [R _{int} = 0.0513, R _{sigma} = 0.0459]
Data/restraints/parameters	7324/1/379
Goodness-of-fit on F ²	0.715
Final R indexes [I ≥ 2σ (I)]	R ₁ = 0.0287, wR ₂ = 0.715
Final R indexes [all data]	R ₁ = 0.0379, wR ₂ = 0.0379
Largest diff. peak/hole / e Å ⁻³	0.89/-0.37
Flack parameter	0.037(7)

Table 1.S3: Fractional Atomic Coordinates ($\times 10^4$) and Equivalent Isotropic Displacement Parameters ($\text{\AA}^2 \times 10^3$) for **1**. U_{eq} is defined as 1/3 of the trace of the orthogonalised U_{IJ} tensor.

Atom	x	y	z	U(eq)
Ni1	5000	11533.1(3)	10000	18.65(11)
Br1	5564.1(3)	12473.37(19)	11688.5(3)	36.72(10)
Ni2	5000	9249.1(3)	15000	20.76(12)
Br2	3959.6(2)	10140.34(18)	13253.9(3)	28.94(8)
O4	5579.3(14)	5226.7(17)	9536(2)	27.0(5)
O1	4028.3(14)	9139.9(14)	10391(2)	21.7(4)
O6	4842.8(16)	2997.6(16)	16001(2)	29.5(5)
O2	4571.5(15)	6874.6(15)	16166(2)	24.8(5)
N3	5000	7397(3)	10000	31.3(9)
N1	4337.7(16)	10568.7(16)	10104(2)	16.6(5)
O3	6237.2(16)	5768.3(16)	11707(2)	28.6(5)
N2	4634.0(17)	8305.1(17)	15579(2)	19.4(5)
N4	5000	5129(3)	15000	40.4(10)
C15	5374(2)	5151(3)	8415(3)	33.0(7)
C11	5000	8202(3)	10000	18.9(8)
C10	5000	9199(3)	10000	19.9(8)
C9	4457.4(19)	9673(2)	10152(3)	17.2(6)
C7	3793.5(18)	10744(2)	10445(3)	17.2(6)
C6	3069.0(18)	11456(2)	9697(3)	19.5(6)
C1	2799(2)	11778(2)	8615(3)	24.9(7)
C2	2116(2)	12428(3)	7961(3)	31.0(7)
C3	1691(2)	12723(2)	8361(3)	32.3(8)
C8	3430(2)	9774(2)	10338(3)	21.2(6)
C12	3531(2)	4860(3)	8432(3)	33.3(8)
C14	6401(2)	4821(2)	10489(3)	32.2(8)
C13	6934(2)	6423(3)	12259(3)	34.8(8)
C5	2632(2)	11754(2)	10087(3)	24.1(6)
C4	1937(2)	12381(2)	9416(3)	31.4(7)
C18	2108(2)	10198(3)	14729(3)	32.1(7)
C19	2037(2)	9337(3)	14241(3)	31.9(8)
C20	2783(2)	8797(2)	14746(3)	27.5(7)
C21	3603(2)	9102(2)	15754(3)	21.2(6)

C22	4410(2)	8501(2)	16344(3)	20.9(6)
C24	4738.1(18)	7401(2)	15568(3)	18.5(6)
C25	5000	6923(3)	15000	21.0(9)
C26	5000	5932(3)	15000	32.4(11)
C30	4203(3)	2272(3)	15539(3)	35.0(8)
C17	2924(2)	10520(2)	15731(3)	33.2(8)
C16	3669(2)	9968(2)	16238(3)	26.6(7)
C23	4321(2)	7507(2)	16669(3)	28.5(7)
C29	5660(2)	2739(2)	17114(3)	31.0(7)
C28	6327(3)	3493(2)	17493(3)	31.3(8)
O5	6381.2(18)	3565.3(17)	16587(2)	35.4(6)
C27	7052(3)	4209(4)	16904(4)	55.9(13)
Li1	5000	5969(5)	10000	23.5(16)
Li2	5000	3711(6)	15000	32.4(19)

Table 1.S4: Anisotropic Displacement Parameters ($\text{\AA}^2 \times 10^3$) for **1**. The Anisotropic displacement factor exponent takes the form: $-2\pi^2[h^2a^2U_{11}+2hka^*b^*U_{12}+\dots]$.

Atom	U_{11}	U_{22}	U_{33}	U_{12}	U_{13}	U_{23}
Ni1	23.4(3)	15.1(2)	26.9(3)	-0	20.5(2)	0
Br1	45.1(2)	41.3(2)	37.78(19)	-18.65(17)	33.14(18)	-17.11(16)
Ni2	29.7(3)	17.6(3)	24.4(3)	-0	21.7(3)	0
Br2	27.98(16)	32.80(17)	26.30(15)	7.23(14)	17.67(13)	3.25(14)
O4	26.5(11)	30.1(12)	32.4(11)	3.0(11)	22.6(10)	-0.0(11)
O1	23.2(10)	19.2(11)	33.8(12)	1.5(9)	23.4(10)	3.5(9)
O6	33.3(13)	29.7(12)	28.4(12)	-3.6(10)	21.3(11)	3.2(10)
O2	32.7(12)	20.3(11)	32.3(12)	-1.8(9)	26.0(11)	1.7(9)
N3	33(2)	27(2)	47(2)	-0	32(2)	0
N1	16.6(12)	17.8(12)	21.9(12)	1.0(10)	15.3(11)	0.7(10)
O3	25.7(12)	32.3(13)	32.6(13)	-1.0(10)	21.0(11)	1.9(10)
N2	19.4(12)	20.9(13)	22.9(12)	-0.3(10)	15.9(11)	-1.8(10)
N4	69(3)	19(2)	57(3)	-0	52(3)	0
C15	36.3(17)	39.0(19)	37.4(17)	-2.1(17)	30.0(16)	-7.3(17)
C11	21(2)	15(2)	29(2)	-0	20.4(19)	0
C10	22(2)	16.1(19)	28(2)	-0	18.3(19)	0
C9	17.3(14)	18.7(14)	18.8(14)	-2.1(11)	13.2(12)	1.1(11)
C7	15.0(13)	22.3(14)	18.4(14)	-0.5(11)	12.6(12)	-1.4(11)
C6	15.3(13)	18.7(14)	24.3(14)	-1.4(12)	12.8(12)	-1.7(12)
C1	19.4(15)	30.6(18)	24.8(15)	1.0(13)	14.4(13)	-0.7(13)
C2	23.7(16)	31.0(18)	24.6(16)	2.9(15)	9.4(13)	4.2(15)
C3	18.3(15)	29.0(18)	34.6(18)	8.4(14)	10.4(15)	-3.5(14)
C8	21.7(15)	22.4(15)	28.9(15)	1.6(12)	20.6(13)	1.6(12)
C12	27.4(17)	32.7(19)	39.6(19)	-7.0(15)	21.6(16)	-11.9(15)
C14	28.5(17)	26.7(17)	48(2)	4.9(14)	27.9(17)	2.9(15)
C13	26.1(17)	45(2)	38.2(19)	-4.7(16)	22.9(16)	-5.5(17)
C5	22.6(15)	25.2(16)	25.8(15)	3.1(13)	16.2(14)	-2.4(12)
C4	23.3(15)	32.1(19)	38.1(18)	2.0(14)	19.5(15)	-7.8(15)
C18	30.8(16)	39.4(19)	37.2(17)	11.6(16)	26.9(15)	11.6(17)
C19	21.1(16)	50(2)	23.4(16)	1.8(15)	13.7(14)	2.5(15)
C20	25.8(16)	34.2(18)	25.4(16)	0.2(14)	17.8(14)	-2.9(14)
C21	23.6(15)	25.6(16)	23.8(14)	-1.7(12)	19.6(13)	1.1(12)
C22	21.4(15)	26.1(16)	20.5(14)	1.0(12)	15.9(13)	2.7(12)

C24	14.7(13)	19.4(14)	21.0(14)	-4.0(12)	11.3(12)	0.0(12)
C25	23(2)	18(2)	25(2)	-0	16.8(19)	0
C26	41(3)	29(3)	41(3)	-0	33(3)	0
C30	36.4(19)	38(2)	32.3(18)	-9.1(16)	22.8(16)	-2.2(15)
C17	39(2)	27.0(17)	47(2)	1.3(15)	34.2(19)	-2.0(15)
C16	24.8(15)	28.8(18)	32.2(16)	-4.6(13)	21.2(14)	-3.7(14)
C23	36.7(17)	27.3(16)	35.4(17)	5.7(15)	29.5(15)	7.6(15)
C29	35.3(18)	31.4(19)	28.9(16)	-0.9(15)	21.9(15)	4.8(14)
C28	40(2)	33.6(18)	27.9(17)	-5.6(16)	25.6(17)	-4.2(14)
O5	43.7(15)	41.1(15)	29.4(13)	-15.5(12)	27.2(12)	-7.1(11)
C27	58(3)	75(3)	40(2)	-35(3)	33(2)	-8(2)
Li1	29(4)	22(4)	35(4)	-0	27(4)	0
Li2	55(5)	18(4)	24(4)	-0	25(4)	0

Table 1.S5: Bond Lengths for **1**.

Atom	Atom	Length/Å	Atom	Atom	Length/Å
Ni1	Br1	2.3726(4)	N4	Li2	2.023(9)
Ni1	Br1 ¹	2.3726(4)	C11	C10	1.422(6)
Ni1	N1 ¹	1.980(2)	C10	C9	1.411(3)
Ni1	N1	1.980(2)	C10	C9 ¹	1.411(3)
Ni2	Br2 ²	2.3730(4)	C7	C6	1.508(4)
Ni2	Br2	2.3730(4)	C7	C8	1.523(4)
Ni2	N2	1.969(2)	C6	C1	1.389(4)
Ni2	N2 ²	1.969(2)	C6	C5	1.385(4)
O4	C15	1.425(4)	C1	C2	1.394(5)
O4	C14	1.419(4)	C2	C3	1.375(5)
O4	Li1	1.986(5)	C3	C4	1.381(5)
O1	C9	1.350(3)	C12	C14 ¹	1.504(5)
O1	C8	1.458(3)	C5	C4	1.387(5)
O6	C30	1.428(4)	C18	C19	1.384(5)
O6	C29	1.422(4)	C18	C17	1.389(5)
O6	Li2	1.976(5)	C19	C20	1.389(5)
O2	C24	1.352(3)	C20	C21	1.388(4)
O2	C23	1.445(4)	C21	C22	1.507(4)
N3	C11	1.149(6)	C21	C16	1.390(4)
N3	Li1	2.036(9)	C22	C23	1.543(4)
N1	C9	1.293(4)	C24	C25 ²	1.414(4)
N1	C7	1.482(4)	C25	C26	1.414(6)
O3	C12 ¹	1.435(4)	C17	C16	1.396(5)
O3	C13	1.415(4)	C29	C28	1.507(5)
O3	Li1	2.113(3)	C28	O5	1.410(4)
N2	C22	1.482(4)	O5	C27	1.429(5)
N2	C24	1.308(4)	O5	Li2 ²	2.182(3)
N4	C26	1.146(6)			

¹1-X,+Y,2-Z; ²1-X,+Y,3-Z

Table 1.S6: Bond Angle for **1**.

Atom	Atom	Atom	Angle/°	Atom	Atom	Atom	Angle/°
Br1 ¹	Ni1	Br1	111.14(2)	C14 ¹	C12	O3 ¹	111.4(3)
N11	Ni1	Br1	125.87(7)	C12 ¹	C14	O4	106.7(3)
N1	Ni1	Br1	101.53(7)	C4	C5	C6	120.6(3)
N1	Ni1	Br11	125.87(7)	C5	C4	C3	119.7(3)
N1 ¹	Ni1	Br11	101.53(7)	C17	C18	C19	120.1(3)
N1 ¹	Ni1	N1	91.96(14)	C20	C19	C18	120.0(3)
Br2 ²	Ni2	Br2	115.19(2)	C21	C20	C19	120.8(3)
N2	Ni2	Br2	121.78(7)	C22	C21	C20	121.2(3)
N2 ²	Ni2	Br2 ²	121.78(7)	C16	C21	C20	118.9(3)
N2	Ni2	Br2 ²	101.92(7)	C16	C21	C22	119.9(3)
N2 ²	Ni2	Br2	101.92(7)	C21	C22	N2	113.8(2)
N2	Ni2	N2 ²	93.68(14)	C23	C22	N2	102.4(2)
C14	O4	C15	113.5(3)	C23	C22	C21	114.0(3)
Li1	O4	C15	130.1(2)	N2	C24	O2	115.6(3)
Li1	O4	C14	115.7(2)	C25 ²	C24	O2	117.2(3)
C8	O1	C9	105.7(2)	C25 ²	C24	N2	127.2(3)
C29	O6	C30	111.5(3)	C24	C25	C24 ²	122.4(4)
Li2	O6	C30	122.8(2)	C26	C25	C24 ²	118.82(19)
Li2	O6	C29	112.1(2)	C26	C25	C24	118.82(19)
C23	O2	C24	107.4(2)	C25	C26	N4	180.0
Li1	N3	C11	180.0	C16	C17	C18	119.5(3)
C9	N1	Ni1	125.6(2)	C17	C16	C21	120.8(3)
C7	N1	Ni1	125.41(18)	C22	C23	O2	105.5(2)
C7	N1	C9	107.3(2)	C28	C29	O6	108.7(3)
C13	O3	C12 ¹	113.1(3)	O5	C28	C29	106.9(3)
Li1	O3	C12 ¹	100.9(3)	C27	O5	C28	111.5(3)
Li1	O3	C13	123.4(3)	Li2 ²	O5	C28	101.8(2)
C22	N2	Ni2 ²	125.34(19)	Li2 ²	O5	C27	123.7(3)
C24	N2	Ni2 ²	124.3(2)	O4 ¹	Li1	O4	115.5(4)
C24	N2	C22	108.9(2)	N3	Li1	O4	122.3(2)
Li2	N4	C26	180.0	N3	Li1	O4 ¹	122.3(2)
C10	C11	N3	180.0	O3 ¹	Li1	O4 ¹	81.11(15)
C9	C10	C11	118.65(19)	O3	Li1	O4	81.11(15)
C9 ¹	C10	C11	118.65(19)	O3 ¹	Li1	O4	90.55(17)

C9 ¹	C10	C9	122.7(4)	O3	Li1	O4 ¹	90.55(17)
N1	C9	O1	116.5(3)	O3	Li1	N3	97.8(2)
C10 ¹	C9	O1	116.8(3)	O3 ¹	Li1	N3	97.8(2)
C10 ¹	C9	N1	126.7(3)	O3 ¹	Li1	O3	164.4(4)
C6	C7	N1	115.5(2)	O6 ²	Li2	O6	118.0(4)
C8	C7	N1	102.4(2)	N4	Li2	O6	121.0(2)
C8	C7	C6	111.7(2)	N4	Li2	O6 ²	121.0(2)
C1	C6	C7	122.6(3)	O5 ²	Li2	O6	92.93(17)
C5	C6	C7	117.8(3)	O5 ²	Li2	O6 ²	81.43(15)
C5	C6	C1	119.5(3)	O5	Li2	O6	81.43(15)
C2	C1	C6	119.5(3)	O5	Li2	O6 ²	92.93(17)
C3	C2	C1	120.4(3)	O5 ²	Li2	N4	95.5(2)
C4	C3	C2	120.2(3)	O5	Li2	N4	95.5(2)
C7	C8	O1	103.9(2)	O5	Li2	O5 ²	169.1(4)

¹1-X,+Y,2-Z; ²1-X,+Y,3-Z

Table 1.S7: Hydrogen Atom Coordinates ($\text{\AA}\times 10^4$) and Isotropic Displacement Parameters ($\text{\AA}^2\times 10^3$) for **1**.

Atom	x	y	z	U(eq)
H15a	4814(9)	5468(17)	7803(5)	49.6(11)
H15b	5841(9)	5446(17)	8465(8)	49.6(11)
H15c	5325(18)	4488(3)	8205(12)	49.6(11)
H7	4185.6(18)	10946(2)	11297(3)	20.7(7)
H1	3078(2)	11558(2)	8322(3)	29.9(8)
H2	1944(2)	12667(3)	7235(3)	37.3(9)
H3	1225(2)	13165(2)	7909(3)	38.8(10)
H8a	2822(2)	9706(2)	9575(3)	25.4(7)
H8b	3433(2)	9653(2)	11003(3)	25.4(7)
H12a	2921(2)	4708(3)	7713(3)	39.9(9)
H12b	3927(2)	4383(3)	8510(3)	39.9(9)
H14a	6430(2)	4164(2)	10301(3)	38.6(9)
H14b	6888(2)	5177(2)	10634(3)	38.6(9)
H13a	7438(7)	6195(10)	13051(11)	52.3(12)
H13b	7107(13)	6501(15)	11773(14)	52.3(12)
H13c	6740(6)	7028(6)	12330(20)	52.3(12)
H5	2809(2)	11527(2)	10821(3)	28.9(8)
H4	1633(2)	12574(2)	9681(3)	37.7(9)
H18	1599(2)	10571(3)	14377(3)	38.6(9)
H19	1477(2)	9115(3)	13560(3)	38.3(9)
H20	2732(2)	8211(2)	14398(3)	33.0(8)
H22	4921(2)	8821(2)	17086(3)	25.1(7)
H30a	4408(9)	1706(7)	15410(20)	52.5(12)
H30b	4116(14)	2136(14)	16109(12)	52.5(12)
H30c	3645(6)	2477(8)	14782(13)	52.5(12)
H17	2974(2)	11109(2)	16070(3)	39.9(9)
H16	4228(2)	10188(2)	16921(3)	31.9(8)
H23a	3708(2)	7387(2)	16327(3)	34.2(8)
H23b	4715(2)	7429(2)	17544(3)	34.2(8)
H29a	5592(2)	2668(2)	17719(3)	37.2(9)
H29b	5861(2)	2133(2)	17036(3)	37.2(9)
H28	6649(3)	3850(2)	18206(3)	37.6(9)
H27a	6905(13)	4838(6)	16990(30)	83.9(19)

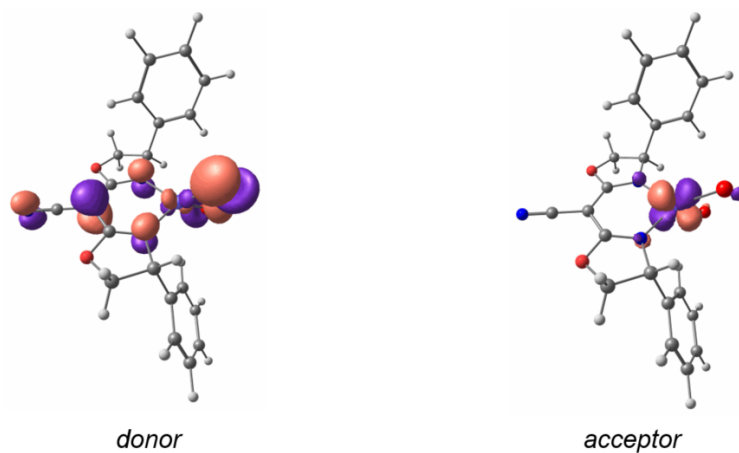
H27b	7617(5)	4013(15)	17658(18)	83.9(19)
H27c	7096(18)	4220(20)	16278(17)	83.9(19)

VIII. Computational Details

General computational methods. All calculations were performed with Gaussian 09 Rev B.01.²¹ The gas-phase geometry optimizations were performed with the B3LYP hybrid functional and 6-31G* basis set for all atoms with spin state being the only restraint, followed by numerical frequency calculations at the same level of theory to characterize stationary points as minima (no imaginary frequencies). td-DFT calculations were carried out on optimized geometries. Natural transition orbital calculations were carried out following td-DFT calculations to assist the assignment of transitions. Natural transition orbital representations were rendered with Chemcraft.²²



Transition 1 (LMCT)



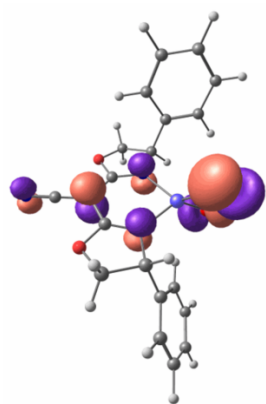
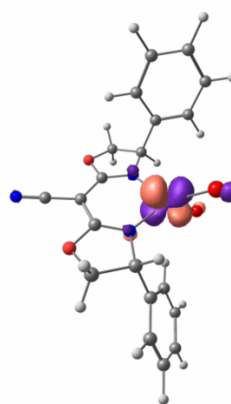
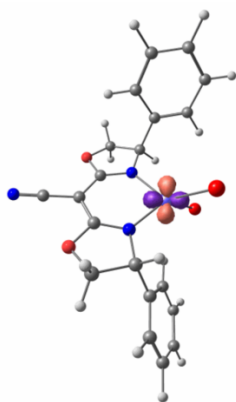
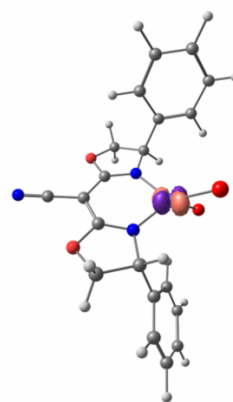
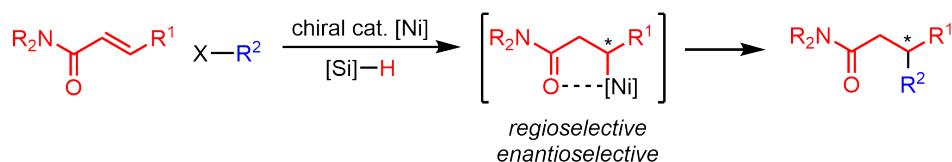
Transition 2 (LMCT)*donor**acceptor**Transition 3 (d→d)**donor**acceptor*

Figure 1.S12: The natural transition orbitals of $[\text{LNi}^{\text{II}}\text{Br}_2]^-$ (contour value = 0.052).

Chapter 2

NICKEL-CATALYZED REGIOSELECTIVE AND ENANTIOSELECTIVE COUPLING OF ALKYL HALIDES WITH INTERNAL OLEFINS

Abstract: The traditional nickel-catalyzed electrophile-nucleophile cross-couplings continue to be a prominent method to construct $C(sp^3)-C(sp^3)$ bonds. However, the reliance on alkyl-metal reagents can limit the functional group compatibility and the applicability of such methodologies. Recently, reductive couplings of alkyl halides with olefins in the presence of a hydrosilane has emerged as an alternative strategy to construct $C(sp^3)-C(sp^3)$ bonds. This new approach affords mild reaction conditions that support couplings with new families of alkyl halides. Here, nickel-catalyzed reductive couplings of alkyl halides with internal olefins is explored. By judicious choice of the directing group, hydroalkylation of internal olefins can be achieved with high regio- and enantioselectivity. The success of using internal olefins for selective $C(sp^3)-C(sp^3)$ bond formation shines a light on vicinal stereocenter constructions from an internal olefin and a racemic alkyl halide.



2.1 Introduction

Nickel-catalyzed enantioselective cross-coupling of racemic alkyl electrophiles with alkyl nucleophiles is an effective strategy for asymmetric $C(sp^3)-C(sp^3)$ bond formations.^{23,24} For these coupling reactions, nickel(II)-alkyl is believed to be a key intermediate.^{25–28} Recently, researchers discovered that an olefin can serve as a pronucleophile in the presence of a hydrosilane.^{29–31} The same active intermediate is presumably accessible through β -migratory insertion of a nickel-hydride intermediate to an olefin substrate.²⁹ Multiple reported methods have demonstrated that this alternative strategy not only obviates the need to synthesize a discrete alkyl-metal reagent, but also affords highly enantioselective coupling products with great functional group tolerance.^{32–35}

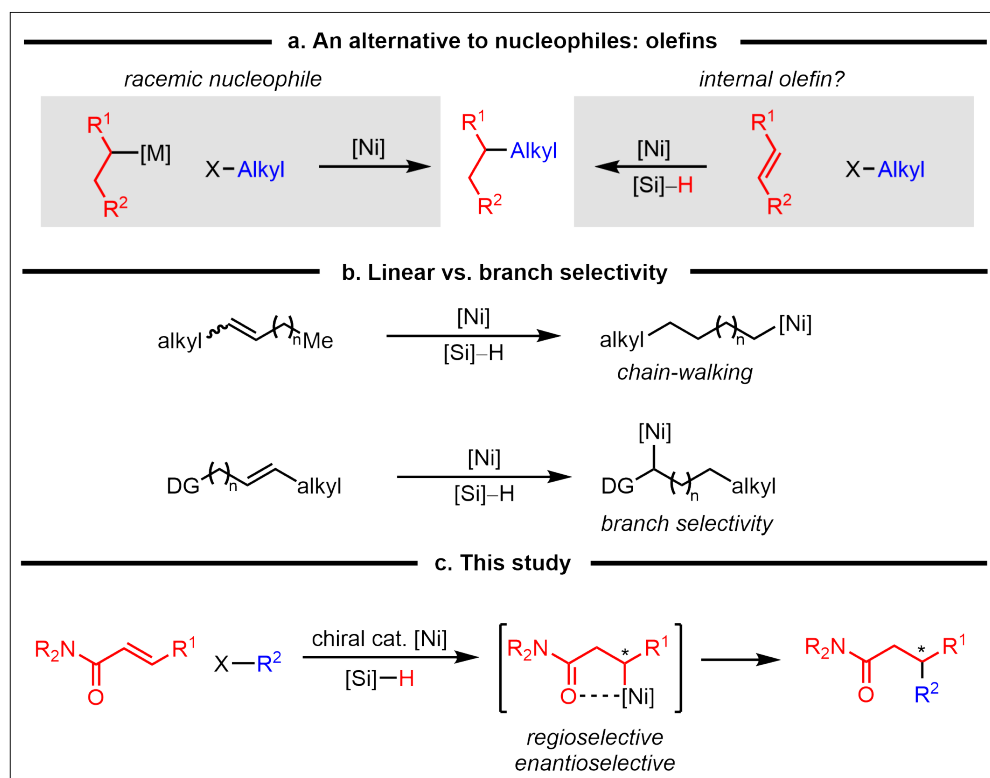


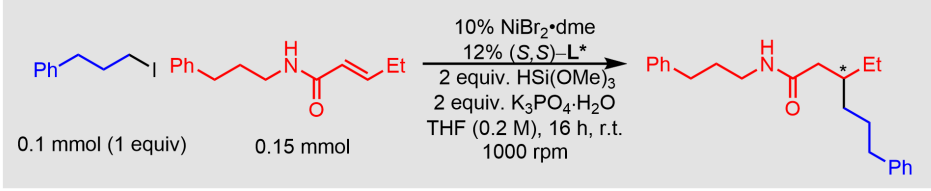
Figure 2.1: (a) Using olefins as an alternative to nucleophiles for nickel-catalyzed cross-coupling reactions. (b) An electronically biased olefin is needed for branch selectivity. (c) This work.

Recent years, efforts have also been made in enantioselective cross-coupling of racemic alkyl nucleophiles with alkyl electrophiles (Figure 2.1a) with the long-term goal of realizing nickel-catalyzed doubly stereoconvergent cross-couplings. However, to the date of this work, there are only isolated examples of enantioconvergent cross-coupling using racemic alkyl nucleophiles.^{36,37} At the same time, researchers

are attempting to use internal olefins in place of racemic alkyl nucleophiles as coupling partners (Figure 2.1a). Due to the relative stability of the nickel-alkyl intermediates, linear selectivity is often obtained with a simple internal olefin *via* chain-walking (Figure 2.1b).^{32,35,38–41} Success in achieving branch selectivity is observed when using an electronically biased olefin. Both aryl and boronic ester are reported to serve as competent directing groups to achieve α -selectivity.^{42–45} In this report, we explore an asymmetric nickel-catalyzed reductive coupling of α,β -unsaturated amides and alkyl halides. Specifically, we are interested in studying how a carbonyl directing group may affect the regioselectivity of the reaction. We envision that in the presence of a carbonyl directing group, a nickel catalyst would preferentially insert at β position, as the resulting intermediate is stabilized by the five-membered ring oxanickelacycle (Figure 2.1c).

2.2 Results and Discussion

We examine the coupling of α,β -unsaturated secondary amide with alkyl iodide (Figure 2.2), and we determine that NiBr₂·dme and chiral box ligand **L1** can accomplish the desired enantioselective reductive coupling in good yield and ee (76% yield, 88% ee; entry 1) with hydrogenated olefin as the major by-product. The alkylation is exclusively β -selective. We believe the proposed interaction between the carbonyl and nickel shown in Figure 2.1c is responsible for the unusual regioselectivity. In the absence of NiBr₂·dme or of ligand **L1**, essentially no C–C bond formation is observed (entries 2 and 3). An array of other ligands are examined in the initial study of the reductive coupling reaction and they are less effective than **L1** (Figure 2.S1). If the coupling is conducted with less catalyst, less olefin, or for less time, a lower yield are obtained though ee remain the same (entries 4–6). Other silane and base commonly employed for reductive coupling reactions afford lower yield and ee (entries 7–8). The presence of water is important for both the yield and ee of this coupling reaction. The use of K₃PO₄ in place of K₃PO₄·H₂O leads to diminished yield and slight decrease in ee (entry 9). The presence of additional water (0.1 or 1.0 equiv), however, does not impact the yield and ee of the reaction at all (entries 10–11). The reaction is compatible with various ethereal solvents. The use of 1,4-dioxane, TBME, and Et₂O in place of THF afford the desired product with comparable yield and ee (entries 12–14). The reaction takes place relatively smoothly under air in a closed vial (entry 15). Under the standard catalytic condition, the corresponding alkyl bromide can also afford the desired product with lower yield but high enantioselectivity (entry 16).



entry	variation from the "standard conditions"	yield (%) ^a	ee (%) ^b
1	none	76	88
2	no NiBr ₂ ·dme	<1	--
3	no (S,S)-L*	<1	--
4	5% NiBr ₂ ·dme, 6% (S,S)-L*	58	88
5	1.0 equiv of olefin	69	89
6	9 h instead of 16 h	42	88
7	2.0 equiv of PMHS, instead of HSi(OMe) ₃	49	88
8	2.0 equiv of KF, instead of K ₃ PO ₄ ·H ₂ O	32	86
9	2.0 equiv of K ₃ PO ₄ , instead of K ₃ PO ₄ ·H ₂ O	31	86
10	0.1 equiv H ₂ O added	82	89
11	1.0 equiv H ₂ O added	75	91
12	1,4-dioxane, instead of THF	70	85
13	TBME, instead of THF	84	90
14	Et ₂ O, instead of THF	85	91
15	under air in a closed vial	49	88
16	the corresponding alkyl bromide as the electrophile	43	90

^a Determined through LC analysis. ^b Determined through SFC analysis.

Figure 2.2: Effects of reaction parameters on the enantioselective and regioselective alkylation of α, β -unsaturated amide.

One important side note is that the commercial source of $K_3PO_4 \cdot H_2O$ can affect the yield and ee of the reductive coupling reaction. $K_3PO_4 \cdot H_2O$ from different vendors, or from the same vendor but different LOT numbers, can lead to different yield and ee. Similar effect has been observed during the development of other reductive coupling reactions, but is not discussed in the published manuscripts.^{32,34} We compare the amount of water in $K_3PO_4 \cdot H_2O$ from different source using quantitative ¹H-NMR and conclude it is not due to inconsistency of water content. We hypothesize that trace amount of metal impurities during manufacturing may affect the catalytic reaction, leading to variations in yield and ee. After comparing $K_3PO_4 \cdot H_2O$ from Acros (A0380189), Alfa Aesar (W26C076), and Sigma Aldrich (BCCC0865), we proceed to explore the scope of the reductive coupling reaction with $K_3PO_4 \cdot H_2O$ from Acros (A0380189) unless mentioned otherwise. Using 1.5 equiv of $K_3PO_4 \cdot H_2O$ from Acros and 6.0 equiv of HSi(OMe)₃, the reaction can

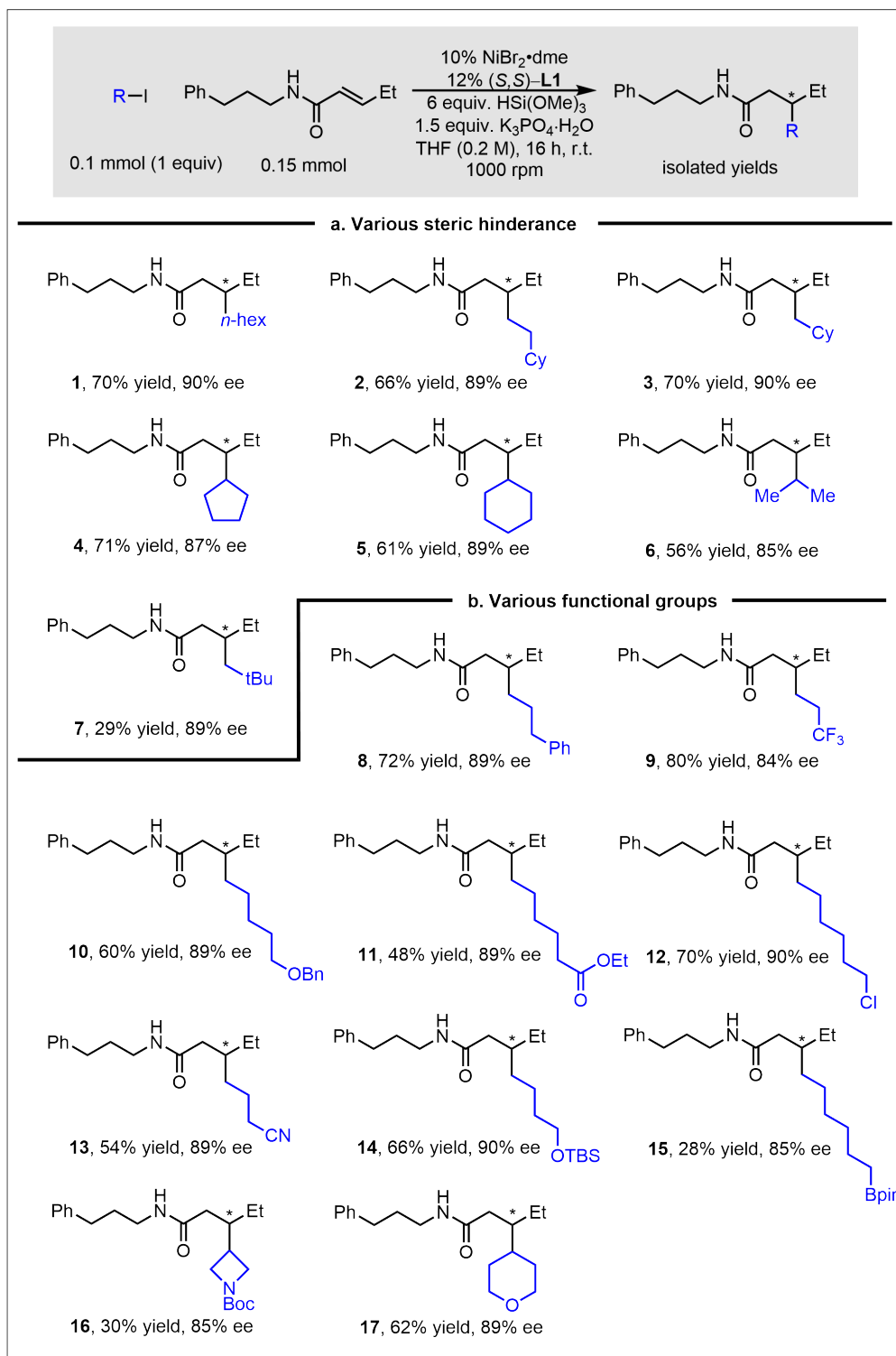


Figure 2.3: Electrophile substrate scope with various (a) steric hinderance and (b) functional groups for the enantioselective and regioselective alkylation of α,β -unsaturated amide.

afford the desirable product with comparable yield and ee to the standard reaction condition shown in Figure 2.2, entry 1.

The electrophile scope of this method for enantioselective and regioselective alkylation of α,β -unsaturated amide is broad with respect to the various substituents (Figure 2.3). For example, the alkyl group of the electrophile can vary in steric bulk from *n*-hex to *i*-propyl, with fairly good yield and high ee's obtained (entries 1-6). It is worth mentioning that no linear product is observed for entry 6, indicating no isomerization after oxidative addition of the alkyl iodide to the nickel catalyst.⁴⁶ The yield of the reaction drops to 29% when neopentyl iodide is used as the electrophile though the enantioselectivity remains high (entry 7). The method is not compatible with tertiary electrophiles. Low yields are obtained with *t*-butyl iodide and adamantyl iodide, and the products obtained are racemic (Figure 2.S2). A variety of functional groups, including a trifluoromethyl, ester, unactivated primary alkyl chloride, nitrile, protected alcohol, and ether are compatible with the method (entries 8-14, 17). The yield of the reaction drops to around 30% in the presence of boronate ester and Boc-protected amine, but the enantioselectivity is not affected (entries 15-16). The method is not compatible with phthaloyl protected amine, pendant olefin, or unactivated primary alkyl bromide (Figure 2.S2).

The scope of the enantioselective and regioselective coupling is fairly broad with respect to the olefin (Figure 2.4). The olefin substituents can vary in size from methyl to *i*-propyl, with fairly good yield and high ee's obtained (entries 18-21). However, *t*-butyl and phenyl substituents are not compatible with this methods (Figure 2.S2). With regard to the amide directing group, Weinred amide and diethyl amide are compatible with the method as well (entries 22-23).

The enantioselective and regioselective reductive coupling reported here shines a light on the vicinal stereocenter construction *via* asymmetric nickel catalysis. The traditional strategy to achieve control of vicinal stereocenters involves cross-coupling of a racemic electrophile and a racemic nucleophile in the presence of a chiral nickel catalyst (Figure 2.5a). To the date of this work, there are only isolated methods that successfully mediate doubly seteroconvergent alkyl-alkyl cross-coupling.^{37,47} The challenge is the formation of the desired C(*sp*³)-C(*sp*³) bond using a racemic nucleophile as the coupling partner. We envision that electronically biased internal olefins can serve as an alternative to racemic nucleophile for vicinal stereocenter constructions. The alternative strategy involves reductive cross-coupling of a racemic electrophile and an internal olefin in the presence of a chiral nickel cata-

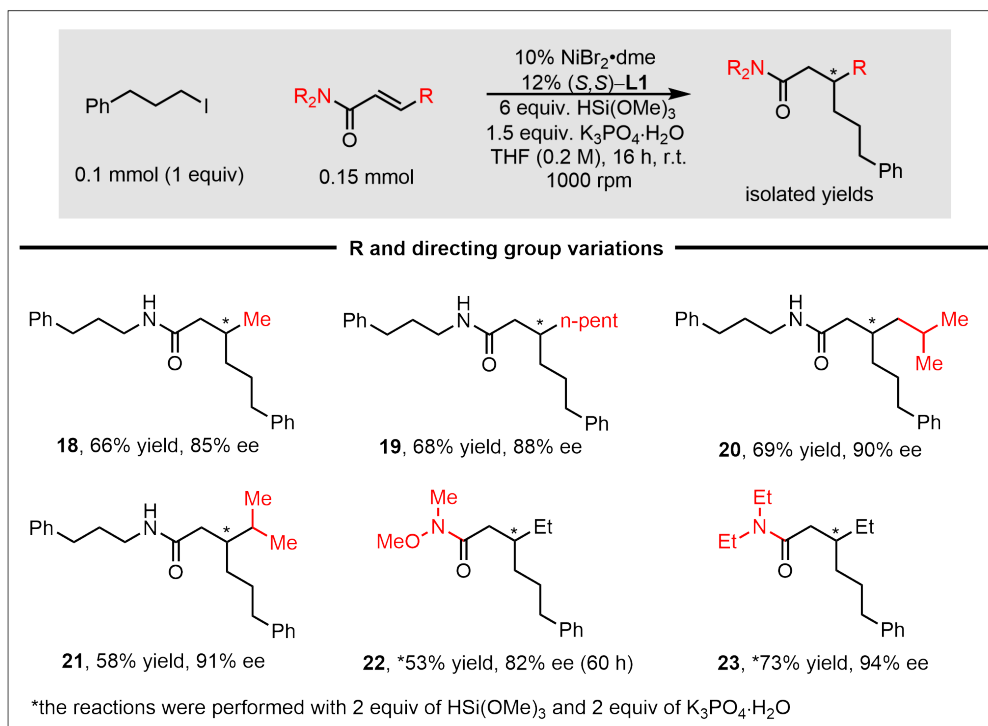


Figure 2.4: Olefin scope for the enantioselective and regioselective alkylation of α, β -unsaturated amide.

lyst (Figure 2.5a). Compare to racemic nucleophiles, electronically biased internal olefins are easier to synthesize, more chemically stable, and serve as a suitable coupling partner in more nickel catalysis methods.

The preliminary result of vicinal stereocenter construction from racemic electrophile and α, β -unsaturated amide is shown in Figure 2.5b. Though the reaction condition has not been optimized, we obtain the desired cross-coupling products with moderate yield (entries 24-27). 1-bromopropyl benzoate, α -iodo- β -lactam, α -bromo- α -trifluoromethyl alkane, and α -iodo- α -fluoro alkane all serve as suitable coupling partners. In all cases, the reductive coupling is exclusively β -selective, and diastereoselectivity is observed. For entries 24-26, the products are also enantio-enriched.

We have begun to investigate the mechanism of the catalytic enantioselective and regioselective alkylation of α, β -unsaturated amide process. Our current hypothesis is that the reaction proceeds through the pathway illustrated in Figure 2.6a, which is consistent with the mechanistic study of an enantioconvergent electrophile-olefin coupling.³² In this mechanism, $\text{LNi}^{\text{II}}\text{X}_2$ reacts with the hydrosilane to generate a nickel-hydride intermediate. Olefin complexation followed by β -migratory insertion then results in a nickel-alkyl intermediate. The nickel center interacts with the

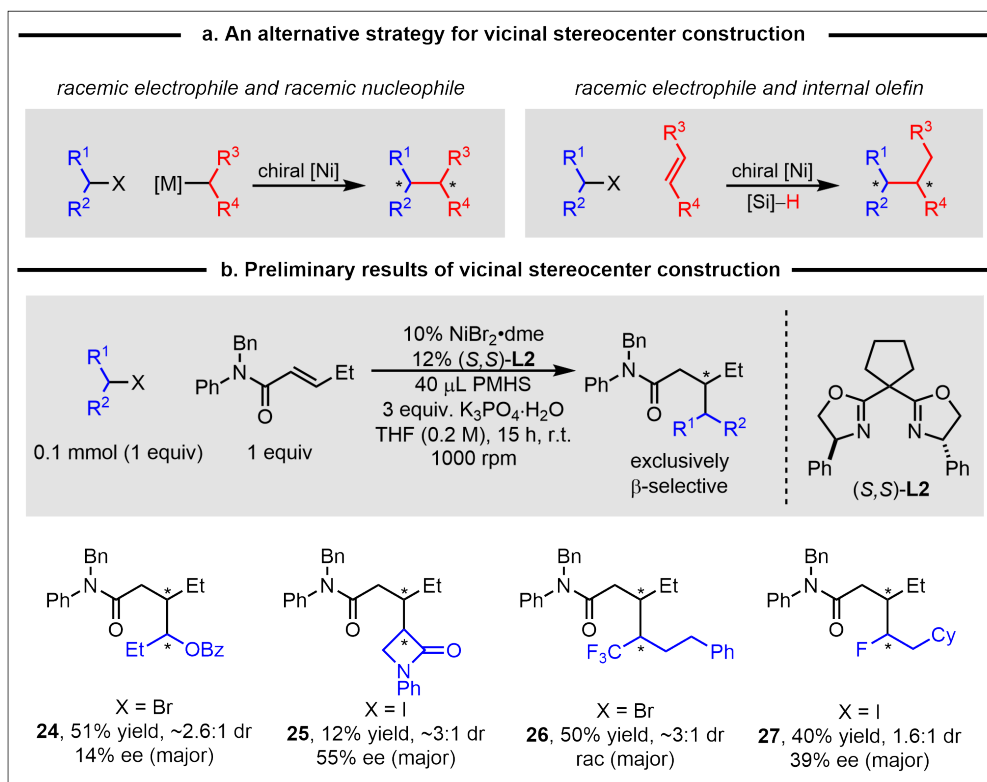


Figure 2.5: (a) Using internal olefin as an alternative coupling partner to construct vicinal stereocenters. (b) The preliminary results of vicinal stereocenter construction using a racemic electrophile and an internal olefin. $\text{K}_3\text{PO}_4 \cdot \text{H}_2\text{O}$ used in these reactions are from Sigma Aldrich (BCCC0865).

oxygen lone pairs in the amide directing group. The five-membered ring oxanickelacycle most likely determines the regioselectivity of the catalytic reaction. The nickel-alkyl intermediate then combines with the alkyl radical generated from halogen abstraction, forming the nickel(III) intermediate. The nickel(III) intermediate then reductively eliminates to give the coupling product.

Using EPR spectroscopy, we examine the catalytic reaction in progress and observe no signal, indicating a nickel(II) intermediate as the resting state (Figure 2.S4). In order to observe the resting state of the catalytic reaction, we independently synthesize $\text{L2Ni}^{\text{II}}\text{I}_2$ and use the isolated crystal as the catalyst to avoid the halogen combinatorial issue (Figure 2.S3a). Using UV-vis spectroscopy, we are able to conclude that the resting state of the catalytic reaction is $\text{LNi}^{\text{II}}\text{X}_2$, consistent with that reported for the enantioconvergent electrophile-olefin coupling (Figure 2.6b).³²

Our current hypothesis of the enantio-determining step of the catalytic reaction is β -migratory insertion of the nickel-hydride intermediate to the olefin. In Figure 2.6c,

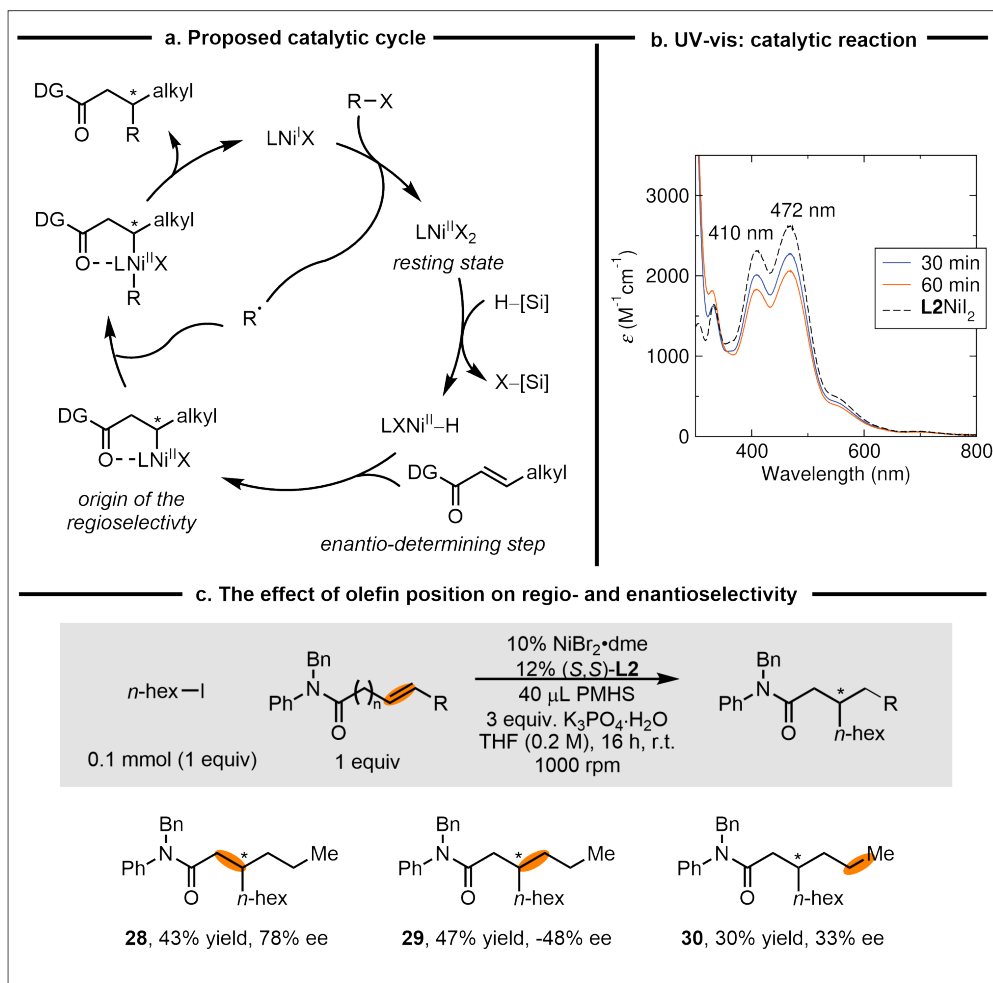


Figure 2.6: (a) Proposed catalytic cycle of the enantioselective and regioselective alkylation of α, β -unsaturated amide. (b) UV-vis spectra of L2Ni(II)_2 and the catalytic reaction in progression. (c) The effect of olefin position on the regio- and enantioselectivity of the coupling reaction. $\text{K}_3\text{PO}_4\cdot\text{H}_2\text{O}$ used in these reactions are from Sigma Aldrich (BCCC0865).

we compare the reactivity of α, β - and β, γ -unsaturated amide (entries 28-29). The reactions are exclusively β -selective. The high regioselectivity suggests that the two catalytic reactions go through the same nickel(II)-alkyl intermediate before recombine with the alkyl radical. However, the significant differences in enantioselectivity (78% ee and -48% ee) indicates that the position of the olefin can affect the geometry of β -migratory insertion. This observation is consistent with the hypothesis of β -migratory insertion being the enantio-determining step. We also test a δ, ϵ -unsaturated amide (entry 30). The reaction is exclusively β -selective, demonstrating that the substrate can undergo nickel-mediated chain walking. Interestingly, the reaction gives 33% ee. We believe that even when the directing group is three carbons

removed from the olefin, it can still interact with the chiral nickel catalyst during β -migratory insertion and affect the enantioselectivity of the coupling reaction.

2.3 Conclusion

In summary, we have developed a method for the enantioselective and regioselective alkylation of α, β -unsaturated amide *via* nickel-catalyzed reductive coupling. The method tolerates substituents of varying size on the electrophile and on the olefin, and it displays good functional-group tolerance. Furthermore, we have demonstrated the potential of using internal olefin as a coupling partner for vicinal stereocenter constructions with selectivity. Preliminary mechanistic study indicates β -migratory insertion being the enantio-determining step. This method demonstrates the importance of directing group on both the enantioselectivity and the regioselectivity of a nickel-catalyzed coupling reaction.

2.4 Supporting Information

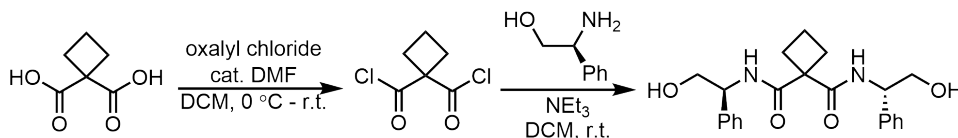
General Information

All manipulations of air-sensitive materials were carried out in oven-dried glassware under an N₂ atmosphere using standard Schlenk or glovebox techniques. THF was purified and dried using a solvent-purification system that contained activated alumina under argon. NiBr₂·dme (99+%, Alfa Aesar), HSi(OMe)₃, K₃PO₄·H₂O (Acros (A0380189), Sigma Aldrich (BCCC0865)) were used as received. The alkyl iodide substrates were either purchased or synthesized by treating alkyl chloride/bromide precursors with NaI in acetone. The electrophiles were distilled prior to use.

Chromatography. GC analyses were carried out on an Agilent 6890N GC system. SFC analyses were carried out on an Agilent 1260 Infinity II system with Daicel CHIRALPAK® or Daicel CHIRALCEL® columns (4.6 x 250 mm, particle size 5 μm). Flash column chromatography was performed using silica gel (SiliaFlash P60, particle size 40-63 μm, Silicycle).

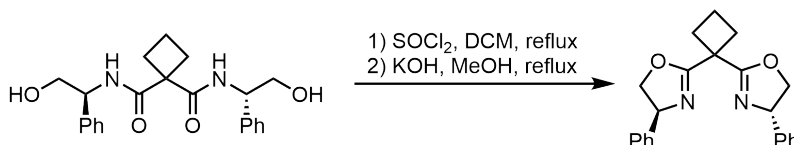
Spectroscopy. ¹H, ¹³C NMR data were collected on a Bruker 400 MHz, Varian 300 MHz spectrometer or a Varian 500 MHz spectrometer at ambient temperature. X-band continuous-wave EPR measurements were conducted on a Bruker EMX spectrometer with the sample in a frozen solvent at 77 K. UV-vis spectra were collected on a Cary 50 UV-vis spectrometer using a 10 nm path-length quartz cuvette. X-ray diffraction studies were carried out at the Beckman Institute Crystallography Facility on a Bruker KAPPA four-circle diffractometer. The crystals were mounted in a nylon loop with Paratone-N oil.

Ligand Synthesis



Step 1. An oven-dried 50 mL round bottom flask equipped with a stir bar was charged with the malonic acid (0.70 g, 4.85 mmol, 1.0 equiv) and anhydrous toluene (15 mL). The mixture was cooled to 0 °C. Next, oxalyl chloride (0.82 mL, 9.7 mmol, 2 equiv) and 1 drop of dry DMF were added. The reaction mixture was stirred under

reflux overnight. In a separate oven-dried 50 mL round bottom flask, amino alcohol (1.33 g, 9.7 mmol, 2.0 equiv) and dry NEt_3 (3.4 mL, 24.3 mmol, 5.0 equiv) were dissolved in DCM at 0 °C. To the solution was added the the crude solution of malonyl dichloride in toluene dropwise. The reaction mixture was allowed to warm to room temperature and was stirred for another 2 h. The solution was washed with 1 M aqueous HCl. The combined organic layers were washed with saturated NaHCO_3 solution, brine, and dried over MgSO_4 . After filtration, the solvent was removed under reduced pressure. The crude chiral amide product was submitted to the next step without further purification.

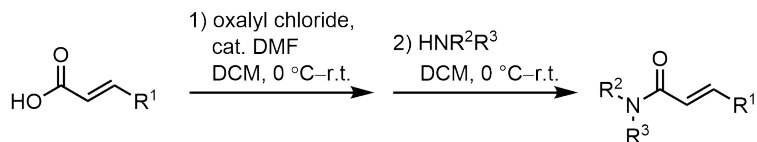


Step 2. To the solution of chiral amides in DCM (100 mL) cooled to 0 °C, thionyl chloride (1.41 mL, 19.4 mmol, 1.0 equiv) was added dropwise. The reaction was allowed to warm to room temperature and was stirred at 70 °C for 4 h. Next, the reaction was cooled to room temperature. Unreacted thionyl chloride was removed under reduced pressure. The crude product obtained was then dissolved in MeOH (100 mL) with KOH (2.72 g, 48.5 mmol, 10 equiv) powder. The suspension was heated at reflux for 4 h. After cooling to room temperature, H_2O was added and the mixture was extracted with DCM (3 x 100 mL). The combined organic layers were washed with brine, and dried over MgSO_4 . After filtration, the solvent was removed under reduced pressure. The residue was purified by flash chromatography (2:1 $\text{Et}_2\text{O}/\text{EtOAc}$) to afford the product as a pale yellow solid.

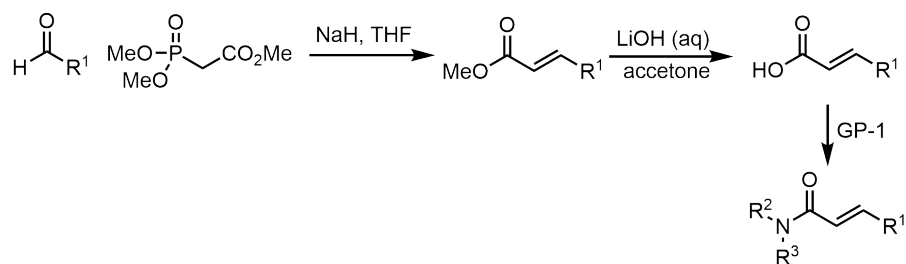
^1H NMR (400 MHz, Chloroform- d) δ 7.36 – 7.26 (m, 10H), 5.29 (dd, J = 9.4, 7.1 Hz, 2H), 4.72 (dd, J = 10.0, 8.4 Hz, 2H), 4.21 (t, J = 8.0 Hz, 2H), 2.83 – 2.74 (m, 4H), 2.15 (p, J = 8.0 Hz, 2H).

Preparation of the Amide Substrates

The yields have not been optimized.

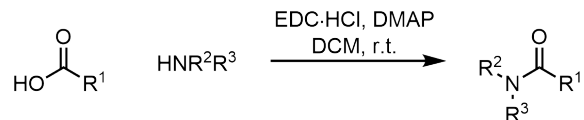


General Procedure 1 (GP-1): Preparation of the α,β -unsaturated amides from the corresponding carboxylic acid. An oven-dried round-bottom flask was charged with a magnetic stir bar and the carboxylic acid (1.0 equiv), and then it was sealed with a rubber septum cap. The flask was placed under a nitrogen atmosphere by evacuating and backfilling the flask (three cycles), followed by the addition of DCM. The resulting solution was cooled to 0 °C. Oxalyl chloride (1.0 equiv) was added dropwise, followed by the addition of 2 drops of DMF. The reaction was stirred at 0 °C for another 10 min and then at room temperature until the gas evolution ceased (2-3 h). Then, the reaction mixture was cooled to 0 °C, and the amine (2.0 equiv) was added dropwise. After stirring for 1 h at room temperature, the reaction mixture was diluted with DCM. The organic layer was washed with 1 M HCl, saturated aqueous $NaHCO_3$, brine, and dried over $MgSO_4$. After filtration, the solvent was removed under reduced pressure. The residue was purified by flash chromatography or recrystallized to afford the pure product.

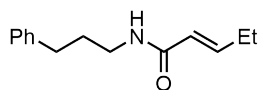


General Procedure 2 (GP-2): Preparation of the α,β -unsaturated amides from the corresponding aldehyde. An oven-dried round-bottom flask was charged with a magnetic stir bar and NaH (60% w/w in oil, 1.1 equiv), and then it was sealed with a rubber septum cap. The flask was placed under a nitrogen atmosphere by evacuating and backfilling the flask (three cycles), followed by the addition of THF. To the stirring suspension, methyl dimethylphosphonoacetate (1.1 equiv) was added dropwise. The reaction mixture was stirred at room temperature for 2 h, followed

by the dropwise addition of the aldehyde (1.0 equiv). After stirring for 12 h at room temperature, the reaction mixture was diluted with Et₂O, and washed with saturated aqueous NaHCO₃, and brine, and dried over MgSO₄. After filtration, the solvent was removed under reduced pressure. The resulting ester crude was dissolved in acetone, and an aqueous solution of LiOH (1.0 M, 1.0 equiv) was added dropwise. After stirring at room temperature for 24 h, the acetone was evaporated. The residue was diluted with Et₂O and washed with saturated aqueous NaHCO₃. The combined aqueous base solutions were acidified using concentrated hydrochloric acid and extracted with Et₂O. The combined organic extracts were dried over MgSO₄. After filtration, the solvent was removed under reduced pressure to afford the α,β -unsaturated carboxylic acid. The carboxylic acid was converted to α,β -unsaturated amides according to GP-1.



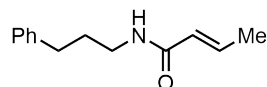
General Procedure 3 (GP-3: Preparation of the other unsaturated amides from the corresponding carboxylic acid). An oven-dried round-bottom flask was charged with a magnetic stir bar, carboxylic acid (1.0 equiv), and EDC·HCl (1.0 equiv), and then it was sealed with a rubber septum cap. The flask was placed under a nitrogen atmosphere by evacuating and backfilling the flask (three cycles), followed by the addition of DCM. DMAP (0.05 equiv) and amine (1.2 equiv) were dissolved in DCM. The solution was degassed with nitrogen gas and added to the reaction mixture. After stirring overnight at room temperature, the reaction mixture was washed with aqueous 2 M HCl, saturated aqueous NaHCO₃, and brine, and dried over MgSO₄. After filtration, the solvent was removed under reduced pressure. The residue was purified by flash chromatography to afford the pure product.



(E)-N-(3-phenylpropyl)pent-2-enamide. The title compound was synthesized according to GP-1 from (E)-pent-2-enoic acid (1.02 mL, 10 mmol), oxalyl chloride (0.84 mL, 10 mmol), 3-phenyl-1-propylamine (2.84 mL, 20 mmol), DMF (2 drops), and DCM (10 mL). The product was purified by column chromatography on silica gel (3:7 EtOAc/hexanes). 1.79 g (8.24 mmol, 82% yield). Pale yellow oil.

^1H NMR (400 MHz, Chloroform- d) δ 7.33 – 7.14 (m, 5H), 6.84 (dt, $J = 15.2$, 6.4 Hz, 1H), 5.70 (dt, $J = 15.4$, 1.8 Hz, 1H), 5.48 (s, 1H), 3.36 (q, $J = 7.1$ Hz, 2H), 2.71 – 2.62 (m, 2H), 2.25 – 2.14 (m, 2H), 1.87 (p, $J = 7.6$ Hz, 2H), 1.05 (t, $J = 7.4$ Hz, 3H).

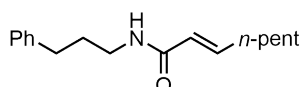
^{13}C NMR (101 MHz, Chloroform- d) δ 166.63, 146.49, 141.96, 128.94, 128.84, 126.46, 123.09, 39.65, 33.81, 31.72, 25.54, 12.92.



(E)-N-(3-phenylpropyl)but-2-enamide. The title compound was synthesized according to GP-1 from (E)-but-2-enoic acid (650 mg, 7.5 mmol), oxalyl chloride (0.64 mL, 7.5 mmol), 3-phenyl-1-propylamine (2.13 mL, 15 mmol), DMF (2 drops), and DCM (7.5 mL). The product was recrystallized from DCM/hexanes. 1.41 g (6.94 mmol, 91% yield). White solid.

^1H NMR (300 MHz, Chloroform- d) δ 7.37 – 7.09 (m, 5H), 6.92 – 6.69 (m, 1H), 5.74 (dd, $J = 15.1$, 1.6 Hz, 1H), 5.52 (s, 1H), 3.35 (q, $J = 7.0$ Hz, 2H), 2.75 – 2.59 (m, 2H), 1.93 – 1.80 (m, 5H).

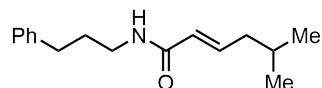
^{13}C NMR (101 MHz, Chloroform- d) δ 166.42, 141.94, 140.18, 128.93, 128.83, 126.45, 125.52, 39.60, 33.80, 31.73, 18.16.



(E)-N-(3-phenylpropyl)oct-2-enamide. The title compound was synthesized according to GP-2 from (E)-oct-2-enoic acid (0.99 mL, 7.5 mmol), oxalyl chloride (0.64 mL, 7.5 mmol), 3-phenyl-1-propylamine (2.13 mL, 15 mmol), DMF (2 drops), and DCM (7.5 mL). The product was purified by column chromatography on silica gel (3:7 EtOAc/hexanes). 0.73 g (2.81 mmol, 38% yield). Colorless oil.

^1H NMR (400 MHz, Chloroform- d) δ 7.34 – 7.12 (m, 5H), 6.79 (dt, $J = 15.2$, 7.0 Hz, 1H), 5.70 (dt, $J = 15.3$, 1.5 Hz, 1H), 5.40 (s, 1H), 3.42 – 3.30 (m, 2H), 2.73 – 2.62 (m, 2H), 2.15 (qd, $J = 7.4$, 1.5 Hz, 2H), 1.87 (p, $J = 7.5$ Hz, 2H), 1.51 – 1.40 (m, 2H), 1.30 (h, $J = 3.6$, 3.0 Hz, 4H), 0.95 – 0.81 (m, 3H).

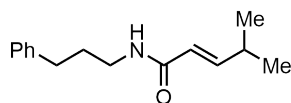
^{13}C NMR (101 MHz, Chloroform- d) δ 166.54, 145.32, 141.96, 128.94, 128.85, 126.47, 123.93, 39.66, 33.83, 32.47, 31.82, 31.74, 28.41, 22.95, 14.47.



(E)-5-methyl-N-(3-phenylpropyl)hex-2-enamide. The title compound was synthesized according to GP-2. The corresponding ester was synthesized from 3-methylbutanal (4.93 mL, 46 mmol), NaH (60% w/w in oil, 2.0 g, 50 mmol), methyl dimethylphosphonoacetate (8.10 mL, 50 mmol), and THF (150 mL). The resulting methyl (E)-5-methylhex-2-enoate was deprotected using LiOH (2.0 M aq, 250 mL, 50 mmol), and acetone (500 mL). The carboxylic acid product (E)-5-methylhex-2-enoic acid was obtained (3.80 g, 29.5 mmol, 59% yield). The title compound was then synthesized from (E)-5-methylhex-2-enoic acid (1.28 g, 10 mmol), oxalyl chloride (0.84 mL, 10 mmol), 3-phenyl-1-propylamine (2.84 mL, 20 mmol), DMF (2 drops), and DCM (10 mL). The product was purified by column chromatography on silica gel (1:4 EtOAc/hexanes). 1.29 g (5.30 mmol, 53% yield). White solid.

^1H NMR (400 MHz, Chloroform- d) δ 7.31 – 7.13 (m, 5H), 6.76 (dt, J = 15.1, 7.4 Hz, 1H), 5.68 (dt, J = 15.2, 1.4 Hz, 1H), 5.42 (s, 1H), 3.35 (q, J = 7.0 Hz, 2H), 2.70 – 2.62 (m, 2H), 2.04 (td, J = 7.5, 1.4 Hz, 2H), 1.86 (p, J = 7.5 Hz, 2H), 1.72 (dp, J = 13.4, 6.7 Hz, 1H), 0.90 (d, J = 6.6 Hz, 6H).

^{13}C NMR (101 MHz, Chloroform- d) δ 166.42, 144.08, 141.95, 128.94, 128.84, 126.47, 125.01, 41.83, 39.67, 33.84, 31.73, 28.35, 22.86.

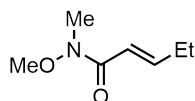


(E)-4-methyl-N-(3-phenylpropyl)pent-2-enamide. The title compound was synthesized according to GP-1 from (E)-4-methylpent-2-enoic acid (0.76 mL, 7.5 mmol), oxalyl chloride (0.64 mL, 7.5 mmol), 3-phenyl-1-propylamine (2.13 mL, 15 mmol), DMF (2 drops), and DCM (7.5 mL). The product was purified by column chromatography on silica gel (3:7 EtOAc/hexanes). 1.32 g (5.71 mmol, 76% yield). Yellow solid.

^1H NMR (400 MHz, Chloroform- d) δ 7.33 – 7.14 (m, 5H), 6.77 (dd, J = 15.4, 6.6 Hz, 1H), 5.66 (dd, J = 15.4, 1.5 Hz, 1H), 5.55 (s, 1H), 3.36 (q, J = 7.0 Hz, 2H), 2.74

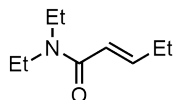
– 2.62 (m, 2H), 2.42 (dq, $J = 13.6, 6.8, 1.4$ Hz, 1H), 1.87 (p, $J = 7.5$ Hz, 2H), 1.04 (d, $J = 6.7$ Hz, 6H).

^{13}C NMR (101 MHz, Chloroform- d) δ 166.79, 151.31, 141.95, 128.92, 128.83, 126.44, 121.27, 39.68, 33.81, 31.69, 31.17, 21.94.



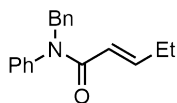
(E)-N-methoxy-N-methylpent-2-enamide. The title compound was synthesized according to modified GP-1 from (E)-pent-2-enoic acid (1.42 mL, 14 mmol), oxalyl chloride (1.19 mL, 14 mmol), HNMe(OMe)·HCl (1.36 g, 14 mmol), NEt₃ (1.95 mmol, 14 mmol), DMF (2 drops), and DCM (5 mL). The product was purified by column chromatography on silica gel (4:6 EtOAc/hexanes). 0.23 g (0.70 mmol, 5% yield). White solid.

^1H NMR (300 MHz, Chloroform- d) δ 7.02 (dt, $J = 15.4, 6.5$ Hz, 1H), 6.39 (dt, $J = 15.4, 1.6$ Hz, 1H), 3.70 (d, $J = 1.0$ Hz, 3H), 3.24 (s, 3H), 2.38 – 2.16 (m, 2H), 1.08 (t, $J = 7.5$ Hz, 3H).



(E)-N,N-diethylpent-2-enamide. The title compound was synthesized according to GP-1 from (E)-pent-2-enoic acid (2.02 mL, 20 mmol), oxalyl chloride (1.70 mL, 20 mmol), diethylamine (4.14 mL, 40 mmol), DMF (2 drops), and DCM (20 mL). The product was purified by column chromatography on silica gel (4:6 EtOAc/hexanes). 1.99 g (12.8 mmol, 64% yield). Pale yellow oil.

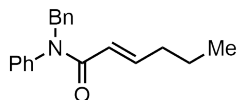
^1H NMR (400 MHz, Chloroform- d) δ 6.95 (dt, $J = 14.9, 6.5$ Hz, 1H), 6.18 (d, $J = 15.0$ Hz, 1H), 3.40 (s, 4H), 2.29 – 2.18 (m, 2H), 1.18 (s, 6H), 1.08 (t, $J = 7.4$ Hz, 3H).



(E)-N-benzyl-N-phenylpent-2-enamide. The title compound was synthesized according to modified GP-1 from (E)-pent-2-enoic acid (5.06 mL, 50 mmol). oxalyl

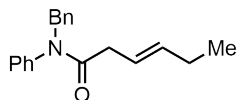
chloride (4.23 mL, 50 mmol), N-benzylaniline (10.1 g, 60 mmol), NEt₃ (7.0 mmol, 50 mmol), and DCM (25 mL). The product was purified by column chromatography on silica gel (2:8 EtOAc/hexanes) and recrystallized from hexanes at 5 °C. White solid.

¹H NMR (300 MHz, Chloroform-d) δ 7.37 – 6.94 (m, 11H), 5.68 (d, J = 15.1 Hz, 1H), 4.96 (s, 2H), 2.17 – 1.98 (m, 2H), 0.92 (t, J = 7.4 Hz, 3H).



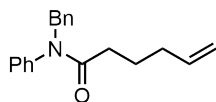
(E)-N-benzyl-N-phenylhex-2-enamide. The title compound was synthesized according to GP-3 from (E)-hex-2-enoic acid (2.28 g, 20 mmol), EDC·HCl (3.83 g, 20 mmol), N-benzylaniline (4.40 g, 24 mmol), DMAP (0.122 g, 1.0 mmol), and DCM (80 mL). The product was purified by column chromatography on silica gel (3:7 EtOAc/hexanes). 0.78 g (2.79 mmol, 14% yield). Colorless oil.

¹H NMR (300 MHz, Chloroform-d) δ 7.37 – 7.17 (m, 8H), 7.11 – 6.85 (m, 3H), 5.69 (d, J = 14.8 Hz, 1H), 4.96 (s, 2H), 2.08 – 1.98 (m, 2H), 1.37 (h, J = 7.3 Hz, 2H), 0.84 (t, J = 7.4 Hz, 3H).



(E)-N-benzyl-N-phenylhex-3-enamide. The title compound was synthesized according to GP-3 from (E)-hex-3-enoic acid (2.37 mL, 20 mmol), EDC·HCl (3.83 g, 20 mmol), N-benzylaniline (4.40 g, 24 mmol), DMAP (0.122 g, 1.0 mmol), and DCM (80 mL). The product was purified by column chromatography on silica gel (3:7 EtOAc/hexanes). 1.86 g (6.66 mmol, 33% yield). Colorless oil.

¹H NMR (300 MHz, Chloroform-d) δ 7.38 – 7.14 (m, 8H), 7.04 – 6.90 (m, 2H), 5.51 (dt, J = 13.6, 6.6 Hz, 1H), 5.40 – 5.26 (m, 1H), 4.88 (s, 2H), 2.82 (d, J = 6.7 Hz, 2H), 2.09 – 1.91 (m, 2H), 0.94 (t, J = 7.4 Hz, 3H).



N-benzyl-N-phenylhex-5-enamide. The title compound was synthesized according to GP-3 from hex-5-enoic acid (1.19 mL, 10 mmol), EDC·HCl (1.92 g, 10 mmol), N-benzylaniline (2.20 g, 12 mmol), DMAP (61.1 mg, 0.5 mmol), and DCM (40 mL). The product was purified by column chromatography on silica gel (3:7 EtOAc/hexanes). 0.37 g (1.32 mmol, 13% yield). Colorless oil.

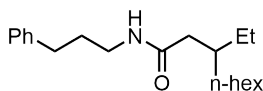
^1H NMR (300 MHz, Chloroform- d) δ 7.38 – 7.15 (m, 8H), 7.00 – 6.91 (m, 2H), 5.68 (ddt, $J = 16.8, 10.2, 6.7$ Hz, 1H), 4.98 – 4.84 (m, 4H), 2.12 – 2.04 (m, 2H), 1.98 (q, $J = 6.9$ Hz, 2H), 1.71 (p, $J = 7.4$ Hz, 2H).

Nickel-Catalyzed Alkylations of α, β -Unsaturated Amides

General Procedure. In a N₂-filled glovebox, NiBr₂·dme (3.1 mg, 0.01 mmol, 0.10 equiv), and (*S,S*)-**L1** (4.2 mg, 0.012 mmol, 0.12 equiv) were added to an oven-dried 4 mL vial equipped with a stir bar. Anhydrous THF (0.5 mL) was added to the vial, and the mixture was stirred at room temperature for 30 min, at which time it was a pink homogeneous solution.

In a N₂-filled glovebox, a separate oven-dried 4 mL vial equipped with a stir bar was charged with the olefin (0.15 mmol, 1.5 equiv), the electrophile (0.1 mmol, 1.0 equiv), and K₃PO₄·H₂O (35 mg, 0.15 mmol, 1.5 equiv). Next, the catalyst solution was transferred to the vial, followed by the addition of trimethoxysilane (76 μ L, 0.60 mmol, 6.0 equiv). The vial was closed with a PTFE septum cap, the joint was wrapped with electrical tape, and the vial was transferred out of the glovebox. The mixture was stirred at 1000 rpm at room temperature for 15 h.

The reaction mixture was passed through a plug of silica gel, and the vial, the cap, and the silica gel was rinsed with Et₂O. The filtrate was concentrated, and the residue was purified by preparative thin layer chromatography.

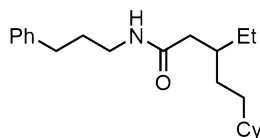


3-Ethyl-N-(3-phenylpropyl)nonanamide (Figure 2.3, entry 1). The title compound was synthesized according to GP-4 from (*E*)-*N*-(3-phenylpropyl)pent-2-enamide and 1-iodohexane. The product was purified by preparative thin layer chromatography (35:65 EtOAc/hexanes). 70% yield, 90% ee.

SFC analysis: the ee was determined on a chiralcel OJ-3 column (10% *i*-PrOH in hexane, 1.0 mL/min); retention times for compound obtained using (*S,S*)-**L1**: 3.15 min (minor), 3.42 min (major).

¹H NMR (300 MHz, Chloroform-*d*) δ 7.33 – 7.25 (m, 2H), 7.19 (td, *J* = 6.6, 1.7 Hz, 3H), 5.37 (s, 1H), 3.30 (td, *J* = 7.1, 5.9 Hz, 2H), 2.72 – 2.58 (m, 2H), 2.03 (d, *J* = 7.0 Hz, 2H), 1.92 – 1.72 (m, 3H), 1.40 – 1.17 (m, 12H), 0.92 – 0.81 (m, 6H).

¹³C NMR (101 MHz, Chloroform-*d*) δ 173.32, 141.97, 128.96, 128.84, 126.49, 42.12, 39.62, 37.21, 33.86, 33.73, 32.36, 31.84, 30.13, 27.02, 26.59, 23.14, 14.59, 11.24.

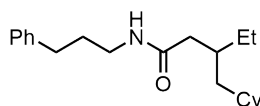


5-Cyclohexyl-3-ethyl-N-(3-phenylpropyl)pentanamide (Figure 2.3, entry 2). The title compound was synthesized according to GP-4 from (E)-N-(3-phenylpropyl)pent-2-enamide and (2-iodoethyl)cyclohexane. The product was purified by preparative thin layer chromatography (35:65 EtOAc/hexanes). 66% yield, 89% ee.

SFC analysis: the ee was determined on a chiralcel OJ-3 column (15% i-PrOH in hexane, 1.0 mL/min); retention times for compound obtained using (*S,S*)-**L1**: 2.91 min (minor), 3.37 min (major).

^1H NMR (300 MHz, Chloroform-*d*) δ 7.33 – 7.26 (m, 2H), 7.23 – 7.14 (m, 3H), 5.38 (s, 1H), 3.29 (q, $J = 6.7$ Hz, 2H), 2.65 (t, $J = 7.7$ Hz, 2H), 2.03 (d, $J = 7.1$ Hz, 2H), 1.94 – 1.56 (m, 8H), 1.45 – 1.01 (m, 10H), 0.95 – 0.72 (m, 5H).

^{13}C NMR (101 MHz, Chloroform-*d*) δ 173.36, 141.97, 128.96, 128.84, 126.49, 42.09, 39.64, 38.46, 37.42, 34.70, 33.97, 33.91, 31.83, 30.79, 27.20, 26.88, 26.55, 11.22.



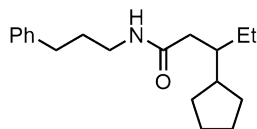
3-(Cyclohexylmethyl)-N-(3-phenylpropyl)pentanamide (Figure 2.3, entry 3).

The title compound was synthesized according to GP-4 from (E)-N-(3-phenylpropyl)pent-2-enamide and (iodomethyl)cyclohexane. The product was purified by preparative thin layer chromatography (35:65 EtOAc/hexanes). 70% yield, 90% ee.

SFC analysis: the ee was determined on a chiralpak IF-3 column (15% i-PrOH in hexane, 1.0 mL/min); retention times for compound obtained using (*S,S*)-**L1**: 9.63 min (minor), 10.78 min (major).

^1H NMR (300 MHz, Chloroform-*d*) δ 7.33 – 7.26 (m, 2H), 7.19 (td, $J = 7.0, 1.3$ Hz, 3H), 5.39 (s, 1H), 3.38 – 3.23 (m, 2H), 2.73 – 2.59 (m, 2H), 2.07 – 1.98 (m, 2H), 1.96 – 1.78 (m, 3H), 1.76 – 1.62 (m, 5H), 1.38 – 0.99 (m, 8H), 0.91 – 0.76 (m, 5H).

^{13}C NMR (101 MHz, Chloroform-*d*) δ 173.30, 141.97, 128.96, 128.85, 126.48, 42.36, 42.06, 39.63, 35.30, 34.24, 34.08, 34.01, 33.86, 31.82, 27.15, 26.90, 11.07.

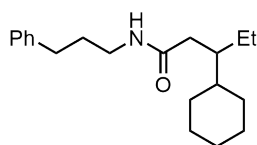


3-Cyclopentyl-N-(3-phenylpropyl)pentanamide (Figure 2.3, entry 4). The title compound was synthesized according to GP-4 from (E)-N-(3-phenylpropyl)pent-2-enamide and iodocyclopentane. The product was purified by preparative thin layer chromatography (35:65 EtOAc/hexanes). 71% yield, 87% ee.

SFC analysis: the ee was determined on a chiralpak IF-3 column (15% i-PrOH in hexane, 1.0 mL/min); retention times for compound obtained using (*S,S*)-L1: 9.82 min (major), 10.25 min (minor).

^1H NMR (300 MHz, Chloroform-*d*) δ 7.32 – 7.26 (m, 2H), 7.19 (td, J = 6.8, 1.5 Hz, 3H), 5.39 (s, 1H), 3.29 (q, J = 6.7 Hz, 2H), 2.72 – 2.56 (m, 2H), 2.17 (dd, J = 14.2, 4.8 Hz, 1H), 2.01 (dd, J = 14.2, 7.5 Hz, 1H), 1.91 – 1.62 (m, 7H), 1.62 – 1.04 (m, 7H), 0.93 – 0.82 (m, 3H).

^{13}C NMR (101 MHz, Chloroform-*d*) δ 173.55, 141.99, 128.97, 128.85, 126.50, 43.67, 41.87, 40.18, 39.67, 33.89, 31.81, 30.73, 25.86, 25.25, 10.97.

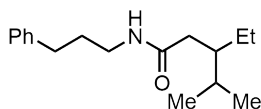


3-Cyclohexyl-N-(3-phenylpropyl)pentanamide (Figure 2.3, entry 5). The title compound was synthesized according to GP-4 from (E)-N-(3-phenylpropyl)pent-2-enamide and iodocyclohexane. The product was purified by preparative thin layer chromatography (35:65 EtOAc/hexanes). 61% yield, 89% ee.

SFC analysis: the ee was determined on a chiralpak IF-3 column (15% i-PrOH in hexane, 1.0 mL/min); retention times for compound obtained using (*S,S*)-L1: 10.47 min (major), 11.54 min (minor).

^1H NMR (300 MHz, Chloroform-*d*) δ 7.33 – 7.26 (m, 2H), 7.19 (td, J = 6.4, 1.6 Hz, 3H), 5.36 (s, 1H), 3.30 (td, J = 7.0, 5.8 Hz, 2H), 2.73 – 2.59 (m, 2H), 2.14 (dd, J = 14.2, 6.1 Hz, 1H), 1.99 – 1.57 (m, 9H), 1.45 – 0.92 (m, 8H), 0.87 (t, J = 7.4 Hz, 3H).

^{13}C NMR (101 MHz, Chloroform- d) δ 173.81, 141.99, 128.97, 128.85, 126.50, 42.75, 40.30, 39.65, 39.10, 33.87, 31.82, 30.50, 29.72, 27.33, 24.08, 12.28.

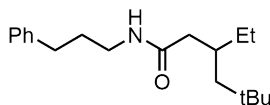


3-Ethyl-4-methyl-N-(3-phenylpropyl)pentanamide (Figure 2.3, entry 6). The title compound was synthesized according to GP-4 from (E)-N-(3-phenylpropyl)pent-2-enamide and 2-iodo-propane. The product was purified by preparative thin layer chromatography (35:65 EtOAc/hexanes). 56% yield, 85% ee.

SFC analysis: the ee was determined on a chiralcel OJ-3 column (10% i-PrOH in hexane, 1.0 mL/min); retention times for compound obtained using (*S,S*)-**L1**: 3.11 min (minor), 3.28 min (major).

^1H NMR (300 MHz, Chloroform- d) δ 7.33 – 7.26 (m, 2H), 7.19 (td, J = 6.5, 1.7 Hz, 3H), 5.34 (s, 1H), 3.30 (td, J = 7.1, 5.9 Hz, 2H), 2.72 – 2.59 (m, 2H), 2.11 (dd, J = 14.2, 5.9 Hz, 1H), 1.99 – 1.64 (m, 5H), 1.44 – 1.13 (m, 2H), 0.95 – 0.76 (m, 9H).

^{13}C NMR (101 MHz, Chloroform- d) δ 173.78, 141.99, 128.97, 128.85, 126.50, 43.17, 39.69, 38.67, 33.88, 31.82, 29.48, 23.94, 19.89, 19.02, 12.24.

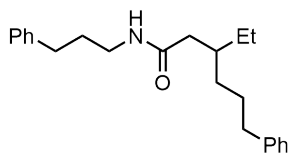


3-Ethyl-5,5-dimethyl-N-(3-phenylpropyl)hexanamide (Figure 2.3, entry 7). The title compound was synthesized according to GP-4 from (E)-N-(3-phenylpropyl)pent-2-enamide and 1-iodo-2,2-dimethylpropane. The product was purified by preparative thin layer chromatography (35:65 EtOAc/hexanes). 29% yield, 89% ee.

SFC analysis: the ee was determined on chiralpak IE-3 column (10% i-PrOH in hexane, 1.0 mL/min); retention times for compound obtained using (*S,S*)-**L1**: 7.33 min (major), 7.72 min (minor).

^1H NMR (300 MHz, Chloroform- d) δ 7.30 (d, J = 7.6 Hz, 2H), 7.24 – 7.12 (m, 3H), 5.35 (s, 1H), 3.29 (q, J = 6.7 Hz, 2H), 2.65 (t, J = 7.7 Hz, 2H), 2.06 (qd, J = 14.1, 7.0 Hz, 2H), 1.84 (p, J = 7.5 Hz, 3H), 1.38 – 1.19 (m, 3H), 1.08 (dd, J = 14.2, 5.0 Hz, 1H), 0.88 (m, 12H).

^{13}C NMR (101 MHz, Chloroform- d) δ 173.12, 141.98, 128.97, 128.85, 126.50, 47.78, 44.20, 39.62, 33.88, 33.73, 31.83, 31.53, 30.42, 29.15, 11.46.

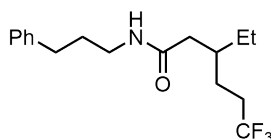


3-Ethyl-6-phenyl-N-(3-phenylpropyl)hexanamide (Figure 2.3, entry 8). The title compound was synthesized according to GP-4 from (E)-N-(3-phenylpropyl)pent-2-enamide and (3-iodopropyl)benzene. The product was purified by preparative thin layer chromatography (35:65 EtOAc/hexanes). 72% yield, 89% ee.

SFC analysis: the ee was determined on a chiralcel OD-3 column (15% *i*-PrOH in hexane, 1.0 mL/min).

^1H NMR (300 MHz, Chloroform- d) δ 7.33 – 7.11 (m, 10H), 5.31 (s, 1H), 3.34 – 3.22 (m, 2H), 2.61 (dt, J = 15.7, 7.7 Hz, 4H), 2.12 – 1.94 (m, 2H), 1.90 – 1.75 (m, 3H), 1.70 – 1.52 (m, 2H), 1.42 – 1.22 (m, 4H), 0.85 (t, J = 7.4 Hz, 3H).

^{13}C NMR (101 MHz, Chloroform- d) δ 173.15, 143.07, 141.95, 128.97, 128.85, 128.74, 126.51, 126.15, 41.97, 39.64, 37.04, 36.63, 33.86, 33.29, 31.80, 28.91, 26.55, 11.23.

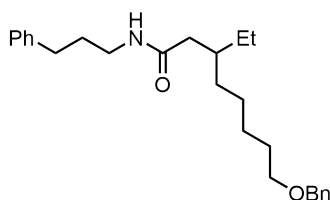


3-Ethyl-6,6,6-trifluoro-N-(3-phenylpropyl)hexanamide (Figure 2.3, entry 9). The title compound was synthesized according to GP-4 from (E)-N-(3-phenylpropyl)pent-2-enamide and 1,1,1-trifluoro-3-iodopropane. The product was purified by preparative thin layer chromatography (1:1 EtOAc/hexanes). 80% yield, 84% ee.

SFC analysis: the ee was determined on a chiralpak IF-3 column (15% *i*-PrOH in hexane, 1.0 mL/min); retention times for compound obtained using (*S,S*)-**L1**: 2.95 min (major), 3.07 min (minor).

^1H NMR (300 MHz, Chloroform- d) δ 7.35 – 7.13 (m, 5H), 5.36 (s, 1H), 3.30 (q, J = 6.8 Hz, 2H), 2.66 (t, J = 7.6 Hz, 2H), 2.19 – 1.78 (m, 7H), 1.54 (m, 2H), 1.36 (q, J = 7.1 Hz, 2H), 0.89 (t, J = 7.4 Hz, 3H).

^{13}C NMR (101 MHz, Chloroform- d) δ 172.24, 141.87, 129.00, 128.84, 126.55, 41.43, 39.76, 36.05, 33.88, 31.87, 31.71, 26.40, 25.68, 11.06.

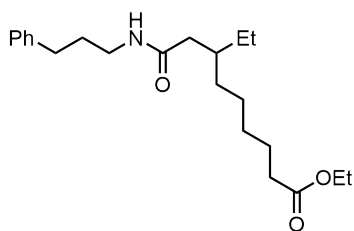


8-(Benzyloxy)-3-ethyl-N-(3-phenylpropyl)octanamide (Figure 2.3, entry 10). The title compound was synthesized according to GP-4 from (E)-N-(3-phenylpropyl)pent-2-enamide and (((5-iodopentyl)oxy)methyl)benzene. The product was purified by preparative thin layer chromatography (35:65 EtOAc/hexanes). 60% yield, 89% ee.

SFC analysis: the ee was determined on a chiralcel OJ-3 column (15% i-PrOH in hexane, 1.0 mL/min); retention times for compound obtained using (*S,S*)-**L1**: 9.08 min (minor), 10.80 min (major).

^1H NMR (300 MHz, Chloroform- d) δ 7.38 – 7.15 (m, 10H), 5.35 (s, 1H), 4.49 (s, 2H), 3.45 (t, J = 6.6 Hz, 2H), 3.29 (td, J = 7.1, 5.9 Hz, 2H), 2.70 – 2.60 (m, 2H), 2.02 (d, J = 7.0 Hz, 2H), 1.91 – 1.73 (m, 3H), 1.60 (p, J = 6.7 Hz, 2H), 1.39 – 1.23 (m, 8H), 0.85 (t, J = 7.4 Hz, 3H).

^{13}C NMR (101 MHz, Chloroform- d) δ 173.25, 141.96, 139.15, 128.97, 128.85, 128.84, 128.12, 127.97, 126.49, 73.36, 70.93, 42.04, 39.63, 37.14, 33.86, 33.63, 31.82, 30.21, 27.02, 26.88, 26.57, 11.24.



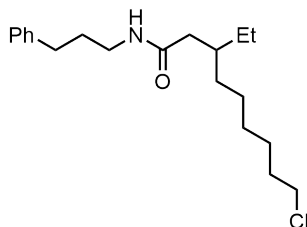
Ethyl 7-ethyl-9-oxo-9-((3-phenylpropyl)amino)nonanoate (Figure 2.3, entry 11).

The title compound was synthesized according to GP-4 from (E)-N-(3-phenylpropyl)pent-2-enamide and ethyl 6-iodohexanoate. The product was purified by preparative thin layer chromatography (9:1 EtOAc/hexane). 48% yield, 89% ee.

SFC analysis: the ee was determined on a chiralcel OJ-3 column (15% i-PrOH in hexane, 1.0 mL/min); retention times for compound obtained using (*S,S*)-**L1**: 2.55 min (minor), 2.89 min (major).

^1H NMR (300 MHz, Chloroform- d) δ 7.34 – 7.13 (m, 5H), 5.38 (s, 1H), 4.11 (q, J = 7.1 Hz, 2H), 3.29 (q, J = 6.4 Hz, 2H), 2.65 (t, J = 7.6 Hz, 2H), 2.27 (t, J = 7.4 Hz, 2H), 2.03 (d, J = 6.9 Hz, 2H), 1.84 (dt, J = 14.7, 7.5 Hz, 3H), 1.28 (dq, J = 14.4, 7.4 Hz, 13H), 0.86 (t, J = 7.2 Hz, 3H).

^{13}C NMR (101 MHz, Chloroform- d) δ 174.35, 173.20, 141.97, 128.97, 128.85, 126.50, 60.67, 42.02, 39.64, 37.08, 34.80, 33.87, 33.49, 31.83, 29.87, 26.68, 26.56, 25.40, 14.74, 11.23.

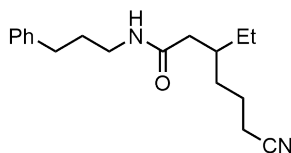


9-Chloro-3-ethyl-N-(3-phenylpropyl)nonanamide (Figure 2.3, entry 12). The title compound was synthesized according to GP-4 from (E)-N-(3-phenylpropyl)pent-2-enamide and 1-chloro-6-iodohexane. The product was purified by preparative thin layer chromatography (1:1 EtOAc/hexanes). 70% yield, 90% ee.

SFC analysis: the ee was determined on a chiralpak IC-3 column (15% i-PrOH in hexane, 1.0 mL/min); retention times for compound obtained using (*S,S*)-**L1**: 12.29 min (minor), 12.90 min (major).

^1H NMR (300 MHz, Chloroform- d) δ 7.33 – 7.14 (m, 5H), 5.34 (s, 1H), 3.51 (t, J = 6.7 Hz, 2H), 3.35 – 3.24 (m, 2H), 2.71 – 2.60 (m, 2H), 2.11 – 1.96 (m, 2H), 1.79 (ddt, J = 26.2, 14.7, 7.2 Hz, 5H), 1.48 – 1.23 (m, 10H), 0.86 (t, J = 7.4 Hz, 3H).

^{13}C NMR (101 MHz, Chloroform- d) δ 173.24, 141.95, 128.97, 128.84, 126.51, 45.64, 42.04, 39.65, 37.12, 33.86, 33.60, 33.08, 31.84, 29.65, 27.33, 26.90, 26.60, 11.25.

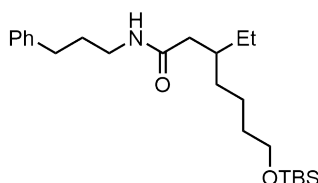


6-Cyano-3-ethyl-N-(3-phenylpropyl)hexanamide (Figure 2.3, entry 13). The title compound was synthesized according to GP-4 from (E)-N-(3-phenylpropyl)pent-2-enamide and 4-iodobutanenitrile. The product was purified by preparative thin layer chromatography (100% Et₂O). 54% yield, 89% ee.

SFC analysis: the ee was determined on a chiralcel OJ-3 column (10% *i*-PrOH in hexane, 1.0 mL/min); retention times for compound obtained using (*S,S*)-**L1**: 6.17 min (minor), 6.94 min (major).

^1H NMR (300 MHz, Chloroform-*d*) δ 7.35 – 7.13 (m, 5H), 5.38 (s, 1H), 3.30 (q, J = 5.5 Hz, 2H), 2.66 (t, J = 7.7 Hz, 2H), 2.34 (td, J = 7.0, 1.7 Hz, 2H), 2.17 – 1.95 (m, 2H), 1.85 (h, J = 7.2, 6.7 Hz, 3H), 1.66 (p, J = 7.3 Hz, 2H), 1.49 – 1.18 (m, 4H), 0.88 (t, J = 7.4 Hz, 3H).

^{13}C NMR (101 MHz, Chloroform-*d*) δ 172.56, 141.89, 129.00, 128.84, 126.55, 120.23, 41.59, 39.74, 36.36, 33.88, 32.97, 31.74, 26.68, 23.28, 17.90, 11.21.

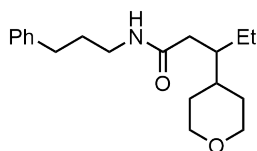


7-((tert-Butyldimethylsilyl)oxy)-3-ethyl-N-(3-phenylpropyl)heptanamide (Figure 2.3, entry 14). The title compound was synthesized according to GP-4 from (*E*)-*N*-(3-phenylpropyl)pent-2-enamide and tert-butyl(4-iodobutoxy)dimethylsilane. The product was purified by preparative thin layer chromatography (35:65 EtOAc/hexanes). 66% yield, 90% ee.

SFC analysis: the ee was determined on a chiralpak AD-3 column (15% *i*-PrOH in hexane, 1.0 mL/min); retention times for compound obtained using (*S,S*)-**L1**: 2.57 min (minor), 2.69 min (major).

^1H NMR (300 MHz, Chloroform-*d*) δ 7.33 – 7.14 (m, 5H), 5.37 (s, 1H), 3.59 (t, J = 6.4 Hz, 2H), 3.29 (q, J = 6.6 Hz, 2H), 2.70 – 2.60 (m, 2H), 2.03 (d, J = 7.1 Hz, 2H), 1.83 (dt, J = 14.6, 7.3 Hz, 3H), 1.56 – 1.43 (m, 2H), 1.31 (dq, J = 15.5, 8.9, 7.5 Hz, 6H), 0.87 (d, J = 7.2 Hz, 12H), 0.04 (s, 6H).

^{13}C NMR (101 MHz, Chloroform-*d*) δ 173.21, 141.97, 128.97, 128.85, 126.50, 63.56, 42.01, 39.63, 37.17, 33.87, 33.59, 33.40, 31.85, 26.49, 26.47, 23.17, 18.85, 11.22, -4.76.

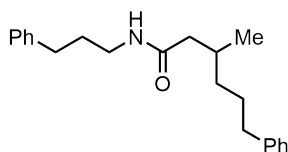


N-(3-phenylpropyl)-3-(tetrahydro-2H-pyran-4-yl)pentanamide (Figure 2.3, entry 17). The title compound was synthesized according to GP-4 from (E)-N-(3-phenylpropyl)pent-2-enamide and 4-iodotetrahydro-2H-pyran. The product was purified by preparative thin layer chromatography (1:1 EtOAc/hexanes). 62% yield, 89% ee.

SFC analysis: the ee was determined on a chiralpak IF-3 column (15% i-PrOH in hexane, 1.0 mL/min); retention times for compound obtained using (*S,S*)-L1: 11.30 min (major), 12.68 min (minor).

^1H NMR (300 MHz, Chloroform-*d*) δ 7.33 – 7.15 (m, 5H), 5.34 (s, 1H), 3.98 (dd, $J = 11.5, 3.7$ Hz, 2H), 3.43 – 3.25 (m, 4H), 2.71 – 2.60 (m, 2H), 2.15 (dd, $J = 14.4, 6.0$ Hz, 1H), 2.02 – 1.54 (m, 5H), 1.53 – 1.18 (m, 6H), 0.88 (t, $J = 7.4$ Hz, 3H).

^{13}C NMR (101 MHz, Chloroform-*d*) δ 173.21, 141.92, 128.99, 128.84, 126.54, 68.89, 41.84, 39.73, 38.45, 37.74, 33.89, 31.77, 30.46, 29.90, 23.69, 11.89.



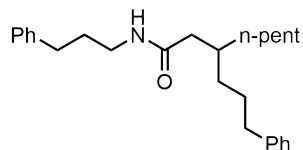
3-Methyl-6-phenyl-N-(3-phenylpropyl)hexanamide (Figure 2.4, entry 18). The title compound was synthesized according to GP-4 from (E)-N-(3-phenylpropyl)but-2-enamide and (3-iodopropyl)benzene. The product was purified by preparative thin layer chromatography (35:65 EtOAc/hexanes). 66% yield, 85% ee.

SFC analysis: the ee was determined on a chiralpak IF-3 column (15% i-PrOH in hexane, 1.0 mL/min); retention times for compound obtained using (*S,S*)-L1: 11.59 min (minor), 13.72 min (major).

^1H NMR (300 MHz, Chloroform-*d*) δ 7.34 – 7.10 (m, 10H), 5.32 (s, 1H), 3.28 (q, $J = 6.7$ Hz, 2H), 2.72 – 2.52 (m, 4H), 2.12 (dd, $J = 12.8, 5.5$ Hz, 1H), 2.04 – 1.76 (m, 4H), 1.74 – 1.49 (m, 2H), 1.45 – 1.14 (m, 2H), 0.91 (d, $J = 6.2$ Hz, 3H).

^{13}C NMR (101 MHz, Chloroform-*d*) δ 172.88, 143.05, 141.95, 128.97, 128.85, 128.76, 126.51, 126.16, 45.12, 39.62, 36.87, 36.51, 33.86, 31.82, 31.16, 29.33, 20.11.

N,3-bis(3-phenylpropyl)octanamide (Figure 2.4, entry 19). The title compound was synthesized according to GP-4 from (E)-N-(3-phenylpropyl)oct-2-enamide and

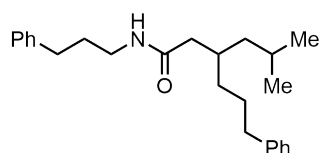


(3-iodopropyl)benzene. The product was purified by preparative thin layer chromatography (35:65 EtOAc/hexanes). 68% yield, 88% ee.

SFC analysis: the ee was determined on a chiralcel OD-3 column (15% i-PrOH in hexane, 1.0 mL/min); retention times for compound obtained using (*S,S*)-**L1**: 15.08 min (major), 16.13 min (minor).

^1H NMR (300 MHz, Chloroform-*d*) δ 7.33 – 7.12 (m, 10H), 5.30 (s, 1H), 3.27 (q, J = 6.7 Hz, 2H), 2.70 – 2.52 (m, 4H), 2.10 – 1.95 (m, 2H), 1.94 – 1.74 (m, 3H), 1.61 (p, J = 7.8, 7.4 Hz, 2H), 1.38 – 1.16 (m, 10H), 0.86 (t, J = 6.6 Hz, 3H).

^{13}C NMR (101 MHz, Chloroform-*d*) δ 173.13, 143.08, 141.95, 128.97, 128.85, 128.74, 126.50, 126.15, 42.41, 39.62, 36.64, 35.71, 34.14, 33.85, 33.82, 32.62, 31.80, 28.89, 26.68, 23.13, 14.56.

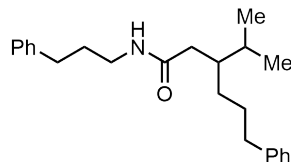


3-Isobutyl-6-phenyl-N-(3-phenylpropyl)hexanamide (Figure 2.4, entry 20). The title compound was synthesized according to GP-4 from (*E*)-5-methyl-N-(3-phenylpropyl)hex-2-enamide and (3-iodopropyl)benzene. The product was purified by preparative thin layer chromatography (35:65 EtOAc/hexanes). 69% yield, 90% ee.

SFC analysis: the ee was determined on a chiralcel OD-3 column (15% i-PrOH in hexane, 1.0 mL/min); retention times for compound obtained using (*S,S*)-**L1**: 12.05 min (major), 13.94 min (minor).

^1H NMR (300 MHz, Chloroform-*d*) δ 7.34 – 7.11 (m, 10H), 5.29 (s, 1H), 3.32 – 3.20 (m, 2H), 2.61 (dt, J = 17.9, 7.6 Hz, 4H), 2.10 – 1.75 (m, 5H), 1.68 – 1.52 (m, 3H), 1.38 – 1.00 (m, 4H), 0.86 (d, J = 6.6 Hz, 6H).

^{13}C NMR (101 MHz, Chloroform-*d*) δ 173.04, 143.07, 141.94, 128.96, 128.85, 128.85, 128.74, 126.49, 126.15, 44.10, 42.60, 39.62, 36.69, 34.16, 33.86, 33.44, 31.79, 28.74, 25.70, 23.28.



3-Isopropyl-6-phenyl-N-(3-phenylpropyl)hexanamide (Figure 2.4, entry 21). The title compound was synthesized according to GP-4 from (E)-4-methyl-N-(3-phenylpropyl)pent-2-enamide and (3-iodopropyl)benzene. The product was purified by preparative thin layer chromatography (35:65 EtOAc/hexanes). 58% yield, 91% ee.

SFC analysis: the ee was determined on a chiralpak AD-3 column (15% i-PrOH in hexane, 1.0 mL/min); retention times for compound obtained using (*S,S*)-**L1**: 8.19 min (minor), 8.99 min (major).

^1H NMR (300 MHz, Chloroform-*d*) δ 7.33 – 7.11 (m, 10H), 5.31 (s, 1H), 3.27 (q, J = 7.0 Hz, 2H), 2.61 (dt, J = 16.0, 7.7 Hz, 4H), 2.11 (dd, J = 13.5, 5.2 Hz, 1H), 1.98 – 1.48 (m, 7H), 1.42 – 1.18 (m, 2H), 0.83 (dd, J = 13.9, 6.7 Hz, 6H).

^{13}C NMR (101 MHz, Chloroform-*d*) δ 173.54, 143.08, 141.96, 128.97, 128.85, 128.73, 126.50, 126.12, 41.33, 39.68, 38.93, 36.66, 33.87, 31.77, 31.09, 29.85, 29.64, 19.88, 18.95.

Initial Broad Ligand Screening

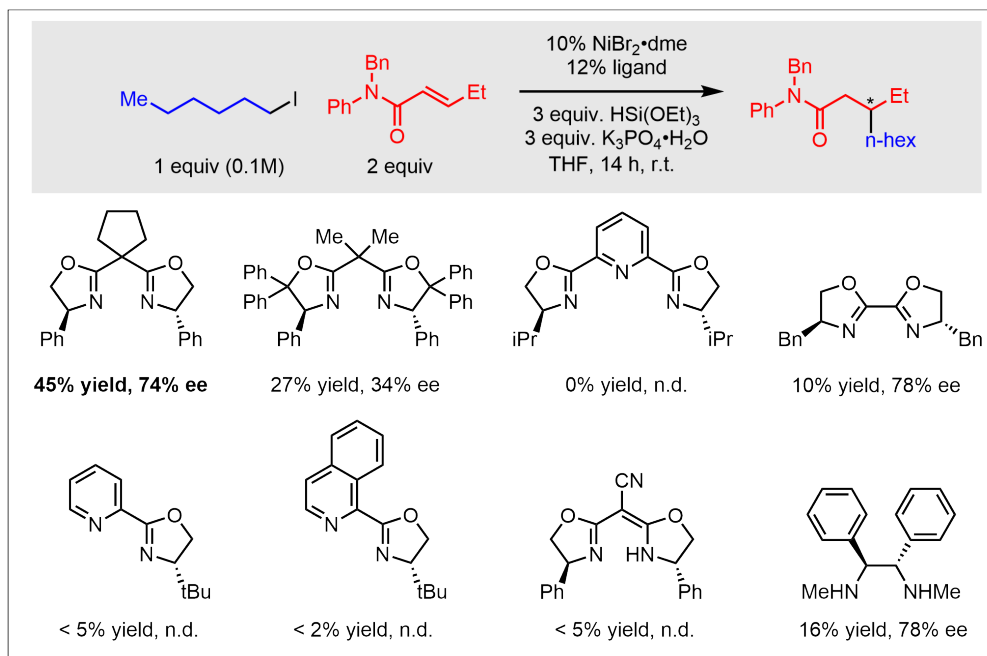


Figure 2.S1: Initial broad ligand screening for the enantioselective, regioselective alkylation of internal olefins.

Incompatible Substrates

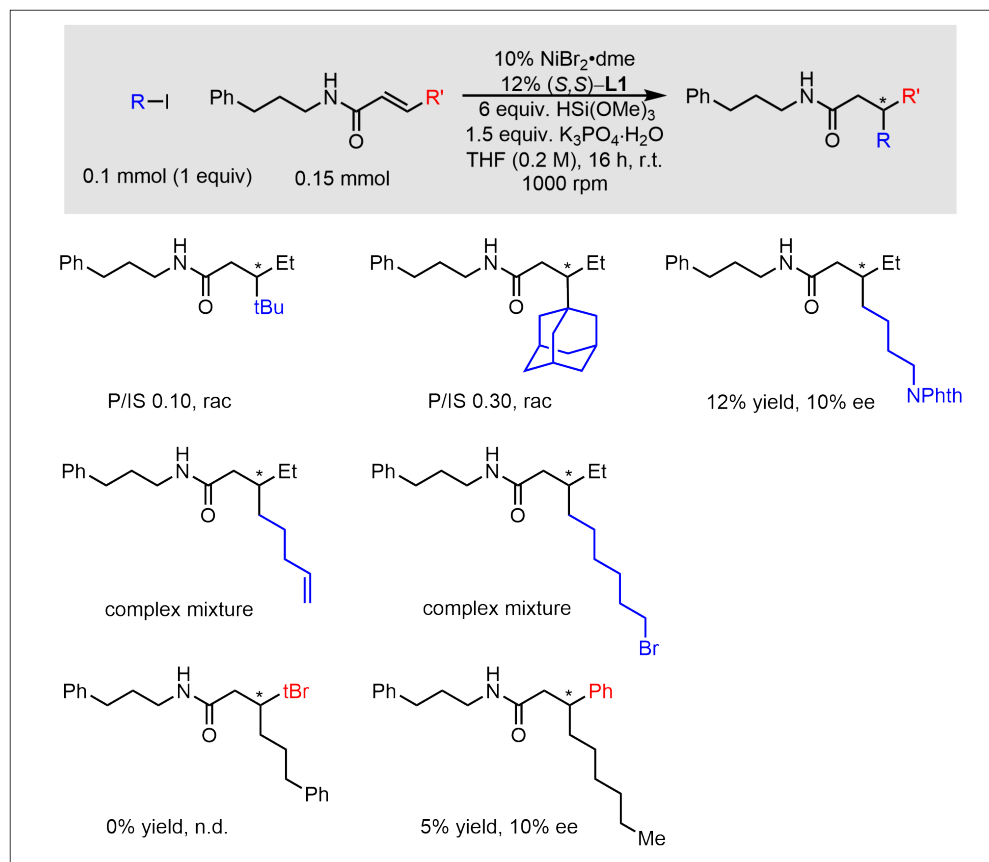


Figure 2.S2: Failed electrophiles for the enantioselective, regioselective alkylation of internal olefins.

Investigation of the Catalytic Resting State

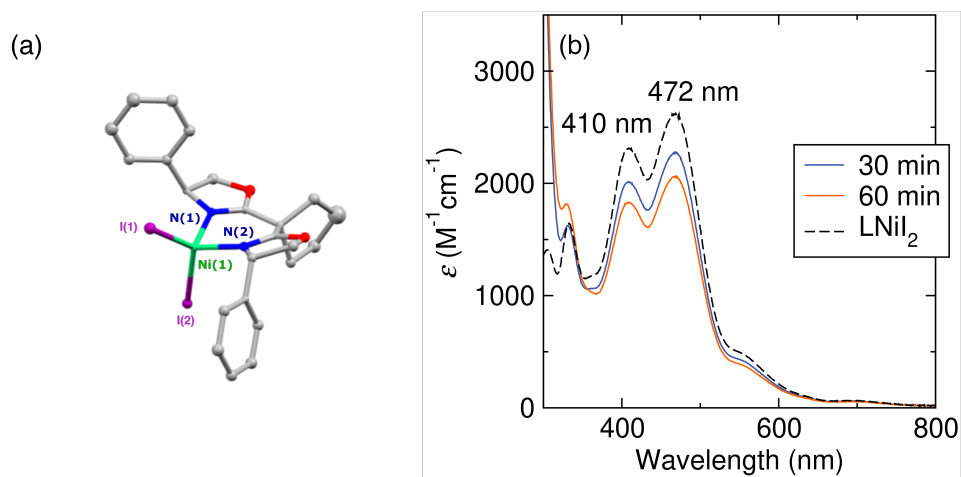


Figure 2.S3: (a) X-ray crystal structure of X (connectivity only; hydrogens and additional solvent molecules in the asymmetric unit are omitted for clarity). (b) UV-vis of X and the catalytic reaction resting state.

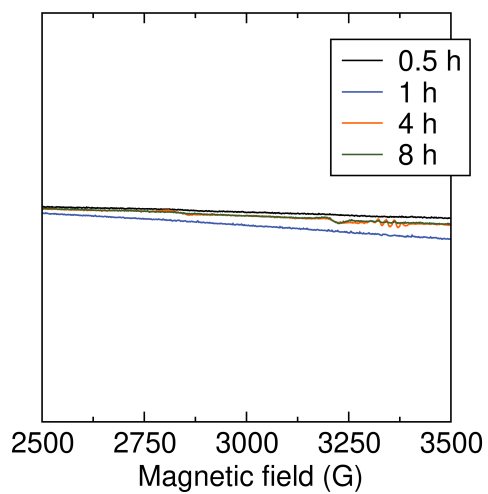
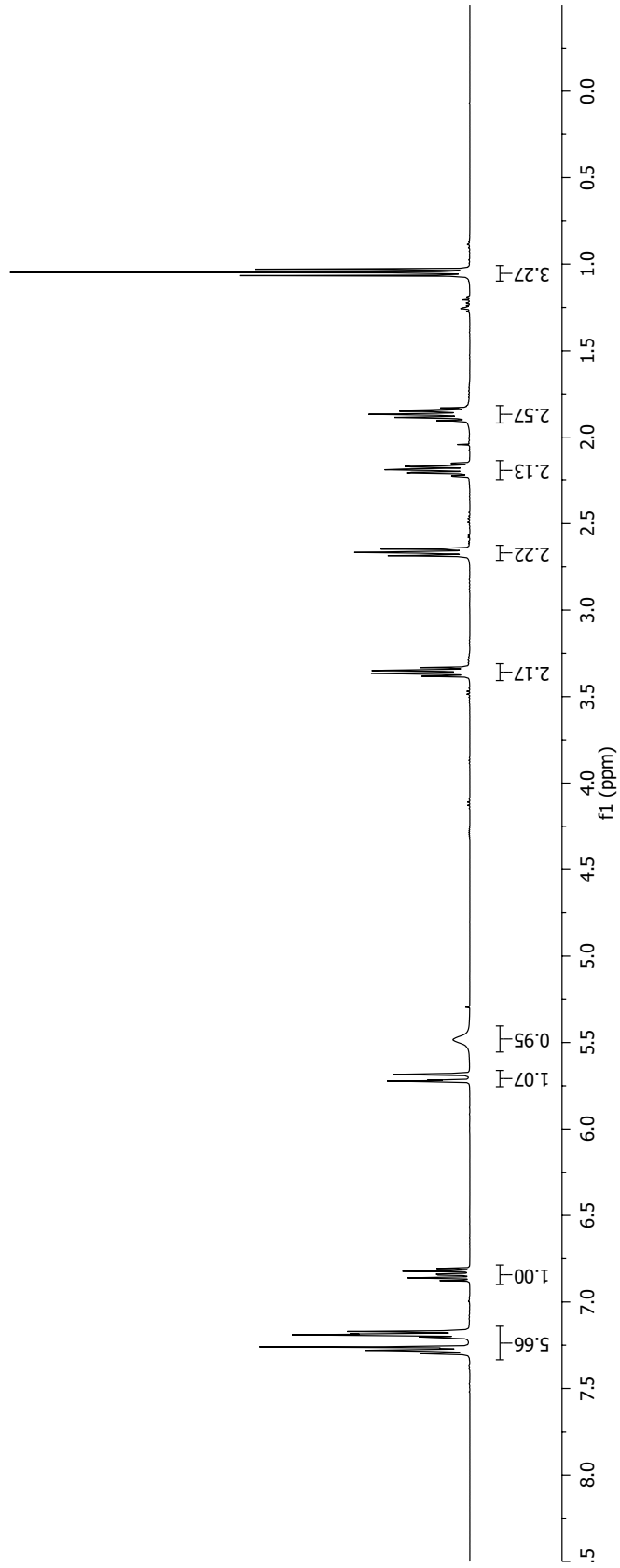
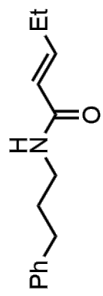
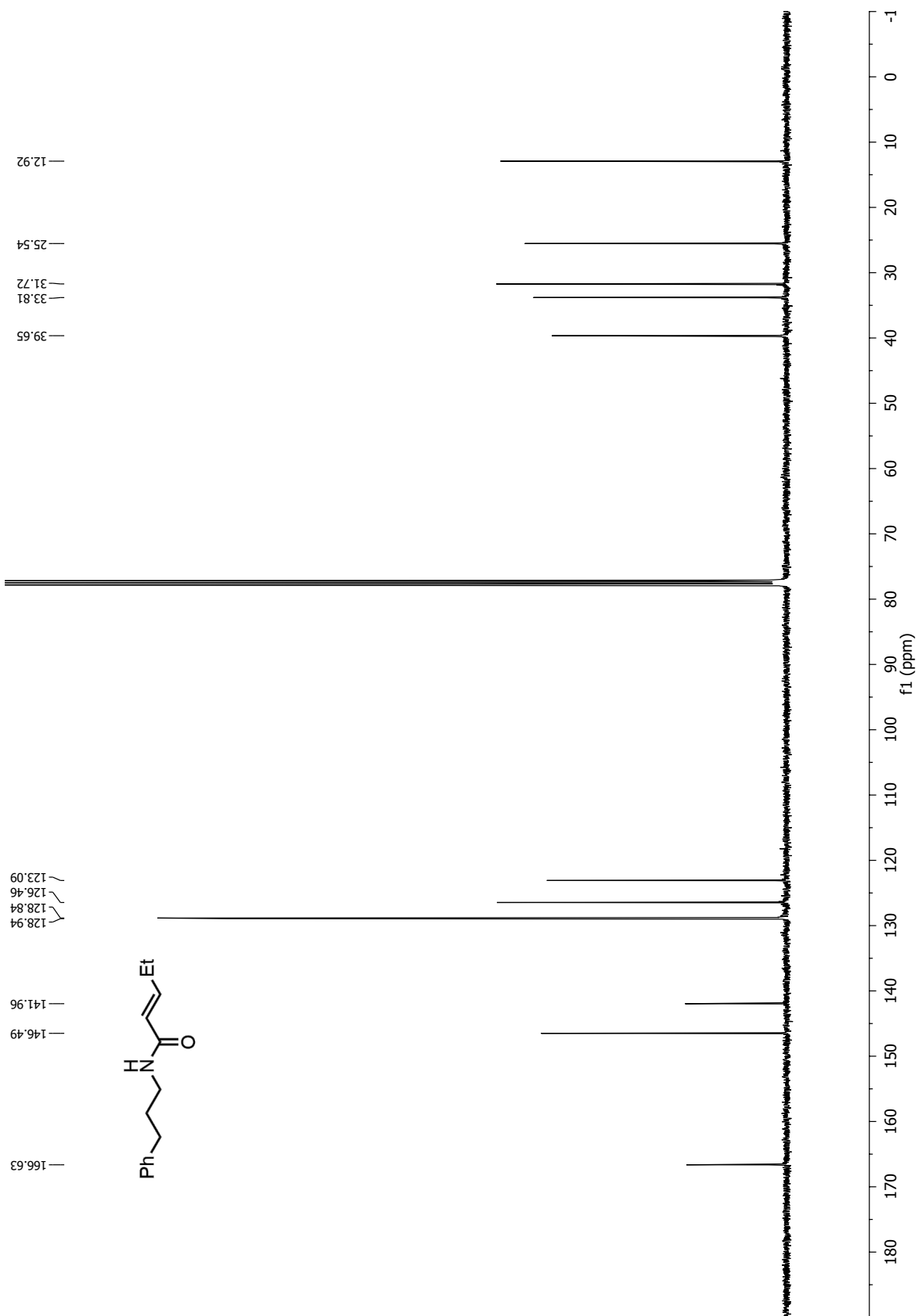
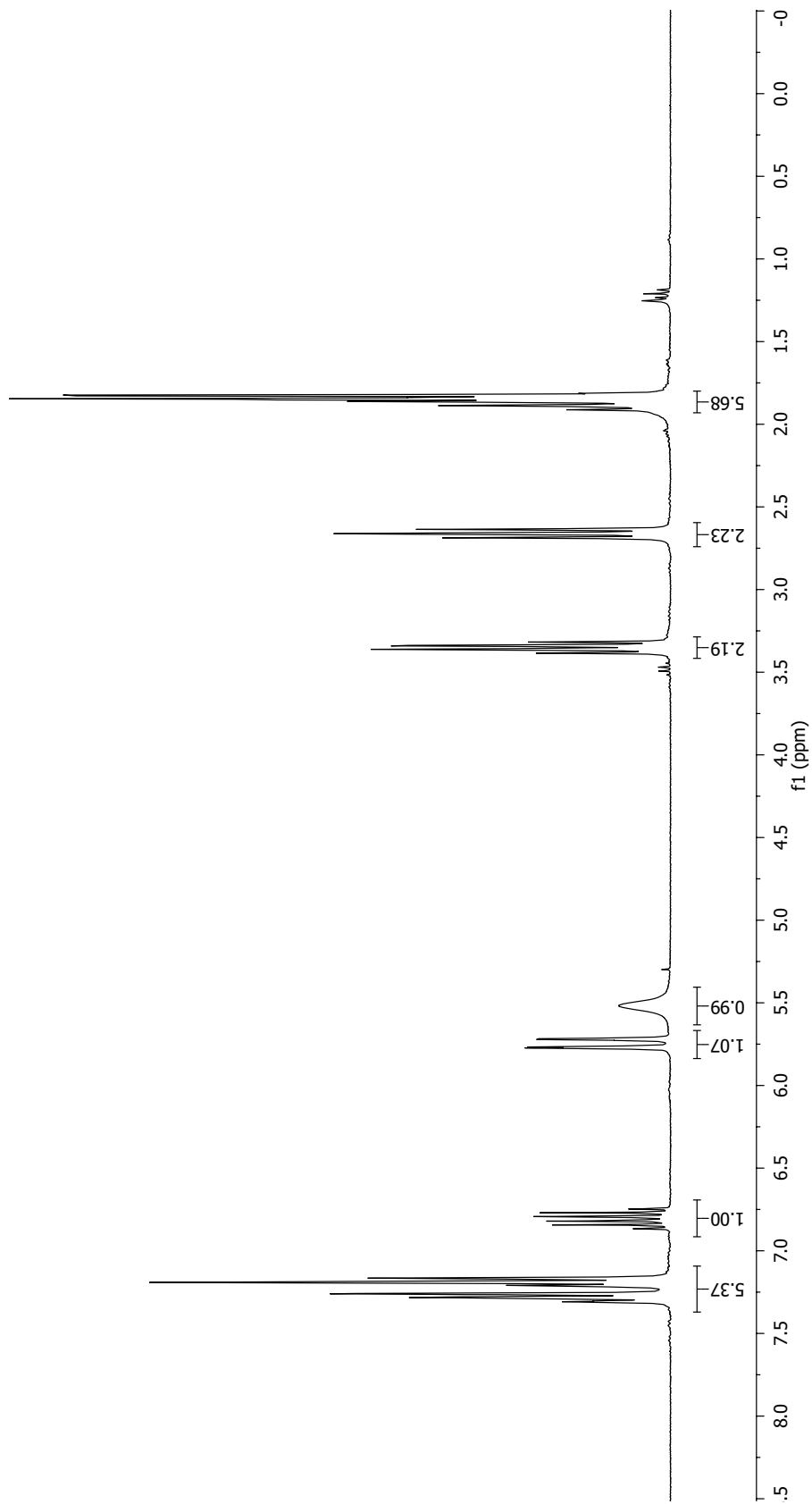
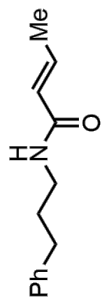
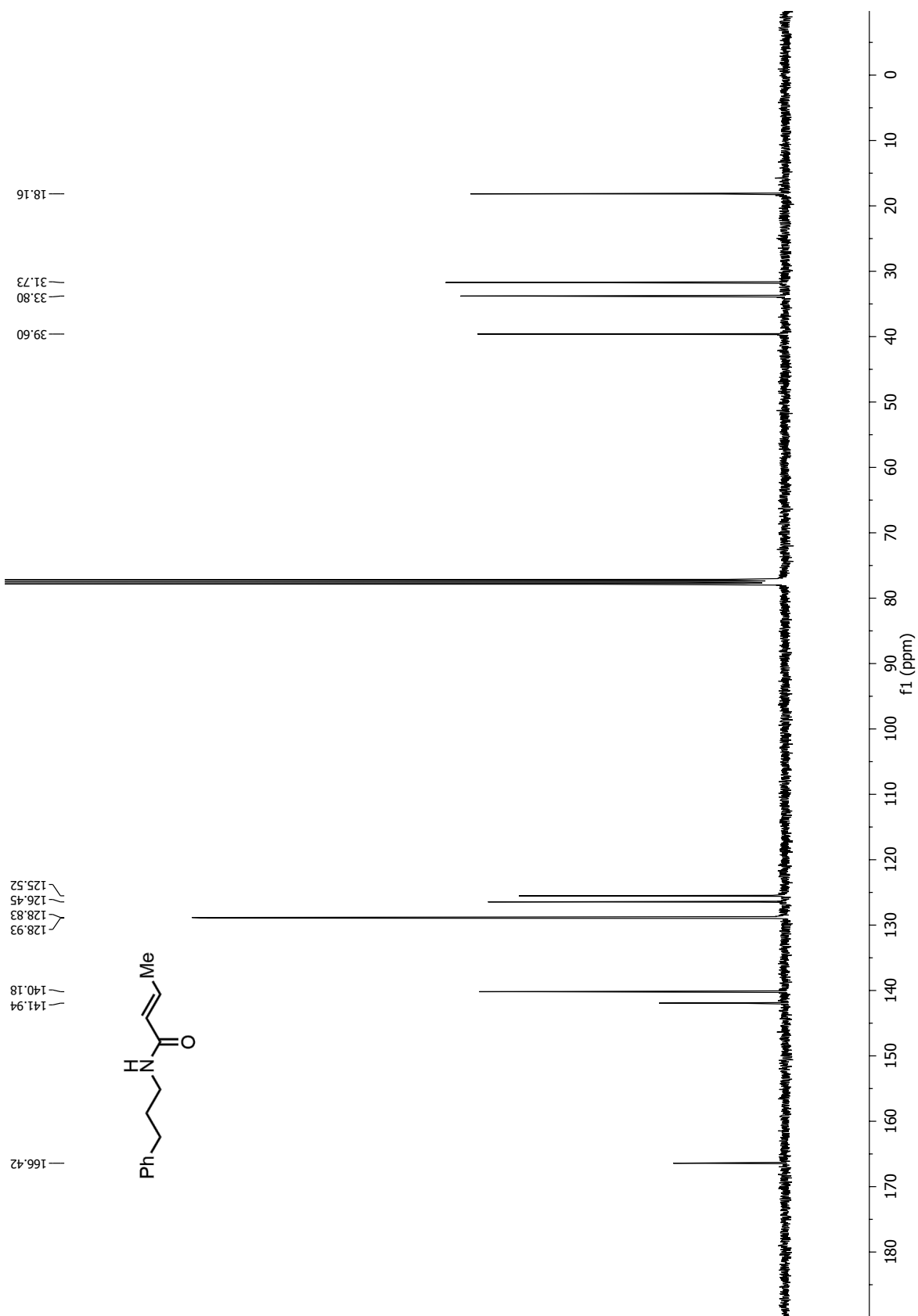


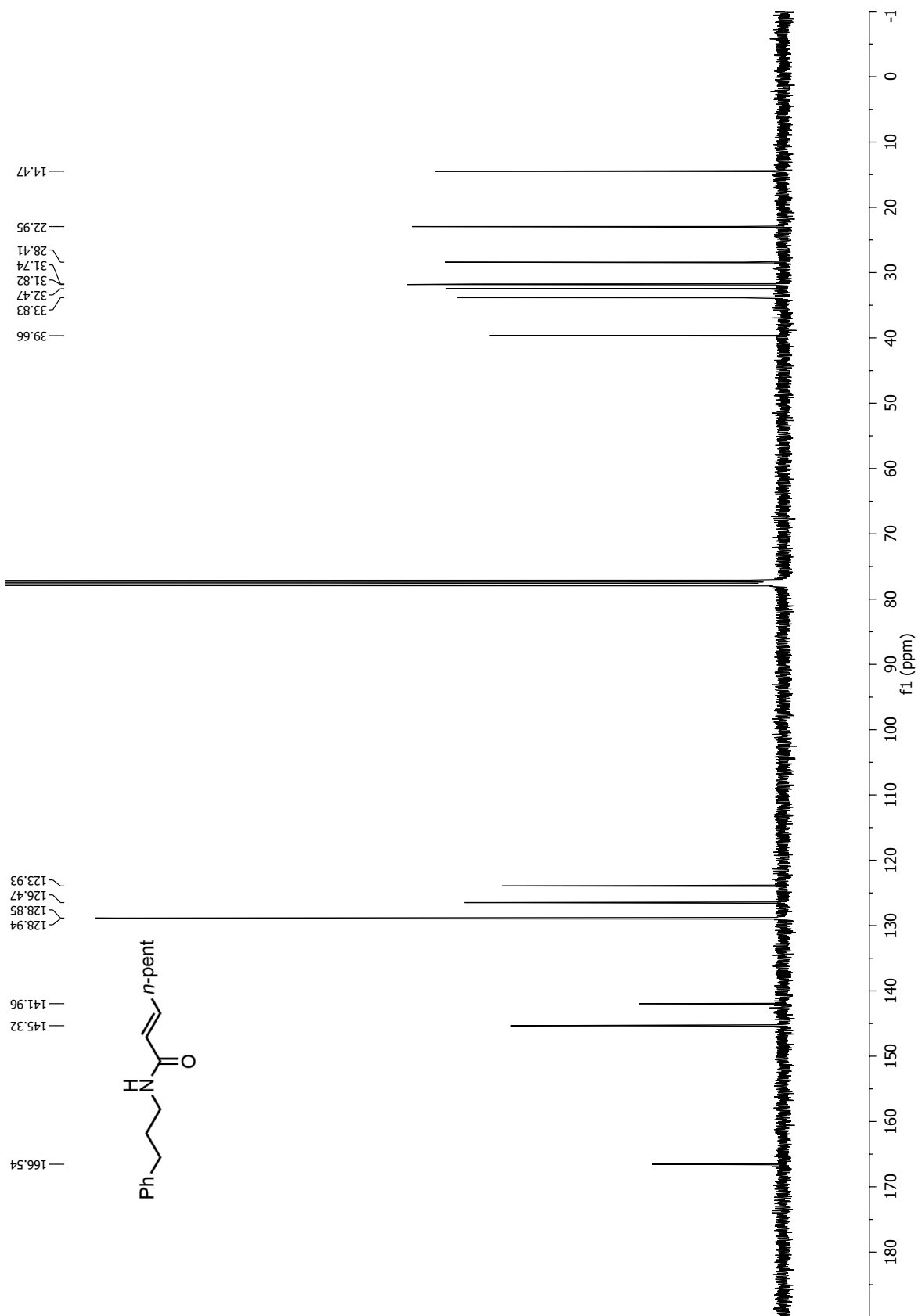
Figure 2.S4: X-band EPR spectra of the catalytic reaction at different time point collected at 77 K frozen THF.

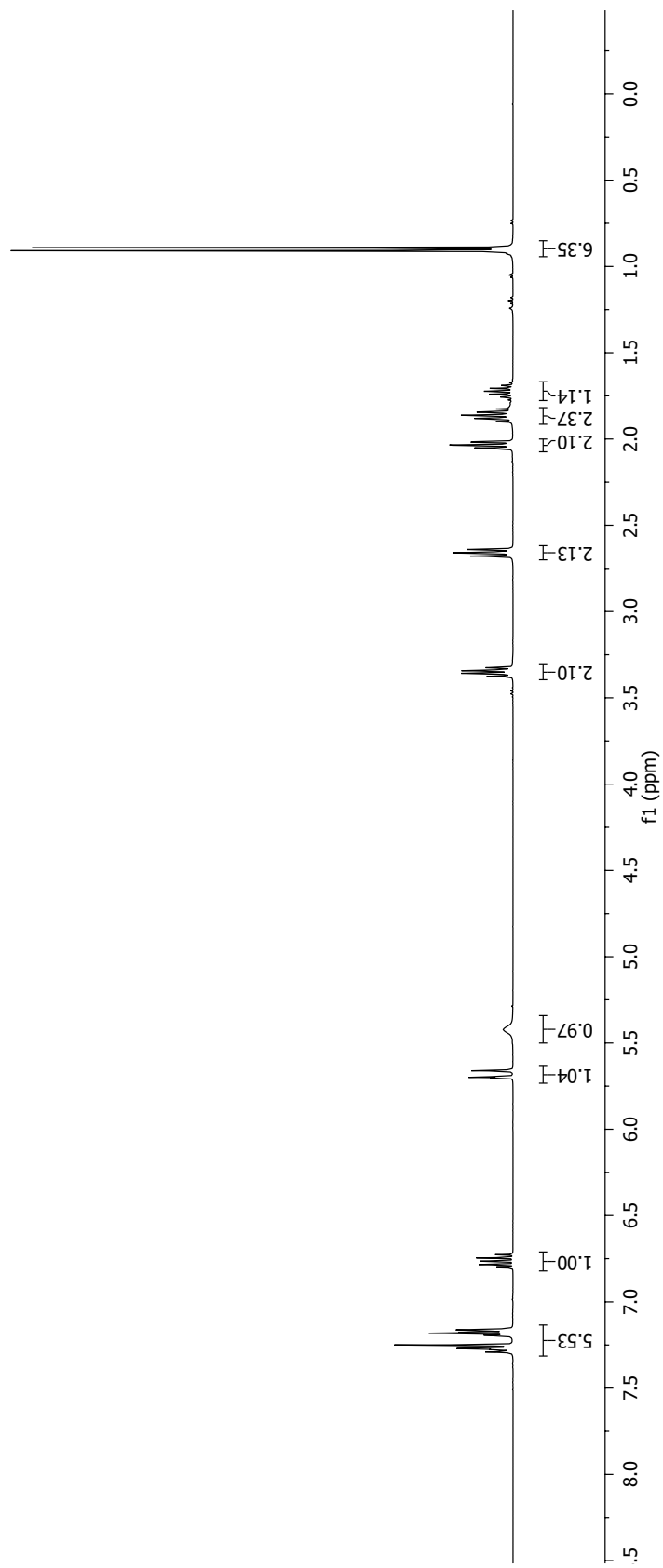
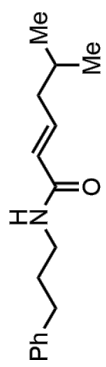


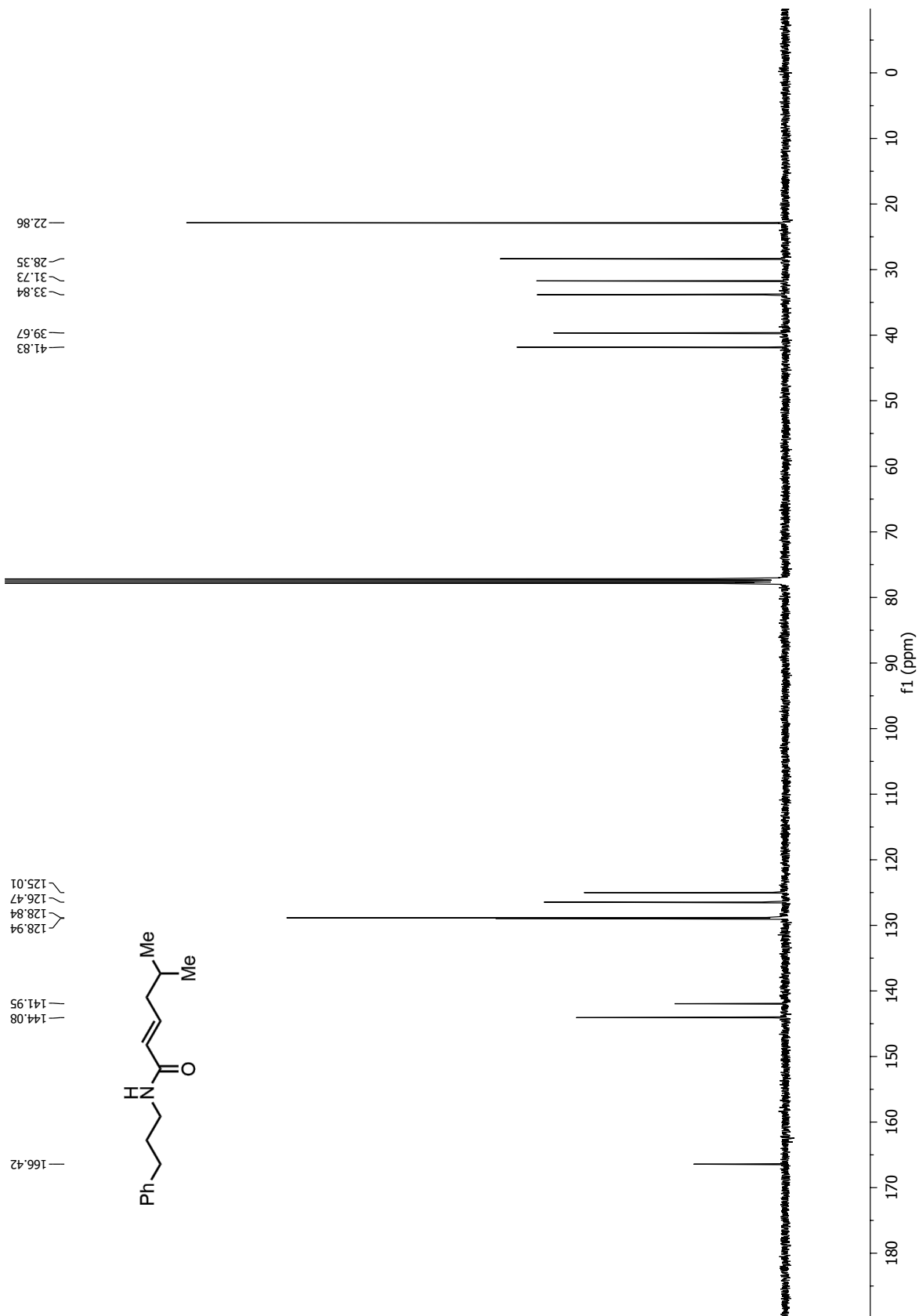


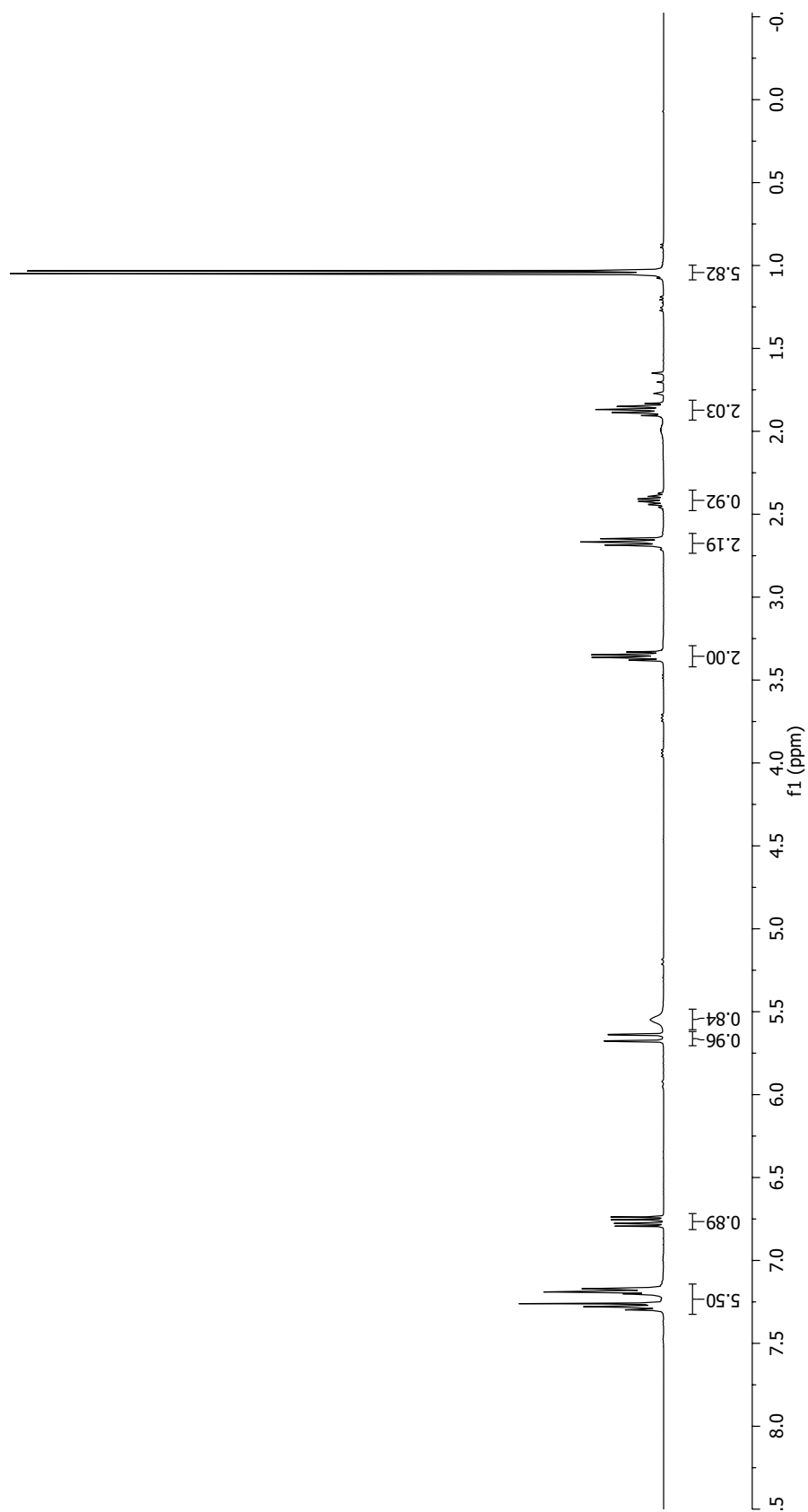
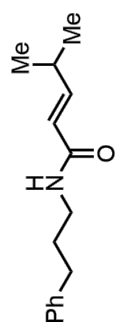


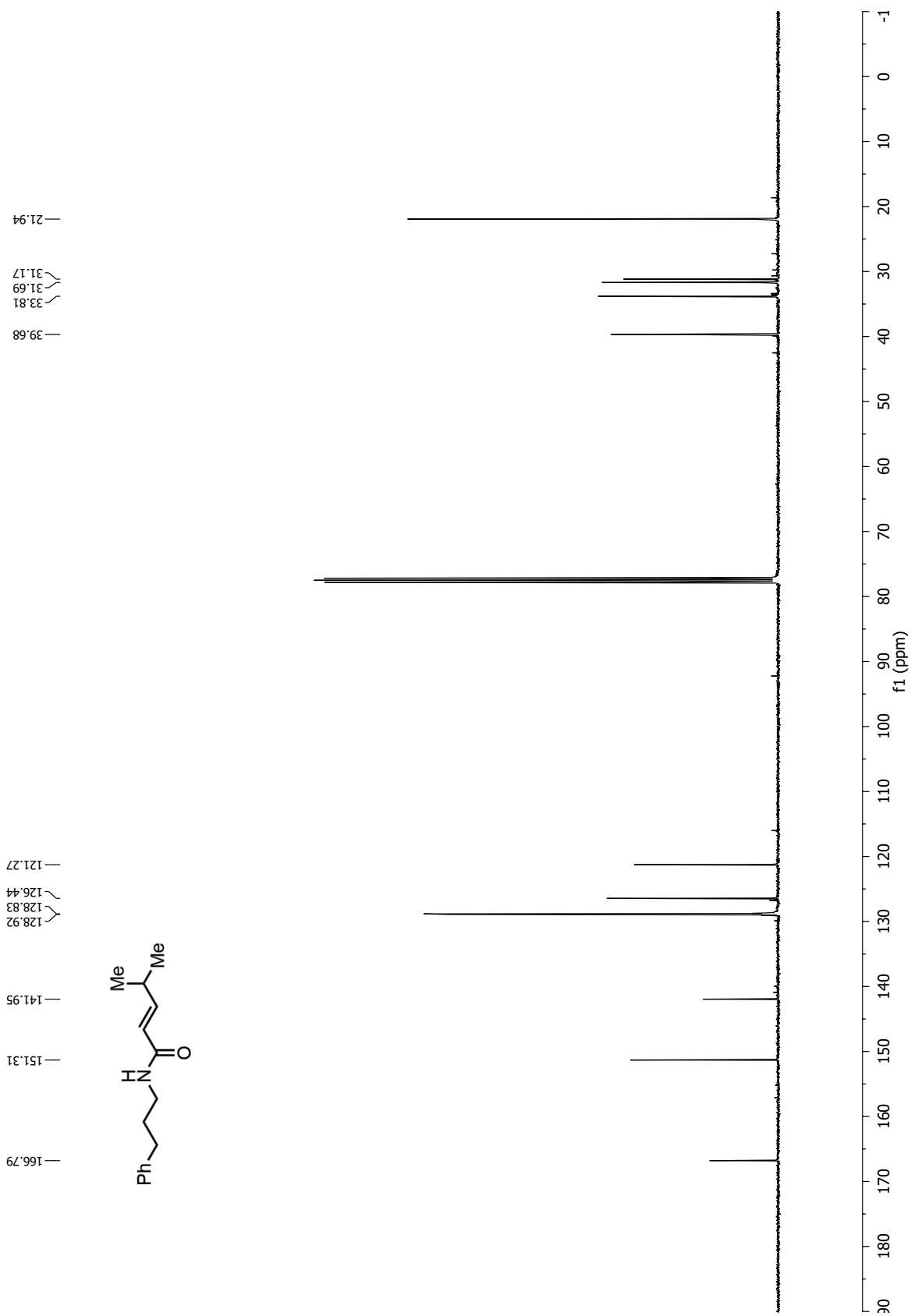


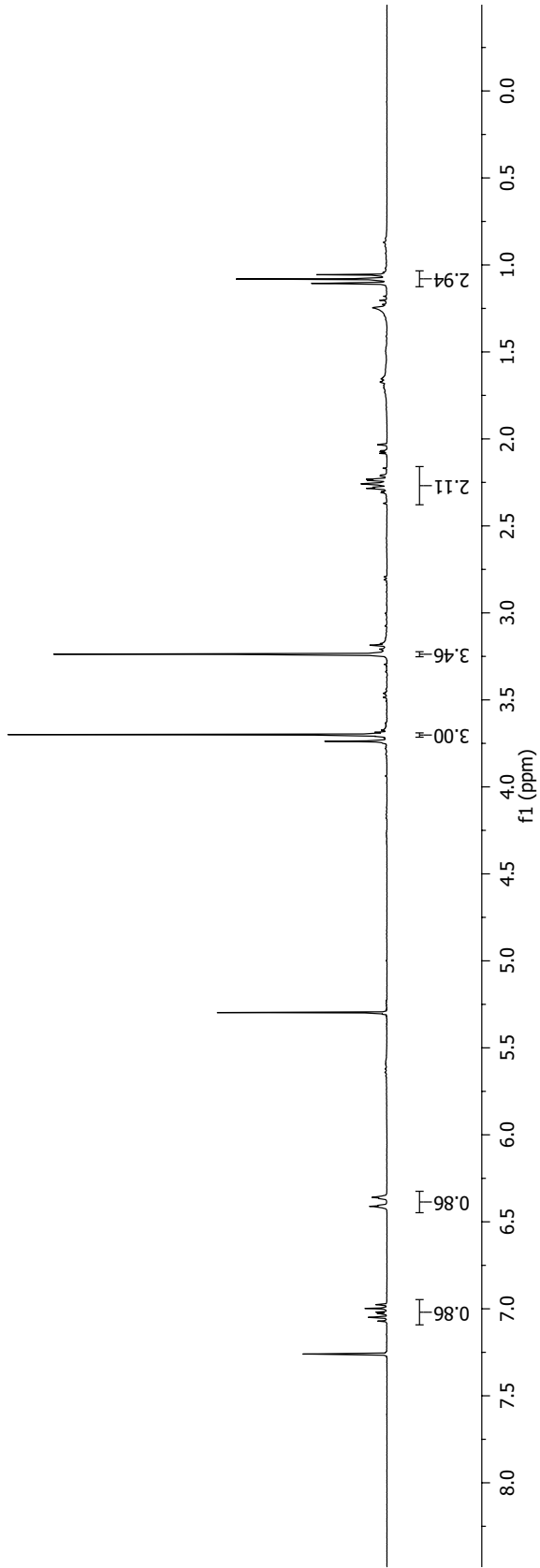
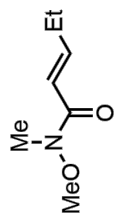


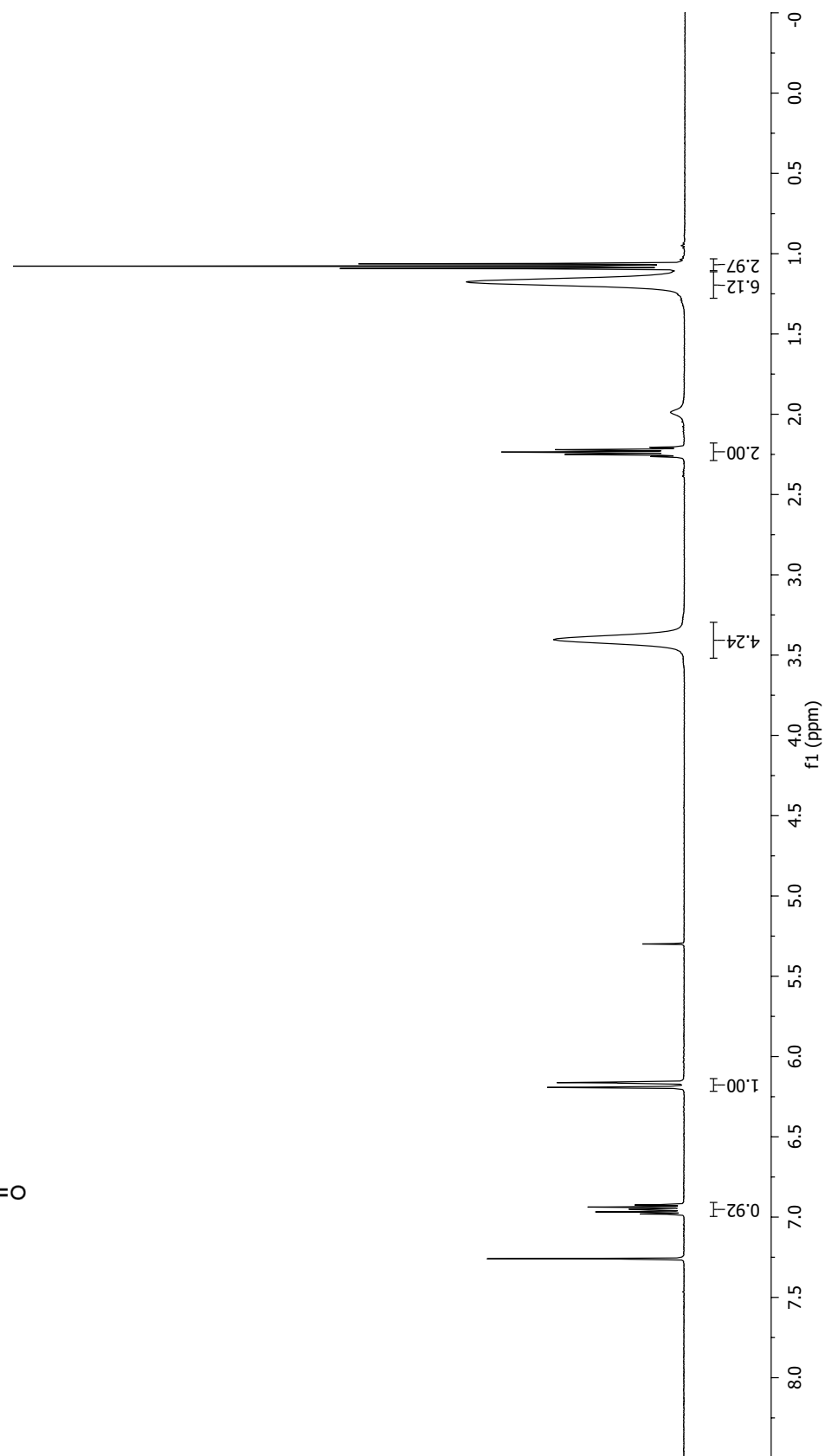
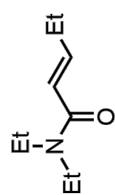


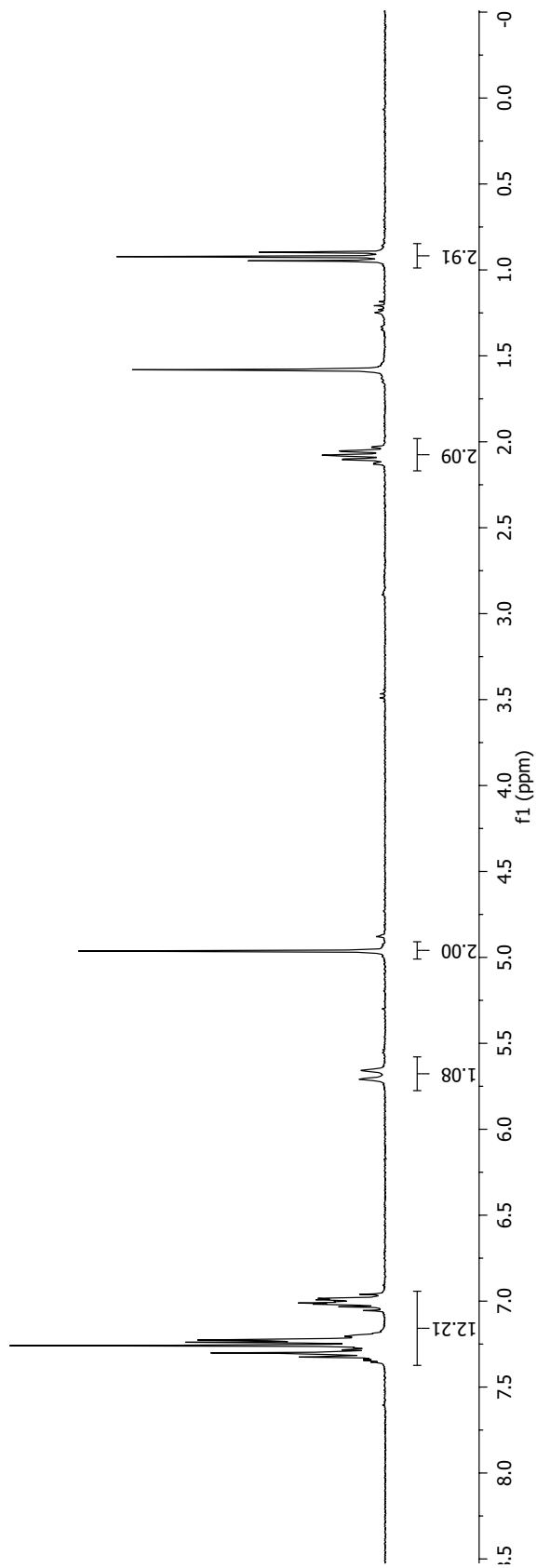
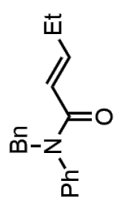


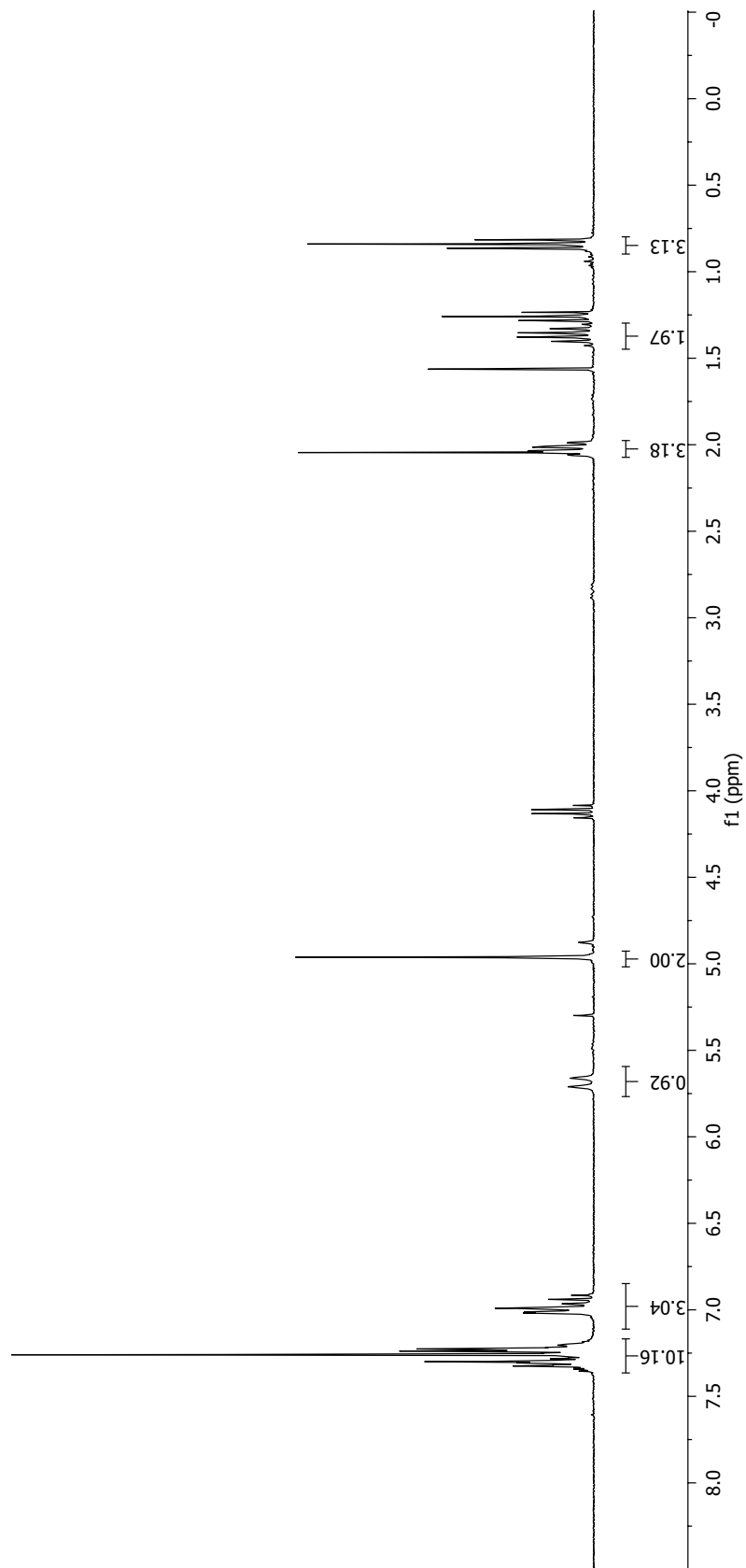
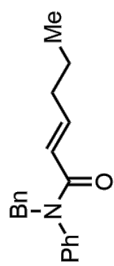


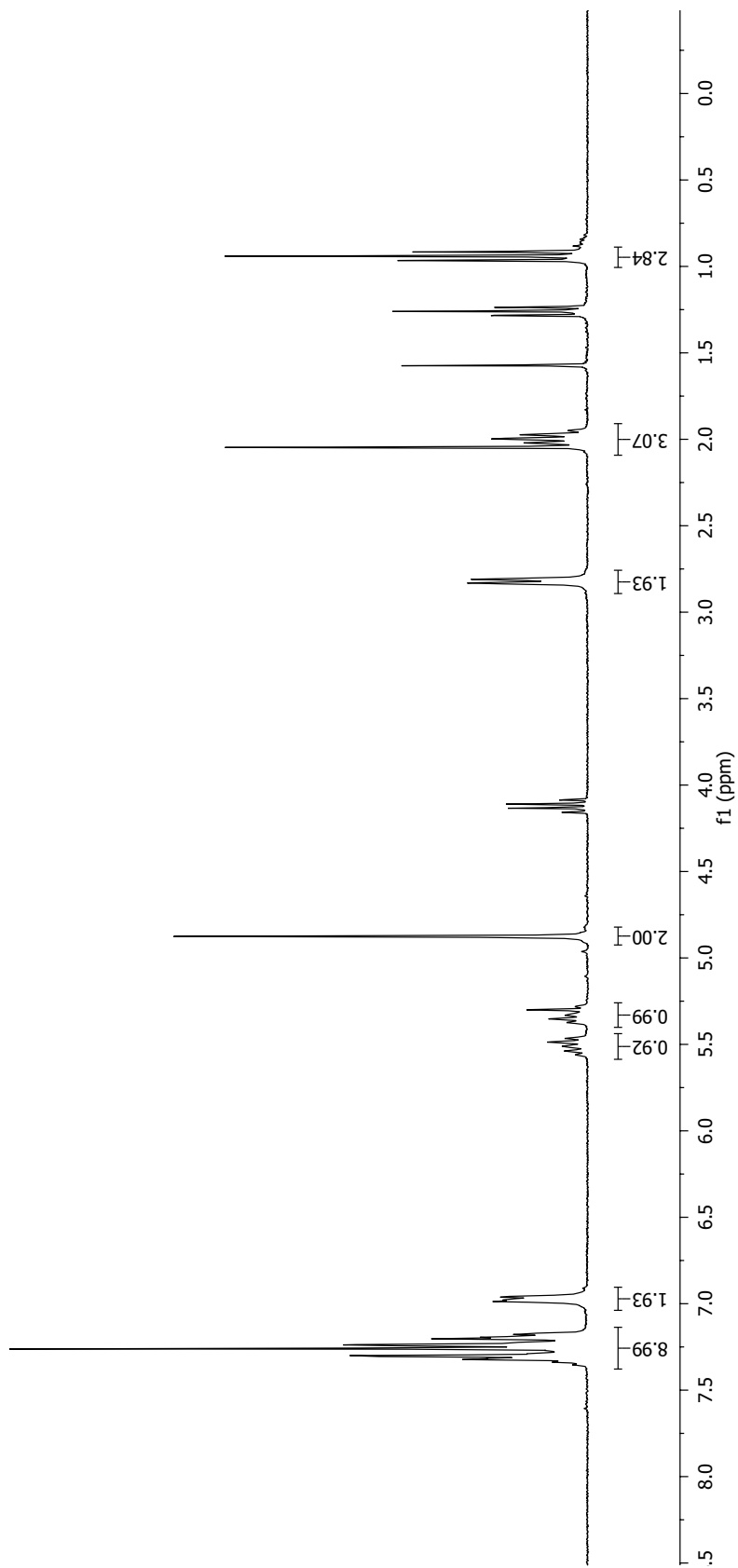
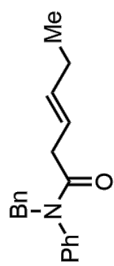


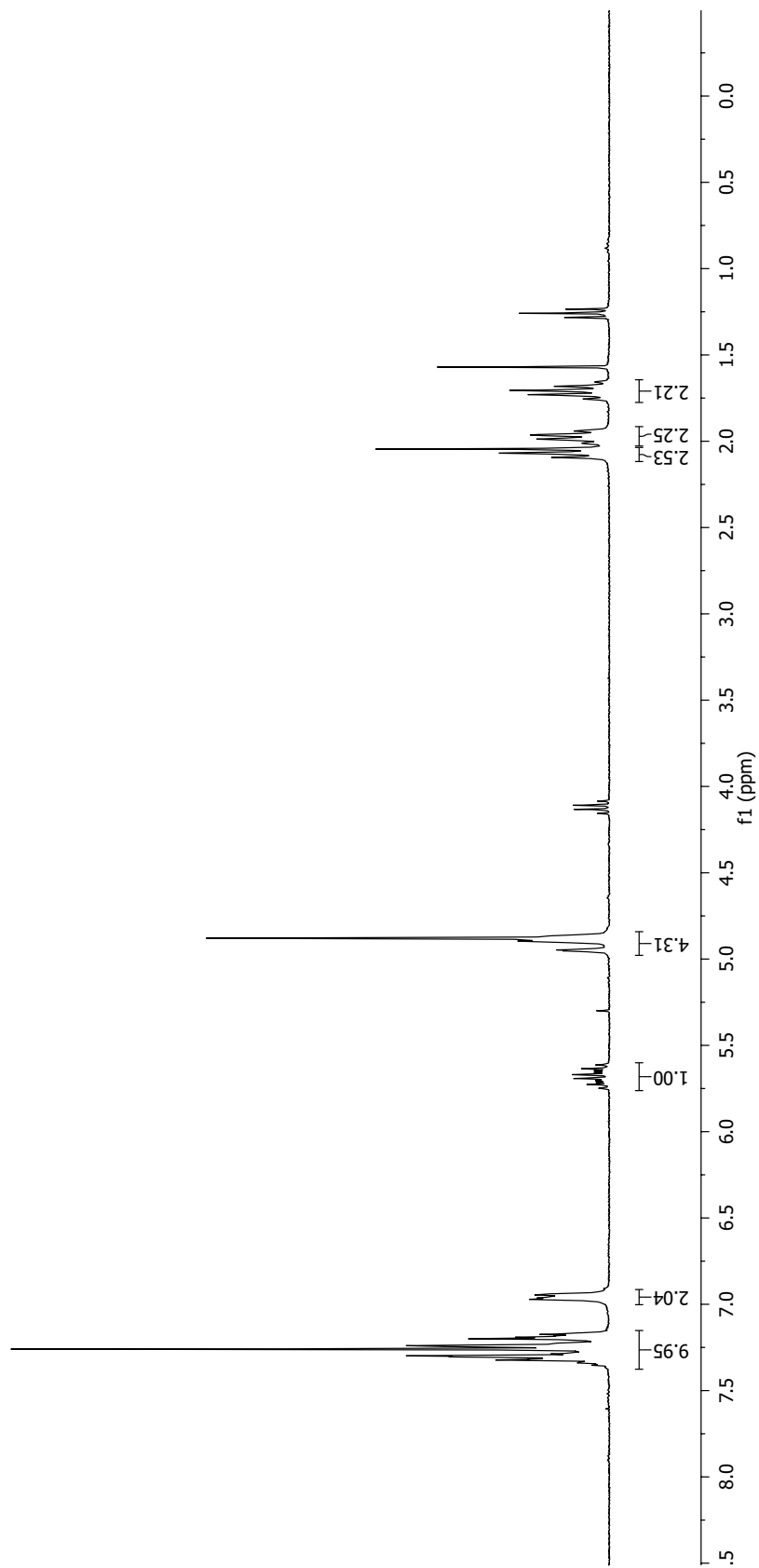
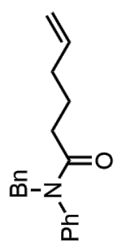


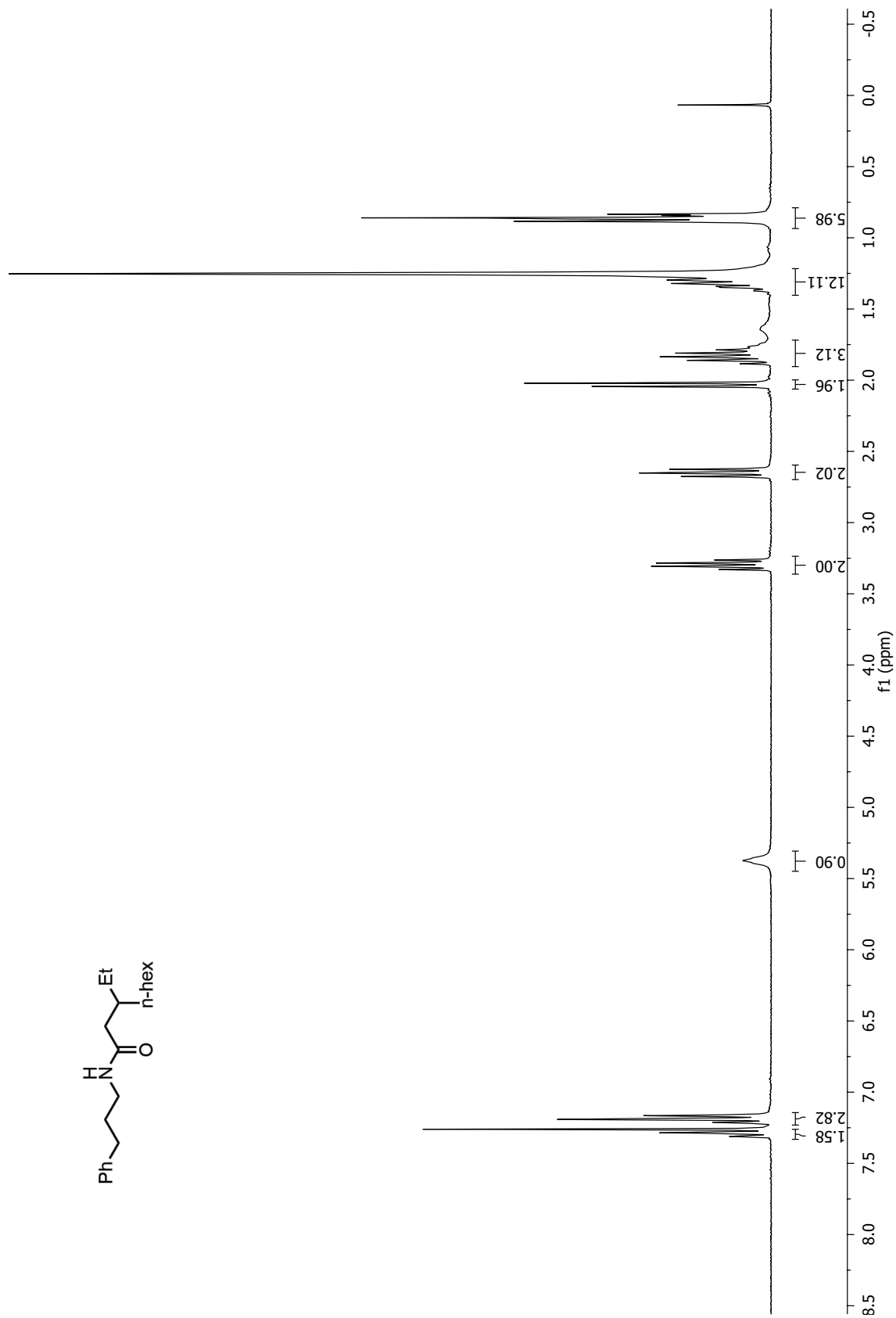


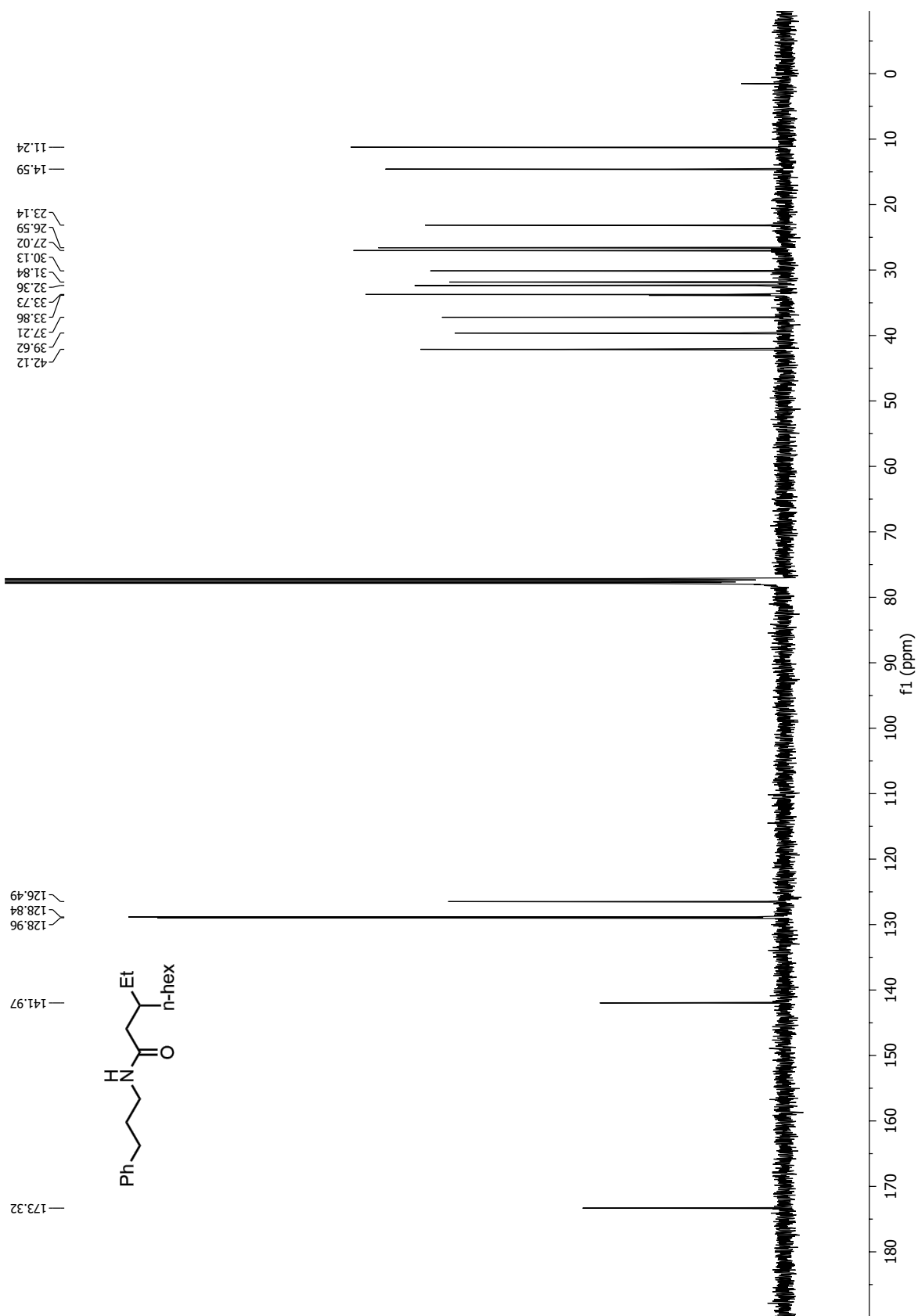


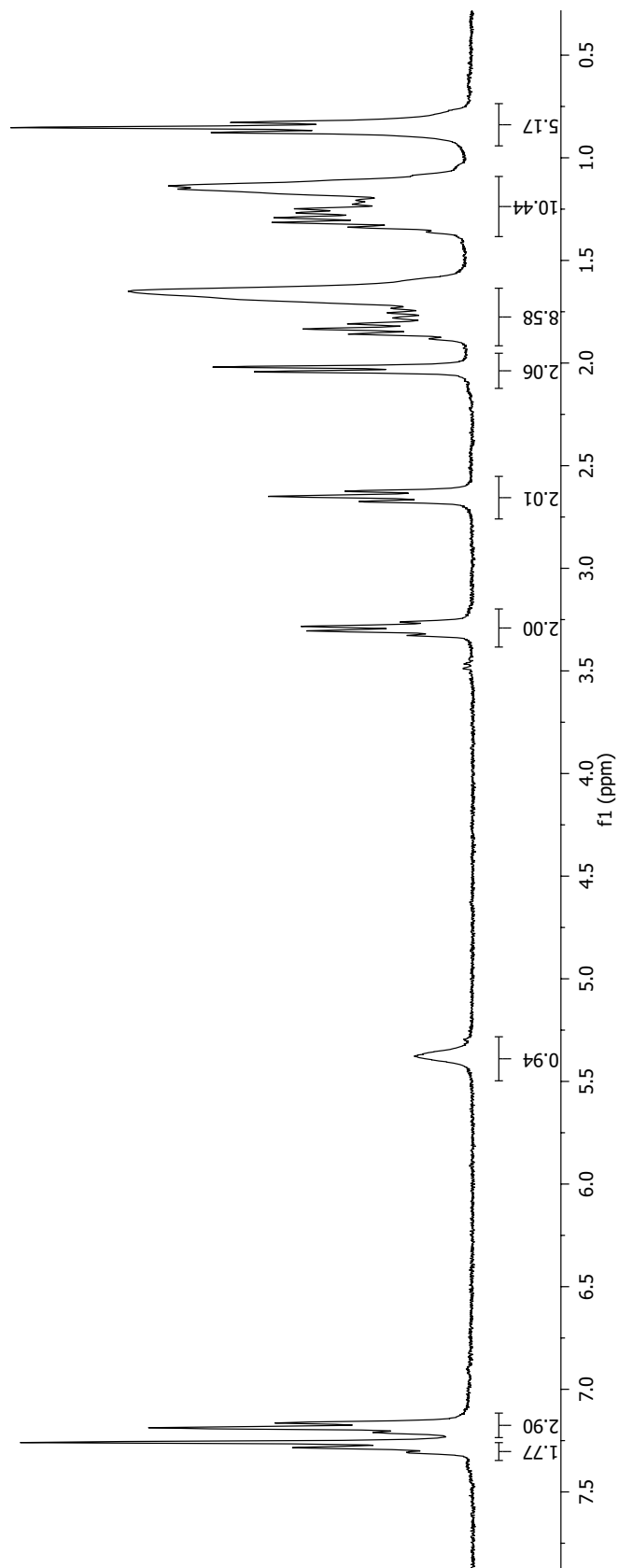
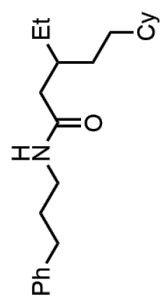


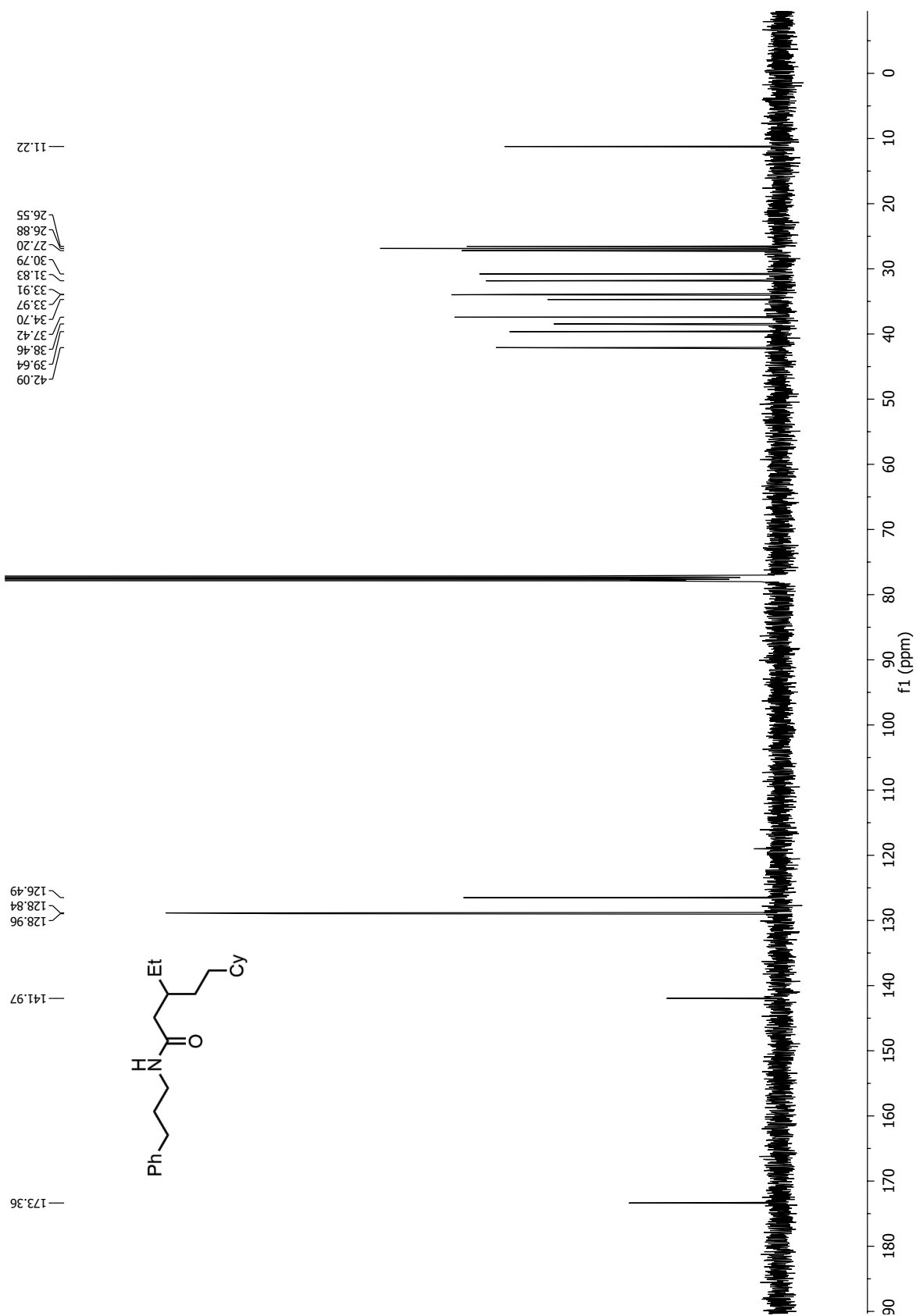


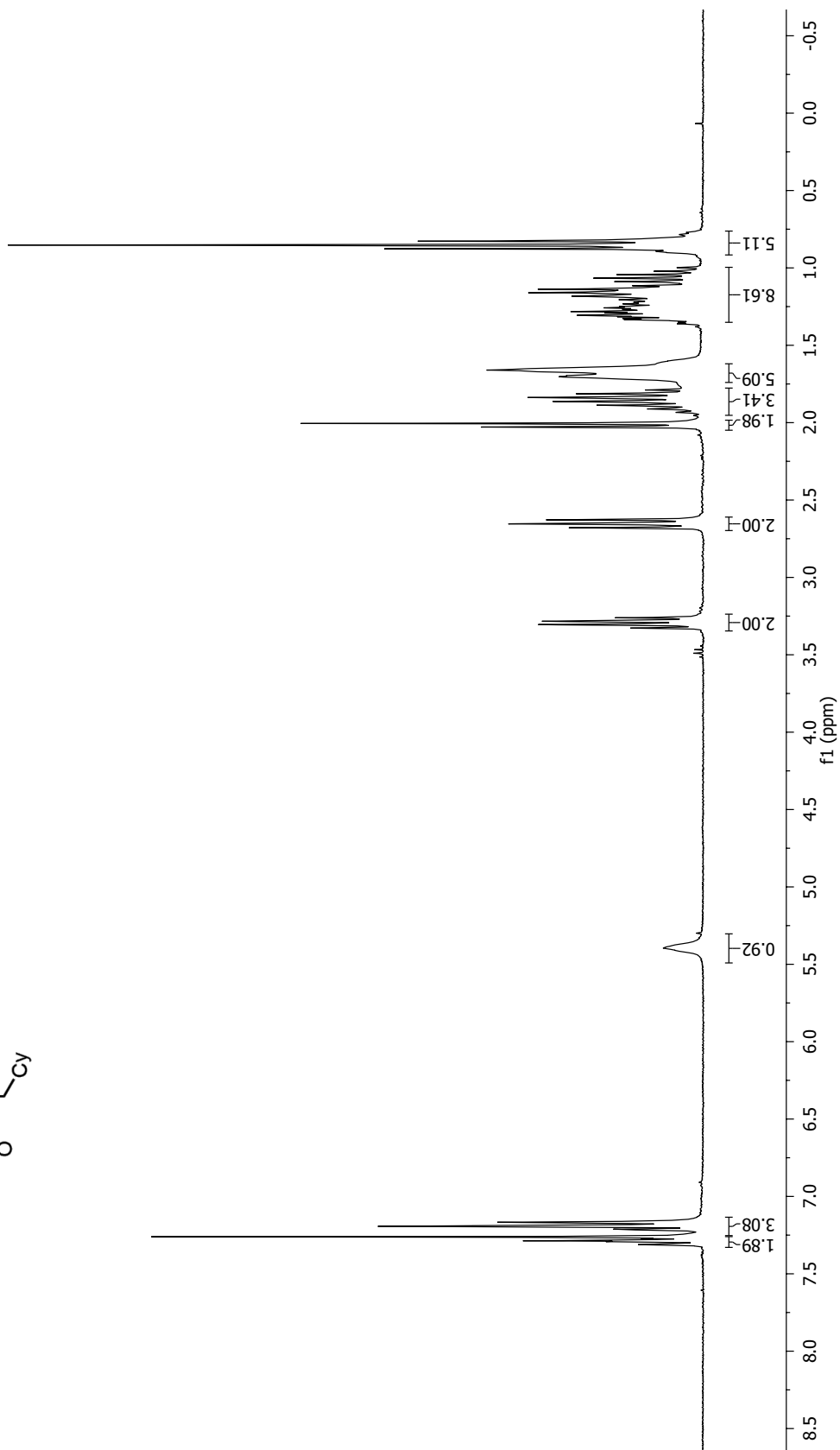
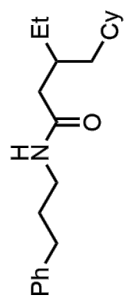


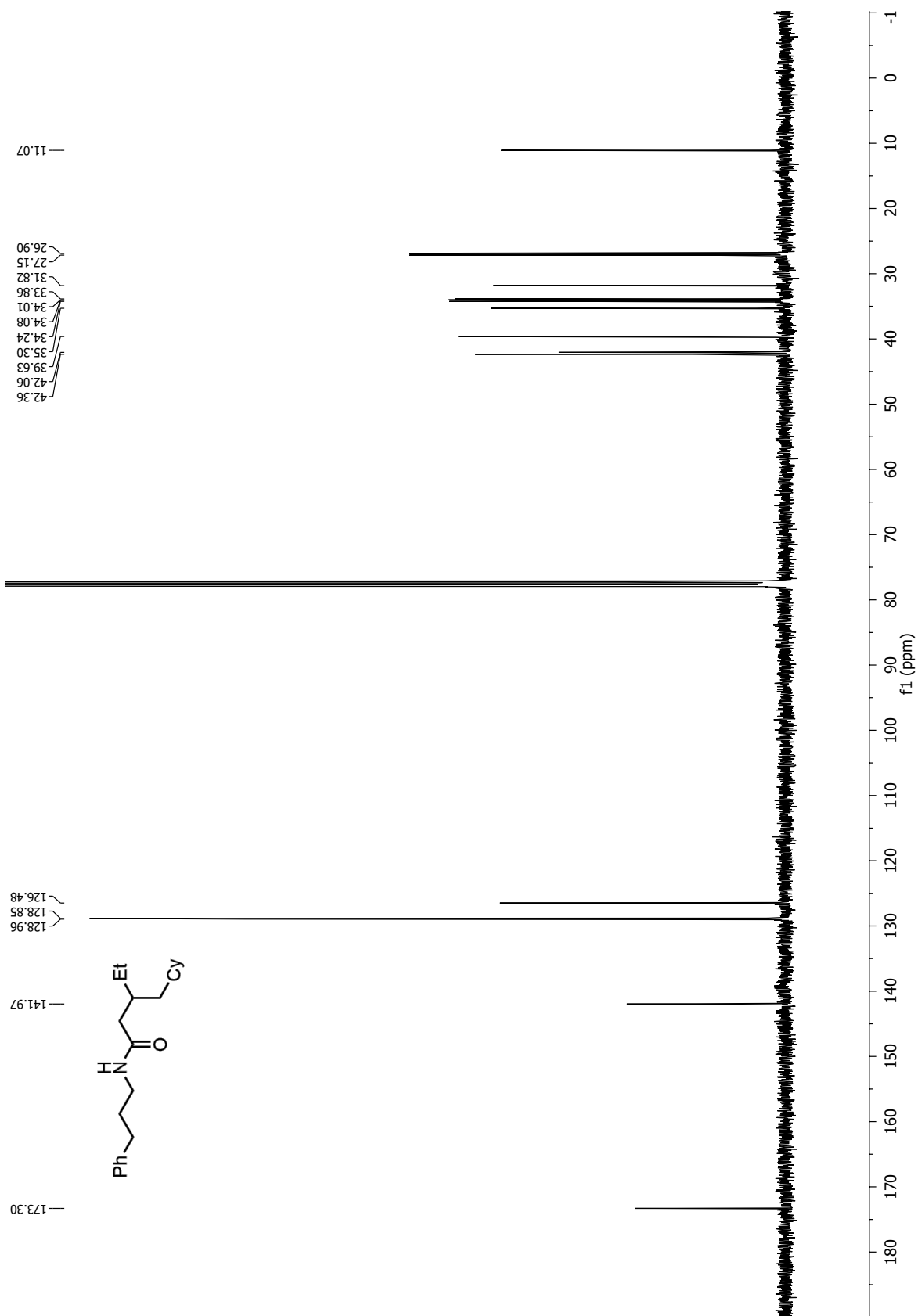


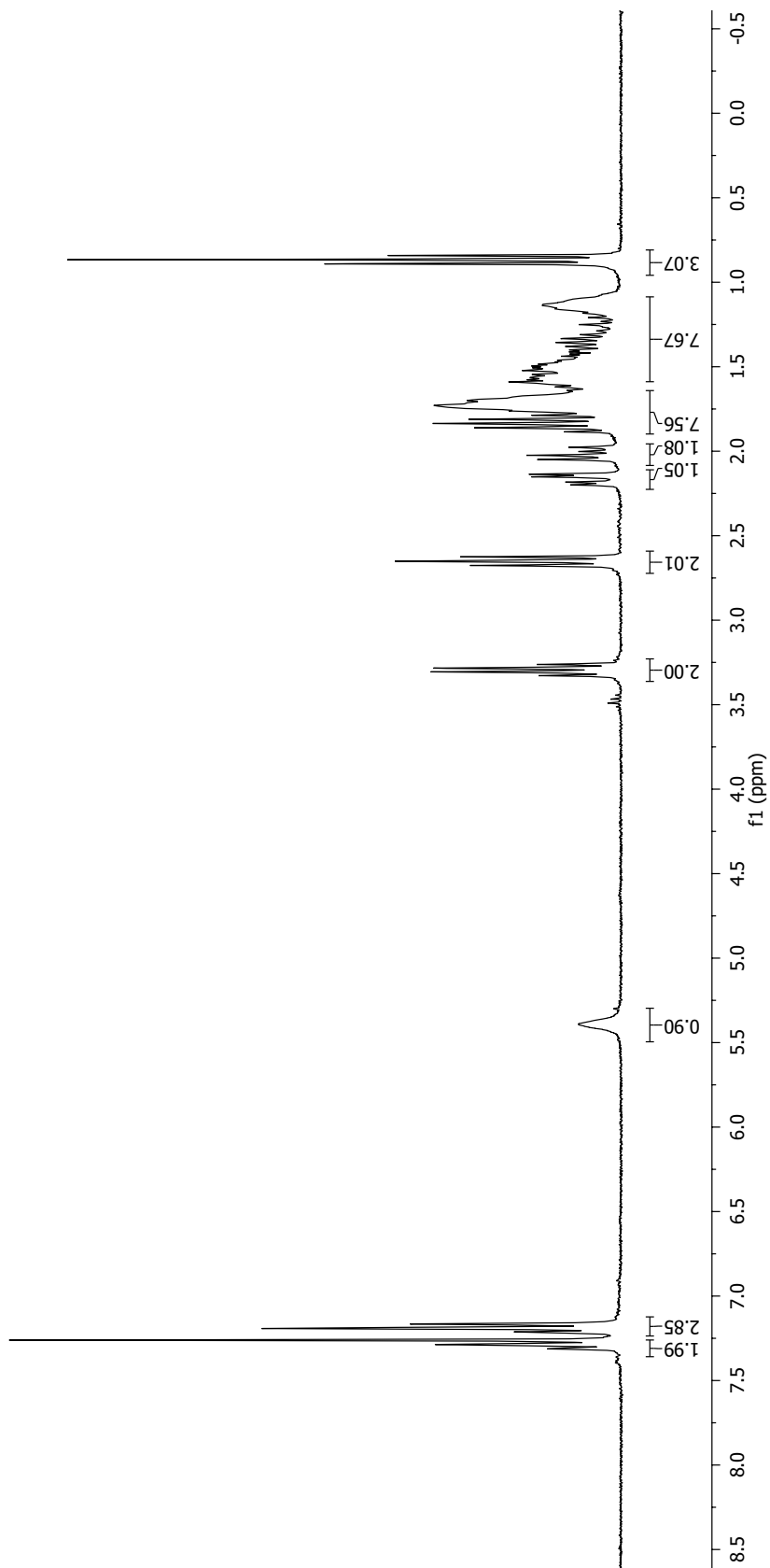
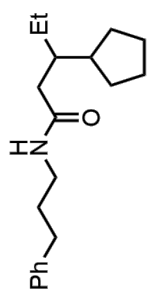


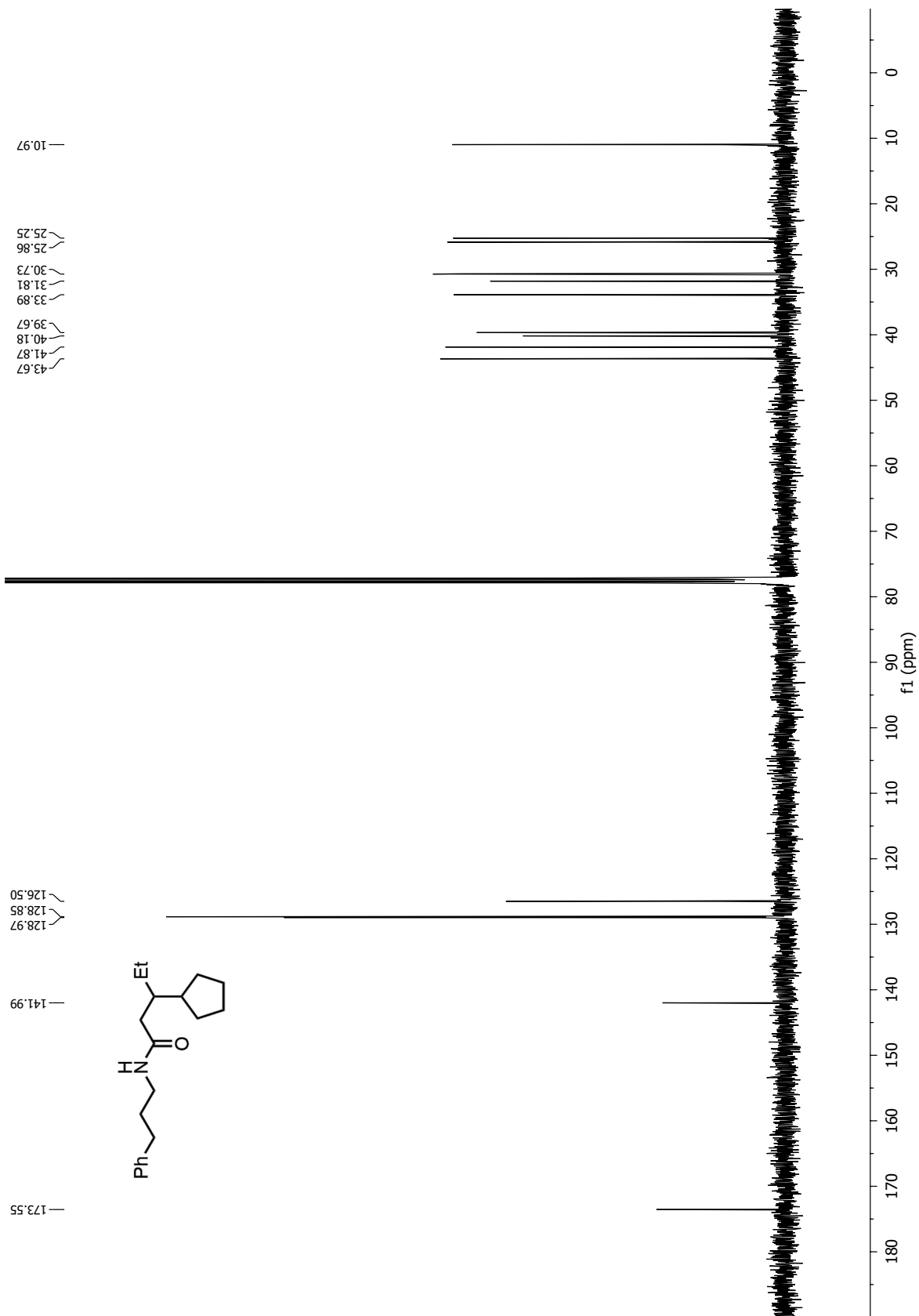


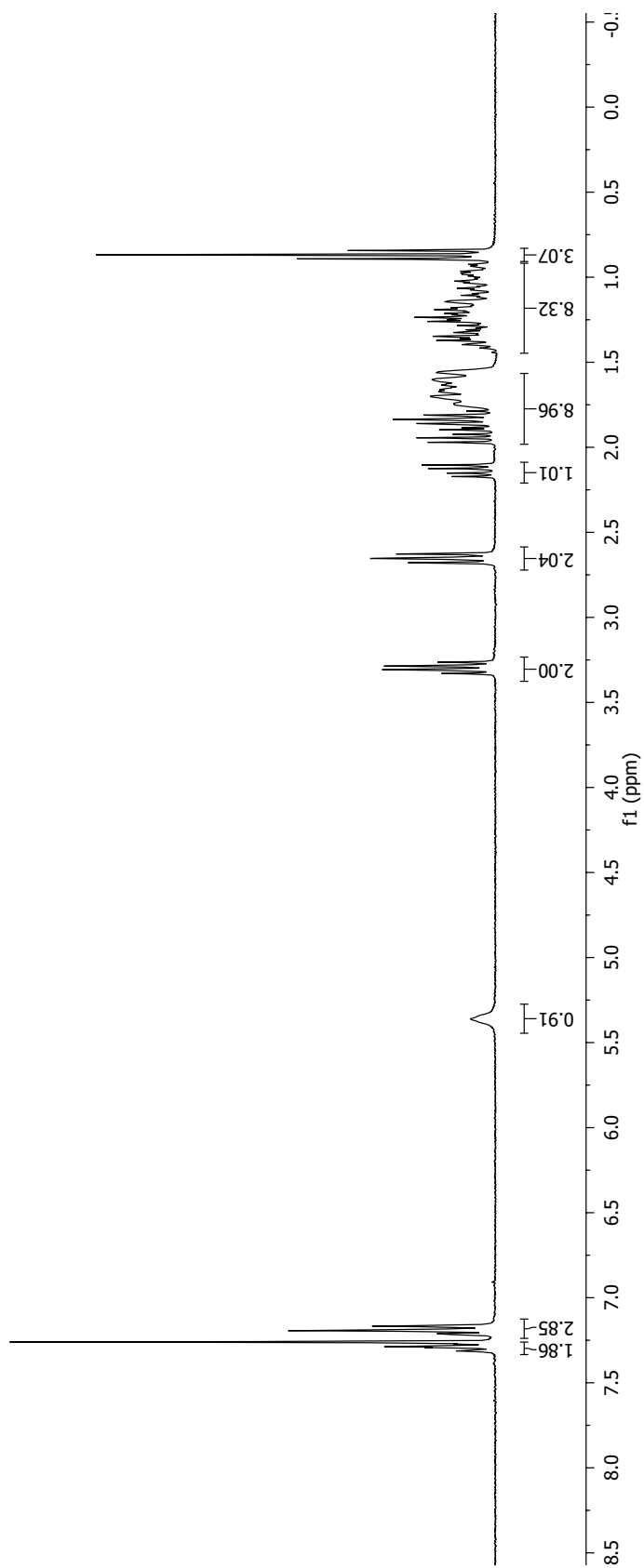
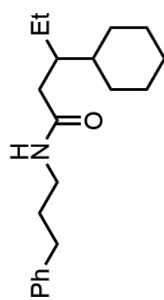


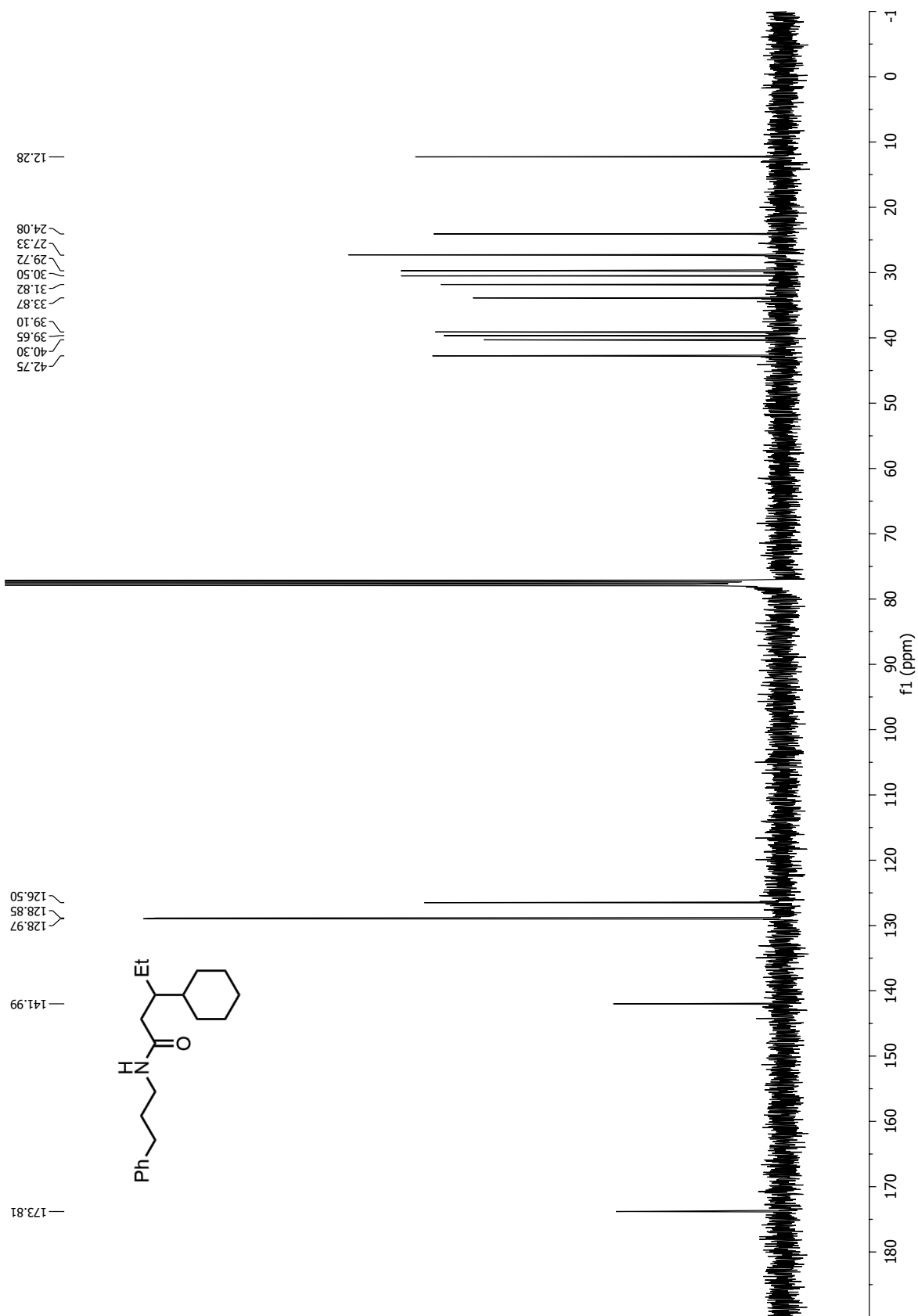


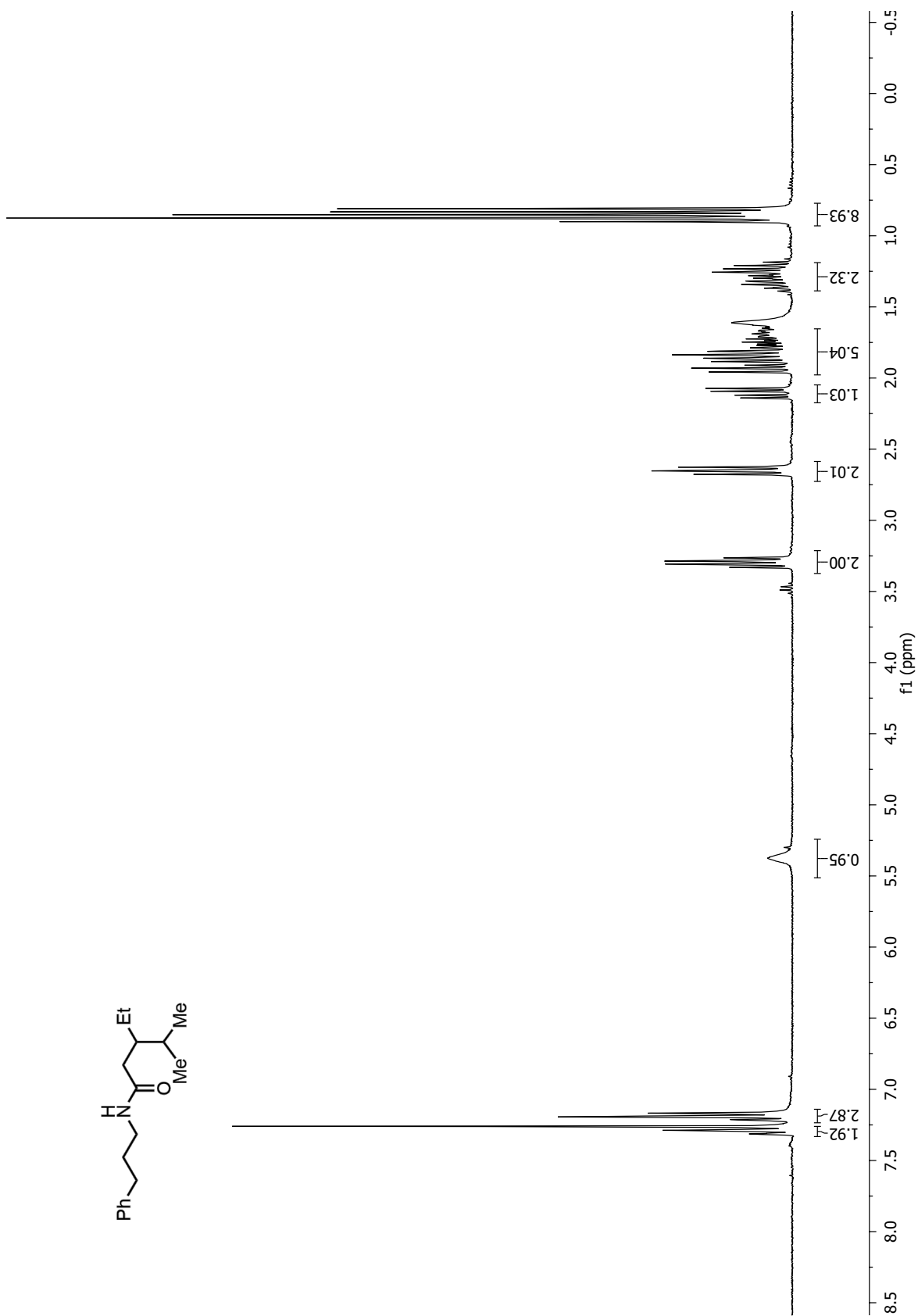


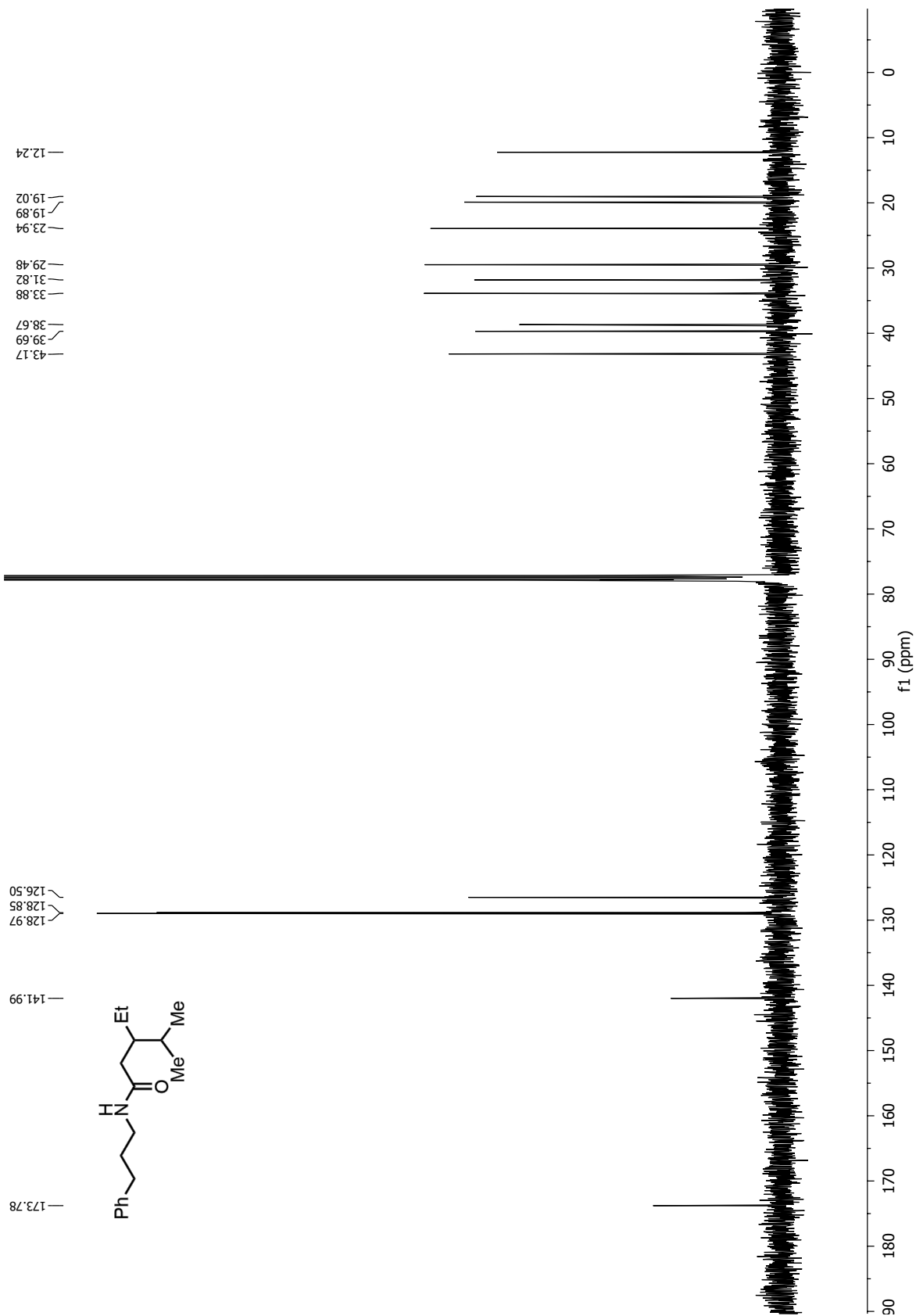


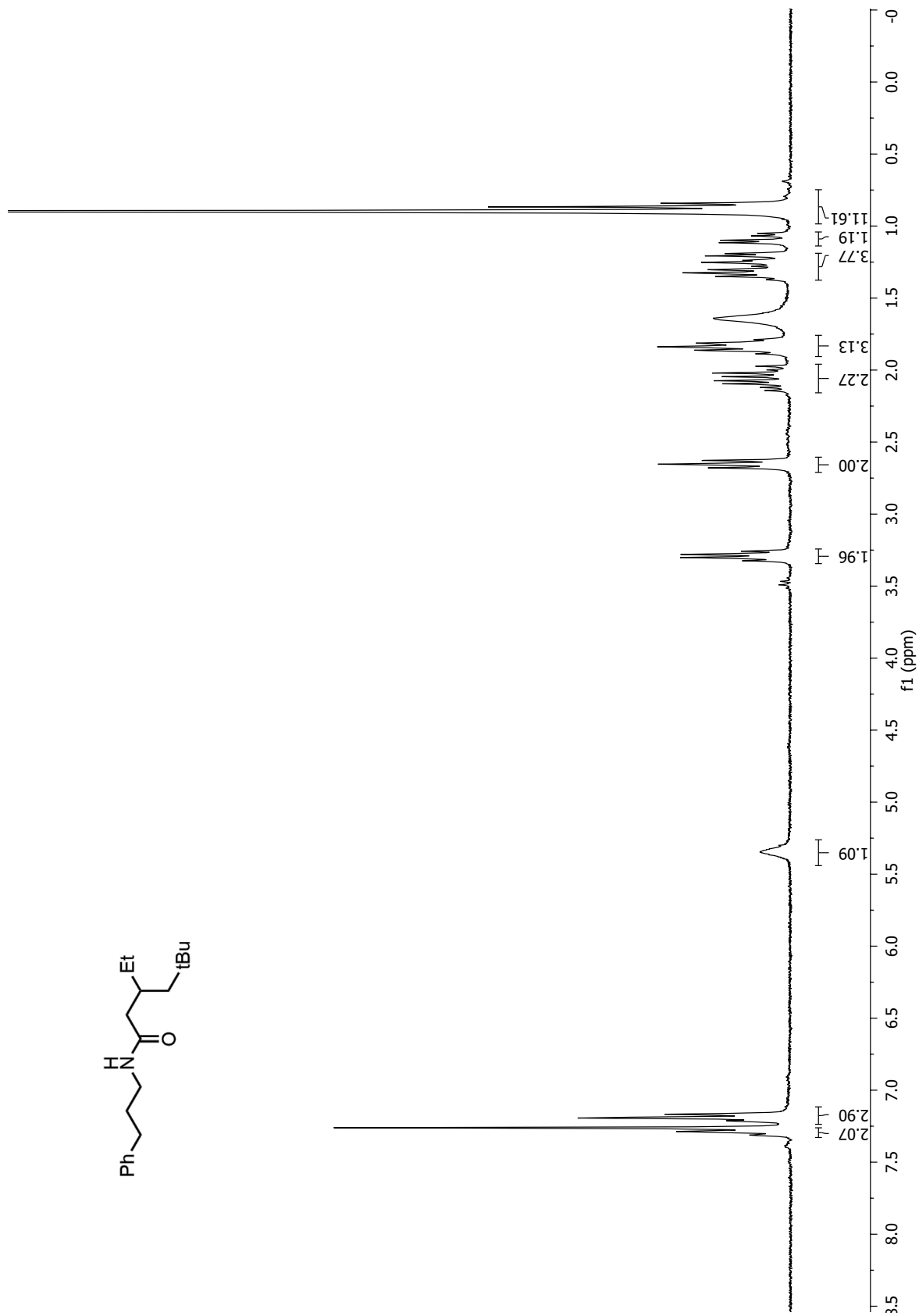
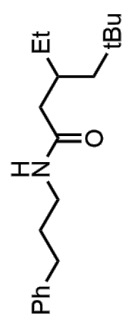


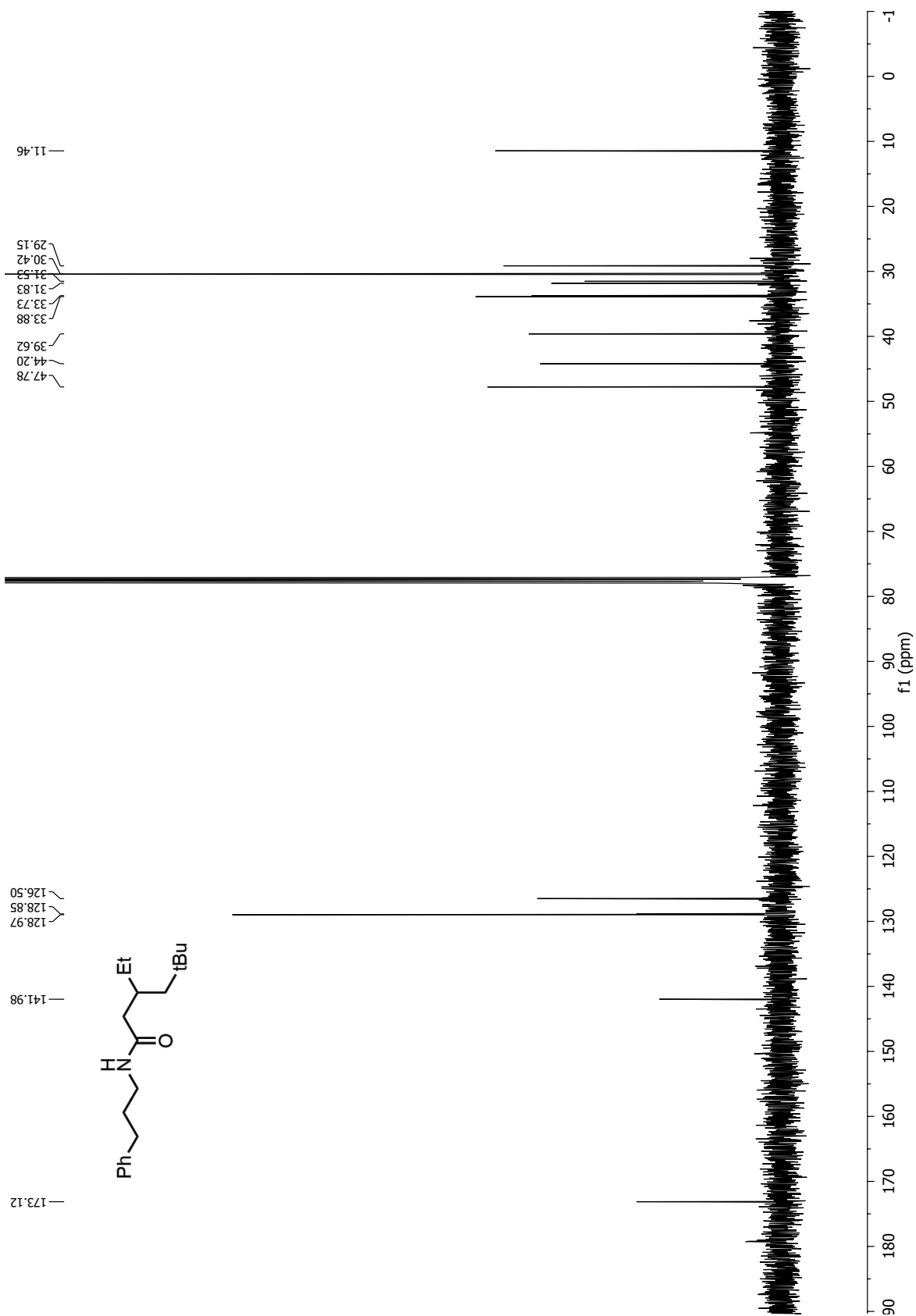


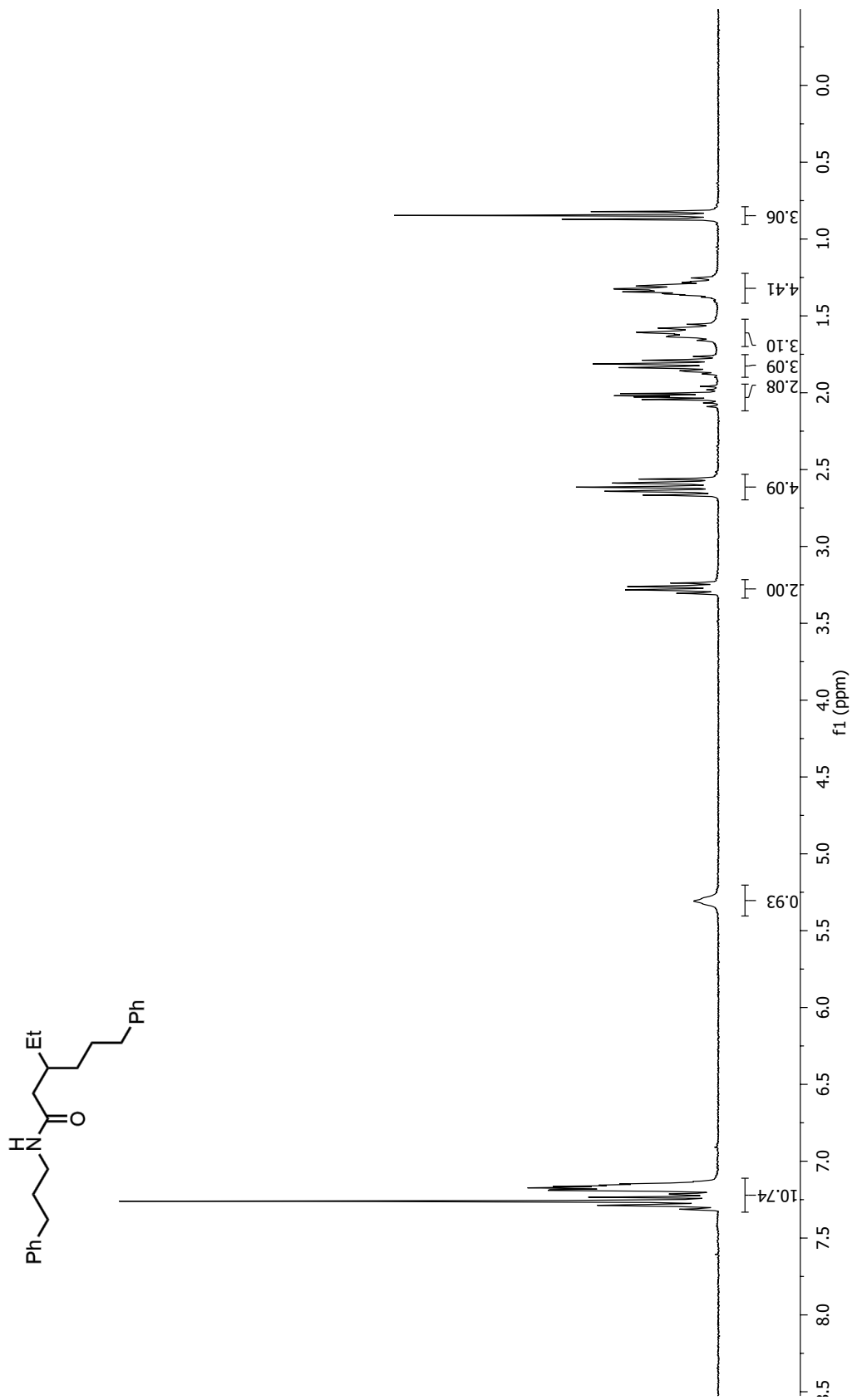


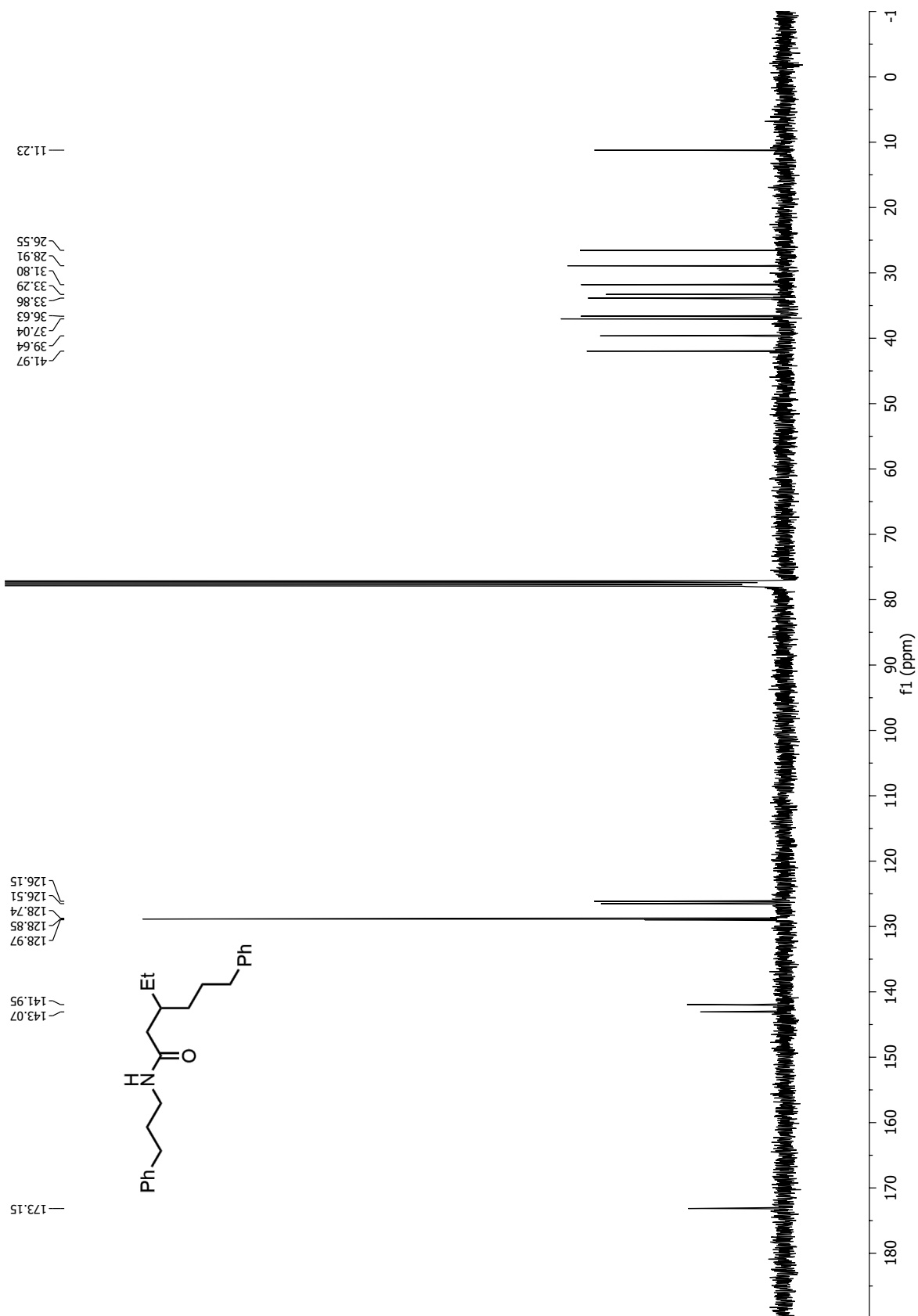


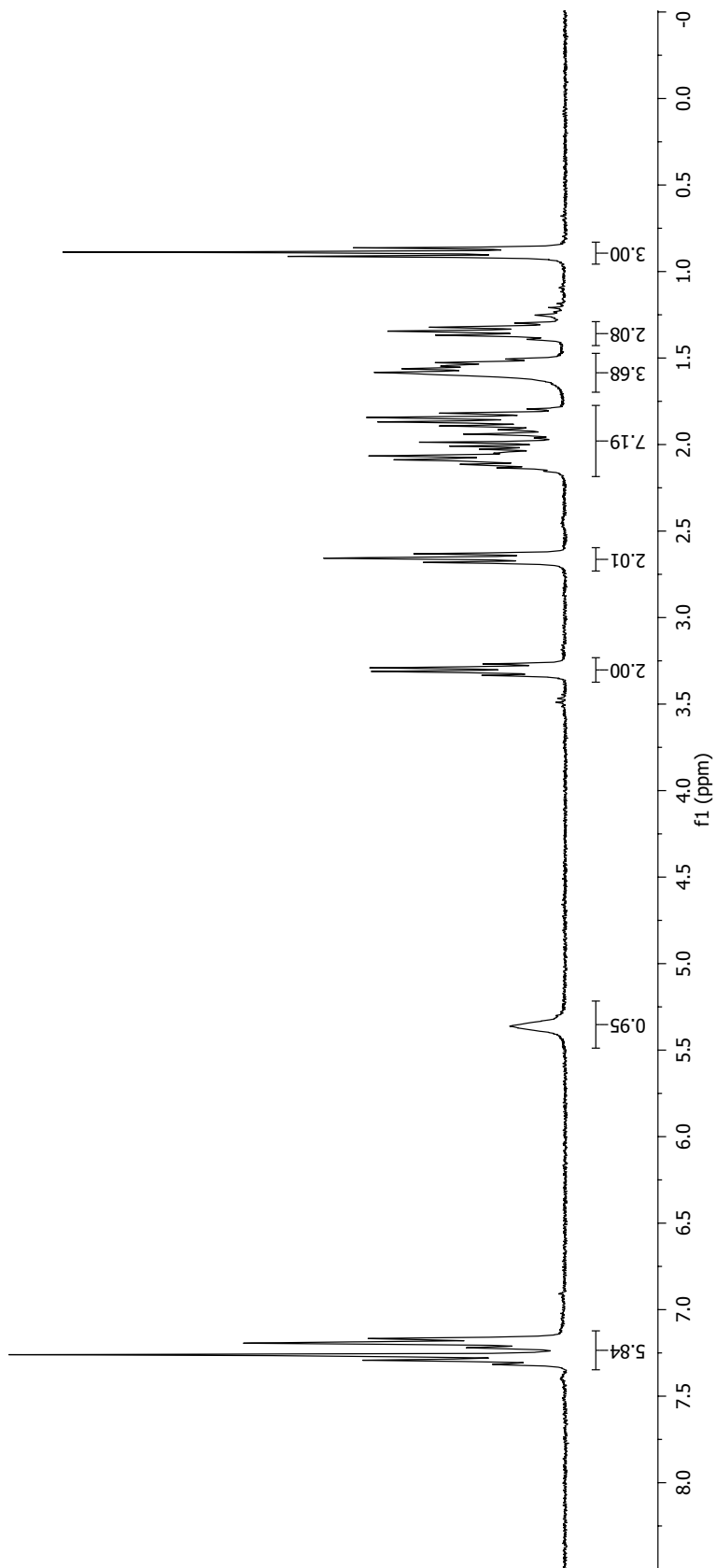
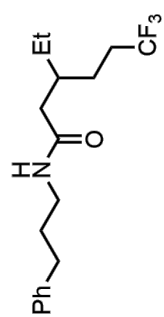


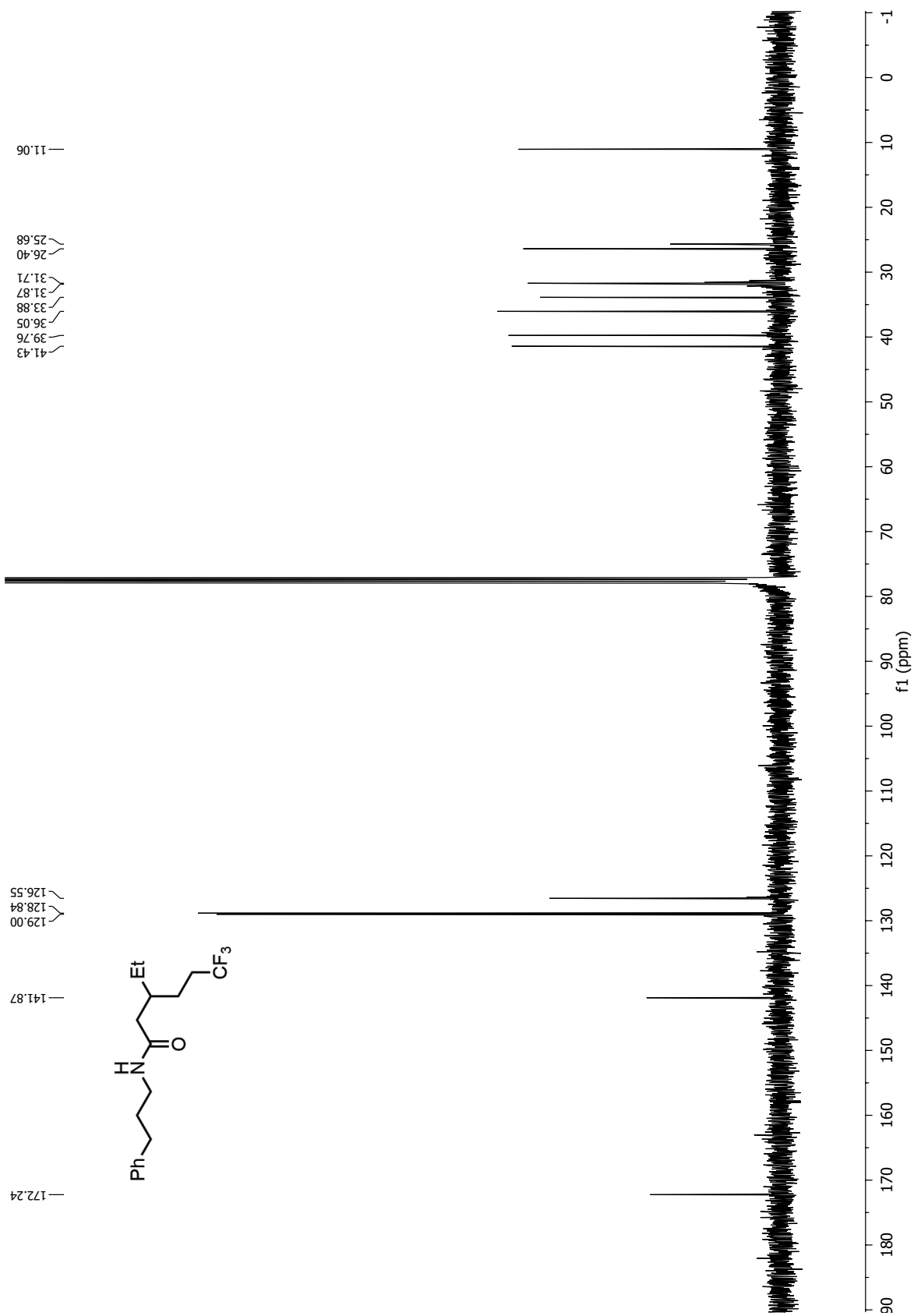


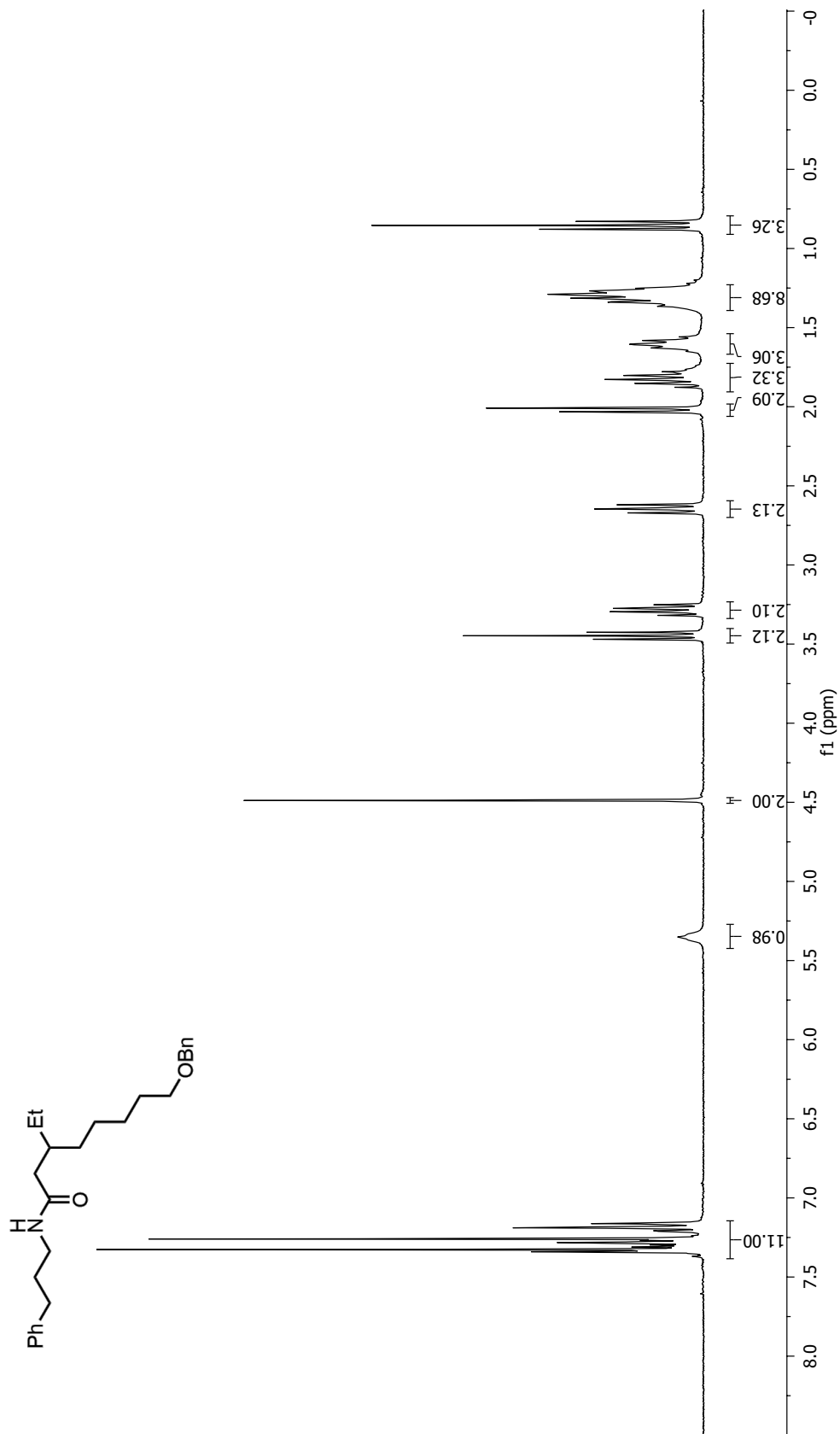


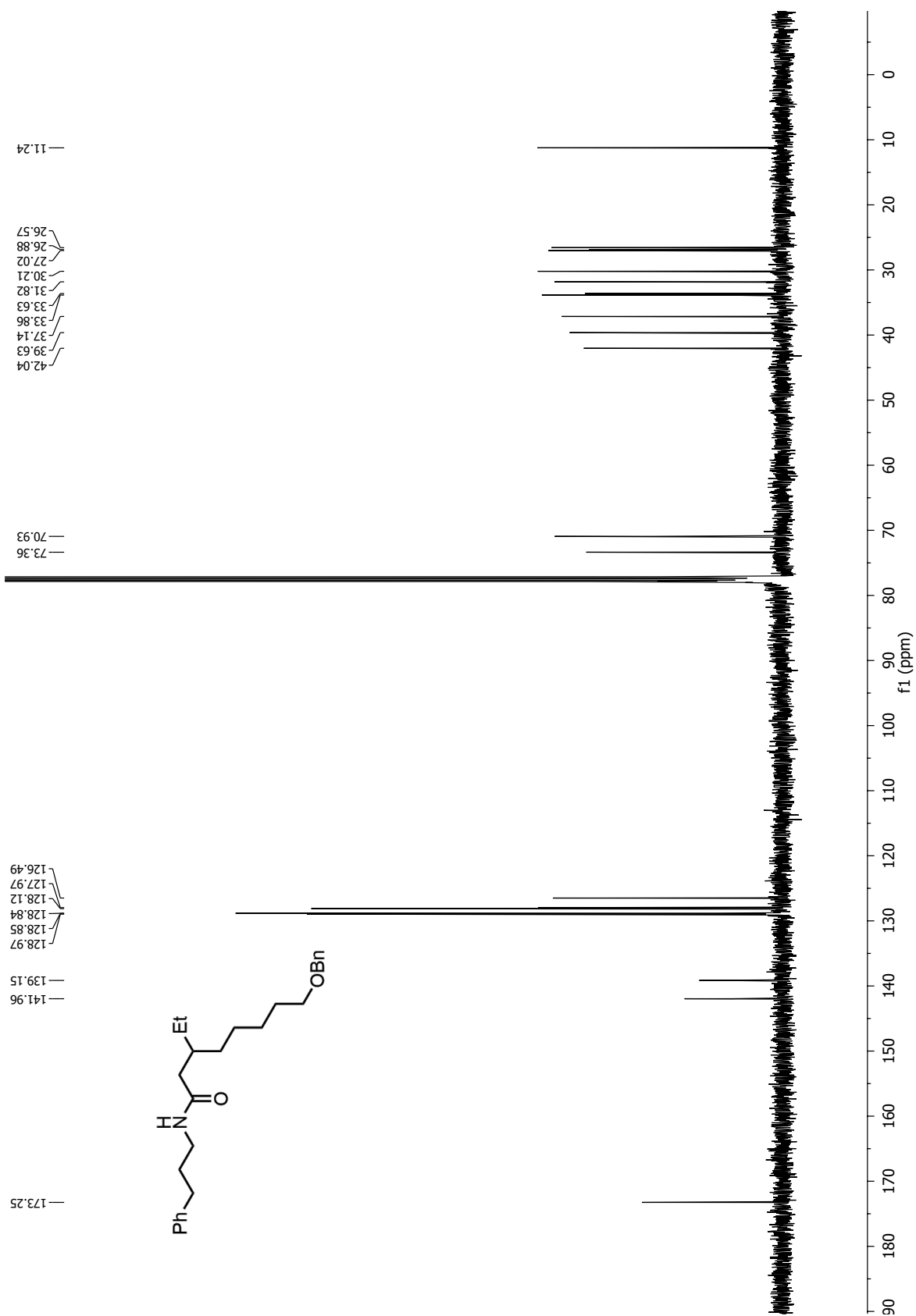


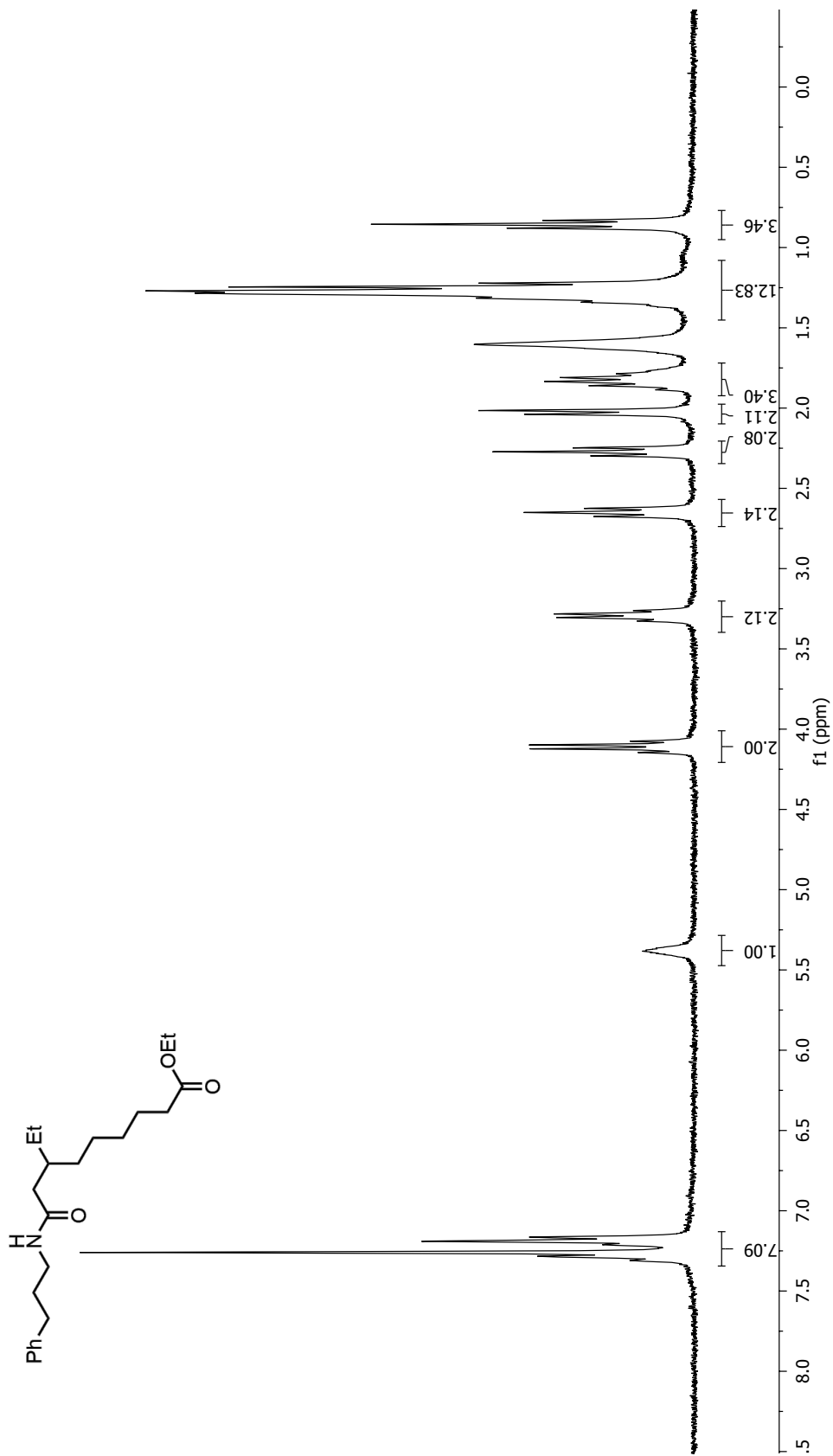


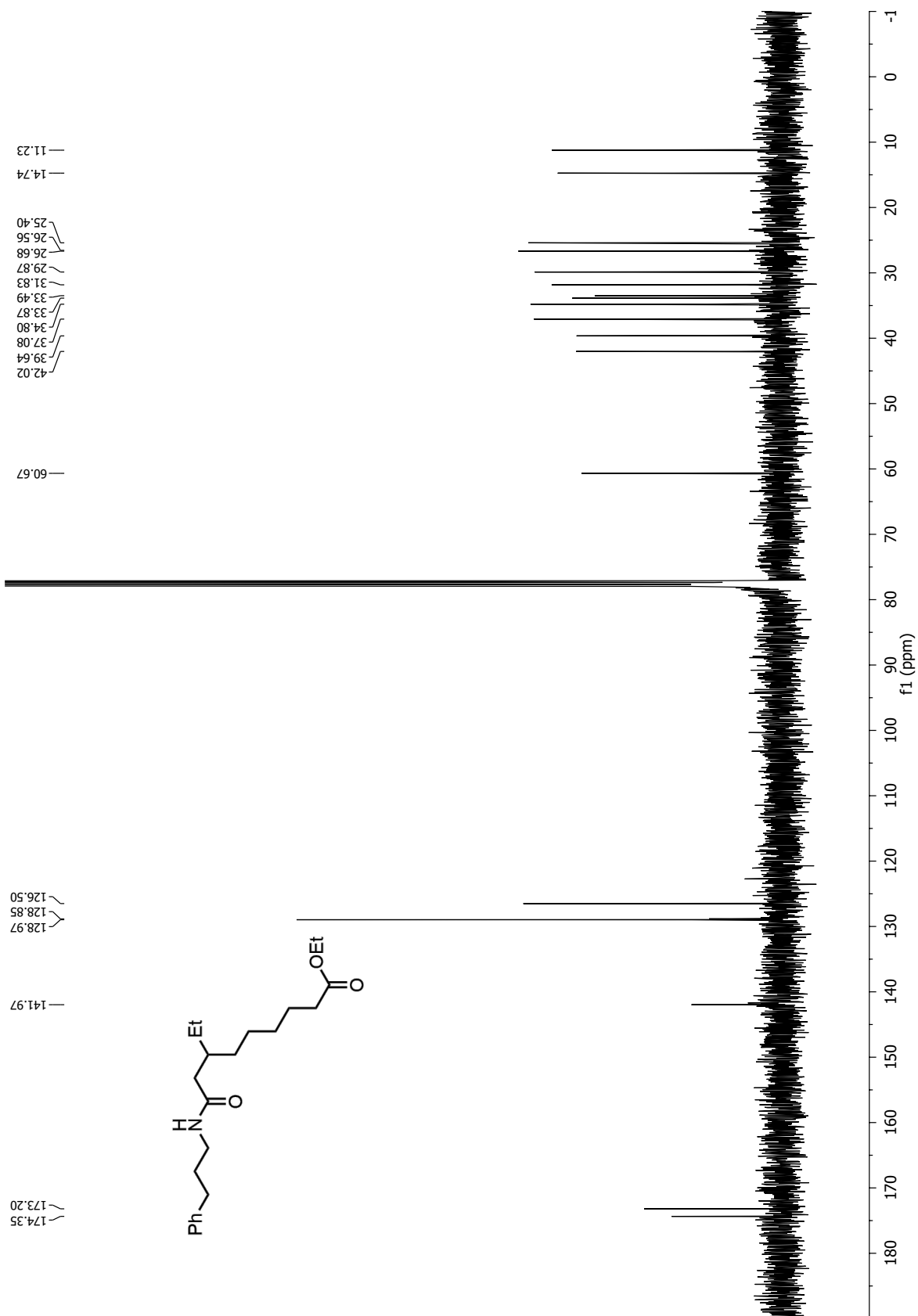


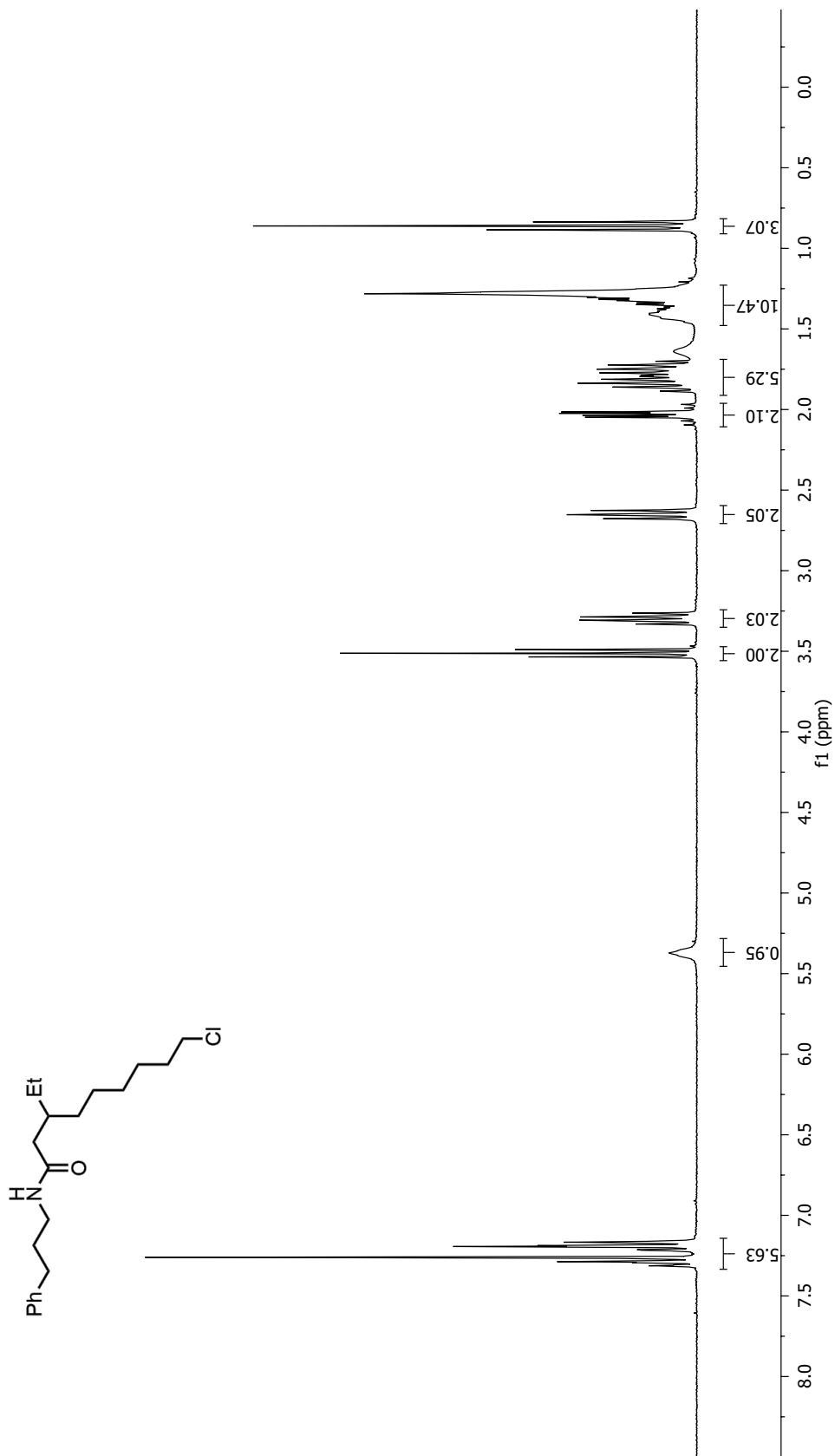


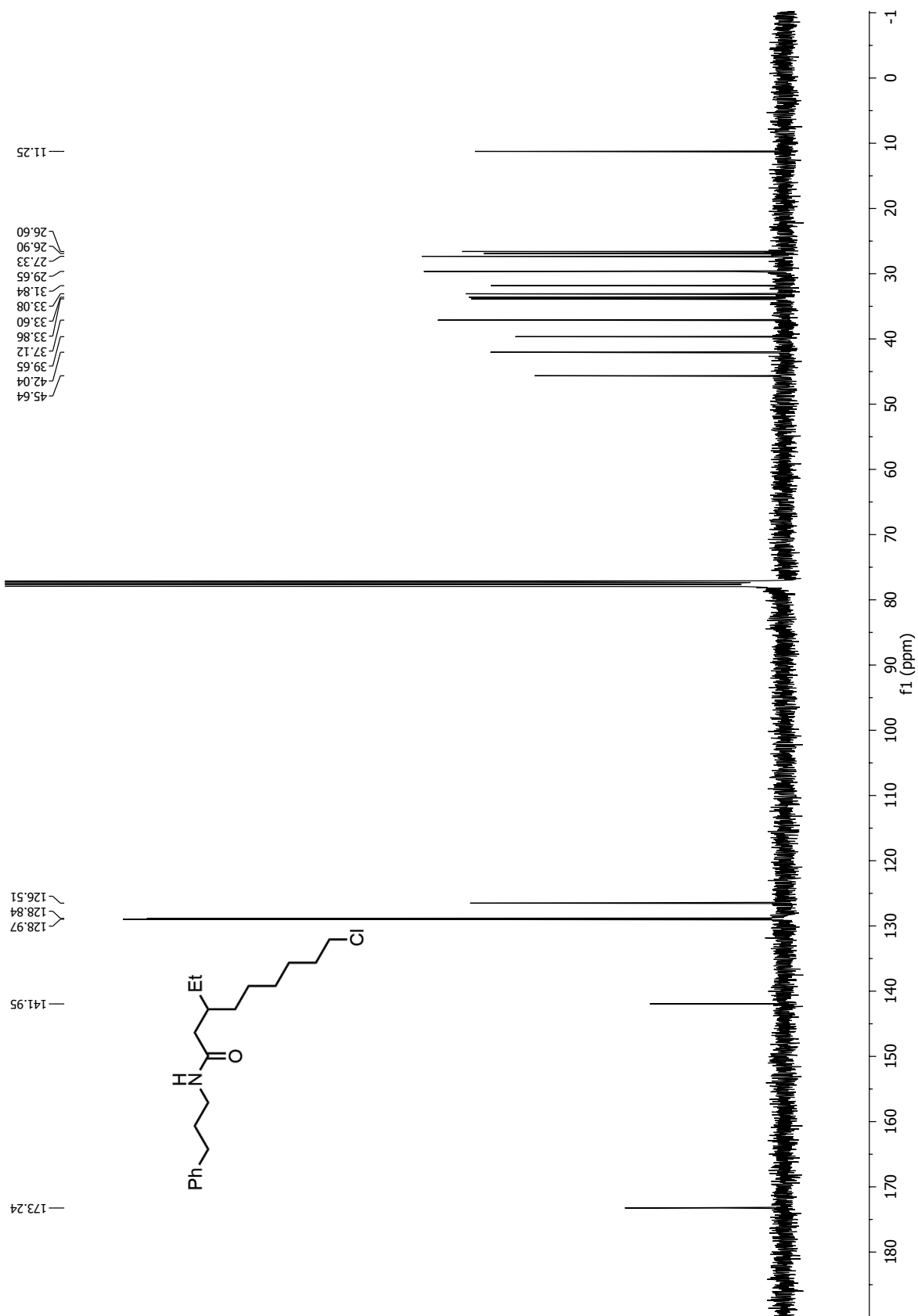


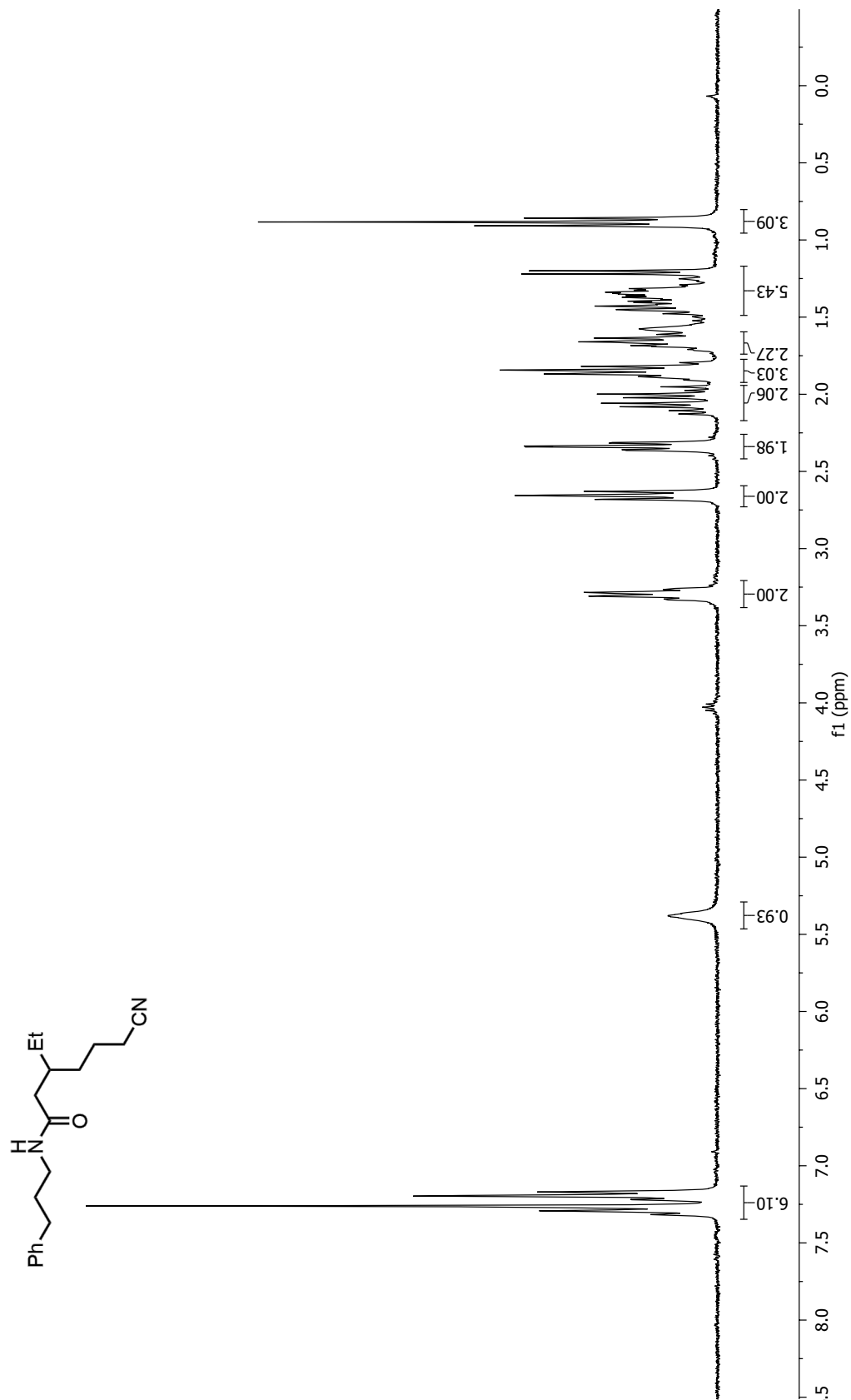


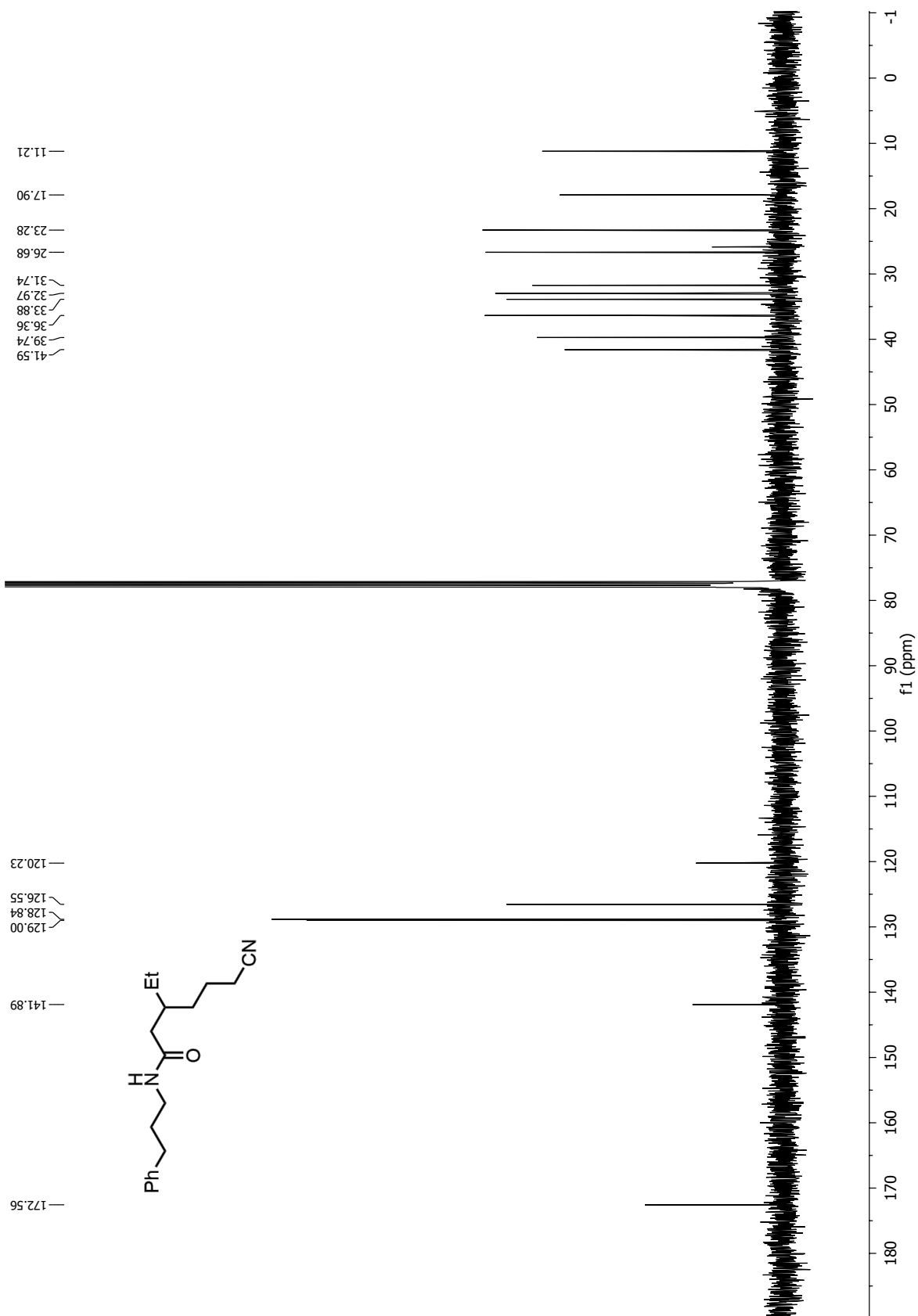


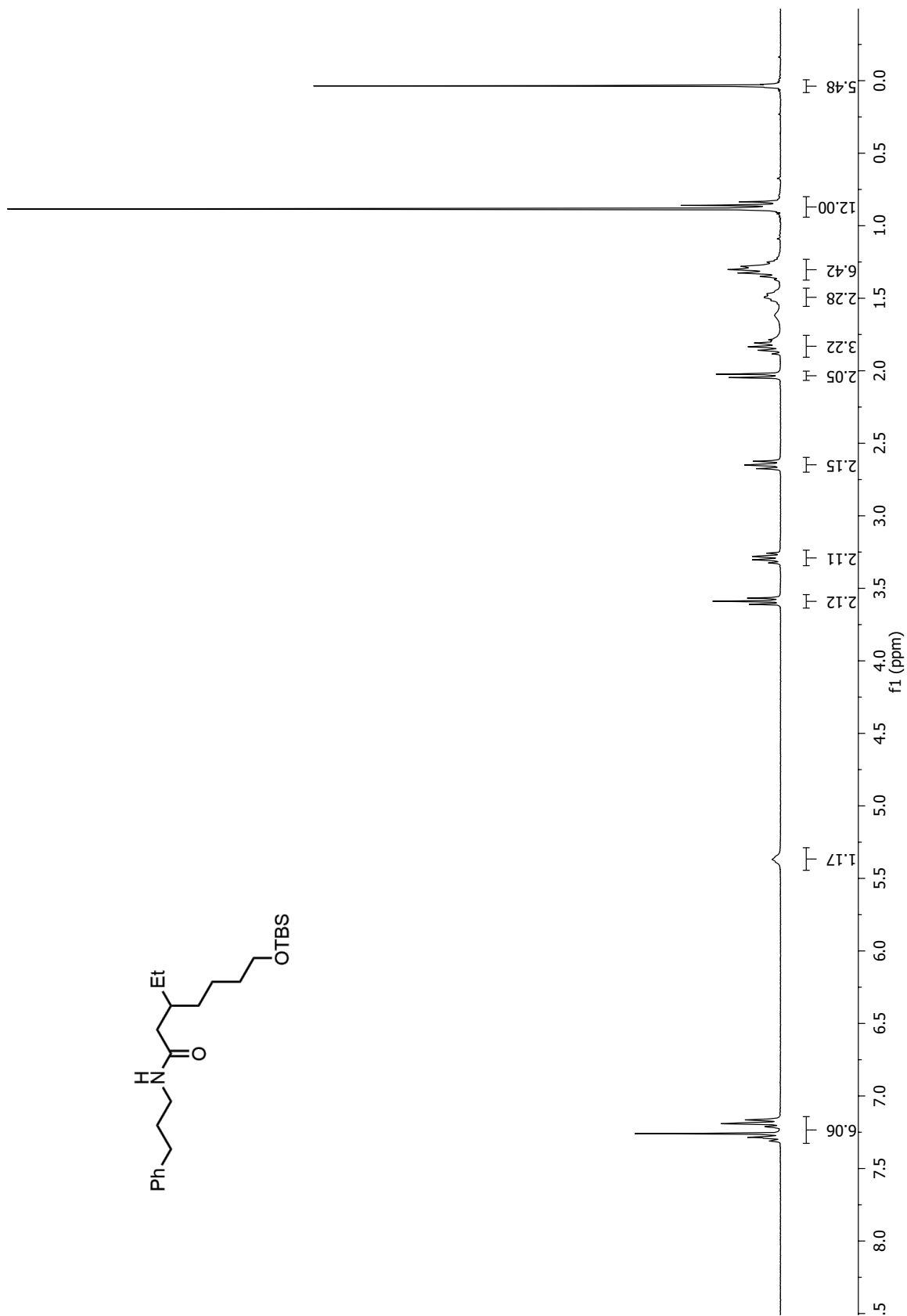


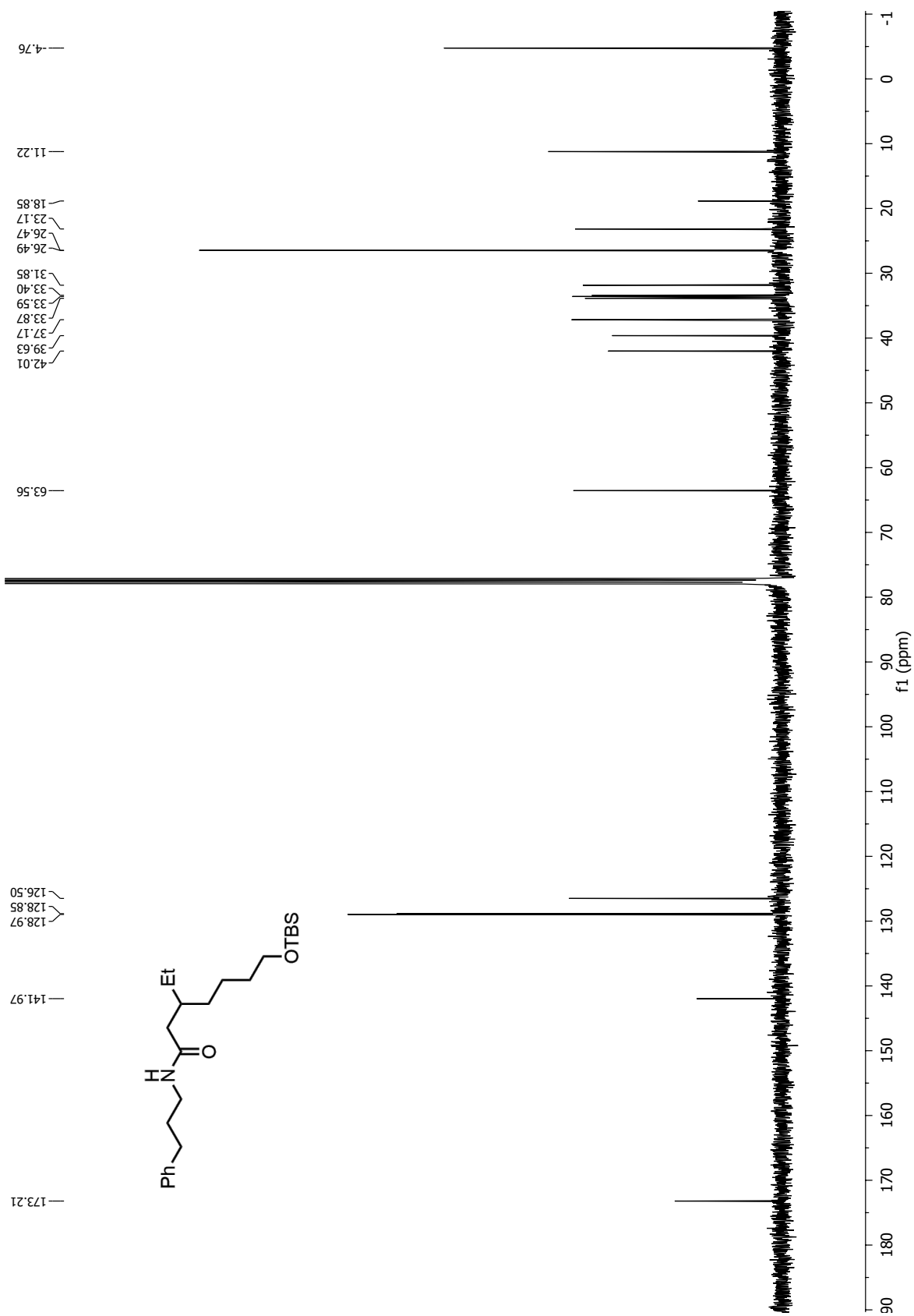


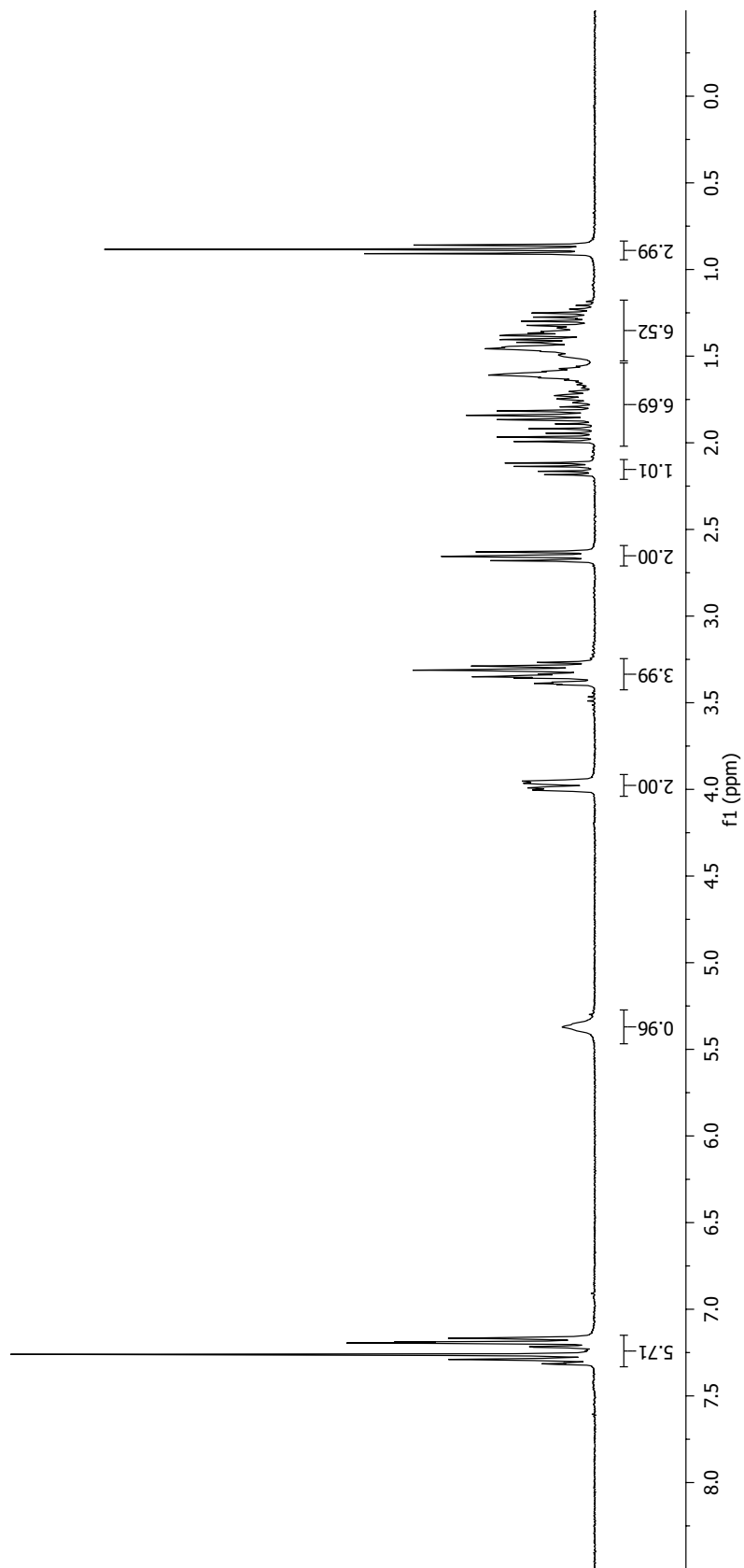
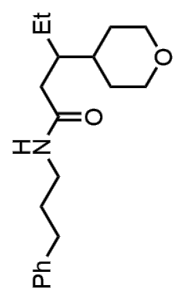


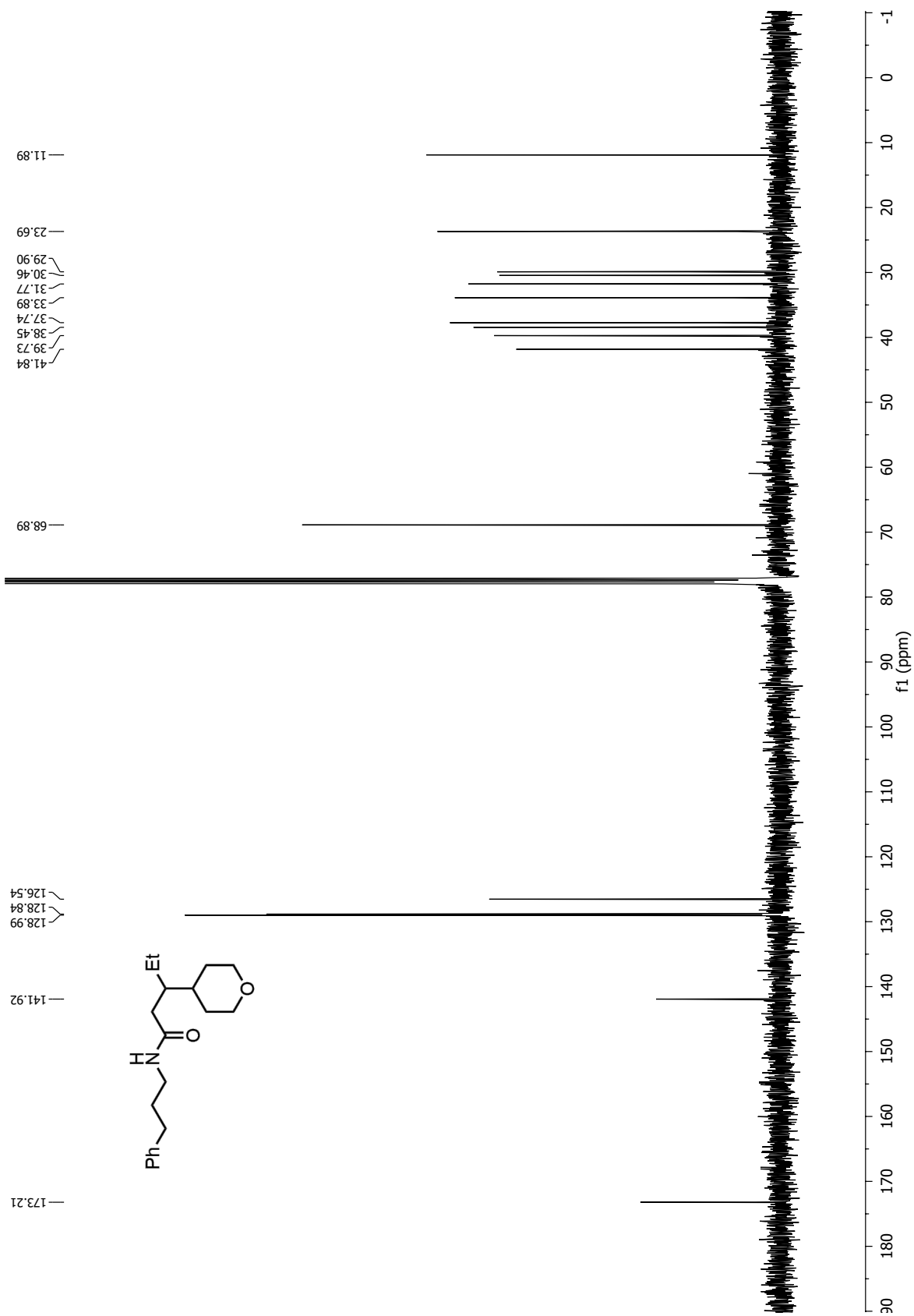


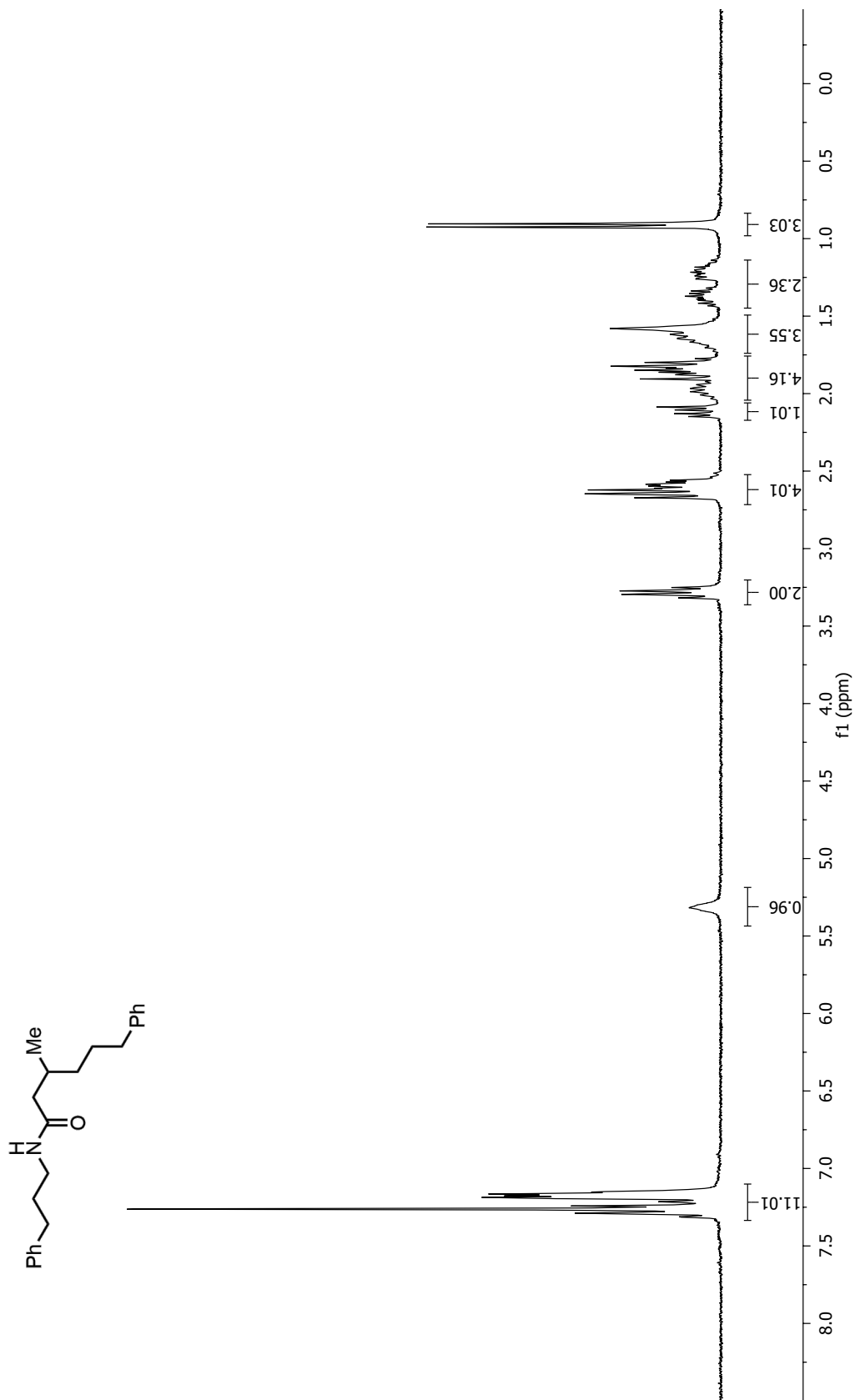


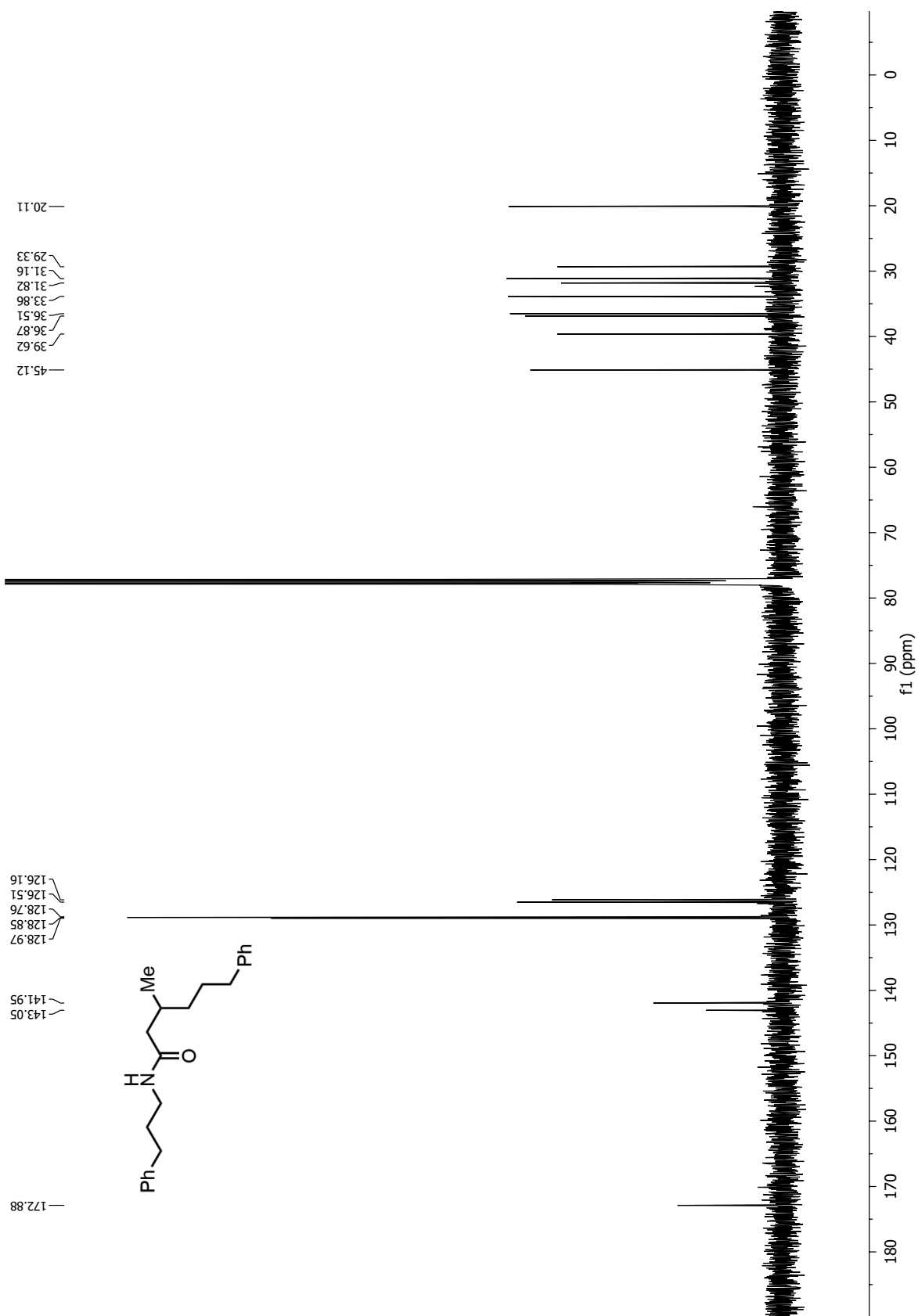


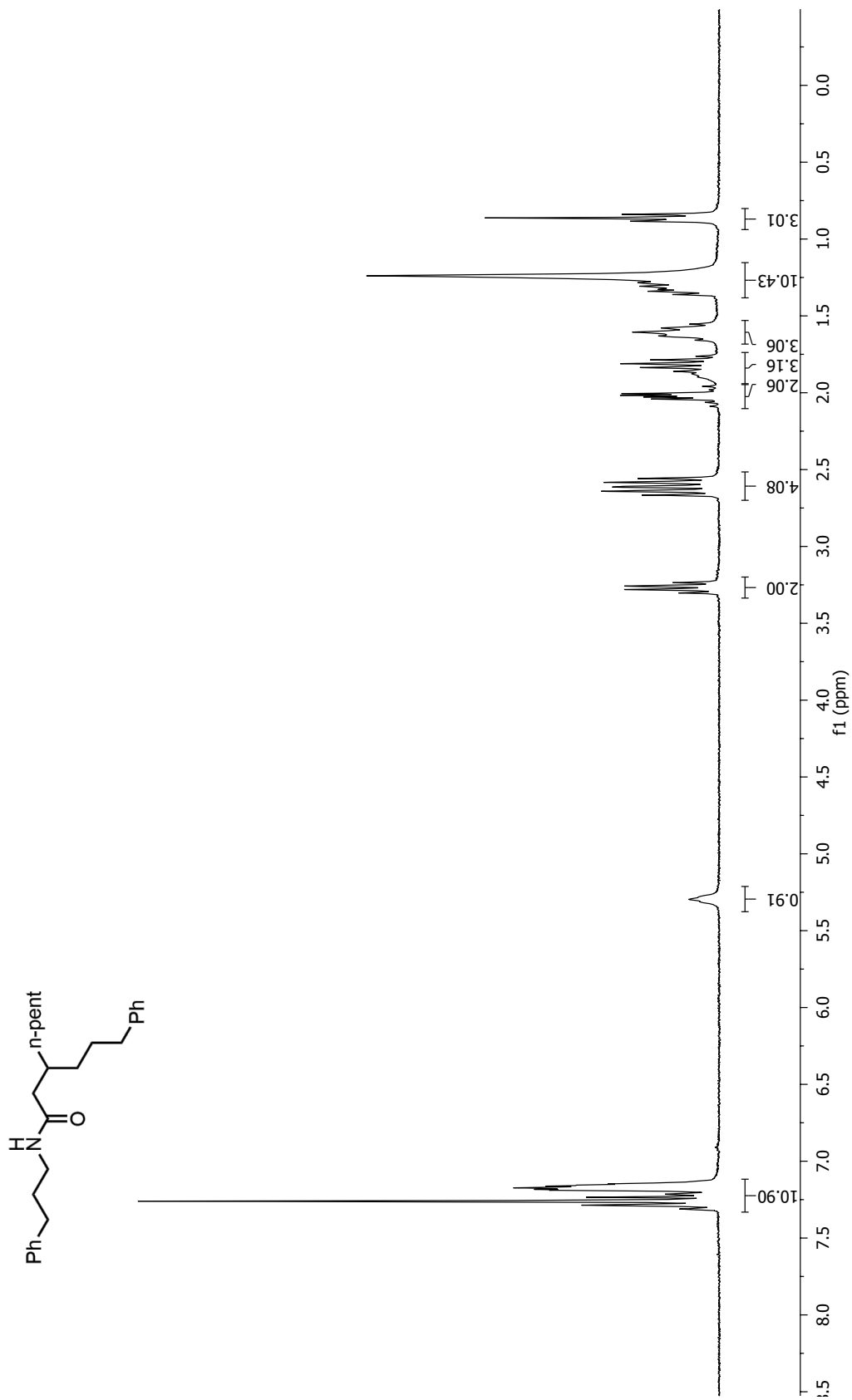


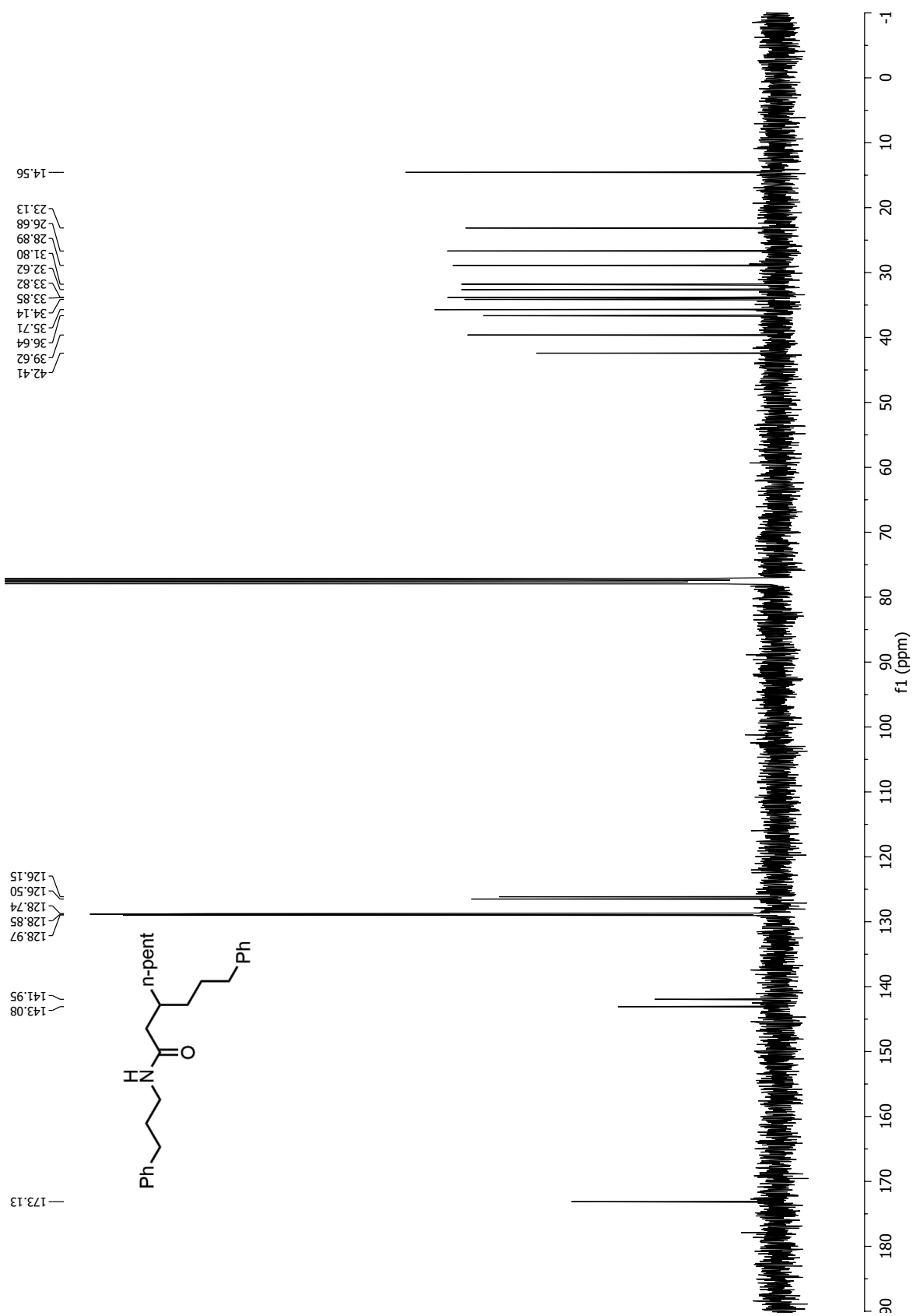


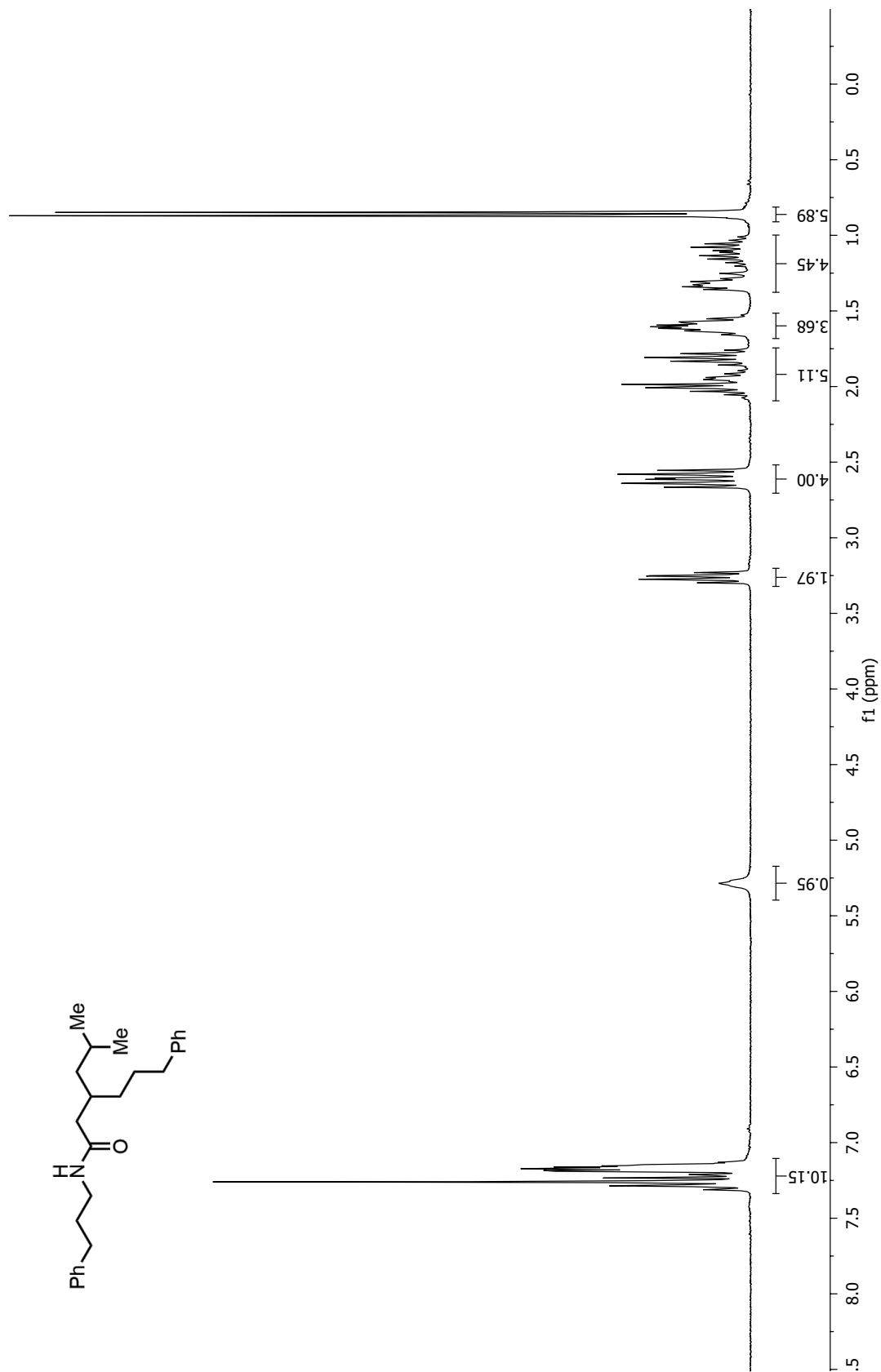


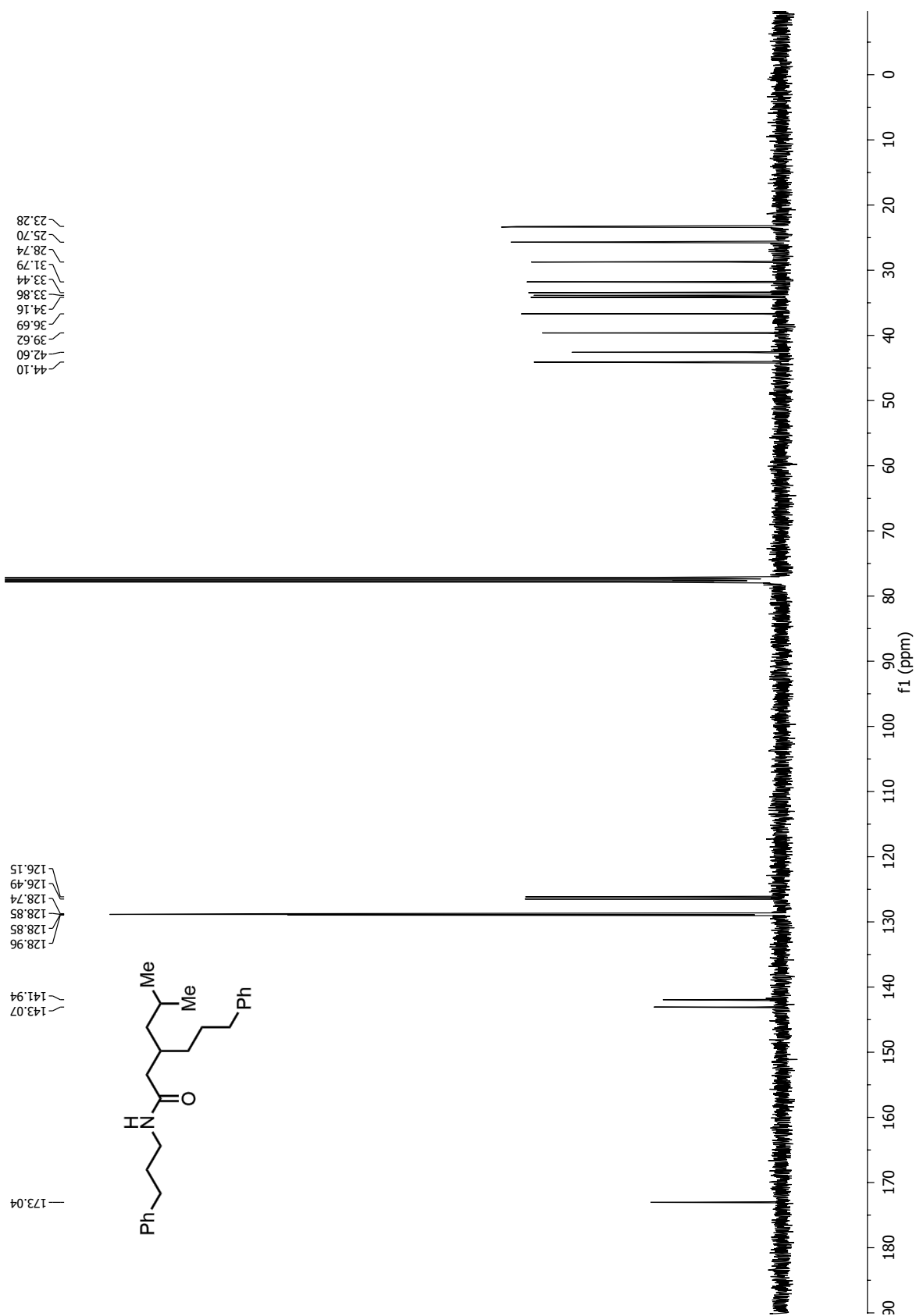


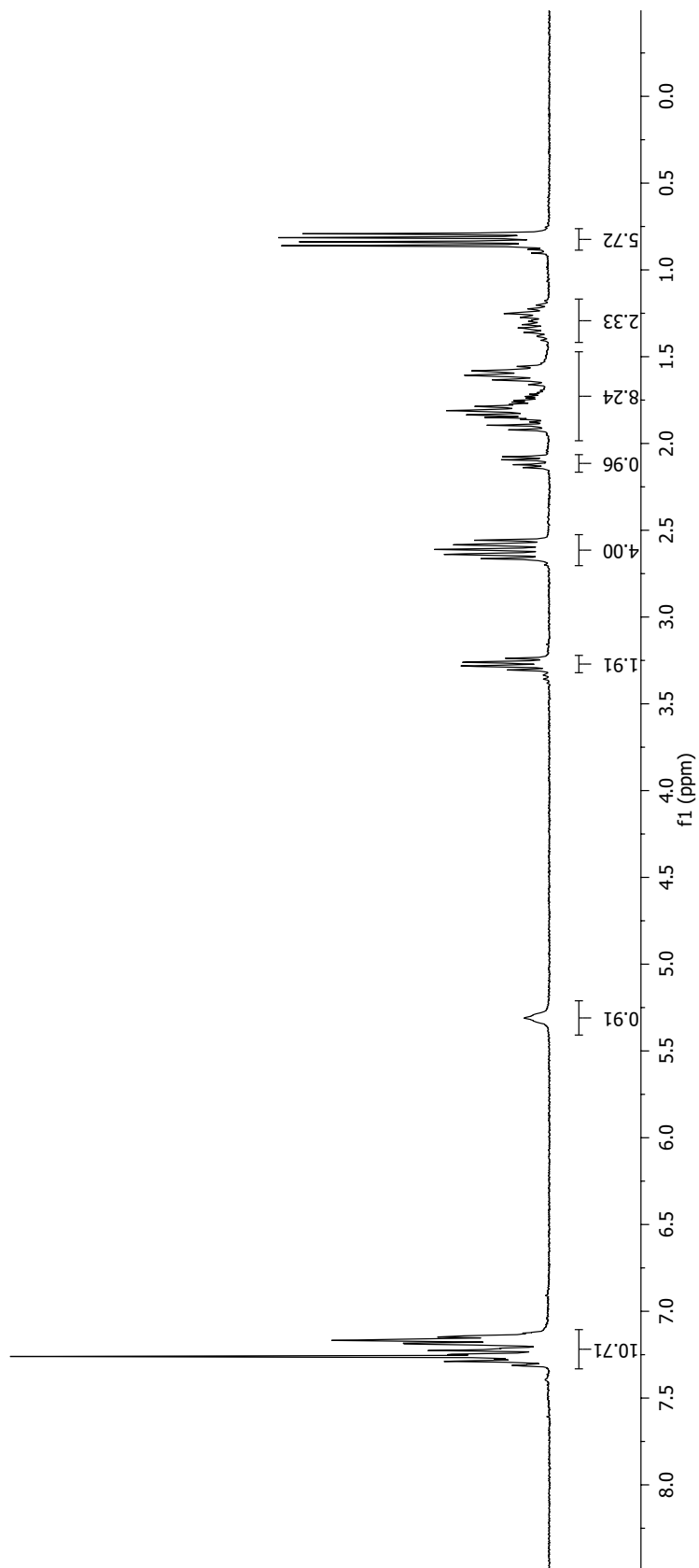
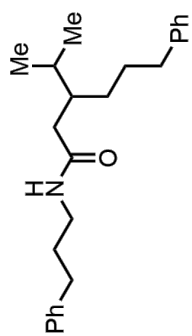


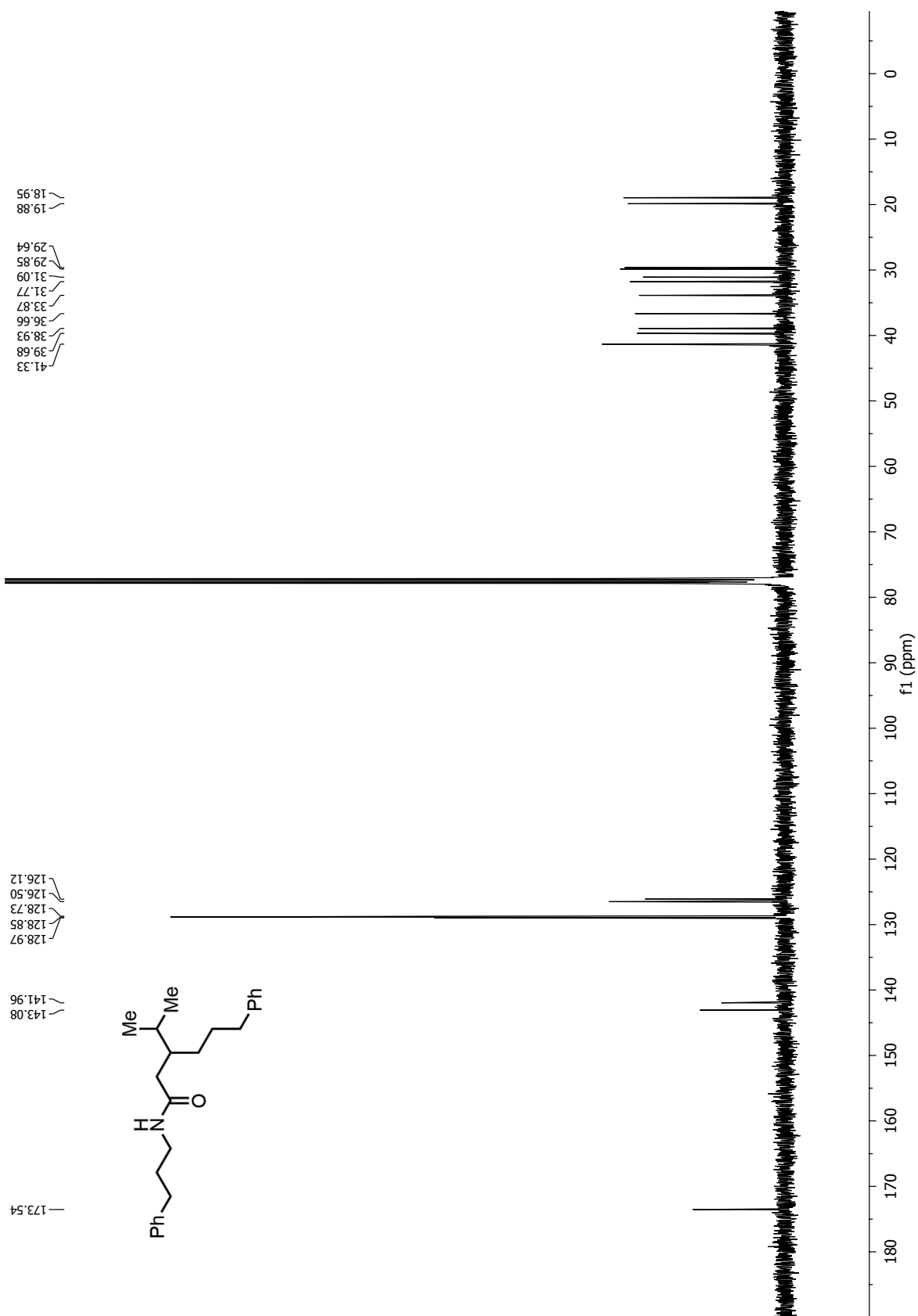








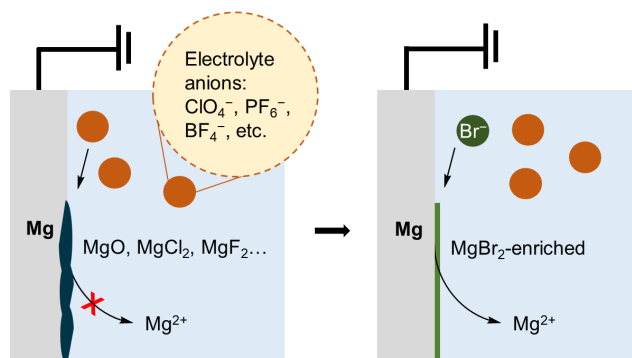




Chapter 3

IMPROVING THE MG SACRIFICIAL ANODE IN
TETRAHYDROFURAN FOR SYNTHETIC
ELECTROCHEMISTRY BY TAILORING ELECTROLYTE
COMPOSITION

Abstract: Mg^0 is commonly used as a sacrificial anode in reductive electrosynthesis. While numerous methodologies using a Mg sacrificial anode have been successfully developed, the optimization of the electrochemistry at the anode, i.e. Mg stripping, remains empirical. In practice, electrolytes and organic substrates often passivate the Mg electrode surface, which leads to high overall cell potential causing poor energy efficiency and limiting reaction scale-up. In this study, we seek to understand and manipulate the Mg metal interfaces for a more effective counter electrode in tetrahydrofuran. Our results suggest that the ionic interactions between the cation and the anion of a supporting electrolyte can influence the electrical double layer, which impacts the Mg stripping efficiency. We find halide salt additives can prevent passivation on the Mg electrode by influencing the composition of the solid electrolyte interphase. This study demonstrates that, by tailoring the electrolyte composition, we can modify the Mg stripping process and enable a streamlined optimization process for the development of new electrosynthetic methodologies.



3.1 Introduction

In recent years, electrochemistry has received renewed interest in the synthetic community as a tool to prepare useful and complex organic molecules.^{48–51} Electrochemistry offers unique advantages over traditional synthetic organic methods due to its ability to achieve highly selective oxidative and reductive transformations.⁵⁰ Using electrons as the reactants, electrochemistry avoids the use of harsh and often toxic traditional oxidants/reductants, giving rise to mild reaction conditions along with high atomic efficiency.^{52,53} Optimizing an electrochemical reaction requires careful consideration of the reactions that occur at both the WE and the CE. The reaction occurring at the CE is called the counter reaction. For organic electrosynthesis, efficient oxidation/reduction of a sacrificial reagent is typically employed as the counter reaction.^{54,55} The simplest counter reaction is metal stripping, in which a sacrificial metal electrode is simply oxidized to form soluble metal cations that dissolve into the reaction mixture.^{56,57} Magnesium is commonly employed as a sacrificial anode due to its low oxidation potential (-2.37 V vs. SHE), high Earth abundance, low toxicity, and apparent ease of handling on the benchtop.^{57–60}

Although Mg CEs nominally involve metal stripping, side reactions can cause issues with electrochemistry. For example, supporting electrolyte anions such as ClO_4^- , PF_6^- , BF_4^- , OTf^- , and TFSI^- react with Mg, generating high impedance, insoluble interphases (Figure 3.1).^{59,61} In addition to reacting with electrolyte anions, Mg can also react with organic substrates, especially commonly used organohalides.⁶² While this reactivity has proven useful for the formation of Grignard reagents, it also causes significant changes to the morphology^{63,64} and composition of the Mg electrode surface. Additionally, the Mg stripping process occurs to such an extent that high concentrations of Mg^{2+} salts are formed in solution. If the solubility of the Mg^{2+} salts formed is low in the organic solvent, the salts will precipitate onto the electrode.⁶⁵ Supporting electrolyte anions are necessary for electrolyte conductivity, organohalides are often used as synthetic building blocks,⁶⁶ and the formation of Mg^{2+} is unavoidable; thus it is challenging to maintain a stable Mg electrode interface during electrolysis. All the aforementioned reactions result in the formation of a high impedance interphase at the CE. The high-impedance interphase increases the cell voltage and lowers the efficiency of the reaction. In extreme cases, the cell voltage increases beyond the compliance limits of the potentiostat, and the reaction at the WE can no longer proceed.

To achieve effective Mg oxidation at the CE, it is therefore important to control

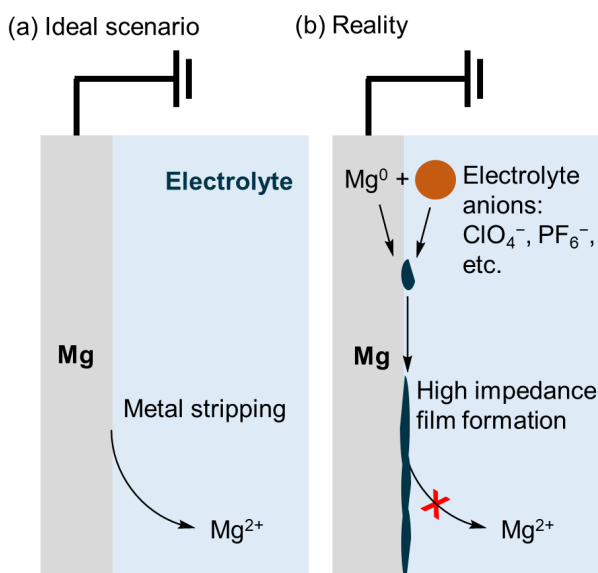


Figure 3.1: Mg sacrificial anodes are common CEs used in reductive organic electrosynthesis. (a) Ideally, Mg CEs undergo extensive Mg oxidation to Mg^{2+} (Mg stripping) without impediment. (b) In reality, Mg^0 reacts with the electrolyte, generating high impedance surface films that inhibit Mg stripping.

the Mg metal interface to avoid the formation of passivating interphases. To date, there has been limited effort to address the nature of passivation or modification of reaction conditions to control the Mg interface during organic electrosynthesis. The electron transfer events at the sacrificial anode occur in a heterogeneous environment, and thus their study requires the use of research techniques not traditionally used by the organic synthetic community.⁵⁷ Traditional optimization of electrochemical reactions involves screening solvents, supporting electrolytes, and sacrificial anodes to achieve high yields of the desired product.⁶⁷ However, this approach lacks any understanding of the individual processes occurring at the electrode interfaces and thus is often met with issues of high cell voltage, which may or may not be due to the CE.

Mg sacrificial anode passivation can not only hamper the optimization of a new organic electrochemical reaction but also make reaction scale-up challenging due to the resulting high cell voltage.^{65,68–75} For instance, Lin, See, and coworkers developed an electrochemically driven cross-electrophile coupling of alkyl halides.⁶⁵ Attempts to perform the electrochemical reaction on gram scale were thwarted by high anodic potential at the Mg CE due to a high impedance interphase. The interphase was composed of $MgBr_2$ and $Mg(ClO_4)_2$ as determined by various surface

characterization techniques. The addition of DME, thought to facilitate Mg^{2+} salt solvation, resulted in a decrease of Mg electrode passivation, leading to a successful scale-up of the reaction. This study demonstrates the practicality of tailoring the electrolyte by intentionally leveraging an understanding of the side reactions at the Mg CE. However, changing the solvent composition can dramatically affect the efficiency and selectivity of an organic reaction. While DME addition effectively limits the Mg anode passivation in the electrochemically driven cross-electrophile coupling reaction, it may not be a suitable solution to all reactions that require a Mg sacrificial anode. Therefore, we would like to study the Mg electrode interfaces under common organic electrosynthesis conditions to gain more insight into sacrificial anode behavior and provide promising alternative solutions to resolve the issues caused by passivation.

Here, we investigate the effect of supporting electrolytes on Mg stripping with the aim of improving Mg sacrificial anode performance in THF-based electrolyte. Currently, the most commonly employed solvent for systems using Mg sacrificial anodes is DMF.⁷⁶ However, the evident solvent limitation could pose challenges when attempting to broaden the application of reductive electrosynthesis to different types of organic transformations. Additionally, due to the toxicity of DMF and the restrictions imposed by the European Commission on its use,⁷⁷ finding alternative solvents is of great interest. Recently, researchers have attempted to use THF as the optimal solvent in combination with Mg sacrificial anodes but have encountered anode passivation issues.^{65,75} By studying the effects of the supporting electrolyte on Mg stripping in THF, we hope to provide insights into the fundamental factors affecting the Mg sacrificial anode performance and pave the way for the discovery of more cathodic reduction transformations that are achievable only in ethereal electrolytes. LSV demonstrates that the supporting electrolyte choice has a significant impact on the stripping overpotential and current density. MD simulations reveal the influence of the ionic interaction between the cation and anion of the supporting electrolyte on the composition of the EDL, which we correlate to the Mg stripping current density. XPS of the Mg anode surface after anodic polarization reveals the formation of insulating interphases upon contact with ClO_4^- , PF_6^- , BF_4^- , and OTs^- anions. Inspired by Mg battery research, we use halide salts as co-supporting electrolytes to inhibit the formation of insulating interphases on the Mg electrode. XPS reveals that bromide salt addition results in a thinner interphase that is MgBr_2 -enriched. The addition of Br^- salts improves the efficiency of Mg stripping in various electrolytes and effectively prevents organohalides from corroding the Mg electrode under electrolysis

conditions.

3.2 Results and Discussion

Effect of the supporting electrolyte cation on Mg stripping

To understand the effects of electrolyte composition on Mg sacrificial anode performance, we probe the Mg stripping behavior in THF with supporting electrolytes commonly employed for organic electrosynthesis using LSV. The LSV experiments are conducted in three-electrode cells with a Mg plate WE, graphite CE, and Pt|Fc/Fc⁺ RE (Figure 3.2a). All potentials referenced hereafter are vs. the Pt|Fc/Fc⁺ RE unless otherwise noted. First, we sweep the voltage positive from the OCV to 0.3 V at 5 mV s⁻¹. At this point, the electrode has been anodically polished to expose fresh Mg metal. Following the oxidation, the cell rests at OCV for 10 min, allowing the freshly exposed Mg metal to chemically react with the electrolyte. The LSV-OCV protocol is repeated 5 times and the resulting 5th LSV is shown in Figure 3.2. The prior LSVs are shown in the Supporting Information. All onset potentials and current densities at 0.2 V of the LSV experiments are tabulated in Table 3.1.

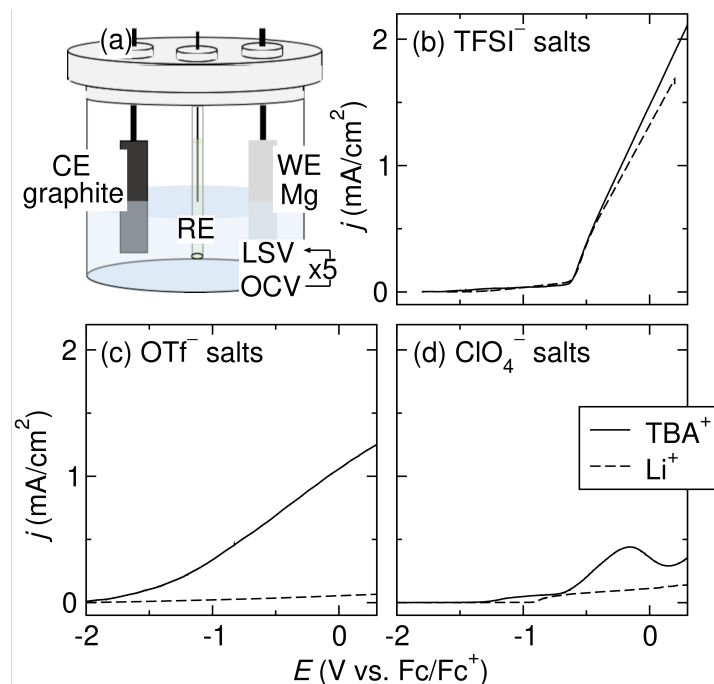


Figure 3.2: (a) Schematic of the three-electrode cell with a Mg WE, graphite CE, Pt|Fc/Fc⁺ RE, and 0.1 M supporting electrolyte in 7 mL of THF. Linear sweep voltammograms of Mg stripping in Li⁺/TBA⁺ electrolytes with (b) TFSI⁻, (c) OTf⁻, and (d) ClO₄⁻ anions. All voltammograms are collected at a scan rate of 5 mV s⁻¹. Generally, the TBA⁺ electrolytes yield higher anodic current densities.

Supporting Electrolyte ^a	σ ($\mu\text{S}/\text{cm}$) ^b	E_{on} ^c	j ^d	Fig. ref.
LiTFSI	869.0	-0.65	1.69	Fig. 3.2b
TBATFSI	846.6	-0.65	1.90	Fig. 3.2b
LiOTf	16.5	–	–	Fig. 3.2c
TBAOTf	327.0	-1.70	1.19	Fig. 3.2c
LiClO ₄	62.6	-0.90	0.13	Fig. 3.2d
TBAClO ₄	289.6	-0.69	0.30	Fig. 3.5a
TBAClO ₄ + LiBr	157.8	-2.37	1.21	Fig. 3.5a
TBAClO ₄ + TBABr	212.7	-2.45	1.60	Fig. 3.5a
TBAOTs	109.0	–	–	Fig. 3.5b
TBAOTs + LiBr	52.6	-1.46	0.26	Fig. 3.5b
TBAOTs + TBABr	110.5	-1.42	0.60	Fig. 3.5b
TBAPF ₆	506.3	–	–	Fig. 3.5c
TBAPF ₆ + LiBr	308.4	-2.36	1.72	Fig. 3.5c
TBAPF ₆ + TBABr	346.3	-2.47	1.57	Fig. 3.5c
TBAPF ₆ + LiCl	254.2	-0.91	0.92	Fig. 3.S3a
TBAPF ₆ + LiI	272.4	-2.25	0.64	Fig. 3.S3b
TBABF ₄	288.5	–	–	Fig. 3.5d
TBABF ₄ + LiBr	118.0	-1.41	0.23	Fig. 3.5d
TBABF ₄ + TBABr	219.2	-1.57	1.08	Fig. 3.5d

^aThe electrolyte is THF with 0.1 M supporting electrolyte of interest or 0.05 M supporting electrolyte + 0.05 M halide salt additive. ^bConductivity is measured at 22.0±1.0 °C. ^c E_{on} (V vs. Fc/Fc⁺) is defined as the potential at which dj/dE exceeds 0.3. ^d j (mA/cm²) at 0.2 V is reported.

Table 3.1: Conductivity (σ), onset potential (E_{on}), and current density (j) of Mg stripping in THF with various supporting electrolytes

To understand how the cations of the supporting electrolyte affect Mg stripping, we compare the LSVs obtained in electrolytes with TBA⁺ and Li⁺ cations. TBA⁺ and Li⁺ salts with weakly coordinating anions are popular supporting electrolytes for organic electrosynthesis due to their high solubility in polar aprotic solvents and minimal interference with organic reactions.⁴⁸ Figure 3.2 shows the LSVs of Mg stripping in TBA⁺/Li⁺ electrolytes with TFSI⁻, OTf⁻, and ClO₄⁻ anions. Interestingly, the Li⁺ electrolytes consistently yield lower current densities for Mg stripping compared to the TBA⁺ electrolytes with the same anions. The current density additionally depends on the anion. While the current densities for Mg stripping are comparable in LiTFSI and TBATFSI electrolytes, TBA⁺ electrolytes support much higher current densities with OTf⁻ and ClO₄⁻ anions compared to their Li⁺ counterparts. The low conductivities of LiOTf and LiClO₄ electrolytes (16.5 and 62.6 $\mu\text{S}/\text{cm}$, respectively) could be responsible for the poor Mg stripping behavior. However, LSVs with *i*R

compensation show that the Li^+ electrolytes afford much lower current densities for Mg stripping (see SI), indicating that low electrolyte conductivity does not explain the observed cation effect. We next hypothesize that the observed Mg stripping behavior stems from the ionic interaction between TBA^+/Li^+ and the anions in the electrolytes. Compared to TBA^+ , Li^+ presumably forms stronger ionic bonds with the anions in the electrolyte due to its greater charge density.⁷⁸ The strength of the ionic interactions can change the composition of the EDL at the Mg electrode surface, which may affect the Mg stripping process.

To experimentally probe the effects of cation identity on ionic interactions in the bulk electrolyte, we measure the Raman spectra of the solutions. Figure 3.3a,b shows the Raman spectra of TBATFSI and LiTFSI in THF. We measure the electrolytes at the concentration that is used for the electrochemistry, 0.1 M, and 0.5 M to observe greater signal to noise. In all cases, the speciation does not shift significantly between the 0.1 M and the 0.5 M solutions. The TBATFSI solution has only one mode at 742 cm^{-1} (mode a). Mode a can be assigned to the symmetric bending mode, δ_s , of the CF_3 in free (i.e. uncoordinated) TFSI^- with minimal interactions with the cation.⁷⁸ However, the LiTFSI solution has two modes, including mode a and a new mode at 747 cm^{-1} (mode b). Mode b is the same $\delta_s\text{CF}_3$ mode in the TFSI^- , but it is shifted due to coordination with the Li^+ .⁷⁸ The TBATFSI electrolyte exhibits only the free TFSI^- mode, indicating weak ionic interactions between TBA^+ and TFSI^- . Deconvolution of the $\delta_s\text{CF}_3$ band of the LiTFSI electrolyte (0.5 M) shows the presence of both free TFSI^- (80%) and Li^+ coordinated TFSI^- (20%). The high concentration of free TFSI^- in LiTFSI electrolyte indicates the ionic interaction between Li^+ and TFSI^- is relatively weak. Figure 3.3c,d shows the Raman spectra of TBAOTf and LiOTf in THF. The TBAOTf electrolyte has one mode at 755 cm^{-1} (mode c), ascribed to the $\delta_s\text{CF}_3$ in free OTf^- .⁷⁹ The LiOTf electrolyte exhibits two modes, both shifted from the frequency associated with free OTf^- . The modes are at 759 cm^{-1} (mode d) and 764 cm^{-1} (mode e), which are assigned to Li^+ coordinated OTf^- (58%) and multiple ion pair aggregates (42%), respectively.⁷⁹ The complete disappearance of free OTf^- in the LiOTf Raman spectrum (Figure 3.3d) suggests strong ionic bonding interactions between Li^+ and OTf^- . Figure 3.3e,f shows the Raman spectra of TBAClO₄ and LiClO₄ in THF. The strong mode at 916 cm^{-1} is the ring breathing mode of the THF solvent.^{80,81} Another mode is observed at 933 cm^{-1} (mode f) that partially overlaps with the solvent mode. Mode f is assigned to the symmetric stretching mode, ν_s , of the ClO_4^- .⁸² The LiClO₄ electrolyte shows the mode associated with free ClO_4^- (57%) and a new mode at 938 cm^{-1} (mode

peak ID	Raman shift (cm^{-1})	mode	assignment	ref.
a	742	$\delta_s\text{CF}_3$	free TFSI ⁻	78
b	747	$\delta_s\text{CF}_3$	Li ⁺ coordinated TFSI ⁻	78
c	755	$\delta_s\text{CF}_3$	free OTf ⁻	79
d	759	$\delta_s\text{CF}_3$	Li ⁺ coordinated OTf ⁻	79
e	764	$\delta_s\text{CF}_3$	Li ⁺ OTf ⁻ ion pair aggregates	79
f	933	$\nu_s\text{ClO}_4^-$	free ClO_4^-	82
g	938	$\nu_s\text{ClO}_4^-$	solvent separated Li ⁺ ClO_4^- ion pair	82

Table 3.2: Assignments of Raman shifts for TBA⁺/Li⁺ electrolytes with TFSI⁻, OTf⁻, and ClO₄⁻ anions

g). Mode g is assigned to solvent-separated ion pairs (43%), indicating moderate ionic interaction between Li⁺ and ClO₄⁻.⁸² Therefore, we observe that Li⁺ generally has greater interactions with the anions in the bulk electrolyte than TBA⁺. All assignments of Raman shifts for the TBA⁺/Li⁺ electrolytes are tabulated in Table 3.2.

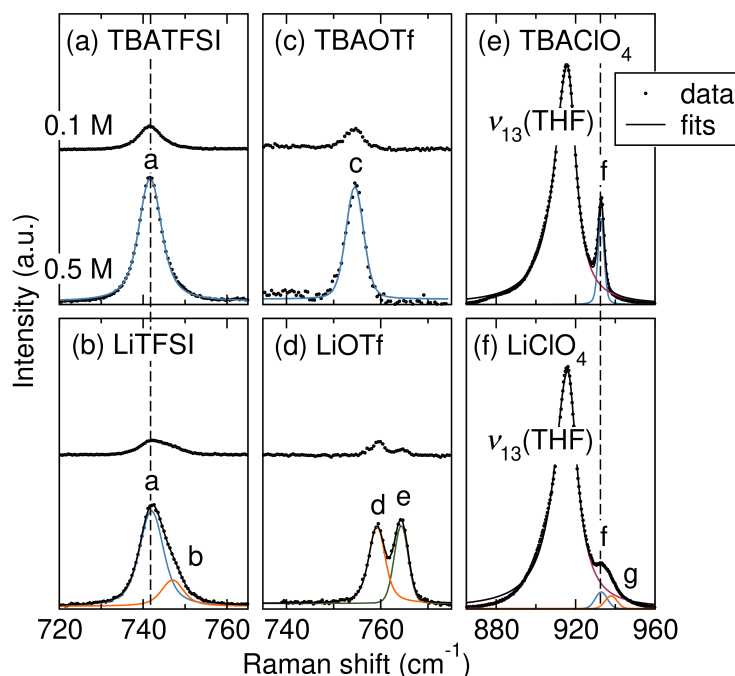


Figure 3.3: Raman spectra of (a) TBATFSI, (b) LiTFSI, (c) TBAOTf, (d) LiOTf, (e) TBAClO₄, and (f) LiClO₄ electrolytes at 0.1 M and 0.5 M in THF. Dashed lines indicate positions of the free TFSI⁻ and ClO₄⁻ anion modes and are guides for the eye.

To understand how the ionic interactions in the bulk electrolyte affect the EDL at the anode, slab-geometry MD simulations are performed. The composition of each MD simulation box corresponds to a 0.5 M THF solution of each ionic species. The

anode and cathode are modeled by inert graphene slabs. The realistic Mg surface is not Mg^0 ; instead it is heterogeneous and usually covered by a complex SEI. Additionally, the impact of van der Waals forces between the SEI and electrolyte is relatively minor compared to the effect of the applied electric field. Therefore, we use graphene as a surrogate for the Mg electrode surface to focus on the influence of electric field on the EDL structure. Prior works have used similar approaches to represent Li and Zn electrodes with graphene in MD simulations.^{83–85} As the graphene slabs are polarized, we observe changes in the electrolyte. Figure 3.4 shows the number density distributions of anions, categorized by their association with the cations (“associated”) or lack thereof (“free”), as a function of the distance to the anode surface after polarization. The identity of the cation species dictates the concentration and the solvation state of anions near the charged anode. With the applied electric field, the positively charged electrode surface repels the TBA^+ cations, leading to free anions dominating the composition of the anode EDL (Figure 3.4a-c). By contrast, there are fewer free anions in the Li^+ electrolytes. The majority of the ion pairs and aggregates remain intact with the applied electric field due to their strong bonding energies. As a result, significantly fewer free anions are observed at the anode EDL in the Li^+ electrolyte (Figure 3.4d-f).

Comparing the LSVs to the MD simulations reveals a strong correlation between effective Mg stripping and the concentration of free anions in the anode EDL. The EDLs of TBATFSI and LiTFSI electrolytes both contain a significant concentration of free anions due to the weak ionic interactions between TBA^+/Li^+ and TFSI^- . Correspondingly, the measured current densities for Mg stripping in TBATFSI and LiTFSI electrolytes are comparable (Figure 3.2b). The distinction in the anode EDL composition is most significant between LiOTf and TBAOTf electrolytes. While free OTf^- anions account for > 90% of the ionic species in the TBAOTf electrolyte anode EDL, Li^+ and OTf^- remain as ion pairs in the LiOTf electrolyte. The predicted EDLs correspond well to the LSV data in which TBAOTf electrolyte supports effective Mg stripping while LiOTf electrolyte only gives minimal stripping current density (Figure 3.2c). The moderate ionic interaction between Li^+ and ClO_4^- significantly lowers the free ClO_4^- concentration in the EDL at the anode, leading to decreased Mg stripping efficiency in LiClO_4 electrolyte compared to in TBAClO_4 electrolyte (Figure 3.2d). Based on these observations, we hypothesize that a high concentration of free anions at the anode surface is crucial to effective Mg stripping. The free anions likely play a role in facilitating the Mg^{2+} transfer into the electrolyte by attracting and solvating the charge dense Mg^{2+} . Efforts are ongoing to further

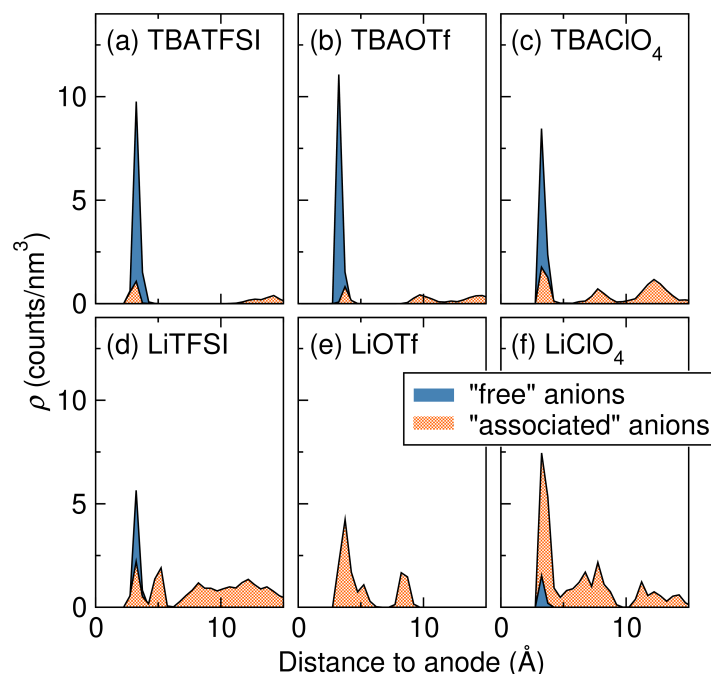


Figure 3.4: The number density of anions near the positively charged anode surface as calculated by MD for (a) TBATFSI, (b) TBAOTf, (c) TBAClO₄, (d) LiTFSI, (e) LiOTf, and (f) LiClO₄ supporting electrolytes in THF. An anion is defined as “free” if its distance to any cation is higher than a defined cutoff value, otherwise it is considered “associated.” The cutoffs are obtained from the radial distribution functions (RDFs) in bulk simulations. Generally, TBA⁺ electrolytes have a higher density of free anions at the anode compared to Li⁺ electrolytes.

investigate the effect of free anions on Mg²⁺ *via* computational methods. In the broader context of organic electrosynthesis, selecting a supporting electrolyte that has weak ionic interactions between the cations and the anions is crucial for an effective Mg sacrificial anode.

Effect of supporting electrolyte anion on Mg stripping

In addition to the cation identity, the anion identity in the supporting electrolyte strongly influences the Mg stripping in THF as well. This effect is observed in Figure 3.2, where both the onset potentials and current densities are drastically different in TBA⁺ electrolytes with TFSI⁻, OTf⁻, or ClO₄⁻ anions. Compared to TBATFSI and TBAOTf, TBAClO₄ affords the lowest current density for Mg stripping despite the predicted high anion concentration in the EDL. We hypothesize this effect is due to the anion and its interaction with the Mg surface. To probe the effect of anion, we expand our study to other anion choices, including OTs⁻, PF₆⁻, and BF₄⁻ anions. The LSVs for Mg stripping in these three electrolytes are shown

in Figure 3.5. While all three electrolytes employ the TBA⁺ cation, the anodic current density is very low, suggesting that they do not support Mg stripping in THF (Figure 3.5). All onset potentials and current densities at 0.2 V of the LSV experiments are tabulated in Table 3.1.

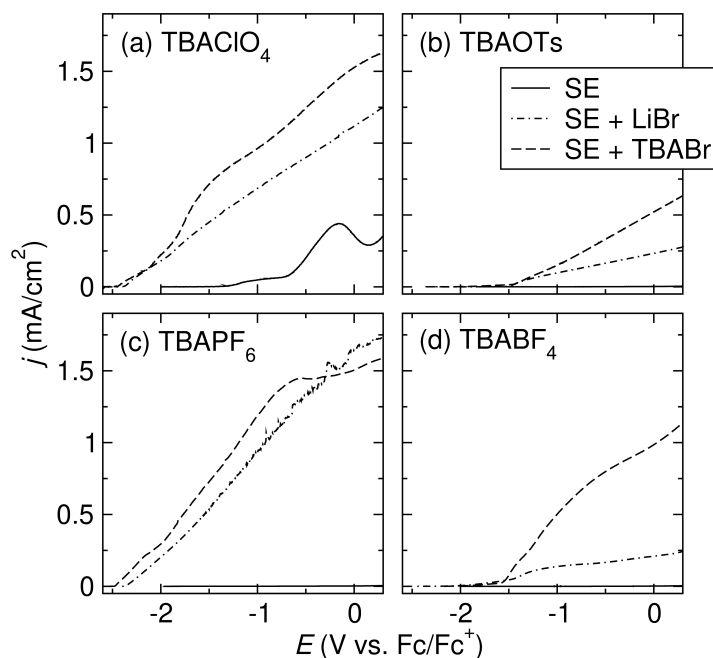


Figure 3.5: Linear sweep voltammograms of Mg stripping in THF with 0.1 M supporting electrolyte (SE) of interest, 0.05 M SE + 0.05 M LiBr, and 0.05 M SE + 0.05 M TBABr. The SEs are (a) TBAClO₄, (b) TBAOTs, (c) TBAPF₆, and (d) TBABF₄. All voltammograms are collected at a scan rate of 5 mV s⁻¹.

We suspect that the Mg SEI composition can influence the Mg stripping behavior in THF. The Mg SEI composition is closely related to the reactivity of the Mg anode surface with the supporting electrolyte anions. Early studies of Mg batteries suggest that supporting electrolytes based on ClO₄⁻, PF₆⁻, or BF₄⁻ are not compatible with Mg electrodes.⁶¹ Upon anodic polarization, these anions can form insulating SEIs (presumably MgO, MgCl₂, or MgF₂) on the Mg anode surface, inhibiting Mg ion conduction.^{59,86} To investigate the effects of anions on SEI composition, we examine the Mg anodes after anodic polarization in TBAClO₄, TBAOTs, and TBAPF₆ electrolytes *via* XPS.

Figure 3.6a-c shows the Mg 2*p* region of the XPS spectra measured on the Mg anode surface after anodic polarization in THF with TBAClO₄, TBAOTs, and TBAPF₆ supporting electrolytes, respectively. All peak BEs and assignments of the Mg 2*p* and other related regions are tabulated in the Supporting Information. Figure 3.6a

reveals two major Mg^{2+} species in the SEI after anodic polarization in the TBAClO_4 electrolyte. The lower BE peak at 50.5 eV is assigned to MgO .⁸⁷ The higher BE peak at 51.4 eV is assigned to MgCl_2 , which is likely a decomposition product derived from ClO_4^- . A trace amount of $\text{Mg}(\text{ClO}_4)_2$ is observed in the O 1s and Cl 2p regions, however, and the peak in the Mg 2p cannot be resolved from the MgCl_2 peak.⁸⁸ The very low intensity peak at 49.4 eV is ascribed to Mg^0 , which is difficult to see in Figure 3.6a. The assignment is supported by the Mg KLL Auger spectrum, where the $\text{KL}_2\text{L}_3(^1\text{D}_2)$ transition of Mg^0 is observed at 1185.9 eV KE (see SI).^{89,90} The weak Mg^0 signal indicates a comparatively thick SEI layer, which prevents deep X-ray penetration. Figure 3.6b also shows two major Mg species in the SEI after anodic polarization in the TBAOTs electrolyte. Other than MgO (50.9 eV), a higher BE peak at 51.7 eV is assigned to $\text{Mg}(\text{OTs})_2$. A small amount of reduced OTs^- , in the form of 4-methyl-sulfinate, is observed in the S 2p and O 1s spectra, but the peak cannot be resolved from $\text{Mg}(\text{OTs})_2$ in the Mg 2p region. A relatively strong Mg^0 signal at 49.4 eV is observed, indicating a comparatively thin SEI. Figure 3.6c shows the presence of two Mg species in the SEI after anodic polarization in the TBAPF_6 electrolyte. In addition to MgO (50.9 eV), MgF_2 is observed at 52.5 eV due to the decomposition of PF_6^- .⁹¹ The assignment is also supported by a signal at 1176.9 eV in the Mg KLL Auger spectrum (see SI), which is ascribed to MgF_2 .⁹² A strong Mg^0 signal (49.4 eV) is also observed, again indicating a comparatively thin SEI. MgF_2 is also the major Mg^{2+} SEI component formed in the TBABF_4 electrolyte (see SI). Because the SEI is similar for the TBABF_4 electrolyte and the TBAPF_6 electrolyte, we will focus only on characterizing the SEI formed in the TBAPF_6 electrolyte.

The species we identify in the Mg SEIs after anodic polarization are largely electronic insulators. More importantly, most of these phases are binary compounds with very low Mg^{2+} conductivity like MgO , MgCl_2 , and MgF_2 that may prevent Mg stripping.⁹³⁻⁹⁶ Interestingly, although the SEIs formed in TBAOTs and TBAPF_6 are thinner than that formed in TBAClO_4 , a higher anodic current is observed when using a TBAClO_4 electrolyte (Figure 3.5). This observation highlights the importance of the composition of the SEI in affecting Mg stripping. For instance, previous studies have found that even an ultra-thin layer of MgF_2 is enough to fully passivate the Mg surface.⁹⁷

The LSVs and XPS spectra reveal that the SEI of the Mg anode can greatly impact the anodic stripping behavior in THF. To encourage effective Mg stripping, we seek to tailor the electrolyte in hopes of manipulating the SEI composition. Mg

battery research has demonstrated the beneficial effects of Cl^- , Br^- , and I^- on Mg stripping.⁸⁶ Free Cl^- , either generated through electrolyte conditioning or added in the form of metal chloride salts, can enable reversible Mg plating/stripping with low overpotential and high current density in $\text{MgCl}_2\text{-AlCl}_3$,⁹⁸⁻¹⁰⁰ TFSI⁻,^{101,102} and PF_6^- ⁹⁷ based electrolytes. Br^- additives also improve the Mg plating/stripping behavior in Mg bis(hexamethyldisilazide) based electrolyte.¹⁰³ Additionally, both Br^- and I^- additives are able to improve voltage hysteresis in Mg-S batteries by decreasing the passivation layer on the Mg anode.^{86,104} We hypothesize that the halides are readily adsorbed on Mg surfaces, as this process is predicted to be exothermic.¹⁰⁵ Therefore, the reactive anions in the electrolyte have less access to the halide-decorated Mg surfaces, inhibiting Mg electrode passivation.⁸⁶ With this halide effect in mind, we hypothesize that the addition of halide salts as co-supporting electrolytes would affect the SEI composition of the Mg anode.

To probe the effect of halide addition, we focus on adding Br^- to the electrolyte solutions. Figure 3.5 shows the LSVs of the electrolytes after Br^- addition from either LiBr or TBABr. In all cases, the addition of TBABr or LiBr increases the anodic current density, suggesting that Br^- has a beneficial effect on the Mg SEI. Compared to TBABr, LiBr as the co-supporting electrolyte affords lower current densities for Mg stripping in most cases. The comparatively low current densities are likely due to Li^+ coordinating with the anions in the electrolyte, lowering the free anion concentration in the anode EDL, as discussed earlier. Cl^- and I^- additives improve Mg stripping as well (see SI). All onset potentials and current densities at 0.2 V of the LSV experiments are tabulated in Table 3.1.

To understand how Br^- salts affect the SEI composition, we examine the Mg anode surface after anodic polarization in TBA^+ electrolytes with LiBr additive *via* XPS. Figure 3.6d-f shows the Mg 2p regions of the XPS spectra. Three Mg species are observed in the SEI after anodic polarization in $\text{TBAClO}_4/\text{LiBr}$ electrolyte (Figure 3.6b). The peaks at 50.5 eV and 51.5 eV are assigned to MgO and MgCl_2 , respectively.^{87,88} The new signal at 51.0 eV is ascribed to MgBr_2 .⁶⁵ Comparing Figure 3.6a and Figure 3.6b, the addition of LiBr results in decreased MgCl_2 formation as indicated by the decrease in the proportion of MgCl_2 signal to the total signal from Mg^{2+} species. We also approximate the relative thickness of the SEI layers by comparing the area of Mg^{2+} -containing species to the area of the Mg^0 signal, which we give the symbol α :

$$\alpha = A_{\text{Mg}^0} / \sum A_{\text{Mg}^{2+}} \quad (3.1)$$

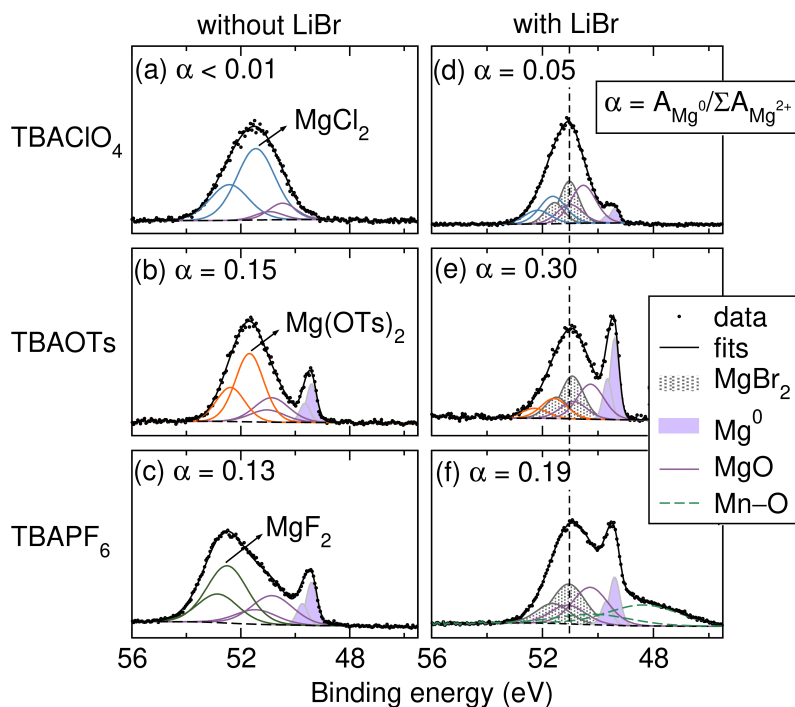


Figure 3.6: Mg 2*p* regions of the XPS spectra of Mg electrodes after the LSV experiments in THF with 0.1 M (a) TBAClO₄, (b) TBAOTs, and (c) TBAPF₆ supporting electrolytes. Mg 2*p* regions of the XPS spectra of Mg electrodes after the LSV experiments in THF with 0.05 M LiBr + 0.05 M (d) TBAClO₄, (e) TBAOTs, and (f) TBAPF₆ supporting electrolytes. The peak at 48.3 eV in (f) is assigned to manganese impurities in the overlapping Mn 3*p* region. The Mn impurity is observed due to extensive Mg stripping in TBAPF₆/LiBr electrolyte. α is the ratio of the area of the Mg⁰ signal and the total area of Mg²⁺-containing species signals. α provides a qualitative assessment of the thickness of the SEI, with lower α indicating thicker SEI. The dashed line indicates the position of MgBr₂ and is a guide for the eye.

Comparing Figure 3.6a and Figure 3.6b, the addition of LiBr leads to increased α ($< 0.01 \rightarrow 0.05$), indicating a comparatively thinner SEI. The addition of LiBr similarly affects the SEI formed in TBAOTs and TBAPF₆ electrolytes (Figure 3.6e,f). With LiBr, less Mg(OTs)₂ and MgF₂ are observed. MgBr₂ becomes the major Mg²⁺ species in the SEI. The new SEI is again comparatively thinner, indicated by the larger α values. The thin, MgBr₂-enriched SEI formed in the presence of Br⁻ additives likely increase the Mg²⁺ conductivity of the surface film, leading to improved Mg stripping behavior observed in Figure 3.5.⁸⁶ All peak BEs and assignments of the Mg 2*p* and other related regions are tabulated in the Supporting Information.

The results discussed above establish the correlation between the SEI composition and Mg stripping efficiency in THF. XPS spectra reveal the formation of passivating

SEIs in TBAClO₄, TBAOTs, TBAPF₆, and TBABF₄ electrolytes. With a halide salt (Cl⁻, Br⁻, and I⁻) co-supporting electrolyte, the modified SEIs are thinner and less passivating which facilitates effective Mg stripping. We envision that modifying the SEI composition *via* halide addition will have important applications in organic electrosynthesis. High cell voltage has been reported in multiple reaction developments when using a Mg sacrificial anode in TBAClO₄, TBAPF₆, and TBABF₄ electrolytes.^{65,69–73} Our research suggests passivating SEI formation as a possible explanation for the observed high cell voltage. The use of halide co-supporting electrolytes can be a simple electrolyte tailoring strategy to improve Mg anode performance in THF in organic electrosynthesis.

Using bromide additives to prevent the reaction of Mg with organohalides during electrolysis

We additionally probe the utility of Br⁻ electrolyte additives on the performance of Mg sacrificial anodes in conditions relevant to electrosynthetic reactions. So far, we have shown that Br⁻ additives yield a functioning SEI and limit reaction with other components of the electrolyte, like ClO₄⁻. Therefore, in our proof-of-concept experiment, we choose to evaluate conditions that demand yet another reactive species: organohalides. Among the substrates commonly used in organic electrosynthesis, organohalides are some of the most versatile yet troublesome due to their high reactivity with Mg metal.⁵⁶ While numerous electrosynthetic methodologies have been successfully developed, the high cell voltage is often observed when a Mg sacrificial anode is used for electrochemical functionalization of organohalides.^{65,68,70,73} We hypothesized that during electrolysis, organohalide substrates can react directly with the Mg anode,⁶⁴ leading to the formation of a high impedance interphase. Therefore, we propose to add Br⁻ to the electrolyte in hopes of forming an interphase that may prevent the reaction of Mg anode with organohalides.

To probe the ability of Br⁻ to modulate reactivity at the Mg surface, we evaluate the effect of Br⁻ addition in the TBAClO₄ electrolyte. The TBAClO₄ electrolyte is a good model electrolyte because we had observed the formation of a thick crust on the surface of Mg during electrochemically driven cross-electrophile coupling of organohalides using the TBAClO₄-THF electrolyte.⁶⁵ The crust is absent when the reaction is performed in a divided cell, which prevents contact between the organohalide and the Mg electrode. Thus, the crust is largely due to the reaction between Mg and the organohalide. To simplify the conditions, we first probe the behavior of the Mg sacrificial anode in the same electrolyte with only the addition of

a single organohalide: t BuBr. A three-electrode cell with a Mg WE, graphite CE, and Ag wire pseudo-RE is used to study the voltage and impedance at the Mg electrode. The electrolyte consists of 0.5 M TBAClO₄ and 0.5 M t BuBr in THF. t BuBr is added as the organohalide, but also serves as a sacrificial reductant. First, galvanostatic stripping of Mg is performed for 2 hours ($j \approx 1 \text{ mA cm}^{-2}$), while the voltage profile at the Mg WE is recorded. Following the galvanostatic oxidation, we measure the interfacial resistance at the Mg electrode using EIS. The chronopotentiometry/EIS protocol is repeated eight times to observe long-term changes in the Mg electrode performance during a typical organic electrosynthesis time frame.

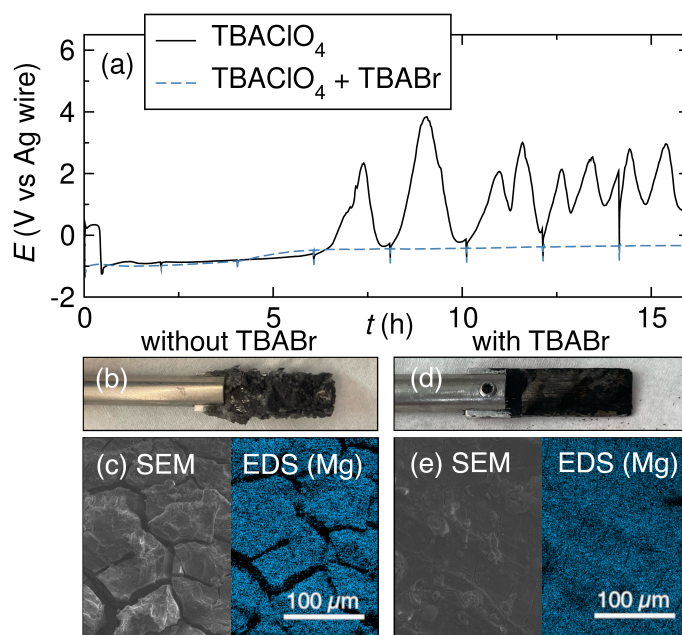


Figure 3.7: (a) Voltage profiles of the Mg WE during galvanostatic Mg stripping ($j \approx 1 \text{ mA cm}^{-2}$) experiments in THF. The experiment is done in two electrolytes: 0.5 M TBAClO₄ and 0.25 M TBAClO₄ + 0.25 M TBABr. The electrolyte contains 0.5 M t BuBr in both cases. EIS is performed every 2 hours (see SI). (b) A photograph and (c) SEM image coupled with EDS of the Mg electrode after Mg stripping in 0.5 M TBAClO₄ with t BuBr show a macroscopic crust and microscopic cracking. (d) A photograph and (e) SEM image coupled with EDS of the Mg electrode after Mg stripping in 0.25 M TBAClO₄ + 0.25 M TBABr with t BuBr show no crust and minimal cracking. The EDS maps show the surface distribution of Mg on the Mg electrodes after the galvanostatic Mg stripping experiments.

Figure 3.7a shows the Mg stripping voltage profile in 0.5 M TBAClO₄/THF electrolyte in the presence of t BuBr. The potential at the Mg electrode increases drastically after 6 hours and fluctuates between -1 V and 4 V vs. Ag wire thereafter. The initial potential increase at the Mg anode is attributed to the formation of a

visibly thick passivation layer (Figure 3.7b), presumably consisting of MgBr_2 and $\text{Mg}(\text{ClO}_4)_2$ salts.⁶⁵ The salt passivation layer is structurally fragile. When the passivation layer grows to a certain limit, some of the salt crust falls off the Mg electrode surface, leading to lower interfacial resistance (see SI) and a sharp decrease of the potential. The dynamic growth and disintegration of the passivation layer is likely the cause of voltage fluctuation during galvanostatic Mg stripping.

The morphology and the surface Mg distribution of the Mg electrode surface are examined using SEM and EDS mapping. To reveal the surface, the MgBr_2 and $\text{Mg}(\text{ClO}_4)_2$ salts are first removed with acetone rinse. The SEM image and corresponding EDS map in Figure 3.7c shows fracture formation on the Mg surface after galvanostatic Mg stripping in the presence of $t\text{BuBr}$. EDS mapping reveals non-uniform Mg distribution on the fractured surface, indicating uneven Mg stripping. We hypothesize that the Mg electrode is corroded upon contact with $t\text{BuBr}$, resulting in a rough electrode surface that has an uneven electric field distribution.^{106–108} The uneven electric field distribution leads to non-uniform Mg stripping, which enhances the roughness of the electrode surface.^{106,109} The fractured surface provides sites for the nucleation of Mg^{2+} salts,¹¹⁰ resulting in an increase in impedance and the observed potential increase at the Mg electrode.

To improve the Mg stripping efficiency in the TBAClO_4 electrolyte and modify the SEI, TBABr is added as a co-supporting electrolyte. With TBABr , the voltage profile during galvanostatic Mg stripping remains stable between -1 V and -0.5 V vs. Ag wire throughout the 16-hour experiment (Figure 3.7a). Visually, we observe minimal salt build-up on the Mg electrode at the end of the experiment (Figure 3.7d). The SEM image and corresponding EDS show a relatively smooth electrode surface with fractures that are much thinner. The EDS mapping reveals a more uniform Mg distribution, indicating even Mg stripping. We suggest that the Br^- -rich SEI on the Mg surface functions as a protecting layer, which limits direct contact of organohalide with the Mg anode. The success of Br^- additives shines a light on its potential application in more complex organic electrosynthesis systems that suffer from passivation build-up on the Mg sacrificial anode.

We note that other electrolyte compositions similarly prevent Mg passivation. The voltage profile of galvanostatic Mg stripping remains stable in TBATFSI and TBAOTf electrolytes (see SI), for example. The Mg anode surface maintains a smooth morphology, giving rise to minimum salt build-up on the electrode. Interestingly, these electrolytes also show large anodic current densities in the LSV

experiments described above. Thus, the SEI in these electrolytes allows for efficient Mg stripping and may also prevent reactivity with organohalides.

3.3 Conclusions

The work described here provides insights into the effect of supporting electrolytes commonly employed in organic electrosynthesis on Mg stripping in THF. The ionic interaction between the cation and the anion of the supporting electrolyte has a significant impact on the Mg stripping efficiency. When the cation is weakly coordinating (e.g. TBA⁺), free anions are widely available in the electrolyte. Upon anodic polarization, the free anions migrate to the positively charged Mg anode surface, forming an EDL that has a high concentration of free anions. The free anions likely facilitate Mg²⁺ transport through the EDL, leading to higher current densities for Mg stripping. When the cation is coordinating (e.g. Li⁺), the concentration of free anions is low, resulting in low Mg stripping efficiency.

However, not all TBA⁺ salts result in beneficial Mg stripping. The anion of the supporting electrolyte must be considered, as well. Anions, such as ClO₄⁻, OTs⁻, PF₆⁻, and BF₄⁻, can react with the Mg surface, forming passivating SEIs that prevent effective Mg stripping. We demonstrate an effective strategy to overcome the passivating SEI. The addition of a halide (Cl⁻, Br⁻, and I⁻) salt improves the Mg stripping significantly due to changes in the SEIs composition. For instance, the addition of Br⁻ yields a thinner SEI that is enriched with MgBr₂, both of which facilitate the Mg stripping process.

The utility of Br⁻ addition is extended to preventing the reaction of Mg with organohalides, a common building block in organic electrosynthesis. The extensive reaction of Mg metal with ^tBuBr manifests as a high impedance crust on the Mg electrode that drives up the cell voltage. The addition of Br⁻ prevents the formation of the crust and yields stable voltage profiles during Mg oxidation, likely due to the SEI preventing the reaction of Mg with the organohalide. Our work demonstrates that understanding the Mg electrode interfaces is crucial to achieving good Mg sacrificial anode performance. The electrolyte tailoring strategies shown here could be used as electrolyte design principles for the optimization of new organic electrosynthetic reactions utilizing a Mg sacrificial anode.

3.4 Methods

Electrolyte Preparation

All electrolytes were prepared in an Ar-filled glovebox. TBATFSI ($\geq 99.0\%$), TBAOTf ($\geq 99.0\%$), TBAClO₄ ($\geq 99.0\%$), TBAOTs (99%), TBAPF₆ ($\geq 99.0\%$), TBABF₄ (99%), TBABr ($\geq 98.0\%$), LiTFSI (99.95%), LiOTf (99.995%), LiClO₄ (99.99%), LiBr ($> 99\%$), LiI (99.9%), and LiCl (99%) were purchased from Sigma-Aldrich. All salts were dried under vacuum at 100 °C overnight prior to use and transferred to the glovebox without exposure to air. THF (99.9%, Fischer Scientific) was dried on a solvent purification system (Pure Process Technology), transferred to the glovebox without exposure to air, and stored over dried 4 Å molecular sieves prior to use. All electrolytes were prepared by stirring the supporting electrolyte of interest in THF until the solution turned homogeneous. Electrolyte conductivity was measured in 5 mL of electrolyte in a 20 mL scintillation vial using a Metrohm 912 conductometer.

Pt|Fc/Fc⁺ Reference Electrode Preparation

The Pt|Fc/Fc⁺ RE was prepared following literature procedure with a 0.5 mm diameter Pt wire (Sigma-Aldrich), ferrocene (Fc, 98%, Sigma-Aldrich), ferrocenium hexafluorophosphate (FcPF₆, 95%, Combi-Blocks), TBAPF₆, and THF.^{111–113} Fc and TBAPF₆ were recrystallized prior to use. The Pt wire, cleaned in concentrated HNO₃ and heated in a H₂ flame prior to use, was sealed within a ceramic-fritted glass tube (inner diameter 3.5 mm, Pine Research Instrumentation). The glass tube was filled with an electrolyte of 4 mM Fc, 4 mM FcPF₆, and 0.1 M TBAPF₆ in THF. The RE was assembled fresh prior to each experiment.

Electrochemical Testing

All electrochemical experiments were performed in an Ar-filled glovebox in a low volume, three-electrode cell (Pine Research Instrumentation). The Mg plate electrodes (2 mm x 8 mm x 30 mm, 99.95%, IKA) were mechanically ablated within the glovebox prior to use. LSV experiments to probe Mg stripping were performed with a Mg plate as the WE, a graphite CE (Pine Research Instrumentation), the Pt|Fc/Fc⁺ RE, and approximately 7 mL of electrolyte. Each electrolyte was prepared with 0.1 M supporting electrolyte. Chronopotentiometry experiments were performed with a Mg WE, graphite CE, Ag wire (Pine Research Instrumentation) as a pseudo-RE, and approximately 7 mL of electrolyte. The electrolyte was prepared with 0.5 M supporting electrolyte and 0.5 M ^tBuBr (98%, Sigma-Aldrich) as the sacrificial oxidant. EIS experiments were performed with ± 10 mV sinus amplitude from 10⁶-1 Hz at 10 points per decade. All electrochemical experiments were conducted on a VMP3 potentiostat (Bio-Logic).

Sample Characterization

Raman spectra were collected using a HORIBA Instruments XploRA PLUS Raman spectrometer. Spectra were collected in a screw-cap cuvette to prevent exposure to air. All spectra were collected by averaging 40 acquisitions lasting 5 s each with an 1800 gr/mm grating, 50 μm slit, and 500 μm hole. The excitation wavelength was 785 nm. Peaks were fit with Voigt line shapes.¹¹⁴

SEM and EDS samples were prepared following chronopotentiometry experiments by rinsing the electrode thrice with acetone in the glovebox to dissolve adsorbed species. The electrodes were then dried in ambient glovebox conditions for 1 h. The samples were briefly exposed to air (< 5 min) when loaded into the instrument. SEM data were collected on a ZEISS 1550VP field emission SEM using a 10 kV acceleration voltage and an in-lens secondary electron detector. EDS data were collected using a silicon drift EDS detector (Oxford X-MAX 80 mm²) with a 30 kV acceleration voltage.

XPS measurements were performed on Mg anode surfaces after LSV experiments. After the LSV scans, the cells were disassembled inside an Ar-filled glovebox and the Mg electrode was removed. Each Mg electrode was rinsed with 10 mL of THF and dried in ambient glovebox conditions for at least 48 h before analysis. The samples were briefly exposed to air (< 10 s) during transfer to the XPS. XPS data were collected using a Kratos Axis Ultra system at a pressure < 3×10^{-9} Torr. Samples were irradiated with a monochromatic Al K α source (1486.7 eV) at 150 W. Low-resolution survey spectra were acquired between BEs of 1-1200 eV. Higher-resolution detailed scans, with a resolution of 0.05 eV (or 0.1 eV for Mg KLL) and a pass energy of 10 eV, were collected on individual XPS lines of interest. The XPS data were analyzed using CasaXPS analysis software, and individual peaks of interest were fit with Shirley backgrounds. Peaks were fit using mixed Gaussian-Lorentzian line shapes. Spectra were referenced to Mg⁰ at 49.4 eV. The Mg⁰ signal was chosen as the reference due to the complicated C 1s and O 1s signals resulting from the electrolytes.

Computational Methods

Classic MD simulations were performed by using the Forcite module in Materials Studio 2020 with COMPASS III force field (see SI for details of forcefield types).¹¹⁵ The electrostatic interactions were computed using the three-dimensional Ewald summation,^{116,117} and van der Waals interactions were computed using the atom-

based summation with a 12.5 Å cutoff distance. Temperature control was achieved using the Nose-Hoover method,^{118,119} while pressure control was achieved using the Berendsen method.¹²⁰

To capture the electrode-electrolyte interfacial properties, slab-geometry simulation boxes were employed, where two graphene slabs served as the electrode surfaces and the liquid electrolyte was confined between the slabs. The dimensions of the simulation box were 34.03 Å × 34.48 Å × 450.00 Å. The schematic view of the geometry of MD boxes is provided in SI. The distance between the slabs was adjusted to reproduce the simulated densities of bulk liquids, which are listed in SI. Periodic boundary conditions were applied in all three directions. An extra vacuum space around three times of the electrolyte length was introduced along the z direction (perpendicular to the slabs) in order to eliminate the interactions between the original box and their z-direction mirror images.¹¹⁶ The constant surface charge densities of the two graphene slabs were set as $\pm 0.7 \text{ e/nm}^2$, respectively. An amorphous cell module in Materials Studio was used to build all the initial structures. We simulated six different salt species: LiTFSI, TBATFSI, LiOTf, TBAOTf, LiClO₄, and TBAClO₄. The composition of each system was 30 salt species and 800 THF molecules, corresponding to a 0.5 M THF solution.

To ensure accurate density calculations, the bulk phases in cubic boxes were relaxed using the NPT ensemble at 298 K and 1 bar for 1000 ps. The last 600 ps of each NPT trajectory was used for density calculation. Then bulk phase systems with the calculated density were simulated under the NVT ensemble at 298 K for 1000 ps as the equilibrium run. Then production runs were conducted for 3000 ps. The calculation of the cation–anion RDFs is provided in SI. The slab-geometry systems were simulated with NVT ensemble at 298 K for 4000 ps, with the last 3000 ps as the production run for structure analysis. The number density distributions were calculated with 0.5 Å bin size.

3.5 Supporting Information

Linear sweep voltammograms of Mg stripping

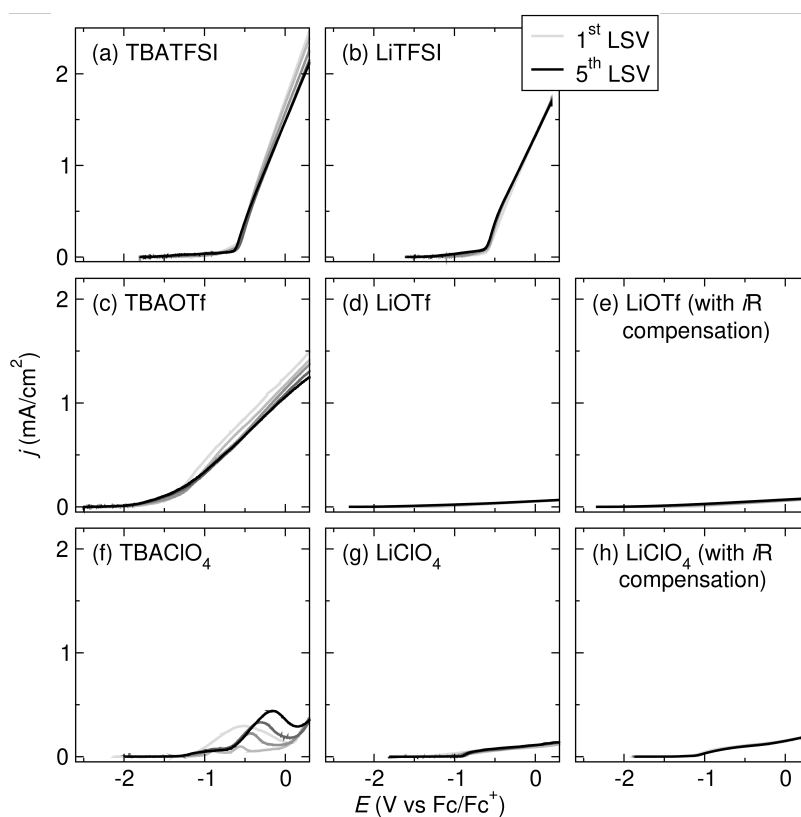


Figure 3.S1: Linear sweep voltammograms of Mg stripping in THF with TBA⁺ and Li⁺ supporting electrolytes. All voltammograms were collected at a scan rate of 5 mV s⁻¹. For each electrolyte, five LSVs were collected with a 10 min OCV between scans. For (e) and (h), the LSVs were collected with 85% iR compensation

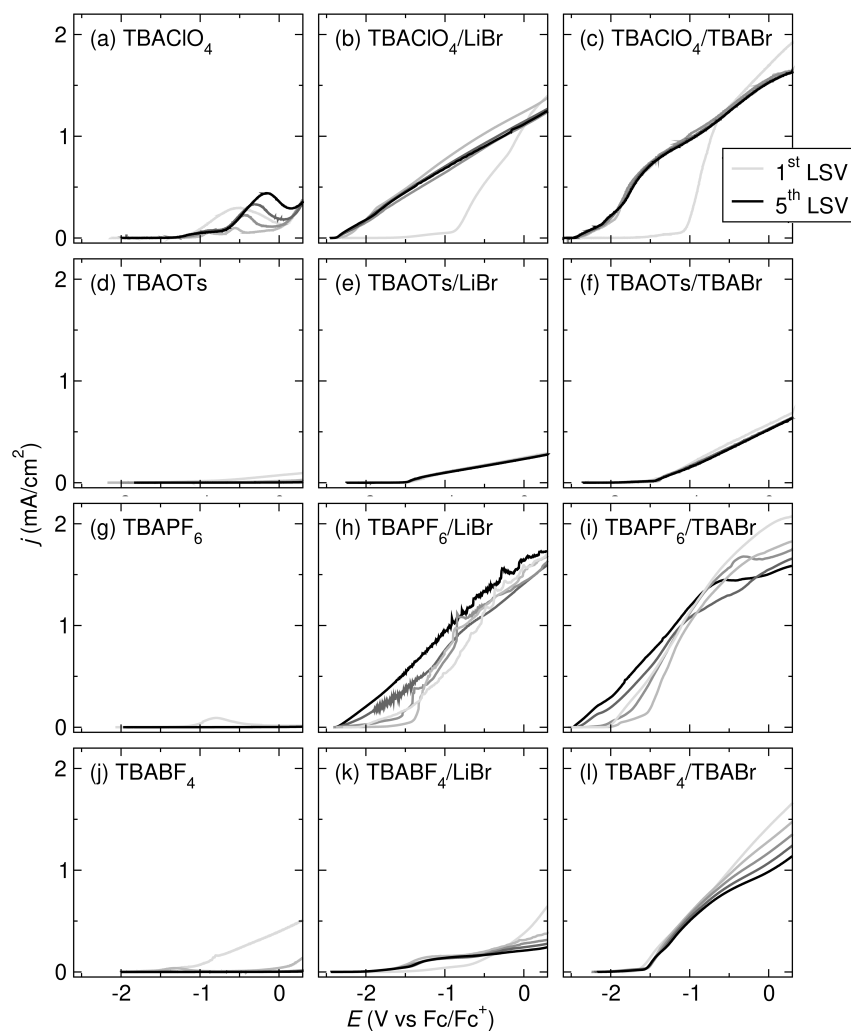


Figure 3.S2: Linear sweep voltammograms of Mg stripping in THF with and without Br^- co-supporting electrolyte. All voltammograms were collected at a scan rate of 5 mV s^{-1} . For each electrolyte, five LSVs were collected with a 10 min OCV between scans.

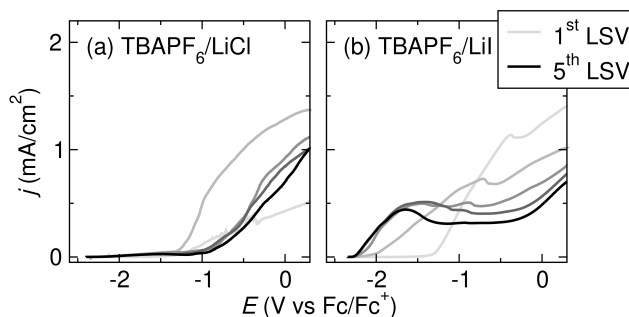


Figure 3.S3: Linear sweep voltammograms of Mg stripping in THF with TBAPF₆/LiX supporting electrolyte. All voltammograms were collected at a scan rate of 5 mV s⁻¹. For each electrolyte, five LSVs were collected with a 10 min OCV between scans.

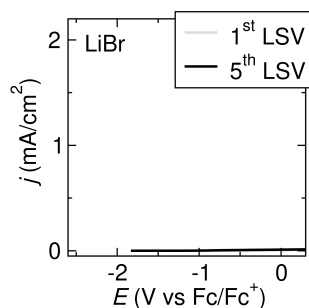


Figure 3.S4: Linear sweep voltammograms of Mg stripping in THF with LiBr supporting electrolyte. All voltammograms were collected at a scan rate of 5 mV s⁻¹. For each electrolyte, five LSVs were collected with a 10 min OCV between scans. LSV in TBABr/THF was not collected due to the low solubility of TBABr in THF.

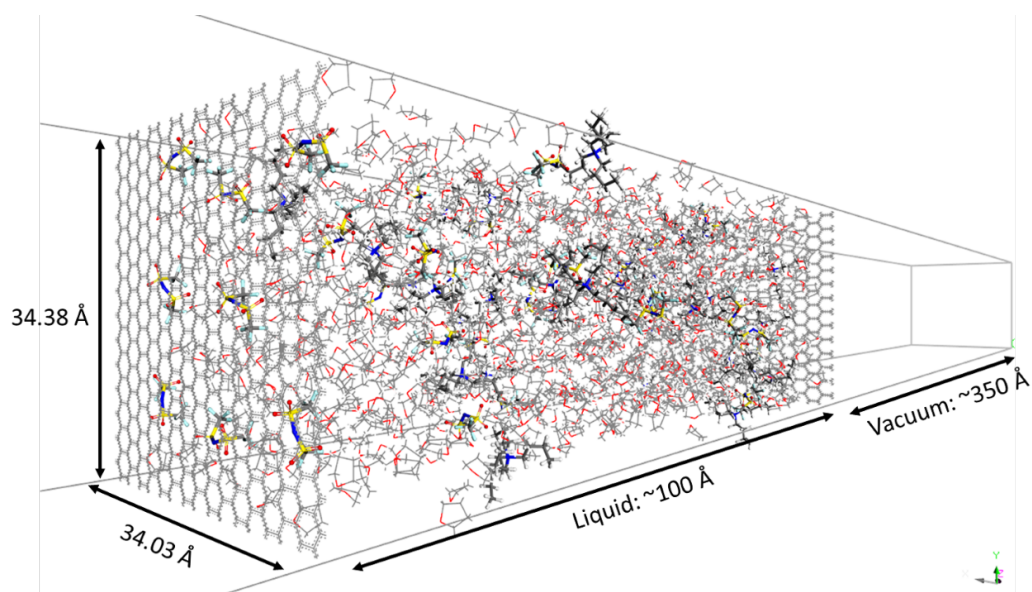
Schematic view of the MD simulation box

Figure 3.S5: Snapshot at 4000 ps of TBATFSI electrolyte as an example of the geometry of the MD simulation box.

Force field details

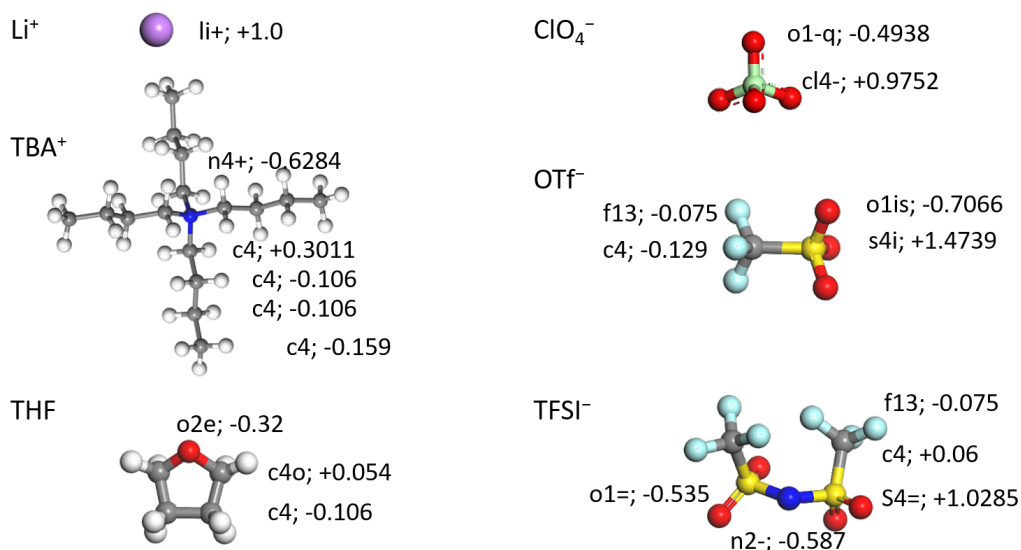


Figure 3.S6: Electrolyte species investigated in this work, including THF, Li⁺, TBA⁺, ClO₄⁻, OTf⁻, and TFSI⁻. Representative atom forcefield types and atomic charges are given accordingly. The charges were assigned by the according COM-PASSIII forcefield type. The forcefield type of hydrogen atoms were automatically assigned by the Forcite module in Materials Studio 2020, unless otherwise specified.

Simulated densities

System	Bulk density (g/mL)	Salt molarity (mol/L)	Distance between slabs (Å)
LiClO ₄	0.952	0.492	97.4
TBAClO ₄	0.920	0.433	109.8
LiOTf	0.929	0.428	98.7
TBAOTf	0.944	0.485	111.1
LiTFSI	0.985	0.475	100.5
TBATFSI	0.962	0.419	113.3

Table 3.S1: The densities of the bulk phases were computed from the last 600 ps of each 1 ns NPT trajectory using cubic boxes. Each system consists of 30 salt species and 800 THF molecules. The distance between the graphene slabs in the slab-geometry cells was adjusted to match the simulated densities of bulk solutions.

DFT binding energy

The binding energies of cation-anion and cation-solvent interactions and anions were calculated by the Gaussian (G09) package using density functional theory (DFT).¹²¹ The M06-2X/6-31+G(d,p) level of theory¹²² along with the D3 dispersion correction¹²³ is used without applying the basis set superposition error (BSSE) correction. Their performance on describing noncovalent interactions¹²⁴ and binding energies of supramolecular complexes,¹²⁵ anions,^{126,127} hydrogen-bonded ions,¹²⁸ and sulfuric acid containing clusters,¹²⁹ have been well discussed in the literature. As a common choice for calculating binding energies for similar systems, they have been used to calculate binding energies of different ions in organic solvents for battery electrolytes. 3 The energies were obtained from gas phase geometry optimization and the bonding energies are calculated as

$$\Delta E_{\text{bonding}} = E_{A-B} - (E_A + E_B)$$

To validate the force fields, the binding energies were calculated using the force fields also by the above equation, and compared with the DFT results.

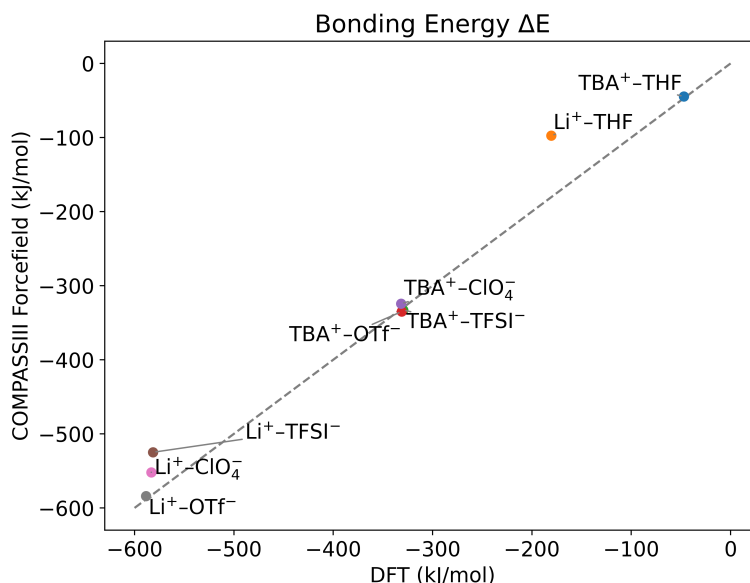


Figure 3.S7: Bonding energies of ion pairs. Li⁺ in general form stronger ionic bond compared to TBA⁺. The DFT results and the forcefield results are consistent in terms of this trend.

Radial distribution functions (RDF) in bulk phase

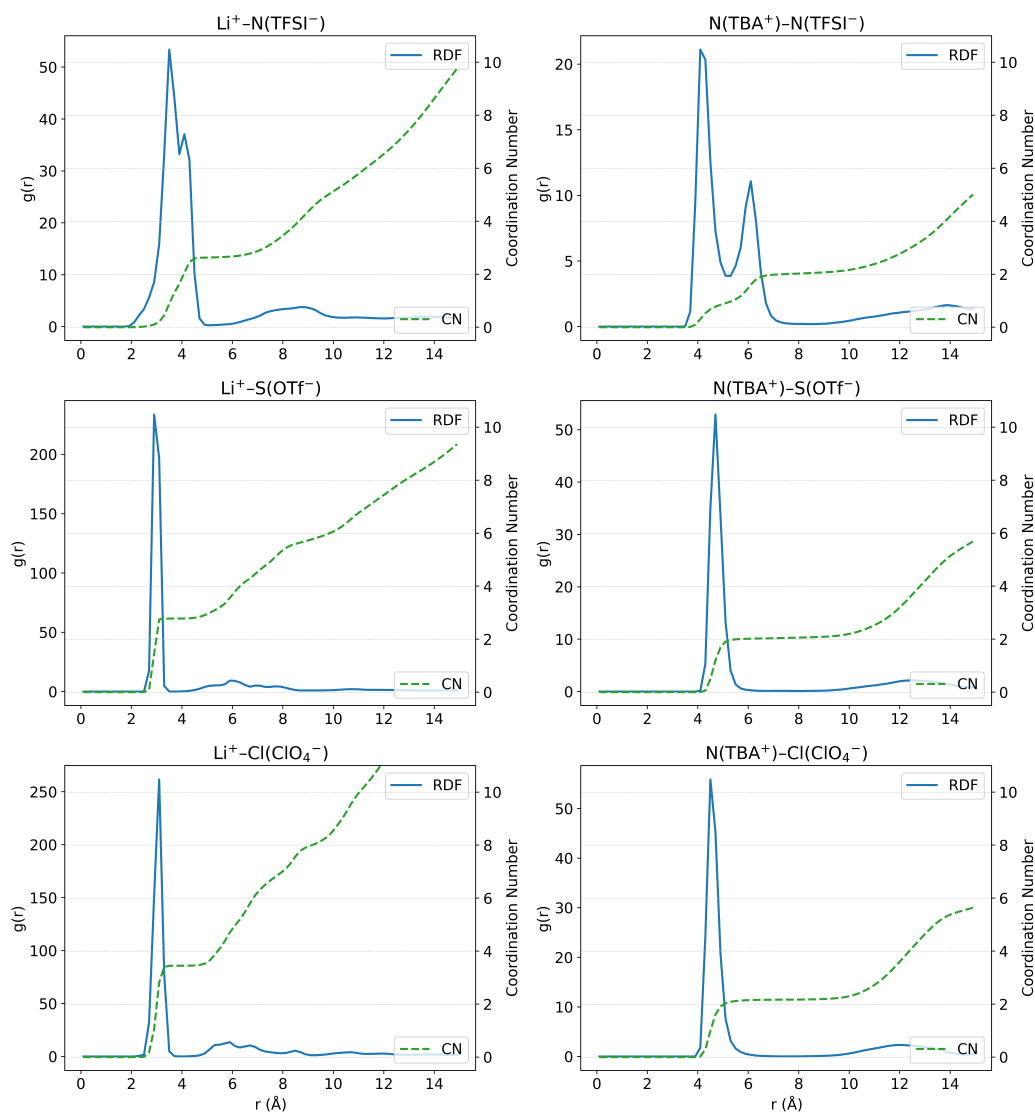


Figure 3.S8: Radial distribution function (RDF) $g(r)$ and coordination number (CN) plots of cation-anion association. The RDFs were calculated from the production runs of bulk phases using 0.2 Å bin size. The distance cutoffs to determine “free or coordinated” ions were based on the distance where the first RDF peak ends. The cutoff values are $\text{N}(\text{TBA}^+)$ - $\text{N}(\text{TFSI}^-)$: 7 Å, $\text{N}(\text{TBA}^+)$ - $\text{S}(\text{OTf}^-)$: 6 Å, $\text{N}(\text{TBA}^+)$ - $\text{Cl}(\text{ClO}_4^-)$: 6 Å, Li^+ - $\text{N}(\text{TFSI}^-)$: 5 Å, Li^+ - $\text{S}(\text{OTf}^-)$: 3.5 Å, Li^+ - $\text{Cl}(\text{ClO}_4^-)$: 3.5 Å.

XPS data

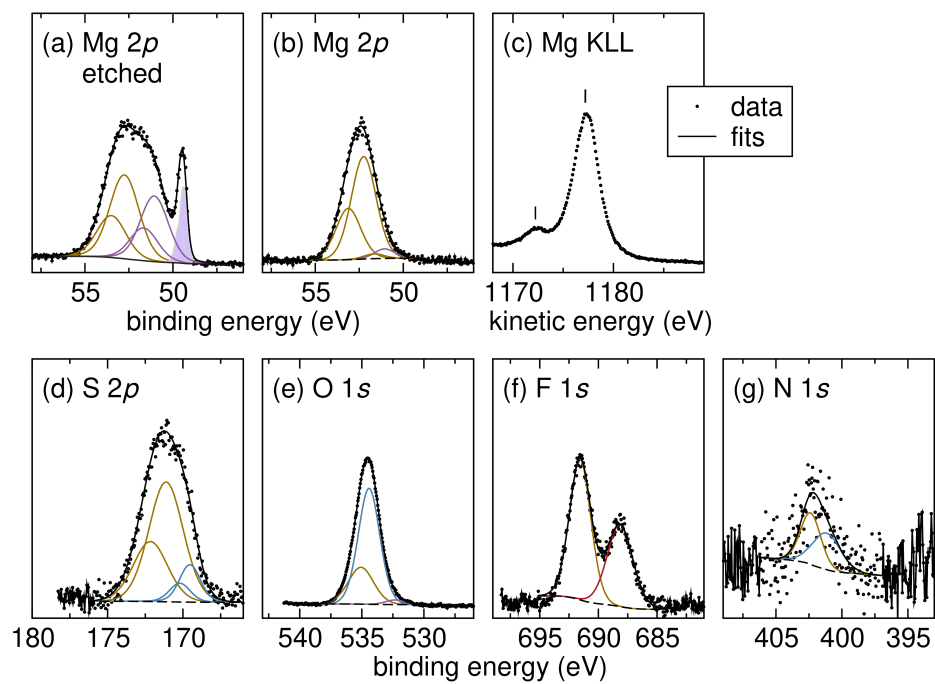


Figure 3.S9: X-ray photoelectron spectra of Mg electrodes after the LSV experiments in THF with TBATFSI as the supporting electrolyte.

Figure	Peak binding energy (eV)	Assignment
Figure 3.S9a. Mg 2 <i>p</i>	49.4	Mg ⁰
	51.1	MgO
	52.8	Mg(TFSI) ₂ /Mg(NSOCF ₃) ₂
Figure 3.S9b. Mg 2 <i>p</i>	51.1	MgO
	52.3	Mg(TFSI) ₂ /Mg(NSOCF ₃) ₂
Figure 3.S9d. S 2 <i>p</i>	169.5	Mg(NSOCF ₃) ₂
	171.1	Mg(TFSI) ₂
Figure 3.S9e. O 1 <i>s</i>	532.3	MgO
	534.4	Mg(NSOCF ₃) ₂
	535.1	Mg(TFSI) ₂
Figure 3.S9f. F 1 <i>s</i>	688.2	-CF ₂
	691.5	-CF ₃
Figure 3.S9g. N 1 <i>s</i>	401.2	Mg(NSOCF ₃) ₂
	402.4	Mg(TFSI) ₂
Peak kinetic energy (eV)		
Figure 3.S9c. Mg KLL	1172.6	bulk plasmon
	1177.4	Mg ²⁺

Table 3.S2: Peak assignments of the X-ray photoelectron spectra of Mg electrodes after the LSV experiments in THF with TBATFSI as the supporting electrolyte.

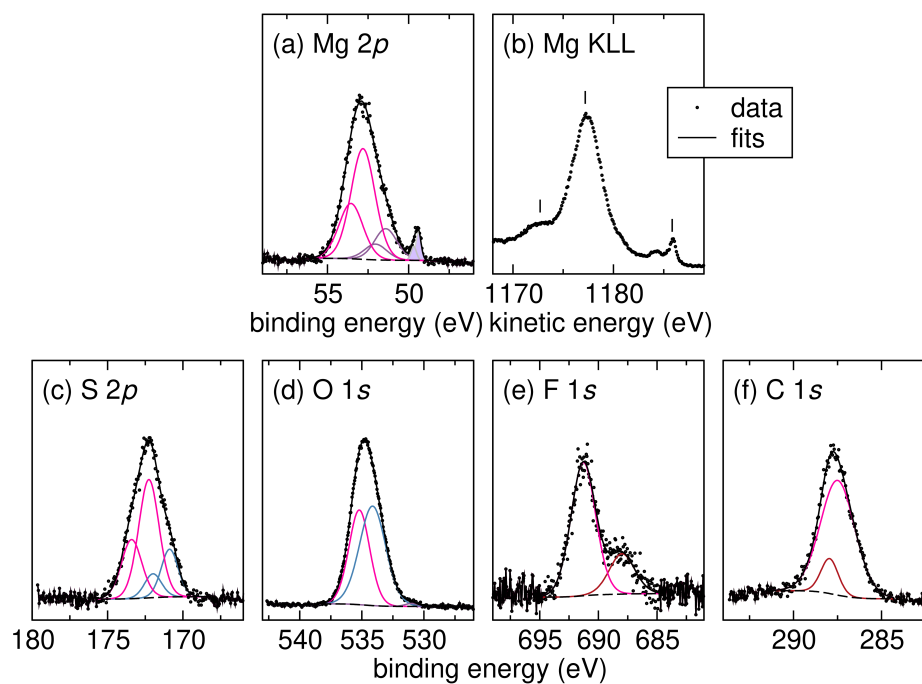


Figure 3.S10: X-ray photoelectron spectra of Mg electrodes after the LSV experiments in THF with TBAOTf as the supporting electrolyte.

Figure	Peak binding energy (eV)	Assignment
Figure 3.S10a. Mg 2 <i>p</i>	49.4	Mg ⁰
	51.4	MgO
	51.7	Mg(OTf) ₂ /Mg(SO ₂ CF ₃) ₂
Figure 3.S10c. S 2 <i>p</i>	170.9	Mg(SO ₂ CF ₃) ₂
	172.3	Mg(OTf) ₂
Figure 3.S10d. O 1 <i>s</i>	531.0	MgO
	534.1	Mg(SO ₂ CF ₃) ₂
	535.2	Mg(OTf) ₂
Figure 3.S10e. F 1 <i>s</i>	688.0	-CF ₂
	691.3	-CF ₃
Figure 3.S10f. C 1 <i>s</i>	287.5	-CF ₃
	288.0	-CF ₂
Peak kinetic energy (eV)		
Figure 3.S10b. Mg KLL	1172.9	bulk plasmon
	1177.4	Mg ²⁺
	1185.9	Mg ⁰

Table 3.S3: Peak assignments of the X-ray photoelectron spectra of Mg electrodes after the LSV experiments in THF with TBAOTf as the supporting electrolyte.

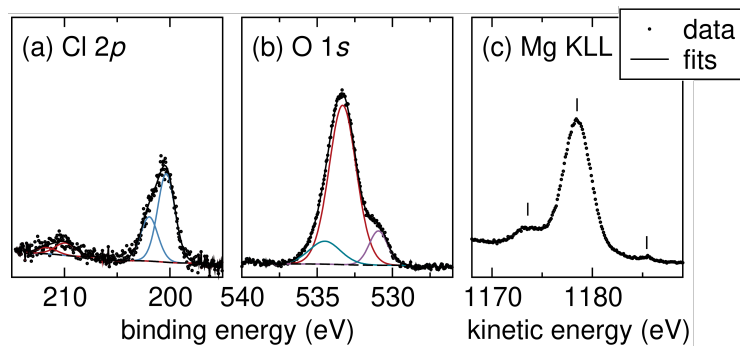


Figure 3.S11: X-ray photoelectron spectra of Mg electrodes after the LSV experiments in THF with TBAClO₄ as the supporting electrolyte.

Figure	Peak binding energy (eV)	Assignment
Figure 3.6a. Mg 2 <i>p</i>	49.4	Mg ⁰
	50.5	MgO
	51.4	MgCl ₂ /Mg(ClO ₄) ₂
Figure 3.S11a. Cl 2 <i>p</i>	200.4	MgCl ₂
	209.9	Mg(ClO ₄) ₂
Figure 3.S11b. O 1 <i>s</i>	530.9	MgO
	533.3	Mg(ClO ₄) ₂
	534.5	C=O
Peak kinetic energy (eV)		
Figure 3.S11c. Mg KLL	1173.9	bulk plasmon
	1178.9	Mg ²⁺
	1185.9	Mg ⁰

Table 3.S4: Peak assignments of the X-ray photoelectron spectra of Mg electrodes after the LSV experiments in THF with TBAClO₄ as the supporting electrolyte.

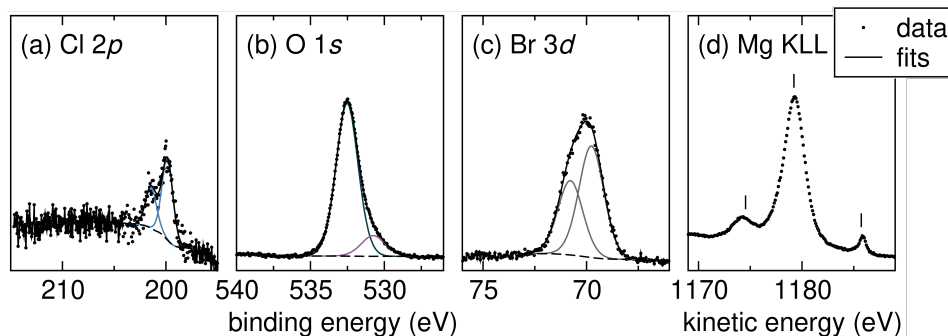


Figure 3.S12: X-ray photoelectron spectra of Mg electrodes after the LSV experiments in THF with TBAClO₄/LiBr as the supporting electrolyte.

Figure	Peak binding energy (eV)	Assignment
Figure 3.6b. Mg 2 <i>p</i>	49.4	Mg ⁰
	50.8	MgO
	51.2	MgBr ₂
	51.8	MgCl ₂
Figure 3.S12a. Cl 2 <i>p</i>	200.1	MgCl ₂
Figure 3.S12b. O 1 <i>s</i>	530.7	MgO
	532.5	C–O
Figure 3.S12c. Br 3 <i>d</i>	69.9	MgBr ₂
Peak kinetic energy (eV)		
Figure 3.S12d. Mg KLL	1174.6	bulk plasmon
	1179.0	Mg ²⁺
	1185.8	Mg ⁰

Table 3.S5: Peak assignments of the X-ray photoelectron spectra of Mg electrodes after the LSV experiments in THF with TBAClO₄/LiBr as the supporting electrolyte.

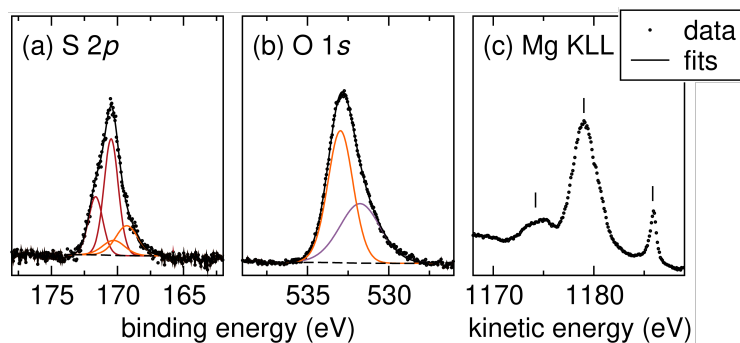


Figure 3.S13: X-ray photoelectron spectra of Mg electrodes after the LSV experiments in THF with TBAOTs as the supporting electrolyte.

Figure	Peak binding energy (eV)	Assignment
Figure 3.6c. Mg 2p	49.4	Mg ⁰
	50.9	MgO
	51.7	Mg(OTs) ₂
Figure 3.S13a. S 2p	169.3	Mg(OTs) ₂
	170.5	S–C
Figure 3.S13b. O 1s	531.8	MgO
	533.0	Mg(OTs) ₂
Peak kinetic energy (eV)		
Figure 3.S13c. Mg KLL	1174.4	bulk plasmon
	1179.2	Mg ²⁺
	1185.9	Mg ⁰

Table 3.S6: Peak assignments of the X-ray photoelectron spectra of Mg electrodes after the LSV experiments in THF with TBAOTs as the supporting electrolyte.

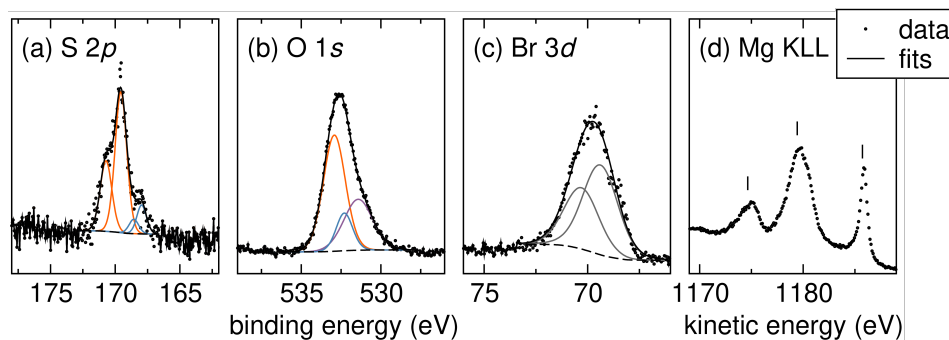


Figure 3.S14: X-ray photoelectron spectra of Mg electrodes after the LSV experiments in THF with TBAOTs/LiBr as the supporting electrolyte.

Figure	Peak binding energy (eV)	Assignment
Figure 3.6d. Mg 2 <i>p</i>	49.4	Mg ⁰
	50.3	MgO
	50.9	MgBr ₂
	51.6	Mg(OTs) ₂ /Mg(SO ₂ C ₆ H ₄ CH ₃) ₂
Figure 3.S14a. S 2 <i>p</i>	168.0	Mg(SO ₂ C ₆ H ₄ CH ₃) ₂
	169.6	Mg(OTs) ₂
Figure 3.S14b. O 1 <i>s</i>	531.4	MgO
	532.3	Mg(SO ₂ C ₆ H ₄ CH ₃) ₂
	532.9	Mg(OTs) ₂
Figure 3.S14c. Br 3 <i>d</i>	69.4	MgBr ₂
Peak kinetic energy (eV)		
Figure 3.S14d. Mg KLL	1174.9	bulk plasmon
	1179.8	Mg ²⁺
	1185.9	Mg ⁰

Table 3.S7: Peak assignments of the X-ray photoelectron spectra of Mg electrodes after the LSV experiments in THF with TBAOTs/LiBr as the supporting electrolyte.

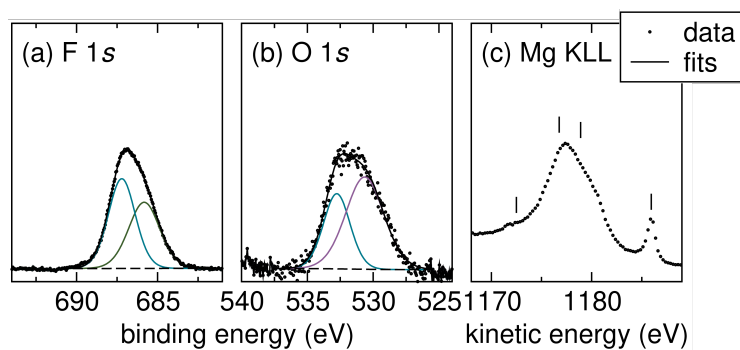


Figure 3.S15: X-ray photoelectron spectra of Mg electrodes after the LSV experiments in THF with TBAPF₆ as the supporting electrolyte.

Figure	Peak binding energy (eV)	Assignment
Figure 3.6e. Mg 2p	49.4	Mg ⁰
	50.9	MgO
	52.5	MgF ₂
Figure 3.S15a. F 1s	685.7	MgF ₂
	687.1	C–F
Figure 3.S15b. O 1s	530.6	MgO
	532.7	C–O
Peak kinetic energy (eV)		
Figure 3.S15c. Mg KLL	1173.0	bulk plasmon
	1176.9	MgF ₂
	1179.3	other Mg ²⁺
	1186.0	Mg ⁰

Table 3.S8: Peak assignments of the X-ray photoelectron spectra of Mg electrodes after the LSV experiments in THF with TBAPF₆ as the supporting electrolyte.

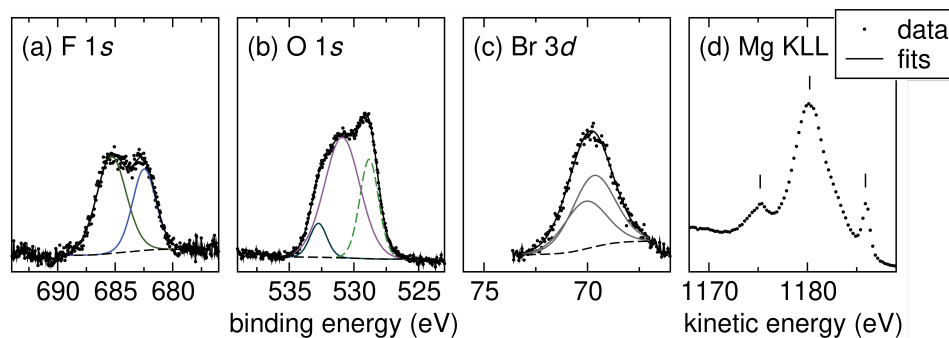


Figure 3.S16: X-ray photoelectron spectra of Mg electrodes after the LSV experiments in THF with TBAPF₆/LiBr as the supporting electrolyte.

Figure	Peak binding energy (eV)	Assignment
Figure 3.6b. Mg 2 <i>p</i>	49.4	Mg ⁰
	50.7	MgO
	51.0	MgBr ₂ /MgF ₂
	48.3	Mn–O
Figure 3.S16a. F 2 <i>p</i>	682.5	MF
	685.3	MgF ₂
Figure 3.S16b. O 1 <i>s</i>	528.8	Mn–O
	530.9	MgO
	532.7	C–O
Figure 3.S16c. Br 3 <i>d</i>	69.7	MgBr ₂
Peak kinetic energy (eV)		
Figure 3.S16d. Mg KLL	1174.9	bulk plasmon
	1180.5	Mg ²⁺
	1185.9	Mg ⁰

Table 3.S9: Peak assignments of the X-ray photoelectron spectra of Mg electrodes after the LSV experiments in THF with TBAPF₆/LiBr as the supporting electrolyte.

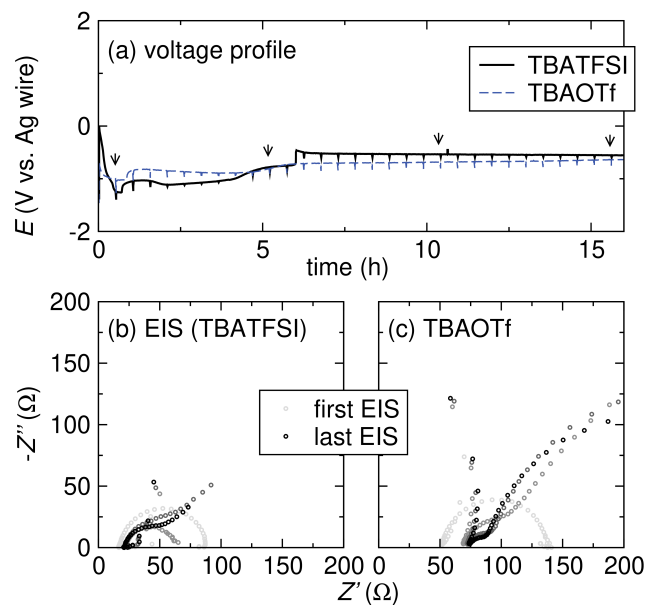


Figure 3.S17: (a) Voltage profiles on the Mg working electrodes of the galvanostatic Mg stripping ($j = 1 \text{ mA/cm}^2$) experiments in THF in the presence of 0.5 M *t*BuBr with 0.5 M TBATFSI or 0.5 M TBAOTf. EIS was performed every 30 min during the galvanostatic Mg stripping experiments. EIS of the Mg working electrodes in (b) 0.5 M TBATFSI electrolyte, and (c) 0.5 M TBAOTf electrolyte. Only the 1st, 10th, 20th, 30th EIS are shown here. The time points are indicated by arrows in (a)

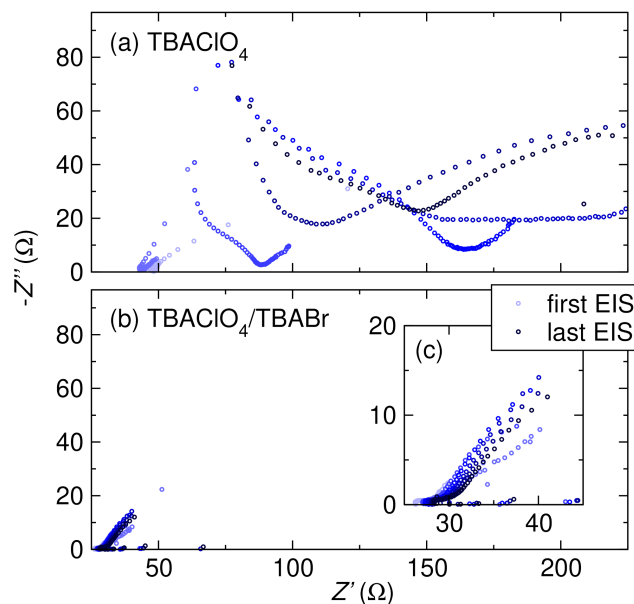
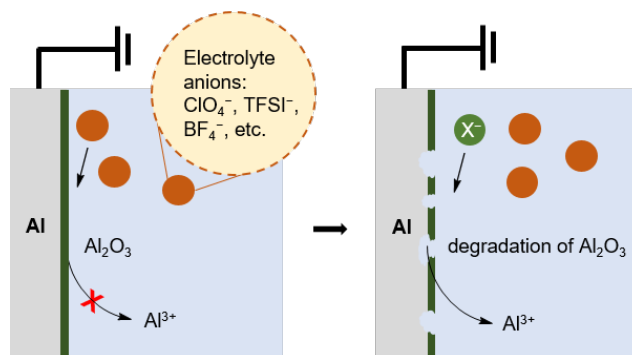


Figure 3.S18: EIS of the Mg working electrodes during galvanostatic Mg stripping in the presence of 0.5 M *t*BuBr in (a) 0.5 M TBAClO₄ electrolyte, and (b) 0.25 M TBAClO₄ + 0.25 M TBABr electrolyte. Comparing (a) and (b), the Mg interface is more stable in TBAClO₄/LiBr electrolyte.

Chapter 4

ENABLING AL SACRIFICIAL ANODES IN
TETRAHYDROFURAN ELECTROLYTES FOR REDUCTIVE
ELECTROSYNTHESIS

Abstract: Al^0 is widely used as a sacrificial anode in organic electrocatalysis. However, there remains a notable knowledge gap in the understanding of Al anode interface chemistry under electrolysis conditions. This knowledge gap might play a pivotal role in the discernible bias observed in solvent selections for reductive electrocatalysis. The majority of existing methodologies that employ an Al sacrificial anode utilize DMF as the preferred solvent, with only isolated examples of ethereal solvents such as THF. Given the crucial role of the solvent in determining the efficiency and selectivity of an organic reaction, such limitation on solvent choices could significantly hinder substrate reactivity and impede the desired transformations. In this study, we aim to understand the Al metal interfaces and manipulate them to improve the performance of an Al sacrificial anode in THF-based electrolytes. We have discovered that the presence of free halide ions (Cl^- , Br^- , I^-) in the electrolyte is crucial for efficient Al stripping. By incorporating halide additive, we have achieved bulk Al stripping in THF-based electrolytes and successfully improved the cell potentials of electrochemically driven reductive methodologies. We hope this study will encourage the use of ethereal solvents in systems using Al sacrificial anodes and guide future endeavors in optimizing electrolytes for reductive electrocatalysis.



4.1 Introduction

Electrosynthesis has emerged as a green and efficient approach for the preparation of valuable organic molecules. In recent years, a wide array of cathodic reduction methodologies has been developed.^{48–51} The setup of these reductive electrosynthesis often involves a metal sacrificial anode in an undivided cell. During electrolysis, metal stripping takes place at the sacrificial anode, forming soluble metal cations that dissolve into the reaction mixture.^{56,57,76,130} Al is commonly employed as a sacrificial anode material for reductive electrosynthesis. It is the most abundant metal element in the Earth's crust while having a low oxidation potential of -1.67 V vs. SHE.¹³¹ Upon oxidation, each Al atom is able to exchange for three electrons ($\text{Al} \rightarrow \text{Al}^{3+} + 3\text{e}^-$). As a result, Al has a high theoretical volumetric capacity of 8050 mAh/cm³ compare to other commonly used sacrificial anode material (Figure 4.1a).^{131–133} The significantly higher volumetric capacity of Al theoretically allows for a larger scale reductive reaction to be sustained within the same volume of sacrificial anode consumed, making Al an appealing option for reductive electrosynthesis.

Despite its desirable properties, Al presents a challenge as a sacrificial anode material due to its high affinity to oxygen. The standard Gibbs free energy of formation ($\Delta_f G^\circ$) of Al_2O_3 at standard conditions is -378.2 kcal/mol.¹³⁴ Consequently, a layer of Al_2O_3 will spontaneously form on a nascent Al surface when the electrode is prepared in air or exposed to an oxidizing media. The layer formation is found to be essentially instantaneous.¹³⁵ While the oxide layer maintains electronic conductivity, the high bond dissociation energy of Al–O ($D^\circ = 120 \pm 2.5$ kcal/mol) creates a substantial barrier for Al stripping (Figure 4.1b).¹³⁴ Further, we suspect that Al^{3+} cannot conduct through the Al_2O_3 surface layer, thereby shutting down any oxidative electrochemistry.

To achieve effective Al stripping in reductive electrosynthesis, it is therefore crucial to control the interface chemistry to prevent the complete passivation of Al by Al_2O_3 during electrolysis. However, the traditional approach of electrochemical reaction optimization typically focuses on achieving a high yield of the organic product. As a result, the effects of solvent, supporting electrolyte, and substrates on the metal sacrificial anode interfaces are rarely discussed, and the performance of Al sacrificial anode under different reductive electrosynthesis conditions is not well understood.^{67,130} Although there isn't a thorough comprehension of the chemical processes occurring at the metal interfaces, the empirical optimization approach has

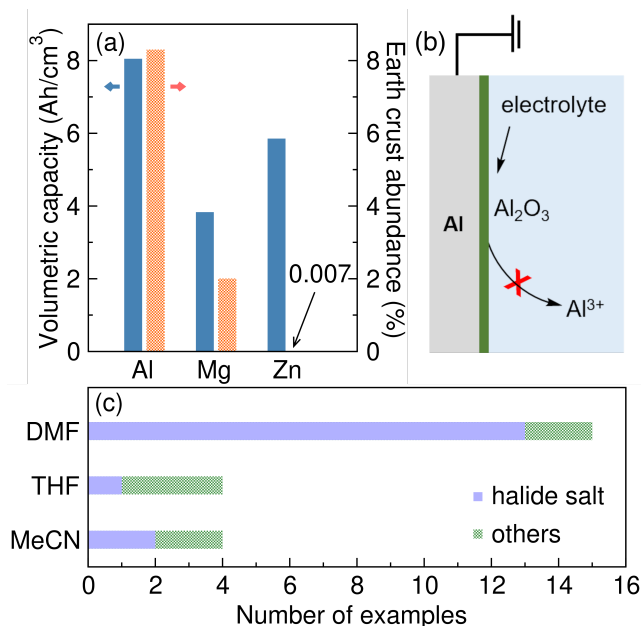


Figure 4.1: Al metal is commonly used as sacrificial anode in reductive organic electrosynthesis. (a) Compare to Mg and Zn, Al has a higher theoretical volumetric capacity and is notably more abundant in the Earth's crust. (b) However, a layer of Al₂O₃ may form on the surface, inhibiting electrochemical Al stripping in organic electrolytes. (c) Among the reductive electrosynthesis methodologies reported since 2000, halide salt/DMF solution is the most popular choice of electrolyte.

some success identifying conditions compatible with an Al sacrificial anode.^{50,76} Interestingly, there is a discernible bias observed in the solvent selection among the reported methodologies that utilize Al sacrificial anodes. As shown in Figure 4.1c, most of the reactions adopt halide salt/DMF solution as the optimal electrolyte^{136–148} with isolated example of TBABF₄/DMF electrolyte^{147,149}. On the contrary, much fewer reactions were successfully optimized in THF and MeCN-based electrolytes.^{150–157} Since solvent can dramatically impact the efficiency and selectivity of an organic reaction, the potential limitation on solvent selection when utilizing an Al sacrificial anode makes it challenging to expand the application of reductive electrosynthesis to various types of organic transformations.

Here, we investigate the Al interphases with the aim to improve the efficacy of Al sacrificial anodes in THF-based electrolytes. THF, in comparison to DMF and MeCN, exhibits weaker coordination ability and possesses a significantly lower dielectric constant of 7.5 (vs. 38.3 for DMF and 36.6 for MeCN).¹³⁴ These differences in solvent properties allow THF to stabilize distinct reaction intermediates, which may result in significant alterations in reaction rates, yields, and selectivities.¹⁵⁸

Additionally, in organic synthesis, THF is considered as a more user-friendly solvent in comparison to DMF due to its reduced toxicity, lower environmental impact, and ease of removal from product mixtures.^{77,159} Therefore, it would be of great interest to enable efficient Al stripping in THF-based electrolytes for its application in reductive electrosynthesis.

Currently, the use of an Al sacrificial anode in THF-based electrolytes is commonly accompanied with extremely high overall cell potentials (> 30 V) that inhibit electrolysis of the organic substrates.^{65,160–162} The escalation in voltage is frequently attributed to the formation of an oxide layer on the Al surface. Thus, to realize a wide application of Al sacrificial anode in THF-based electrolyte, the ability to modify the Al SEI is essential. Previously, we have demonstrated that simple electrolyte tailoring strategies can change the composition of the SEI and improve the performance of a Mg sacrificial anode in THF-based electrolyte.¹³⁰ In this work, we explore the influence of electrolyte composition on Al SEI and stripping behavior. LSV demonstrates that supporting electrolytes such as TBABF₄, TBAClO₄, and TBATFSI do not support efficient Al stripping in THF. XPS reveals the formation of Al₂O₃ layer on the Al surface, which can inhibit Al dissolution. Inspired by Al corrosion chemistry, we use halide salts as co-supporting electrolytes to induce local disintegration of the oxide layer. With halide salts, Al stripping becomes feasible in THF, which enables bulk Al stripping under electrolysis conditions that are applicable to organic electrosynthesis.

4.2 Results and Discussion

Effect of the supporting electrolyte on Al stripping

To understand the Al stripping behavior in THF, we perform LSV experiments with 0.1 M TBABF₄, TBAClO₄, and TBATFSI supporting electrolytes. The three supporting electrolytes are chemically representative and are routinely screened for reductive electrosynthesis. The LSV experiments are conducted in three-electrode cells with an Al plate WE, graphite CE, and Pt|Fc/Fc⁺ RE (Figure 4.2a). All potentials referenced in THF electrolytes are vs. the Pt|Fc/Fc⁺ RE unless otherwise noted. The LSV experiment starts with anodic polarization of the Al electrode from OCV to 0.3 V at 5 mV s⁻¹ with 85% iR compensation. After the first LSV scan, the Al electrode has been electropolished to expose fresh Al metal. The cell is then rested at OCV for 10 min, allowing the freshly exposed Al metal to chemically react with the electrolyte. Following the rest, we repeat the LSV-OCV protocol

4 times to observe how Al stripping behavior evolves with each consecutive scan. The resulting 2nd-5th LSV scans are shown in Figure 4.2b-d. The 1st LSVs of Al electropolishing are shown in the Supporting Information. All onset potentials and current densities of the 5th LSV scans are tabulated in Table 1.

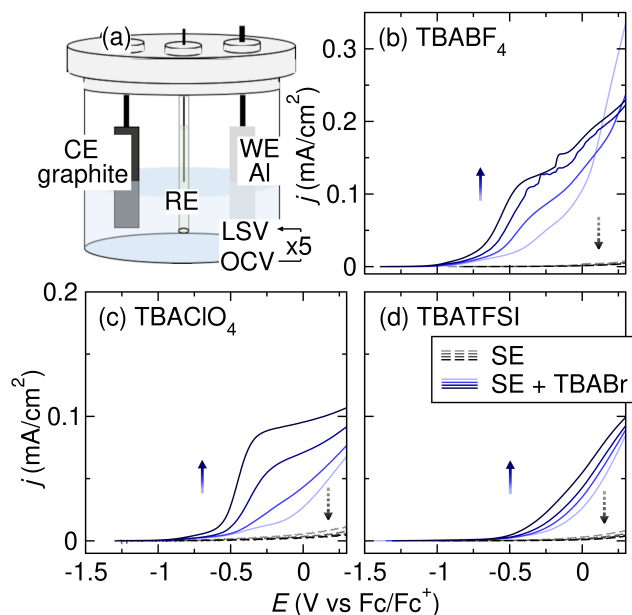


Figure 4.2: (a) A schematic of the three-electrode cell with an Al WE, graphite CE, Pt|Fc/Fc⁺ RE, and 0.1 M supporting electrolyte in 7 mL of THF. Linear sweep voltammograms of Al in THF with 0.1 M supporting electrolyte (SE) of interest, or 0.05 M SE + 0.05 M TBABr. The SEs are (b) TBABF₄, (c) TBAClO₄, and (d) TBATFSI. All voltammograms are collected at a scan rate of 5 mV s⁻¹ with 85% iR compensation. The direction of the arrows indicates the trend of changes in current densities as the number of scans increases.

As shown in Figure 4.2b-d, the current densities for Al stripping are extremely low on the 2nd LSV scan (<0.01 mA/cm² at 0 V) in all three electrolytes. The current densities decrease further with successive LSV scans. We suspect that the poor Al stripping behavior is caused by the formation of a passivating SEI on the Al electrode surface upon contact with the electrolytes. As the Al electrode remains in the electrolyte longer, the surface layers become more passivating, leading to a progressive decline of Al stripping performance. To investigate the SEI composition, we examine the Al anodes after anodic polarization in TBABF₄ and TBAClO₄ electrolytes *via* XPS.

Figure 4.3a-b shows the Al 2p region of the XPS spectra measured on the Al anode surface after the LSV experiments in THF with TBABF₄ and TBAClO₄ supporting electrolytes. All peak BEs and assignments of the Al 2p and other related regions

are tabulated in the Supporting Information. Figure 4.3a shows two Al^{3+} species after anodic polarization in the TBABF_4 electrolyte. The lower BE peak at 75.1 eV is assigned to Al_2O_3 ,¹⁶³ which is the major component of the Al SEI. The weak signal at 76.7 eV is assigned to AlF_3 ,¹⁶⁴ likely a decomposition product derived from BF_4^- . The sharp signal at 72.5 eV is ascribed to Al^0 .¹⁶⁵ The high signal intensity indicates a thin passivating layer (<10 nm), which allows the x-ray to penetration beneath the oxide layer to Al^0 . Figure 4.3b shows only Al_2O_3 at 75.0 eV as the major component of the Al SEI formed in the TBAClO_4 electrolyte. A weak signal at 199.2 eV is observed in the Cl 2*p* region that likely corresponds to AlCl_x ,¹⁶⁶ a possible decomposition product derived from ClO_4^- (Figure 4.S7c). However, the peak in the Al 2*p* region cannot be resolved from the Al_2O_3 due to its low intensity. A strong Al^0 signal is again observed at 72.5 eV, indicating a thin SEI layer. A similar Al_2O_3 -based SEI is observed on the surface of Al electrode polarized in TBATFSI electrolyte as well (Figure 4.S8). Despite the SEI's formed in the three electrolytes being thin, both Al_2O_3 and AlF_3 have been reported to inhibit Al dissolution even when present in only a thin layer.^{131,167} The composition of the SEI supports the hypothesis of a passivating Al SEI inhibiting the effective Al stripping in THF-based electrolytes.

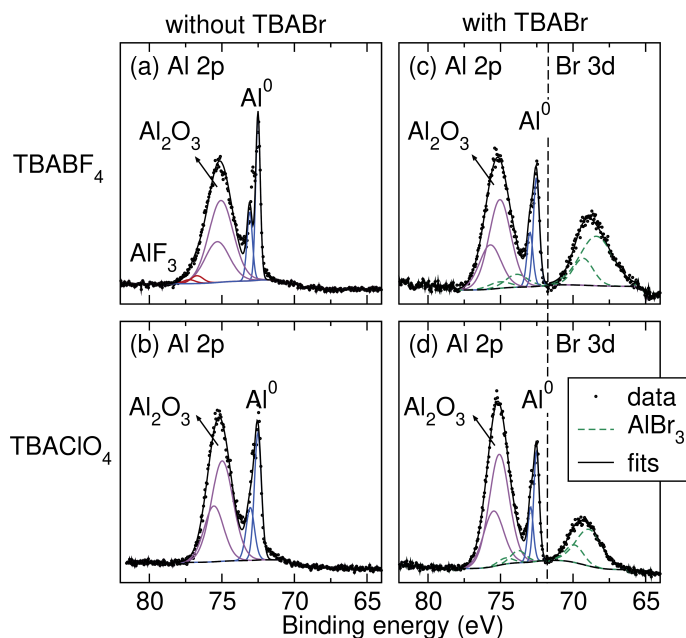


Figure 4.3: Al 2*p* and Br 3*d* regions of the XPS spectra of Al electrodes after the LSV experiments in THF with 0.1 M (a) TBABF_4 , (b) TBABF_4 + TBABr , (c) TBAClO_4 , and (d) TBAClO_4 + TBABr supporting electrolytes.

To improve Al stripping in THF-based electrolyte, we seek to tailor the electrolyte

composition in hopes of reducing the Al passivation caused by Al_2O_3 . Research on Al corrosion has demonstrated the ability of F^- , Cl^- , Br^- , and I^- to destabilize an Al_2O_3 layer.^{168–171} Free Cl^- in a solution can adsorb on the oxide layer and penetrate through the oxide film *via* oxygen vacancies.¹⁷² This process leads to destabilization and local degradation of the oxide layer.¹⁷² The degradation of Al_2O_3 by Cl^- is commonly associated with Al pitting corrosion in aqueous environments. Upon the localized degradation of the Al_2O_3 , the underlying Al becomes susceptible to dissolution in the presence of H_2O , leading to pitting corrosion.¹⁷¹ The halide-initiated Al pitting corrosion finds utility in various applications. For instance, Al is often employed as galvanic anodes to protect metal parts exposed to saltwater from corrosion.¹⁷³ Additionally, researchers have used halide salts to activate Al as an efficient reducing agent for wet-chemical synthesis.¹⁷¹

Inspired by the Al corrosion chemistry, we attempt to improve the Al stripping behavior in THF-based electrolyte with halide additives. Previous research has also demonstrated the mobility of halides within an Al oxide film in the presence of an electric field. When subjected to an anodic potential, Cl^- , Br^- , and I^- can migrate towards the $\text{Al}_2\text{O}_3/\text{Al}$ interface, leading to localized degradation of the oxide layer.^{170,174–176} We hypothesize that with halide additives in the electrolyte, the free halides can permeate Al_2O_3 upon anodic polarization, creating pathways for Al dissolution and ultimately improving the Al stripping behavior in THF-based electrolyte.

To probe the effects of halide, we add TBABr as the co-supporting electrolyte and measure the changes in Al stripping efficiency. Figure 4.2b-d shows the LSVs of Al stripping in 0.05 M TBABF_4 , TBAClO_4 , and TBATFSI electrolytes with 0.05 M TBABr co-supporting electrolyte. In all cases, Al stripping improves significantly in the presence of TBABr. Additionally, the current densities increase with each successive LSV scans, indicating that the Al SEI becomes less passivating as its duration in contact with the Br^- containing electrolyte is extended. TBACl as a co-supporting electrolyte improves Al stripping in THF as well (Figure 4.S2a). It is worth noting that TBA halide salts have poor solubility in THF. TBABr and TBACl can only reach a high concentration in THF in the presence of another supporting electrolyte that is highly soluble in THF. TBAI, however, is not soluble in THF even in the presence of a co-supporting electrolyte. Using LiI , we are able to demonstrate that I^- can also improve Al stripping in THF-based electrolyte (Figure 4.S2b).

We hypothesize that the improved Al stripping behavior is a direct result of the

free halide changing the composition of the Al SEI. To test the hypothesis, we examine the Al electrode surface after anodic polarization in TBA⁺ electrolytes with TBABr additive *via* XPS. Figure 4.3c-d shows the Al 2*p* and Br 3*d* regions of the XPS spectra. Two Al³⁺ species are observed in the SEI after anodic polarization in TBABF₄/TBABr electrolyte (Figure 4.3c). Addition to the Al₂O₃ signal at 75.0 eV, a small amount of AlBr₃ is also observed at 73.9 eV.¹⁷⁷ The assignment is supported by the signal at 68.4 eV in the Br 3*d* region, which is also consistent with reported AlBr₃ signal.¹⁷⁷ The SEI still contains AlF_x, as indicated by the F 1*s* signals (Figure 4.S9d). However, compare to the SEI formed in TBABF₄ electrolyte, the SEI formed in the presence of TBABr contains comparatively less AlF_x. As a result, the AlF_x signal cannot be resolved from the Al₂O₃ signal. A similar change in the Al SEI is observed in TBAClO₄ electrolyte in the presence of TBABr additive (Figure 4.3d). Addition to Al₂O₃ (75.1 eV) being the dominant species in the SEI, the presence of AlBr₃ is confirmed by the Al 2*p* signal at 73.8 eV and the Br 3*d* signal at 68.8 eV. All peak BEs and assignments of the related regions are tabulated in the Supporting Information. The XPS spectra reveal that free halide can modify the composition of Al SEI. In the presence of TBABr co-supporting electrolyte, the SEIs contain Br⁻, which likely destabilize the oxide layer and provide pathways for Al dissolution upon anodic polarization.

Earlier, we discussed the fact that halide salt/DMF solution stands out as the prevailing choice of electrolyte when using an Al sacrificial anode (Figure 4.1c). We hypothesize that the presence of free halides is crucial for Al stripping in DMF as well. To test the effect of halide on Al stripping in DMF, we perform similar LSV of Al stripping in DMF with 0.1 M of supporting electrolyte of interest (Figure 4.4). All potentials referenced in DMF electrolytes are vs. Fc/Fc⁺ unless noted otherwise. All onset potentials and current densities of the 5th LSV scans are tabulated in Table 4.1.

First, we test Al stripping in TBABr/DMF, the most commonly employed electrolyte for systems using an Al sacrificial anode.⁵⁰ In TBABr/DMF, the current density reaches 1.75 mA/cm² at 0.5 V vs. *E*_{on}, indicating highly effective Al stripping (Figure 4.4a). Figure 4.4b shows that TBACl/DMF is able to support effective Al stripping as well. High current density for Al stripping can initially be achieved in TBAI/DMF. However, the current density decreases significantly with successive scans, which is likely caused by changes at the Al interface after prolonged exposure to the iodide-containing electrolyte (Figure 4.4c). In the absence of free halides,

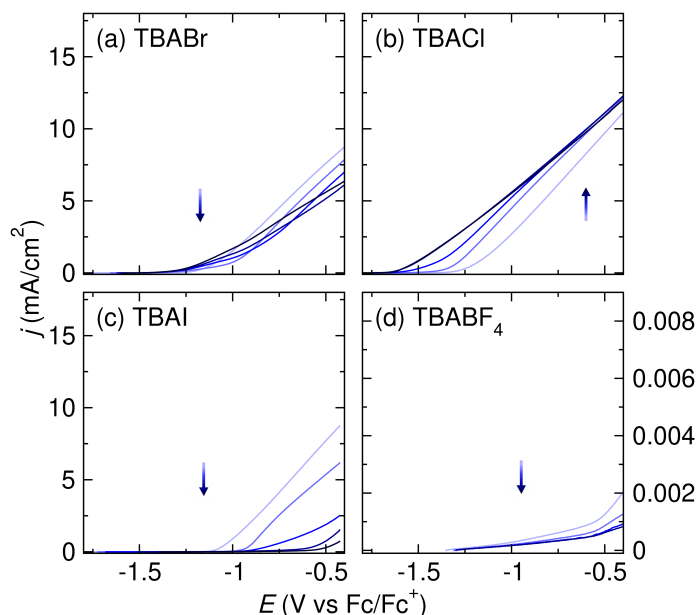


Figure 4.4: Linear sweep voltammograms of Al in 7 mL DMF with 0.1 M (a) TBABF₄, (b) TBACl, (c) TBABr, and (d) TBAI. All voltammograms are collected at a scan rate of 5 mV s⁻¹. The LSVs are measured in three-electrode cells with a Al WE, graphite CE, and Ag/Ag(cryptand)⁺ RE. The direction of the arrows indicates the trend of changes in current densities as the number of scans increases.

however, the Al stripping efficiency is extremely poor in DMF. Figure 4.4d shows the Al stripping in TBABF₄/DMF electrolyte. The current densities for Al stripping is extremely low within the electrolyte stability window. The LSV results in Figure 4.4 demonstrates the importance of free halide to Al stripping in DMF-based electrolyte as well.

Unlike THF, DMF can easily dissolve a high concentration of TBA halide salt without the aid of a co-supporting electrolyte. We believe the high solubility of TBA halide salts in DMF contributes to the observed bias in solvent selections for reductive electrosynthesis employing an Al sacrificial anode (Figure 4.1c). The limited solubility of TBA halide salts in THF is likely the reason why they are not regularly considered for the optimization of reductive electrosynthesis reactions. We envision that the use of halide co-supporting electrolytes can be a simple electrolyte tailoring strategy to enable the performance of Al sacrificial anode in THF for reductive electrosynthesis.

Bulk Al stripping in halide containing THF-based electrolyte

We next probe the effect of Br⁻ co-supporting electrolyte on bulk Al stripping in THF, a condition more relevant to reductive electrosynthesis conditions. We

Solvent	Supporting Electrolyte	E_{on}^a	j (mA/cm ²) ^b	Figure ref.
THF	TBABF ₄	–	< 0.01	Fig. 4.2b
	TBABF ₄ + TBABr	-0.77	0.13	Fig. 4.2b
	TBABF ₄ + TBACl	-0.31	0.30	Fig 4.S2a
	TBABF ₄ + LiI	-0.31	0.12	Fig 4.S2b
	TBAClO ₄	–	< 0.01	Fig. 4.2c
	TBAClO ₄ + TBABr	-0.58	0.09	Fig. 4.2c
	TBATFSI	–	< 0.01	Fig. 4.2d
	TBATFSI + TBABr	-0.26	0.09	Fig. 4.2d
DMF	TBABr	-1.49	1.75	Fig. 4.4a
	TBACl	-1.73	3.23	Fig. 4.4b
	TBAI	-0.96	0.48	Fig. 4.4c
	TBABF ₄	–	< 0.01	Fig. 4.4d

^a E_{on} (V vs. Fc/Fc⁺) is defined as the potential at which dj/dE exceeds 0.1. ^b j at +0.5 V vs. E_{on} .

Table 3.S1: Onset potential (E_{on}), and current density (j) of Al stripping in THF and DMF electrolytes.

perform galvanostatic oxidation of Al and measure the voltage profile and impedance change at the Al electrode during electrolysis. The experiments are conducted in three-electrode cells with an Al plate WE, graphite CE, and Ag wire pseudo-RE. The electrolyte consists of 0.5 M supporting electrolyte of interest and 0.5 M ^tBuBr. ^tBuBr serves as the sacrificial reductant of the galvanostatic oxidation experiment.¹³⁰ The experiment begins with galvanostatic stripping of Al at $j \approx 1 \text{ mA cm}^{-2}$ while the voltage profiles at the Al WE and graphite CE are recorded. After every 2 hours of galvanostatic oxidation, we measure the series resistance at the Al WE using EIS. The galvanostatic oxidation/EIS protocol is repeated 8 times over a duration of 16 hours to observe any changes in the performance of the Al electrode during a typical time frame of reductive electrosynthesis.

Figure 4.5a shows the voltage profiles at the Al WE and graphite CE in 0.5 M TBABF₄/THF electrolyte. The potential at the Al electrode increases immediately after the galvanostatic oxidation starts. The cell voltage reaches the compliance limit of the potentiostat within 1 min and the experiment can no longer proceed. EIS is measured before and after, and the Nyquist plot shows no changes, likely due to the minimal charge passed during the oxidation. The series resistance, which is taken as the intercept with Z' , remains low around 74 Ω , at the end of the experiment (Figure 4.S5). The low resistance coupled with the high cell voltage suggests that the SEI layer likely conducts electrons but not Al³⁺, leading to difficulties in Al stripping.

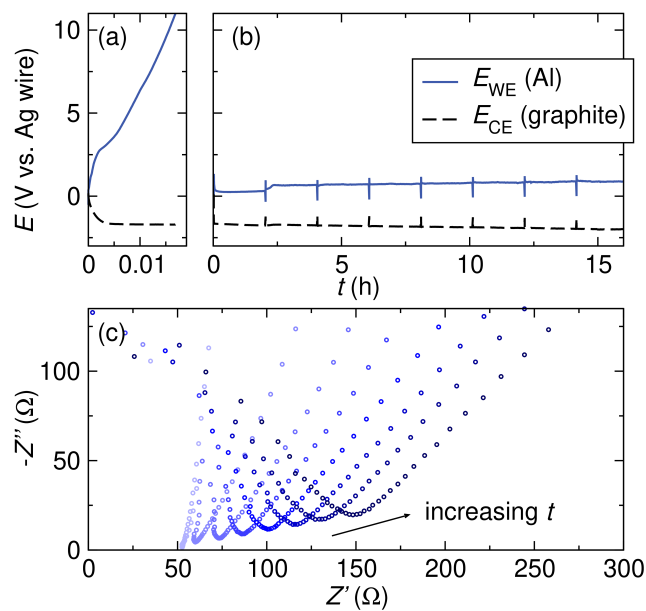


Figure 4.5: Voltage profiles of the Al WE and graphite CE during galvanostatic Al stripping ($j \approx 1 \text{ mA cm}^{-2}$) experiments in THF. The experiments are performed in (a) 0.5 M TBABF₄ and (b) 0.25 M TBABF₄ + 0.25 M TBABr, respectively, in the presence of ^tBuBr. (c) EIS is performed every 2 hours for the galvanostatic Al stripping in 0.25 M TBABF₄ + 0.25 M TBABr electrolyte. As more Al is electrochemically stripped, the series resistance increases.

The observation is consistent with our hypothesis that an Al₂O₃-dominant SEI is prohibiting the effective Al stripping.

Earlier, we have demonstrated that Br⁻ is beneficial for Al stripping in THF-based electrolytes (Figure 4.2). To enable bulk Al stripping in THF, we perform the galvanostatic oxidation experiment in electrolyte containing 0.25 M TBABF₄ and 0.25 M TBABr. With TBABr, we achieve bulk Al stripping in THF-based electrolyte. The voltage profile at the Al electrode remains stable during the 16 hours of galvanostatic Al stripping (Figure 4.5b). Throughout the course of the experiment, the voltage at the Al electrode increases from 0.25 V to 0.88 V vs. Ag wire. The increase in voltage overtime is likely the result of increasing series resistance from ~50 to 150 Ω at the Al electrode (Figure 4.5c).

To understand the reason behind the increase of series resistance at the Al electrode during the galvanostatic oxidation experiment, we examine the Al electrode post electrolysis. Visually, we observe a thin layer of salt build-up on the Al electrode at the end of the experiment (Figure 4.6a). The composition of the salt is investigated by EDS. The EDS spectrum (Figure 4.6b) reveals the presence of Al, F, O, and C,

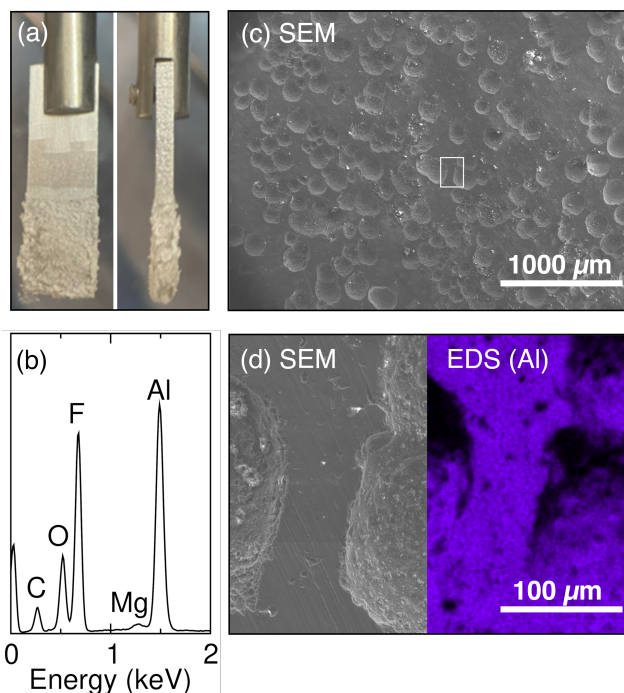


Figure 4.6: (a) Photographs of the Al electrode (front and side view) after the galvanostatic stripping experiment in the 0.25 M TBABF₄ + 0.25 M TBABr electrolyte. Visually, a salt crust is formed on top of the Al surface. (b) The EDS spectrum of the salt crust. (c) The SEM image of the Al electrode upon removal of the salt crust reveals an uneven surface morphology. (d) An enlarged SEM image coupled with EDS mapping of the Al electrode. The EDS map shows the surface distribution of Al on the Al electrode after the galvanostatic Al stripping experiment.

indicating the formation of Al salt as the product of Al stripping. The trace amount of Mg is likely a result of Mg impurity present in the Al electrode. We hypothesize that during the galvanostatic Al stripping experiment, a small quantity of the formed Al salt precipitates onto the surface of Al, consequently contributing to the observed increase in series resistance and voltage at the Al electrode. A previous study on a system utilizing a Mg electrode has demonstrated a similar phenomenon where the accumulation of Mg salts on the surface on the Mg electrode leads to increased cell voltage.^{65,130}

We then examine the morphology of the Al electrode surface with SEM and EDS mapping. The Al salts are first removed with acetone rinse to reveal the electrode surface. The SEM image in Figure 4.6c reveals a pitted Al surface post the galvanostatic stripping experiment. The pitted morphology resembles the patterns observed in the corrosion of Al in aqueous halide solutions.¹⁷⁸ We hypothesize that the free Br⁻ in the electrolyte first attack the Al SEI and incorporate itself into

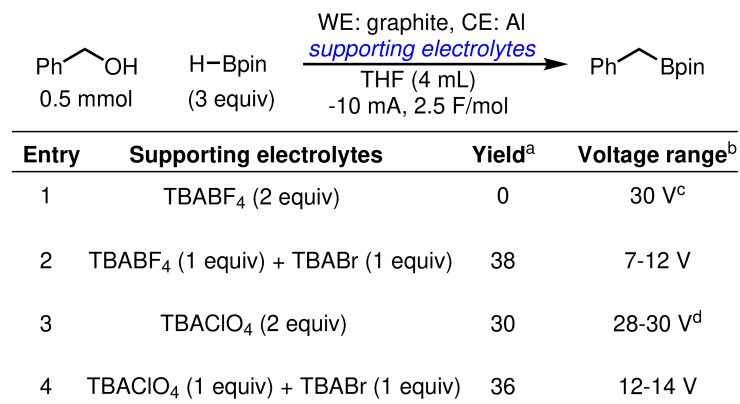
the Al₂O₃ surface layer as indicated by the XPS result in Figure 4.3. The process can make the oxide layer unstable and degrade locally. As the oxide layer is not evenly degraded, Al stripping will take place at locations where the oxide layer is most fragile during electrolysis, resulting in the observed pitted morphology. The enlarged SEM image with the corresponding EDS mapping shows non-uniform Al distribution (Figure 4.6d), which further supports an uneven Al stripping process. The pitted surface likely serve as nucleation sites for Al salts generated during electrolysis, leading to the salt build-up on the electrode surface.¹¹⁰ The salt build-up is responsible for the observed increase in both R₂ and voltage at the Al anode.

Despite the increase in R₂ caused by salt accumulation on the Al anode, the voltage profile maintains low and stable during the 16-hour galvanostatic oxidation experiment (Figure 4.5b). A stable voltage is crucial for reductive electrosynthesis, as it helps prevent the occurrence of high cell-voltage resulting from metal sacrificial passivation. The success of halide-induced Al stripping shines a light on its potential application in reductive electrosynthesis in THF.

Using halide additive to improve the cell potentials of reductive electrosynthesis reactions employing an Al sacrificial anode

To demonstrate the efficacy of halide additive in alleviating the passivation of an Al sacrificial anode, we employ the electrolyte tailoring strategy in reported cathodic reduction methodologies. The reductive electrosynthesis are carried out in an ElectraSyn, a widely adopted setup among synthetic organic chemists. We first focus on an electrochemically driven deoxygenative borylation reaction in THF (Scheme 4.1), where Al was tested in previous effort of reaction optimization but gave 0% yield of the desired product.¹⁶¹ As shown in entry 1, in TBABF₄/THF electrolyte, the overall cell potential rapidly reaches 30 V, the upper limit of the ElectraSyn capability, and merely 0.03 F/mol of the charges was passed even after prolonged reaction time. The observation aligns with the high potential at the Al anode shown in Figure 4.5a, where the elevated cell potential is observed at the beginning of electrolysis is likely a result of Al anode passivation. By partially substituting the supporting electrolyte with TBABr, the electrolysis progresses smoothly, maintaining a voltage range of 7-12 V throughout the reaction (entry 2). The simple electrolyte modification affords 38% yield of the desired product. When the same reaction is carried out in TBAClO₄/THF electrolyte, the overall cell potential remains persistently high at 28-30 V (entry 3). Using TBABr as the co-supporting electrolyte again effectively reduces the cell potential to 10-14 V, and affords a slight improvement of yield of

36% (entry 4).

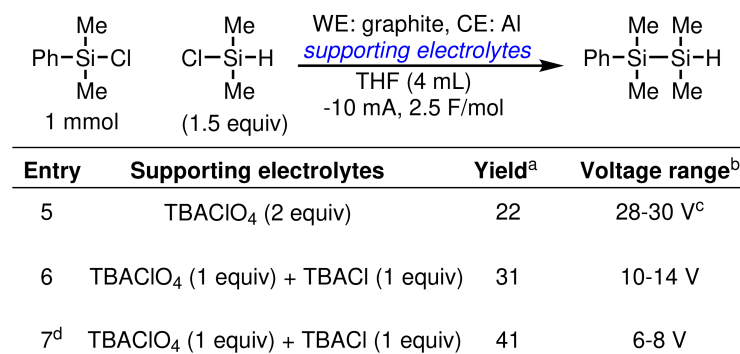


^a NMR yield was determined with dibromomethane as the internal standard.

^b Estimated range. ^c The reaction starts at very high voltage and only 0.03 F/mol of charge was passed after overnight electrolysis. ^d The reaction ran as constant voltage when the voltage hits 30 V.

Scheme 4.1: Deoxygenative borylation of benzylic alcohols.

The halide additive strategy is effective at reducing the overall cell potential in other types of organic transformation as well. Scheme 4.2 illustrates an electrochemically driven silyl cross-electrophile coupling reaction.¹⁶² The reaction has a notable high cell potential of 28-30 V during electrolysis when an Al sacrificial anode is used in combination with TBAClO₄/THF electrolyte (entry 5). Using TBACl as a co-supporting electrolyte results in a reduction in cell potential to the range of 10-14 V with improved yield of the disilane product (entry 6). By reducing the current to -5 mA, we can further reduce the voltage range to 6-8 V and improve the yield to 41% (entry 7).



^a NMR yield was determined with dibromomethane as the internal standard.

^b Estimated range. ^c The reaction ran as constant voltage when the voltage hits 30 V. ^d The reaction was electrolyzed at -5 mA instead.

Scheme 4.2: Silyl cross-electrophile coupling.

It is worth noting that both the borylation and silylation reactions have not undergone exhaustive optimization with an Al sacrificial anode to improve the yields. Despite that, the results shown here undeniably highlight the effectiveness of halide additives in reducing the overall cell potential caused by Al sacrificial anode passivation. We hope the simple electrolyte tailoring strategy can encourage the use of Al sacrificial anodes in THF-based electrolyte in future reductive electrosynthesis endeavors.

4.3 Conclusions

The work described here provides insights into the influence of supporting electrolytes on Al stripping in THF. Supporting electrolytes that are commonly employed in organic electrosynthesis, such as TBABF₄, TBFCIO₄, TBATFSI, do not support Al stripping in THF. XPS indicates that the formation of Al₂O₃ on the Al electrode surface after anodic polarization is potentially inhibiting Al dissolution. Inspired by Al corrosion chemistry, we use halide (Cl⁻, Br⁻, I⁻) salts to enable Al stripping. The new SEIs formed in the presence of TBABr co-supporting electrolyte contains AlBr₃, which likely leads to destabilization of the Al oxide layer and allows Al stripping.

In the presence of TBABr co-supporting electrolyte, we have successfully demonstrated the feasibility of bulk Al stripping in THF. The Al₂O₃ passivating layer inhibits Al stripping in TBABF₄/THF electrolyte. With the introduction of Br⁻, the oxide layer experiences localized degradation. Al stripping can take place at these specific sites, resulting in pitting morphology after prolonged metal stripping. The voltage profile at the Al anode remains stable throughout the 16-hour experiment, which holds promising for its application in reductive electrosynthesis without causing elevated cell voltage. Using halide additives, the high overall cell potentials caused by Al anode passivation are reduced significantly in a deoxygenative borylation reaction and a silyl cross-electrophile coupling reaction. Our study demonstrate the significance of understanding the interface chemistry to enhance the performance of Al sacrificial anodes. The utilization of halide co-supporting electrolytes presents an effective electrolyte tailoring strategy and potentially opens avenues for the development of more reductive electrosynthesis reactions in THF with an Al sacrificial anode.

4.4 Methods

Materials preparation

All electrolytes for LSV and galvanostatic oxidation experiments were prepared in a

N₂-filled glovebox. TBATFSI ($\geq 99.0\%$), TBAClO₄ ($\geq 99.0\%$), TBAPF₆ ($\geq 99.0\%$), TBABF₄ (99%), TBABr ($\geq 98.0\%$), TBACl ($\geq 95.0\%$), and TBAI (98%) were purchased from Sigma-Aldrich. All salts were dried under vacuum at 100 °C overnight prior to use and transferred to the glovebox without exposure to air. THF (99.9%, Fischer Scientific) was dried on a solvent purification system (Pure Process Technology), transferred to the glovebox without exposure to air, and stored over dried 4 Å molecular sieves prior to use. Anhydrous DMF (99.8%, Sure/SealTM, Sigma-Aldrich) was stored in the glovebox prior to use. All electrolytes were prepared by stirring the supporting electrolyte of interest in THF or DMF until the solution turned homogeneous.

Benzyl alcohol (Sigma-Aldrich, >99%), H-Bpin (Sigma-Aldrich, 97%), Ph(Me)₂SiCl (TCI, >96%), H(Me)₂SiCl (Sigma-Aldrich, 98%), TBABF₄ (TCI, >98%), TBAClO₄ (TCI, >98%), TBABr (TCI, >98%), and TBACl (TCI, >98%) were used as received for reductive electrosynthesis.

Pt|Fc/Fc⁺ Reference Electrode Preparation

The Pt|Fc/Fc⁺ RE was prepared following literature procedure with a 0.5 mm diameter Pt wire (Sigma-Aldrich), Fc (98%, Sigma-Aldrich), FcPF₆ (95%, Combi-Blocks), TBAPF₆, and THF.^{111–113} Fc and TBAPF₆ were recrystallized prior to use. The Pt wire, cleaned in concentrated HNO₃ and heated in a H₂ flame prior to use, was sealed within a ceramic-fritted glass tube (inner diameter 3.5 mm, Pine Research Instrumentation). The glass tube was filled with an electrolyte of 4 mM Fc, 4 mM FcPF₆, and 0.1 M TBAPF₆ in THF. The RE was assembled fresh prior to each experiment.

Ag/Ag(cryptand)⁺ Reference Electrode Preparation

The Ag/Ag(cryptand)⁺ RE was prepared following literature procedure^{179,180} with a nonaqueous reference electrode kit purchased from BASi. The RE was filled with an electrolyte of 10 mM AgNO₃ ($\geq 99.0\%$, Sigma-Aldrich), 41.2 mM Cryptand 222 (Kryptofix®, 98%, Sigma-Aldrich), and 0.1 M TBAPF₆ in DMF. The standard potential of the RE was determined to be $E^{\circ}_{Ag/Ag(cryptand)^+} = -0.523$ V vs. Fc/Fc⁺, which is consistent with the reported value (Figure 4.S4). The RE was assembled fresh prior to each experiment.

Electrochemical Testing

All electrochemical experiments were performed in a N₂-filled glovebox in a low volume, three-electrode cell (Pine Research Instrumentation). The Al plate elec-

trodes (2 mm x 8 mm x 30 mm, IKA) were mechanically ablated within the glovebox prior to use. LSV experiments to probe Al stripping were performed with an Al plate as the WE, a graphite CE (Pine Research Instrumentation), the Pt|Fc/Fc⁺ or Ag/Ag(cryptand)⁺ RE, and approximately 7 mL of electrolyte. Each electrolyte was prepared with 0.1 M supporting electrolyte. The LSV of Al stripping in THF were collected with iR compensation. Galvanostatic oxidation experiments were performed with an Al WE, graphite CE, Ag wire (Pine Research Instrumentation) as a pseudo-RE, and approximately 7 mL of electrolyte. The electrolyte was prepared with 0.5 M supporting electrolyte and 0.5 M ^tBuBr (98%, Sigma-Aldrich) as the sacrificial oxidant. EIS experiments were performed with ± 10 mV sinus amplitude from 10⁶-1 Hz at 10 points per decade. All electrochemical experiments were conducted on a VMP3 potentiostat (Bio-Logic).

Sample Characterization

XPS measurements were performed on Al anode surfaces after LSV experiments. After the LSV scans, the cells were disassembled inside a N₂-filled glovebox and the Al electrode was removed. Each Al electrode was rinsed with 10 mL of THF and dried in ambient glovebox conditions for at least 48 h before analysis. XPS data were collected using a Kratos Axis Ultra system at a pressure < 3 × 10⁻⁹ Torr. Samples were irradiated with a monochromatic Al K α source (1486.7 eV) at 150 W. Samples were irradiated with a monochromatic Al K α source (1486.7 eV) at 150 W. A charge neutralizer was used with a filament current of 2 A, filament bias of 1.3 V and charge balance of 3.5 V. Low-resolution survey spectra were acquired between BEs of 1-1200 eV. Higher-resolution detailed scans, with a resolution of 0.05 eV and a pass energy of 10 eV, were collected on individual XPS lines of interest. The XPS data were analyzed using CasaXPS analysis software, and individual peaks of interest were fit with Shirley backgrounds. Peaks were fit using mixed Gaussian-Lorentzian line shapes. Spectra were referenced to Al⁰ at 72.5 eV. Al⁰ signal was chosen as the reference due to the complicated C 1s and O 1s signals resulting from the electrolytes.

All proton NMR spectra were recorded on Varian-Mercury 400 (400 MHz) at 20 °C. Chemical shifts for proton are reported in parts per million downfield from tetramethylsilane and are reference to residual protium in the NMR solvent according to values reported in literature: $\delta(\text{CDCl}_3) = 7.26$ ppm.

Deoxygenative Borylation of Benzylic Alcohols

Al and graphite electrodes (2 mm x 8 mm x 52.5 mm, IKA) were prepared in air by polishing with 500 grit silicon carbide sandpaper until a shiny finish was obtained. Both electrodes were rinsed with acetone and the graphite electrode was dried in oven (130°C) for >10 min prior to use and transferred to the N₂-filled glovebox. In the glovebox, the corresponding electrolytes (1 mmol, 2 equiv.) and benzyl alcohol (0.5 mmol, 1 equiv.) were added into an oven dried ElectraSyn vial (5 mL) equipped with a magnetic stir bar. Dried THF (1 mL) was then added to the mixture. H-Bpin (1.5 mmol, 3 equiv.) was slowly added to the solution. The reaction usually starts bubbling at this stage and the bubbling becomes more vigorous when stirring. The whole mixture was slowly stirred until the bubbling becomes less vigorous. Then, 3 mL dried THF was added to the mixture. The vial was sealed with the ElectraSyn vial cap equipped with anode (Al) and cathode (graphite), and then the assembly was brought out of the glovebox. A nitrogen balloon was attached to the cap, and the reaction mixture was electrolyzed at a constant current of -10 mA ($j \approx -2.38 \text{ mA cm}^{-2}$) until passing 2.5 F/mol of charge at room temperature. After electrolysis, the reaction mixture was added to diethyl ether (10 mL) to precipitate electrolytes. The resultant mixture was then filtered through a short silica plug (8 cm thick, ca. 10 g) and flushed with diethyl ether (100 mL). The crude mixture was concentrated under vacuum and the yield was analyzed by ¹H NMR using dibromoethane (0.4 equiv added) as internal standard. The reaction procedure is adapted from ref.¹⁶¹

Disilane Synthesis via Silyl Cross-Electrophile Coupling

Al and graphite electrodes (2 mm x 8 mm x 52.5 mm, IKA) were prepared in air by polishing with 500 grit silicon carbide sandpaper until a shiny finish was obtained. Both electrodes were rinsed with acetone and the graphite electrode was dried in oven (130 °C) for >10 min prior to use and transferred to the N₂-filled glovebox. The corresponding electrolytes (1 mmol, 2 equiv.), chlorodimethylphenyl silane (1 mmol, 1 equiv.) and chlorodimethyl silane (1.5 mmol, 1.5 equiv.) was added into an oven dried ElectraSyn vial (5 mL) equipped with a magnetic stir bar. Dried THF (4 mL) was then added to the mixture. The vial was sealed with the ElectraSyn vial cap equipped with anode (Al) and cathode (graphite), and then bring it out of glove box. The reaction mixture was electrolyzed at a constant current of -10 mA ($j \approx -2.38 \text{ mA cm}^{-2}$) until passing 2.5 F/mol of charge at room temperature. After electrolysis, the reaction mixture was added to hexanes (10 mL) to precipitate electrolytes. The resultant mixture was then filtrated through a short silica plug (8 cm thick, ca. 10 g) and flushed with 5% diethyl ether/Hex (100 mL).

The crude was concentrated in vacuum and the yield was analyzed by ^1H NMR using dibromoethane (0.4 equiv added) as internal standard. The reaction procedure is adapted from ref.¹⁶²

4.5 Supporting Information

Linear sweep voltammograms of Al stripping

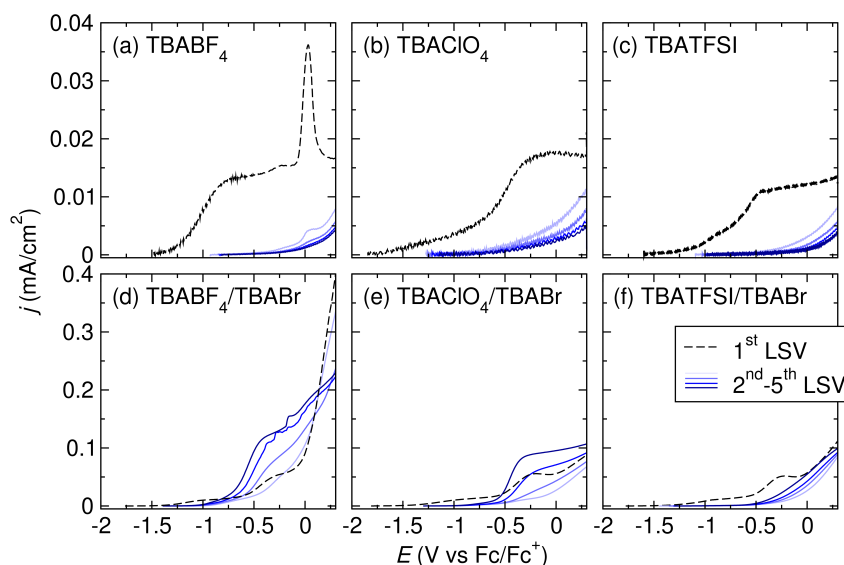


Figure 4.S1: Linear sweep voltammograms of Al stripping in THF with 0.1 M TBA⁺ supporting electrolyte or 0.05 M TBA⁺ supporting electrolyte of interest + 0.05 M TBABr. All voltammograms were collected at a scan rate of 5 mV s⁻¹ with 85% iR compensation. For each electrolyte, five LSVs were collected with a 10 min OCV between scans.

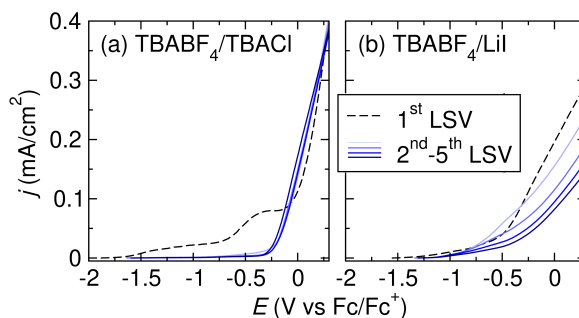


Figure 4.S2: Linear sweep voltammograms of Al stripping in THF with 0.05 M TBABF₄ + 0.05 M TBACl or TBAI. All voltammograms were collected at a scan rate of 5 mV s⁻¹ with 85% iR compensation. For each electrolyte, five LSVs were collected with a 10 min OCV between scans.

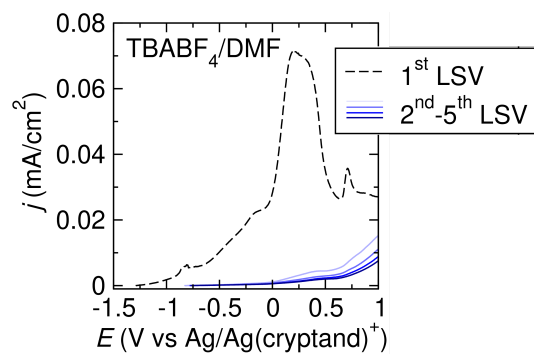


Figure 4.S3: Linear sweep voltammograms of Al stripping in DMF with 0.1 M TBABF₄. All voltammograms were collected at a scan rate of 5 mV s⁻¹. Five LSVs were collected with a 10 min OCV between scans.

Fc/Fc⁺ vs Ag/Ag(cryptand)⁺ RE

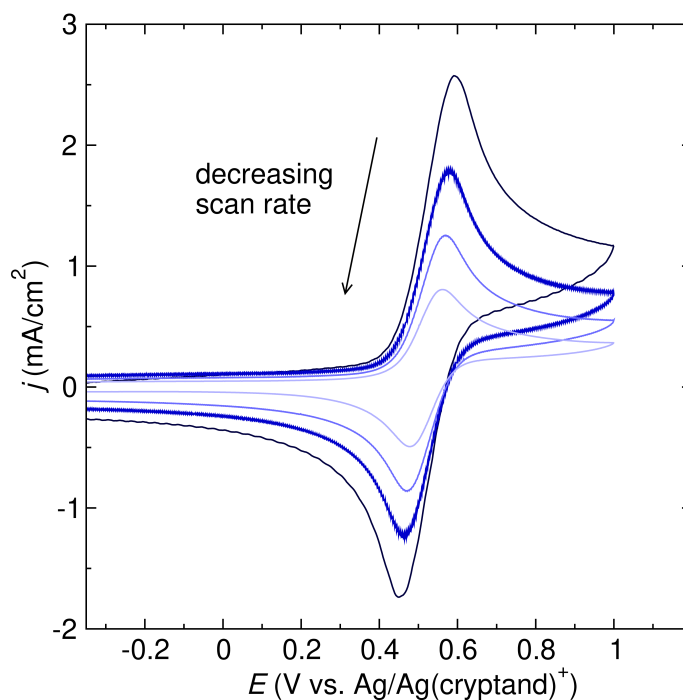


Figure 4.S4: Cyclic voltammograms of Fc in 0.1 M TBAPF₆/DMF. WE: Pt disk, CE: Pt wire, RE: Ag/Ag(cryptand)⁺. The voltammograms are collected at 200, 100, 50, and 20 mV s⁻¹ scan rate without iR compensation.

EIS data

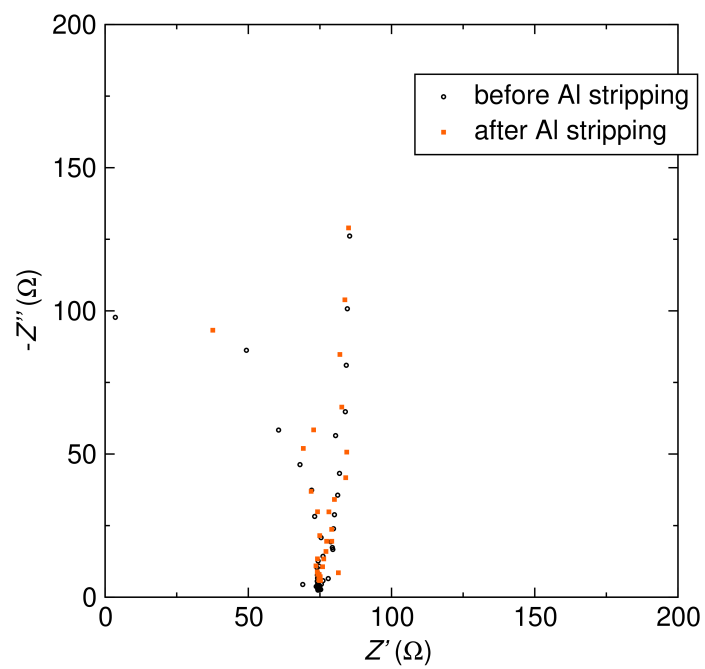


Figure 4.S5: EIS of the Al working electrodes after galvanostatic Al stripping in the presence of 0.5 M *t*BuBr in 0.5 M TBABF₄ electrolyte.

XPS data

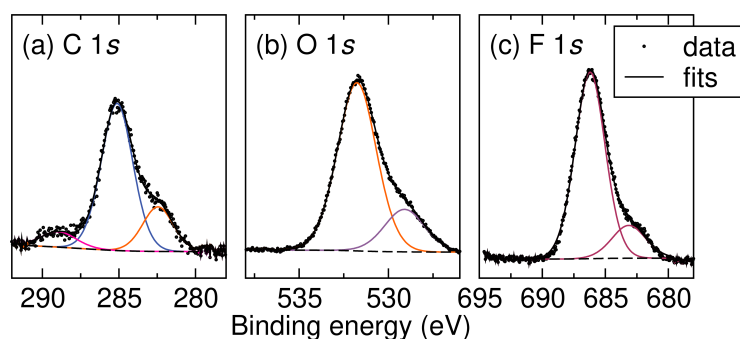


Figure 4.S6: X-ray photoelectron spectra of Al electrodes after the LSV experiments in THF with TBABF₄ as the supporting electrolyte.

Figure	Peak binding energy (eV)	Assignment
Figure 4.3a. Al 2p	72.5	Al ⁰
	75.1	Al ₂ O ₃
	76.7	AlF _x
Figure 4.S6a. C 1s	282.5	C–O
	285.1	adventitious C
	288.9	C=O
Figure 4.S6b. O 1s	529.1	Al ₂ O ₃
	531.8	C–O
Figure 4.S6c. F 1s	683.1, 686.2	AlF _x

Table 4.S1: Peak assignments of the X-ray photoelectron spectra of Al electrodes after the LSV experiments in THF with TBAClO₄ as the supporting electrolyte.

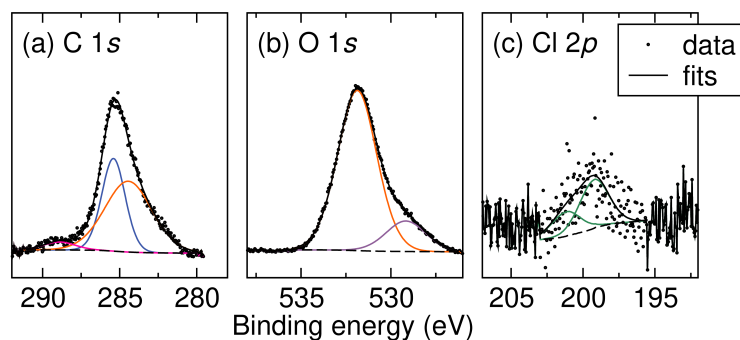


Figure 4.S7: X-ray photoelectron spectra of Al electrodes after the LSV experiments in THF with TBAClO₄ as the supporting electrolyte.

Figure	Peak binding energy (eV)	Assignment
Figure 4.3b. Al 2p	72.5	Al ⁰
	75.0	Al ₂ O ₃
Figure 4.S7a. C 1s	284.1	C–O
	285.4	adventitious C
	288.9	C=O
Figure 4.S7b. O 1s	529.2	Al ₂ O ₃
	531.9	C–O
Figure 4.S7c. Cl 2p	199.2	AlCl _x

Table 4.S2: Peak assignments of the X-ray photoelectron spectra of Al electrodes after the LSV experiments in THF with TBABF₄ as the supporting electrolyte.

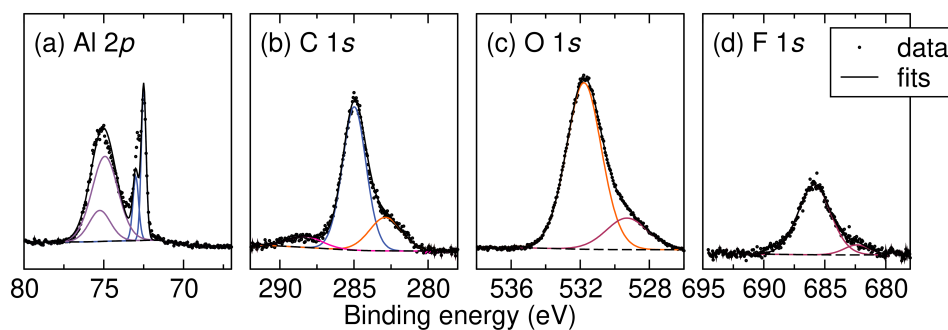


Figure 4.S8: X-ray photoelectron spectra of Al electrodes after the LSV experiments in THF with TBATFSI as the supporting electrolyte.

Figure	Peak binding energy (eV)	Assignment
Figure 4.S8a. Al 2p	72.5	Al ⁰
	75.0	Al ₂ O ₃
Figure 4.S8b. C 1s	282.9	C–O
	285.0	adventitious C
	288.3	C=O
Figure 4.S8c. O 1s	529.3	Al ₂ O ₃
	531.8	C–O
Figure 4.S8d. F 1s	682.4, 685.9	AlF _x

Table 4.S3: Peak assignments of the X-ray photoelectron spectra of Al electrodes after the LSV experiments in THF with TBATFSI as the supporting electrolyte.

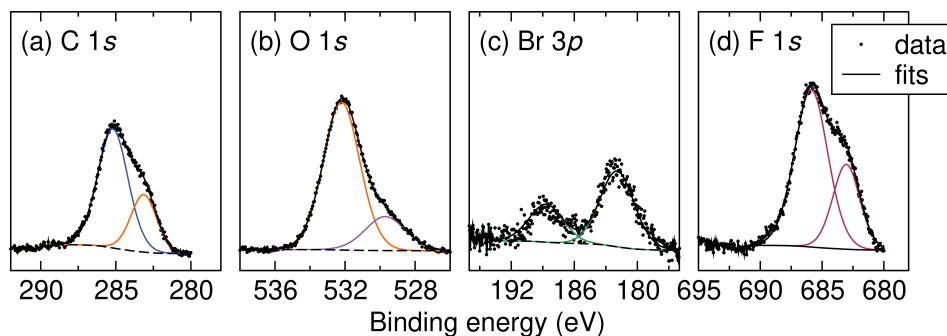


Figure 4.S9: X-ray photoelectron spectra of Al electrodes after the LSV experiments in THF with TBABF₄/TBABr as the supporting electrolyte.

Figure	Peak binding energy (eV)	Assignment
Figure 4.3c. Al 2 <i>p</i>	72.5	Al ⁰
	73.9	AlBr ₃
	75.0	Al ₂ O ₃
Figure 4.3c. Br 3 <i>d</i>	68.4	AlBr ₃
Figure 4.S9a. C 1 <i>s</i>	283.1	C–O
	285.2	adventitious C
Figure 4.S9b. O 1 <i>s</i>	529.7	Al ₂ O ₃
	532.2	C–O
Figure 4.S9c. Br 3 <i>p</i>	181.9	AlBr ₃
Figure 4.S9d. F 1 <i>s</i>	683.0, 685.9	AlF _{<i>x</i>}

Table 4.S4: Peak assignments of the X-ray photoelectron spectra of Al electrodes after the LSV experiments in THF with TBABF₄/TBABr as the supporting electrolyte.

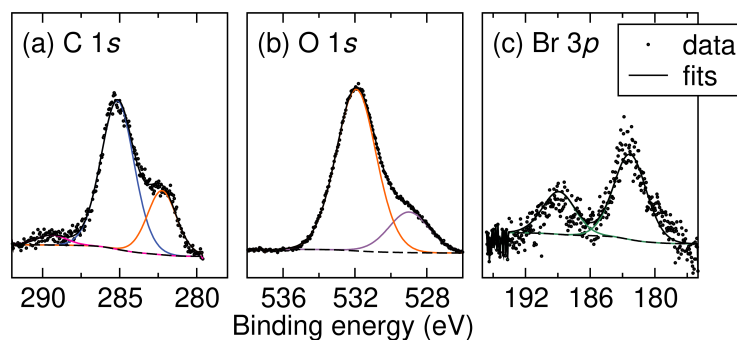


Figure 4.S10: X-ray photoelectron spectra of Al electrodes after the LSV experiments in THF with TBAClO₄/TBABr as the supporting electrolyte.

Figure	Peak binding energy (eV)	Assignment
Figure 4.3d. Al 2 <i>p</i>	72.5	Al ⁰
	73.8	AlBr ₃
	75.1	Al ₂ O ₃
Figure 4.3d. Br 3 <i>d</i>	68.8	AlBr ₃
Figure 4.S10a. C 1 <i>s</i>	282.2	C–O
	285.1	adventitious C
	289.4	C=O
Figure 4.S10b. O 1 <i>s</i>	529.7	Al ₂ O ₃
	532.2	C–O
Figure 4.S10c. Br 3 <i>p</i>	182.3	AlBr ₃

Table 4.S5: Peak assignments of the X-ray photoelectron spectra of Al electrodes after the LSV experiments in THF with TBAClO₄/TBABr as the supporting electrolyte.

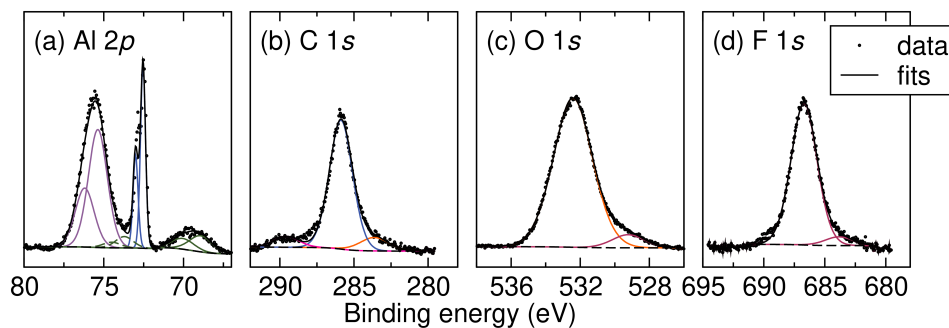


Figure 4.S11: X-ray photoelectron spectra of Al electrodes after the LSV experiments in THF with TBATFSI/TBABr as the supporting electrolyte.

Figure	Peak binding energy (eV)	Assignment
Figure 4.S13a. Al 2p	72.5	Al ⁰
	73.7	AlBr ₃
	75.4	Al ₂ O ₃
Figure 4.S13a. Br 3d	68.9	AlBr ₃
Figure 4.S13b. C 1s	283.6	C–O
	285.8	adventitious C
	289.6	C=O
Figure 4.S13c. O 1s	529.2	Al ₂ O ₃
	532.4	C–O
Figure 4.S13d. F 1s	683.8, 686.7	AlF _x

Table 4.S6: Peak assignments of the X-ray photoelectron spectra of Al electrodes after the LSV experiments in THF with TBATFSI/TBABr as the supporting electrolyte.

NMR data

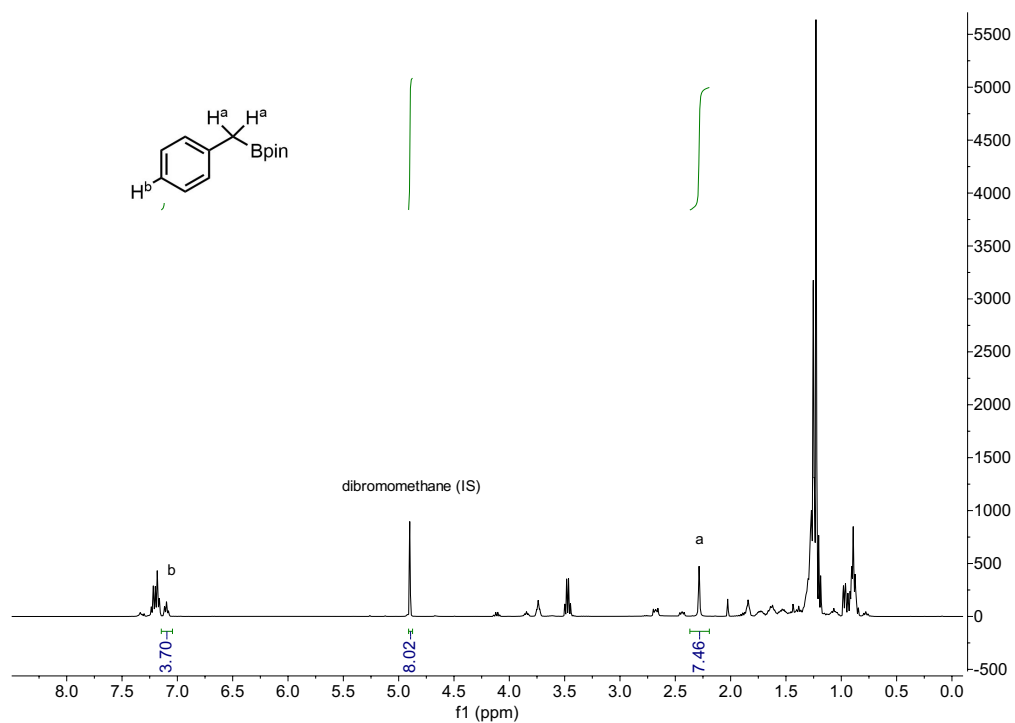


Figure 4.S12: An example of the ^1H -NMR spectra of the borylation reaction crude mixture.

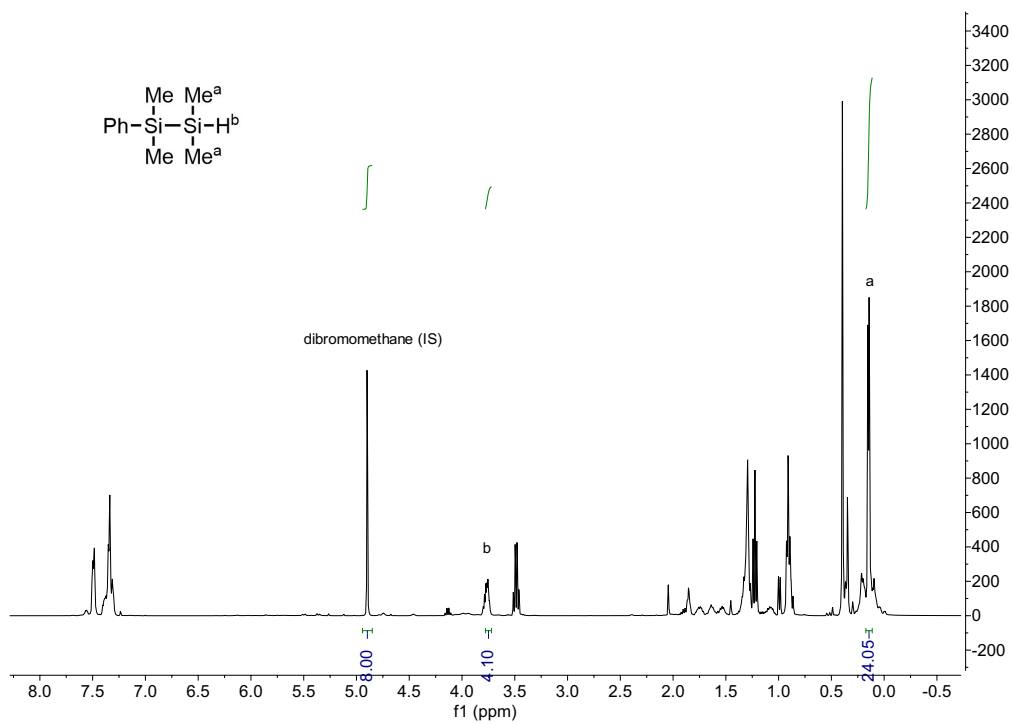


Figure 4.S13: An example of the ^1H -NMR spectra of the silylation reaction crude mixture.

Bibliography

- [1] Choi, J.; Fu, G. C. Transition Metal-Catalyzed Alkyl–Alkyl Bond Formation: Another Dimension in Cross-Coupling Chemistry. *Science* **2017**, 356.
- [2] Tasker, S. Z.; Standley, E. A.; Jamison, T. F. Recent Advances in Homogeneous Nickel Catalysis. *Nature* **2014**, 509, 299–309.
- [3] Hu, X. Nickel-Catalyzed Cross Coupling of Non-Activated Alkyl Halides: A Mechanistic Perspective. *Chem. Sci.* **2011**, 2, 1867.
- [4] González-Bobes, F.; Fu, G. C. Amino Alcohols as Ligands for Nickel-Catalyzed Suzuki Reactions of Unactivated Alkyl Halides, Including Secondary Alkyl Chlorides, with Arylboronic Acids. *J. Am. Chem. Soc.* **2006**, 128, 5360–5361.
- [5] Fu, G. C. Transition-Metal Catalysis of Nucleophilic Substitution Reactions: A Radical Alternative to SN1 and SN2 Processes. *ACS Cent. Sci.* **2017**, 3, 692–700.
- [6] Jones, G. D.; McFarland, C.; Anderson, T. J.; Vicic, D. A. Analysis of Key Steps in the Catalytic Cross-Coupling of Alkyl Electrophiles under Negishi-Like Conditions. *Chem. Commun.* **2005**, 4211–4213.
- [7] Li, Z.; Jiang, Y.-Y.; Fu, Y. Theoretical Study on the Mechanism of Ni-Catalyzed Alkyl–Alkyl Suzuki Cross-Coupling. *Chem. Eur. J.* **18**, 4345–4357.
- [8] Lin, X.; Sun, J.; Xi, Y.; Lin, D. How Racemic Secondary Alkyl Electrophiles Proceed to Enantioselective Products in Negishi Cross-Coupling Reactions. *Organometallics* **2011**, 30, 3284–3292.
- [9] Gutierrez, O.; Tellis, J. C.; Primer, D. N.; Molander, G. A.; Kozlowski, M. C. Nickel-Catalyzed Cross-Coupling of Photoredox-Generated Radicals: Uncovering a General Manifold for Stereoconvergence in Nickel-Catalyzed Cross-Couplings. *J. Am. Chem. Soc.* **2015**, 137, 4896–4899.
- [10] Jones, G. D.; Martin, J. L.; McFarland, C.; Allen, O. R.; Hall, R. E.; Haley, A. D.; Brandon, R. J.; Konovalova, T.; Desrochers, P. J.; Pulay, P.; Vicic, D. A. Ligand Redox Effects in the Synthesis, Electronic Structure, and Reactivity of an Alkyl–Alkyl Cross-Coupling Catalyst. *J. Am. Chem. Soc.* **2006**, 128, 13175–13183.
- [11] Lin, X.; Phillips, D. L. Density Functional Theory Studies of Negishi Alkyl–Alkyl Cross-Coupling Reactions Catalyzed by a Methylterpyridyl-Ni(I) Complex. *J. Org. Chem.* **2008**, 73, 3680–3688.

- [12] Breitenfeld, J.; Ruiz, J.; Wodrich, M. D.; Hu, X. Bimetallic Oxidative Addition Involving Radical Intermediates in Nickel-Catalyzed Alkyl–Alkyl Kumada Coupling Reactions. *J. Am. Chem. Soc.* **2013**, *135*, 12004–12012.
- [13] Schley, N. D.; Fu, G. C. Nickel-Catalyzed Negishi Arylations of Propargylic Bromides: A Mechanistic Investigation. *J. Am. Chem. Soc.* **2014**, *136*, 16588–16593.
- [14] Yin, H.; Fu, G. C. Mechanistic Investigation of Enantioconvergent Kumada Reactions of Racemic α -Bromoketones Catalyzed by a Nickel/Bis(Oxazoline) Complex. *J. Am. Chem. Soc.* **2019**, *141*, 15433–15440.
- [15] Liang, Y. Applications of Nickel-Catalyzed Cross-Coupling Methods in the Synthesis of Organofluorine Compounds. Ph.D. thesis, California Institute of Technology, Pasadena, CA, 2016.
- [16] Chatt, J.; Shaw, B. Alkyls and Aryls of Transition Metals. Part III. Nickel(II) Derivatives. *J. Chem. Soc.* **1960**, 1718–1729.
- [17] Klein, H.-F.; Zwiener, M.; Petermann, A.; Jung, T.; Cordier, G.; Hammerschmitt, B.; Flörke, U.; Haupt, H.-J.; Dartiguenave, Y. Thermisch kontrollierte oxidative Lineartrimerisierung von Alkynylgruppen in (Trimethylphosphan)nickel-Komplexen: Strukturen und die Rolle ligandreicher Vorstufen NiX(CCR)(PMe)_n (n = 2-4). *Chem. Ber.* **1994**, *127*, 1569–1578.
- [18] Klein, H.-F.; Peterman, A. Nickel-Mediated Synthesis of Dialkynyl and Trialkynyl Ethenes — Demetallation Reactions. *Inorganica Chim. Acta* **1997**, *261*, 187–195.
- [19] Dolomanov, O. V.; Bourhis, L. J.; Gildea, R. J.; Howard, J. A. K.; Puschmann, H. OLEX2 : A Complete Structure Solution, Refinement and Analysis Program. *J. Appl. Crystallogr.* **2009**, *42*, 339–341.
- [20] Sheldrick, G. M. Crystal Structure Refinement with *SHELXL*. *Acta Crystallogr. C Struct. Chem.* **2015**, *71*, 3–8.
- [21] Frisch, M. J. et al. Gaussian~16 Revision C.01. 2016; Gaussian Inc. Wallingford CT.
- [22] Chemcraft - graphical software for visualization of quantum chemistry computations. Version 1.8, build 648. <https://www.chemcraftprog.com>.
- [23] Choi, J.; Fu, G. C. Transition Metal-Catalyzed Alkyl–Alkyl Bond Formation: Another Dimension in Cross-Coupling Chemistry. *Science* **2017**, *356*, eaaf7230.
- [24] Tasker, S. Z.; Standley, E. A.; Jamison, T. F. Recent Advances in Homogeneous Nickel Catalysis. *Nature* **2014**, *509*, 299–309.

- [25] Jones, G. D.; Martin, J. L.; McFarland, C.; Allen, O. R.; Hall, R. E.; Haley, A. D.; Brandon, R. J.; Konovalova, T.; Desrochers, P. J.; Pulay, P.; Vicic, D. A. Ligand Redox Effects in the Synthesis, Electronic Structure, and Reactivity of an Alkyl-Alkyl Cross-Coupling Catalyst. *J. Am. Chem. Soc.* **2006**, *128*, 13175–13183.
- [26] Breitenfeld, J.; Ruiz, J.; Wodrich, M. D.; Hu, X. Bimetallic Oxidative Addition Involving Radical Intermediates in Nickel-Catalyzed Alkyl-Alkyl Kumada Coupling Reactions. *J. Am. Chem. Soc.* **2013**, *135*, 12004–12012.
- [27] Schley, N. D.; Fu, G. C. Nickel-Catalyzed Negishi Arylations of Propargylic Bromides: A Mechanistic Investigation. *J. Am. Chem. Soc.* **2014**, *136*, 16588–16593.
- [28] Yin, H.; Fu, G. C. Mechanistic Investigation of Enantioconvergent Kumada Reactions of Racemic α -Bromoketones Catalyzed by a Nickel/Bis(Oxazoline) Complex. *J. Am. Chem. Soc.* **2019**, *141*, 15433–15440.
- [29] Breitenfeld, J.; Scopelliti, R.; Hu, X. Synthesis, Reactivity, and Catalytic Application of a Nickel Pincer Hydride Complex. *Organometallics* **2012**, *31*, 2128–2136.
- [30] Lu, X.; Xiao, B.; Liu, L.; Fu, Y. Formation of C(sp³)-C(sp³) Bonds through Nickel-Catalyzed Decarboxylative Olefin Hydroalkylation Reactions. *Chem. Eur. J.* **2016**, *22*, 11161–11164.
- [31] Lu, X.; Xiao, B.; Zhang, Z.; Gong, T.; Su, W.; Yi, J.; Fu, Y.; Liu, L. Practical Carbon-Carbon Bond Formation from Olefins through Nickel-Catalyzed Reductive Olefin Hydrocarbonation. *Nat. Commun.* **2016**, *7*, 11129.
- [32] Wang, Z.; Yin, H.; Fu, G. C. Catalytic Enantioconvergent Coupling of Secondary and Tertiary Electrophiles with Olefins. *Nature* **2018**, *563*, 379–383.
- [33] He, S.-J.; Wang, J.-W.; Li, Y.; Xu, Z.-Y.; Wang, X.-X.; Lu, X.; Fu, Y. Nickel-Catalyzed Enantioconvergent Reductive Hydroalkylation of Olefins with α -Heteroatom Phosphorus or Sulfur Alkyl Electrophiles. *J. Am. Chem. Soc.* **2020**, *142*, 214–221.
- [34] Yang, Z.-P.; Fu, G. C. Convergent Catalytic Asymmetric Synthesis of Esters of Chiral Dialkyl Carbinols. *J. Am. Chem. Soc.* **2020**, *142*, 5870–5875.
- [35] Sun, S.-Z.; Börjesson, M.; Martin-Montero, R.; Martin, R. Site-Selective Ni-Catalyzed Reductive Coupling of α -Haloboranes with Unactivated Olefins. *J. Am. Chem. Soc.* **2018**, *140*, 12765–12769.
- [36] Cordier, C. J.; Lundgren, R. J.; Fu, G. C. Enantioconvergent Cross-Couplings of Racemic Alkylmetal Reagents with Unactivated Secondary Alkyl Electrophiles: Catalytic Asymmetric Negishi α -Alkylations of *N*-Boc-pyrrolidine. *J. Am. Chem. Soc.* **2013**, *135*, 10946–10949.

- [37] Huo, H.; Gorsline, B. J.; Fu, G. C. Catalyst-Controlled Doubly Enantioconvergent Coupling of Racemic Alkyl Nucleophiles and Electrophiles. *Science* **2020**, *367*, 559–564.
- [38] Wang, Z.-Y.; Wan, J.-H.; Wang, G.-Y.; Wang, R.; Jin, R.-X.; Lan, Q.; Wang, X.-S. Terminal C(sp³) H Alkylation of Internal Alkenes via Ni/H-Catalyzed Isomerization. *Tetrahedron Lett.* **2018**, *59*, 2302–2305.
- [39] Sun, S.-Z.; Romano, C.; Martin, R. Site-Selective Catalytic Deaminative Alkylation of Unactivated Olefins. *J. Am. Chem. Soc.* **2019**, *141*, 16197–16201.
- [40] Zhou, F.; Zhu, J.; Zhang, Y.; Zhu, S. NiH-Catalyzed Reductive Relay Hydroalkylation: A Strategy for the Remote C(sp³)-H Alkylation of Alkenes. *Angew. Chem. Int. Ed.* **2018**, *57*, 4058–4062.
- [41] Zhou, F.; Zhang, Y.; Xu, X.; Zhu, S. NiH-Catalyzed Remote Asymmetric Hydroalkylation of Alkenes with Racemic α -Bromo Amides. *Angew. Chem. Int. Ed.* **2019**, *58*, 1754–1758.
- [42] He, Y.; Cai, Y.; Zhu, S. Mild and Regioselective Benzylic C–H Functionalization: Ni-Catalyzed Reductive Arylation of Remote and Proximal Olefins. *J. Am. Chem. Soc.* **2017**, *139*, 1061–1064.
- [43] Bera, S.; Hu, X. Nickel-Catalyzed Regioselective Hydroalkylation and Hydroarylation of Alkenyl Boronic Esters. *Angew. Chem. Int. Ed.* **2019**, *58*, 13854–13859.
- [44] Chen, F.; Chen, K.; Zhang, Y.; He, Y.; Wang, Y.-M.; Zhu, S. Remote Migratory Cross-Electrophile Coupling and Olefin Hydroarylation Reactions Enabled by in Situ Generation of NiH. *J. Am. Chem. Soc.* **2017**, *139*, 13929–13935.
- [45] Xiao, J.; He, Y.; Ye, F.; Zhu, S. Remote sp³ C–H Amination of Alkenes with Nitroarenes. *Chem* **2018**, *4*, 1645–1657.
- [46] Binder, J. T.; Cordier, C. J.; Fu, G. C. Catalytic Enantioselective Cross-Couplings of Secondary Alkyl Electrophiles with Secondary Alkylmetal Nucleophiles: Negishi Reactions of Racemic Benzylic Bromides with Achiral Alkylzinc Reagents. *J. Am. Chem. Soc.* **2012**, *134*, 17003–17006.
- [47] Mu, X.; Shibata, Y.; Makida, Y.; Fu, G. C. Control of Vicinal Stereocenters through Nickel-Catalyzed Alkyl-Alkyl Cross-Coupling. *Angew. Chem. Int. Ed.* **2017**, *56*, 5821–5824.
- [48] Schotten, C.; Nicholls, T. P.; Bourne, R. A.; Kapur, N.; Nguyen, B. N.; Willans, C. E. Making Electrochemistry Easily Accessible to the Synthetic Chemist. *Green Chem.* **2020**, *22*, 3358–3375.

- [49] Little, R. D.; Moeller, K. D. Introduction: Electrochemistry: Technology, Synthesis, Energy, and Materials. *Chem. Rev.* **2018**, *118*, 4483–4484.
- [50] Yan, M.; Kawamata, Y.; Baran, P. S. Synthetic Organic Electrochemical Methods Since 2000: On the Verge of a Renaissance. *Chem. Rev.* **2017**, *117*, 13230–13319.
- [51] Minter, S. D.; Baran, P. Electrifying Synthesis: Recent Advances in the Methods, Materials, and Techniques for Organic Electrosynthesis. *Acc. Chem. Res.* **2020**, *53*, 545–546.
- [52] Frontana-Urbe, B. A.; Little, R. D.; Ibanez, J. G.; Palma, A.; Vasquez-Medrano, R. Organic Electrosynthesis: A Promising Green Methodology in Organic Chemistry. *Green Chem.* **2010**, *12*, 2099.
- [53] Yuan, Y.; Lei, A. Is Electrosynthesis Always Green and Advantageous Compared to Traditional Methods? *Nat. Commun.* **2020**, *11*, 802.
- [54] Liu, J.; Lu, L.; Wood, D.; Lin, S. New Redox Strategies in Organic Synthesis by Means of Electrochemistry and Photochemistry. *ACS Cent. Sci.* **2020**, *6*, 1317–1340.
- [55] Kingston, C.; Palkowitz, M. D.; Takahira, Y.; Vantourout, J. C.; Peters, B. K.; Kawamata, Y.; Baran, P. S. A Survival Guide for the “Electro-curious”. *Acc. Chem. Res.* **2020**, *53*, 72–83.
- [56] Chaussard, J.; Folest, J.-C.; Nedelec, J.-Y.; Perichon, J.; Sibille, S.; Troupel, M. Use of Sacrificial Anodes in Electrochemical Functionalization of Organic Halides. *Synthesis* **2002**, *1990*, 369–381.
- [57] Heard, D. M.; Lennox, A. J. J. Electrode Materials in Modern Organic Electrochemistry. *Angew. Chem., Int. Ed.* **2020**, *59*, 18866–18884.
- [58] Saboureau, C.; Troupel, M.; Perichon, J. Organic Electrosynthesis with a Sacrificial Anode. Chemical Reductive Degradation of the Solvent N,N-dimethyl Formamide. *J. Appl. Electrochem.* **1990**, *20*, 97–101.
- [59] Gregory, T. D.; Hoffman, R. J.; Winterton, R. C. Nonaqueous Electrochemistry of Magnesium: Applications to Energy Storage. *J. Electrochem. Soc.* **1990**, *137*, 775–780.
- [60] Novák, P.; Desilvestro, J. Electrochemical Insertion of Magnesium in Metal Oxides and Sulfides from Aprotic Electrolytes. *J. Electrochem. Soc.* **1993**, *140*, 140–144.
- [61] Zhang, Z.; Cui, Z.; Qiao, L.; Guan, J.; Xu, H.; Wang, X.; Hu, P.; Du, H.; Li, S.; Zhou, X.; Dong, S.; Liu, Z.; Cui, G.; Chen, L. Novel Design Concepts of Efficient Mg-Ion Electrolytes toward High-Performance Magnesium-Selenium and Magnesium-Sulfur Batteries. *Adv. Energy Mater.* **2017**, *7*, 1602055.

- [62] Seyferth, D. The Grignard Reagents. *Organometallics* **2009**, *28*, 1598–1605.
- [63] Koon, S. E.; Oyler, C. E.; Hill, J. H. M.; Bowyer, W. J. Visualization of the Areal Distribution of the Reactivity of Magnesium Surfaces in the Formation of Grignard Reagents. *J. Org. Chem.* **1993**, *58*, 3225–3226.
- [64] Teerlinck, C. E.; Bowyer, W. J. Reactivity of Magnesium Surfaces during the Formation of Grignard Reagents. *J. Org. Chem.* **1996**, *61*, 1059–1064.
- [65] Zhang, W.; Lu, L.; Zhang, W.; Wang, Y.; Ware, S. D.; Mondragon, J.; Rein, J.; Strotman, N.; Lehnher, D.; See, K. A.; Lin, S. Electrochemically Driven Cross-Electrophile Coupling of Alkyl Halides. *Nature* **2022**, *604*, 292–297.
- [66] Malapit, C. A.; Prater, M. B.; Cabrera-Pardo, J. R.; Li, M.; Pham, T. D.; McFadden, T. P.; Blank, S.; Minter, S. D. Advances on the Merger of Electrochemistry and Transition Metal Catalysis for Organic Synthesis. *Chem. Rev.* **2022**, *122*, 3180–3218.
- [67] Dörr, M.; Hielscher, M. M.; Proppe, J.; Waldvogel, S. R. Electrosynthetic Screening and Modern Optimization Strategies for Electrosynthesis of Highly Value-added Products. *ChemElectroChem* **2021**, *8*, 2621–2629.
- [68] DeLano, T. J.; Reisman, S. E. Enantioselective Electroreductive Coupling of Alkenyl and Benzyl Halides via Nickel Catalysis. *ACS Catal.* **2019**, *9*, 6751–6754.
- [69] Gnaim, S. et al. Cobalt-Electrocatalytic HAT for Functionalization of Unsaturated C–C Bonds. *Nature* **2022**, *605*, 687–695.
- [70] Mitsudo, K.; Nakagawa, Y.; Mizukawa, J.-i.; Tanaka, H.; Akaba, R.; Okada, T.; Suga, S. Electro-Reductive Cyclization of Aryl Halides Promoted by Fluorene Derivatives. *Electrochim. Acta* **2012**, *82*, 444–449.
- [71] Franco, D.; Riahi, A.; Hénin, F.; Muzart, J.; Duñach, E. Electrochemical Reduction of a Racemic Allyl β -Keto Ester Catalyzed by Nickel Complexes: Asymmetric Induction. *Eur. J. Org. Chem.* **2002**, *2002*, 2257.
- [72] Köster, F.; Dinjus, E.; Duñach, E. Electrochemical Selective Incorporation of CO₂ into Terminal Alkynes and Diynes. *Eur. J. Org. Chem.* **2001**, *2001*, 2507–2511.
- [73] Harwood, S. J.; Palkowitz, M. D.; Gannett, C. N.; Perez, P.; Yao, Z.; Sun, L.; Abruña, H. D.; Anderson, S. L.; Baran, P. S. Modular Terpene Synthesis Enabled by Mild Electrochemical Couplings. *Science* **2022**, *375*, 745–752.
- [74] Peters, B. K. et al. Scalable and Safe Synthetic Organic Electroreduction Inspired by Li-ion Battery Chemistry. *Science* **2019**, *363*, 838–845.

- [75] Huang, C.; Ma, W.; Zheng, X.; Xu, M.; Qi, X.; Lu, Q. Epoxide Electroreduction. *J. Am. Chem. Soc.* **2022**, *144*, 1389–1395.
- [76] Li, Y.; Wen, L.; Guo, W. A Guide to Organic Electroreduction Using Sacrificial Anodes. *Chem. Soc. Rev.* **2023**, *52*, 1168–1188.
- [77] COMMISSION REGULATION (EU) 2021/2030 of 19 November 2021 Amending Annex XVII to Regulation (EC) No 1907/2006 of the European Parliament and of the Council Concerning the Restriction, Evaluation, Authorisation and Restriction of Chemicals (REACH) as Regards N,N-dimethylformamide. 2021.
- [78] Hardwick, L. J.; Holzapfel, M.; Wokaun, A.; Novák, P. Raman Study of Lithium Coordination in EMI-TFSI Additive Systems as Lithium-Ion Battery Ionic Liquid Electrolytes. *J. Raman Spectrosc.* **2007**, *38*, 110–112.
- [79] Alía, J. M.; Edwards, H. G. Ion Solvation and Ion Association in Lithium Trifluoromethanesulfonate Solutions in Three Aprotic Solvents. An FT-Raman Spectroscopic Study. *Vib. Spectrosc.* **2000**, *24*, 185–200.
- [80] Cadioli, B.; Gallinella, E.; Coulombeau, C.; Jobic, H.; Berthier, G. Geometric Structure and Vibrational Spectrum of Tetrahydrofuran. *J. Phys. Chem.* **1993**, *97*, 7844–7856.
- [81] Shurvell, H.; Southby, M. Infrared and Raman Spectra of Tetrahydrofuran Hydroperoxide. *Vib. Spectrosc.* **1997**, *15*, 137–146.
- [82] Kim, Y.-S.; Jeong, S.-K. Raman Spectroscopy for Understanding of Lithium Intercalation into Graphite in Propylene Carbonated-Based Solutions. *J. Spectrosc.* **2015**, *2015*, 1–5.
- [83] Wu, Q.; McDowell, M. T.; Qi, Y. Effect of the Electric Double Layer (EDL) in Multicomponent Electrolyte Reduction and Solid Electrolyte Interphase (SEI) Formation in Lithium Batteries. *J. Am. Chem. Soc.* **2023**, *145*, 2473–2484.
- [84] Rakov, D.; Hasanpoor, M.; Baskin, A.; Lawson, J. W.; Chen, F.; Cherepanov, P. V.; Simonov, A. N.; Howlett, P. C.; Forsyth, M. Stable and Efficient Lithium Metal Anode Cycling through Understanding the Effects of Electrolyte Composition and Electrode Preconditioning. *Chem. Mater.* **2022**, *34*, 165–177.
- [85] Liu, S.; Mao, J.; Pang, W. K.; Vongsvivut, J.; Zeng, X.; Thomsen, L.; Wang, Y.; Liu, J.; Li, D.; Guo, Z. Tuning the Electrolyte Solvation Structure to Suppress Cathode Dissolution, Water Reactivity, and Zn Dendrite Growth in Zinc-Ion Batteries. *Adv. Funct. Mater.* **2021**, *31*, 2104281.

- [86] Li, R.; Li, Y.; Zhang, R.; He, M.; Ma, Y.; Huo, H.; Zuo, P.; Yin, G. Voltage Hysteresis of Magnesium Anode: Taking Magnesium-Sulfur Battery as an Example. *Electrochim. Acta* **2021**, *369*, 137685.
- [87] Inoue, Y.; Yasumori, I. Catalysis by Alkaline Earth Metal Oxides. XPS Study of Catalytically Active MgO, CaO, and BaO Surfaces. *Bull. Chem. Soc. Jpn.* **1981**, *54*, 1505–1510.
- [88] Fischer, P.; Reinsberg, P.; Schwarz, R. M.; Marinaro, M.; Wachtler, M.; Diemant, T.; Behm, R. J.; Baltruschat, H.; Jörissen, L. Electrochemical Formation and Characterization of Surface Blocking Layers on Gold and Platinum by Oxygen Reduction in $\text{Mg}(\text{ClO}_4)_2$ in DMSO. *J. Electrochem. Soc.* **2018**, *165*, A2037–A2046.
- [89] Ley, L.; McFeely, F. R.; Kowalczyk, S. P.; Jenkin, J. G.; Shirley, D. A. Many-Body Effects in x-Ray Photoemission from Magnesium. *Phys. Rev. B* **1975**, *11*, 600–612.
- [90] Steiner, P.; Reiter, F. J.; Höchst, H.; Hüfner, S. The KLL Auger Spectra of Na and Mg Metal and Their Plasmon Structure. *Phys. Stat. Sol. (b)* **1978**, *90*, 45–51.
- [91] Deifel, N. P.; Holman, K. T.; Cahill, C. L. PF₆⁻ Hydrolysis as a Route to Unique Uranium Phosphate Materials. *Chem. Commun.* **2008**, 6037.
- [92] Seyama, H.; Soma, M. X-Ray Photoelectron Spectroscopic Study of Montmorillonite Containing Exchangeable Divalent Cations. *J. Chem. Soc., Faraday Trans. 1* **1984**, *80*, 237.
- [93] Li, B.; Masse, R.; Liu, C.; Hu, Y.; Li, W.; Zhang, G.; Cao, G. Kinetic Surface Control for Improved Magnesium-Electrolyte Interfaces for Magnesium Ion Batteries. *Energy Storage Materials* **2019**, *22*, 96–104.
- [94] Yoo, H. D.; Shterenberg, I.; Gofer, Y.; Gershinshy, G.; Pour, N.; Aurbach, D. Mg Rechargeable Batteries: An on-Going Challenge. *Energy Environ. Sci.* **2013**, *6*, 2265.
- [95] Meitav, A.; Peled, E. Solid Electrolyte Interphase (SEI) Electrode: II . The Formation and Properties of the SEI on Magnesium in Solutions. *J. Electrochem. Soc.* **1981**, *128*, 825–831.
- [96] Miles, M. H.; Park, K. H.; Stilwell, D. E. Discharge and AC Impedance Studies of Lithium, Calcium, and Magnesium Anodes in Bromine Trifluoride. *J. Electrochem. Soc.* **1990**, *137*, 3393–3400.
- [97] Shterenberg, I.; Salama, M.; Gofer, Y.; Aurbach, D. Hexafluorophosphate-Based Solutions for Mg Batteries and the Importance of Chlorides. *Langmuir* **2017**, *33*, 9472–9478.

- [98] See, K. A.; Chapman, K. W.; Zhu, L.; Wiaderek, K. M.; Borkiewicz, O. J.; Barile, C. J.; Chupas, P. J.; Gewirth, A. A. The Interplay of Al and Mg Speciation in Advanced Mg Battery Electrolyte Solutions. *J. Am. Chem. Soc.* **2016**, *138*, 328–337.
- [99] Kim, S. S.; Bevilacqua, S. C.; See, K. A. Conditioning-Free Mg Electrolyte by the Minor Addition of Mg(HMDS)₂. *ACS Appl. Mater. Interfaces* **2020**, *12*, 5226–5233.
- [100] Kim, S. S.; See, K. A. Activating Magnesium Electrolytes through Chemical Generation of Free Chloride and Removal of Trace Water. *ACS Appl. Mater. Interfaces* **2021**, *13*, 671–680.
- [101] Shterenberg, I.; Salama, M.; Yoo, H. D.; Gofer, Y.; Park, J.-B.; Sun, Y.-K.; Aurbach, D. Evaluation of (CF₃SO₂)₂N⁻ (TFSI) Based Electrolyte Solutions for Mg Batteries. *J. Electrochem. Soc.* **2015**, *162*, A7118–A7128.
- [102] Sa, N.; Pan, B.; Saha-Shah, A.; Hubaud, A. A.; Vaughey, J. T.; Baker, L. A.; Liao, C.; Burrell, A. K. Role of Chloride for a Simple, Non-Grignard Mg Electrolyte in Ether-Based Solvents. *ACS Appl. Mater. Interfaces* **2016**, *8*, 16002–16008.
- [103] Chinnadurai, D.; Lieu, W. Y.; Kumar, S.; Yang, G.; Li, Y.; Seh, Z. W. A Passivation-Free Solid Electrolyte Interface Regulated by Magnesium Bromide Additive for Highly Reversible Magnesium Batteries. *Nano Lett.* **2023**, *23*, 1564–1572.
- [104] Li, X.; Gao, T.; Han, F.; Ma, Z.; Fan, X.; Hou, S.; Eidson, N.; Li, W.; Wang, C. Reducing Mg Anode Overpotential via Ion Conductive Surface Layer Formation by Iodine Additive. *Adv. Energy Mater.* **2018**, *8*, 1701728.
- [105] Canepa, P.; Gautam, G. S.; Malik, R.; Jayaraman, S.; Rong, Z.; Zavadil, K. R.; Persson, K.; Ceder, G. Understanding the Initial Stages of Reversible Mg Deposition and Stripping in Inorganic Nonaqueous Electrolytes. *Chem. Mater.* **2015**, *27*, 3317–3325.
- [106] Hu, Z.; Li, J.; Zhang, X.; Zhu, Y. Strategies to Improve the Performance of Li Metal Anode for Rechargeable Batteries. *Front. Chem.* **2020**, *8*, 409.
- [107] Rašljić, M.; Obradov, M.; Lazić, Ž.; Vasiljević Radović, D.; Čupić, Ž.; Stanisavljev, D. Metal Layers with Subwavelength Texturing for Broadband Enhancement of Photocatalytic Processes in Microreactors. *Opt. Quant. Electron.* **2018**, *50*, 237.
- [108] Tyagi, P.; Goulet, T.; Riso, C.; Klein, K.; Garcia-Moreno, F. Electropolishing of Additively Manufactured High Carbon Grade 316 Stainless Steel. 2018.

- [109] Shen, X.; Zhang, R.; Chen, X.; Cheng, X.-B.; Li, X.; Zhang, Q. The Failure of Solid Electrolyte Interphase on Li Metal Anode: Structural Uniformity or Mechanical Strength? *Adv. Energy Mater.* **2020**, *10*, 1903645.
- [110] Zeng, Q.; Xu, S. Thermodynamics and Characteristics of Heterogeneous Nucleation on Fractal Surfaces. *J. Phys. Chem. C* **2015**, *119*, 27426–27433.
- [111] Paddon, C. A.; Compton, R. G. A Reference Electrode for Electrochemical and Cryoelectrochemical Use in Tetrahydrofuran Solvent. *Electroanalysis* **2005**, *17*, 1919–1923.
- [112] Paddon, C. A.; Compton, R. G. Underpotential Deposition of Lithium on Platinum Single Crystal Electrodes in Tetrahydrofuran. *J. Phys. Chem. C* **2007**, *111*, 9016–9018.
- [113] Donohoe, T. J.; Kershaw, N. M.; Baron, R.; Compton, R. G. The Effect of Ortho-Substitution on the Efficacy of Biphenyls in Mediating Electron Transfer from Lithium. *Tetrahedron* **2009**, *65*, 5377–5384.
- [114] Bradley, M. *Curve Fitting in Raman and IR Spectroscopy*. 2007.
- [115] BIOVIA, Dassault Systèmes, Materials Studio, 2020, San Diego: Dassault Systèmes. 2020.
- [116] Yeh, I.-C.; Berkowitz, M. L. Ewald Summation for Systems with Slab Geometry. *J. Chem. Phys.* **1999**, *111*, 3155–3162.
- [117] Ewald, P. P. Die Berechnung optischer und elektrostatischer Gitterpotentiale. *Ann. Phys.* **1921**, *369*, 253–287.
- [118] Hoover, W. G. Canonical Dynamics: Equilibrium Phase-Space Distributions. *Phys. Rev. A* **1985**, *31*, 1695–1697.
- [119] Nosé, S. Constant Temperature Molecular Dynamics Methods. *Prog. Theor. Phys. Suppl.* **1991**, *103*, 1–46.
- [120] Berendsen, H. J. C.; Postma, J. P. M.; Van Gunsteren, W. F.; DiNola, A.; Haak, J. R. Molecular Dynamics with Coupling to an External Bath. *J. Chem. Phys.* **1984**, *81*, 3684–3690.
- [121] Frisch, M. J. et al. Gaussian09 Revision E.01. Gaussian Inc. Wallingford CT 2009.
- [122] Zhao, Y.; Truhlar, D. G. The M06 Suite of Density Functionals for Main Group Thermochemistry, Thermochemical Kinetics, Noncovalent Interactions, Excited States, and Transition Elements: Two New Functionals and Systematic Testing of Four M06-class Functionals and 12 Other Functionals. *Theor. Chem. Account.* **2008**, *120*, 215–241.

- [123] Grimme, S.; Ehrlich, S.; Goerigk, L. Effect of the Damping Function in Dispersion Corrected Density Functional Theory. *J. Comput. Chem.* **2011**, *32*, 1456–1465.
- [124] Goerigk, L.; Hansen, A.; Bauer, C.; Ehrlich, S.; Najibi, A.; Grimme, S. A Look at the Density Functional Theory Zoo with the Advanced GMTKN55 Database for General Main Group Thermochemistry, Kinetics and Noncovalent Interactions. *Phys. Chem. Chem. Phys.* **2017**, *19*, 32184–32215.
- [125] Antony, J.; Sure, R.; Grimme, S. Using Dispersion-Corrected Density Functional Theory to Understand Supramolecular Binding Thermodynamics. *Chem. Commun.* **2015**, *51*, 1764–1774.
- [126] Walker, M.; Harvey, A. J. A.; Sen, A.; Dessent, C. E. H. Performance of M06, M06-2X, and M06-HF Density Functionals for Conformationally Flexible Anionic Clusters: M06 Functionals Perform Better than B3LYP for a Model System with Dispersion and Ionic Hydrogen-Bonding Interactions. *J. Phys. Chem. A* **2013**, *117*, 12590–12600.
- [127] Sandler, I.; Sharma, S.; Chan, B.; Ho, J. Accurate Quantum Chemical Prediction of Gas-Phase Anion Binding Affinities and Their Structure-Binding Relationships. *J. Phys. Chem. A* **2021**, *125*, 9838–9851.
- [128] Rodrigues-Oliveira, A. F.; M. Ribeiro, F. W.; Cervi, G.; C. Correra, T. Evaluation of Common Theoretical Methods for Predicting Infrared Multiphotonic Dissociation Vibrational Spectra of Intramolecular Hydrogen-Bonded Ions. *ACS Omega* **2018**, *3*, 9075–9085.
- [129] Myllys, N.; Elm, J.; Kurtén, T. Density Functional Theory Basis Set Convergence of Sulfuric Acid-Containing Molecular Clusters. *Comput. Theor. Chem.* **2016**, *1098*, 1–12.
- [130] Zhang, W.; Gu, C.; Wang, Y.; Ware, S. D.; Lu, L.; Lin, S.; Qi, Y.; See, K. A. Improving the Mg Sacrificial Anode in Tetrahydrofuran for Synthetic Electrochemistry by Tailoring Electrolyte Composition. *JACS Au* **2023**, jacsau.3c00305.
- [131] Leisegang, T.; Meutzner, F.; Zschornak, M.; Münchgesang, W.; Schmid, R.; Nestler, T.; Eremin, R. A.; Kabanov, A. A.; Blatov, V. A.; Meyer, D. C. The Aluminum-Ion Battery: A Sustainable and Seminal Concept? *Front. Chem.* **2019**, *7*, 268.
- [132] Brugger, J. In *Encyclopedia of Geochemistry*; White, W. M., Ed.; Springer International Publishing: Cham, 2016; pp 1–4.
- [133] Li, W.; Wang, X. In *Sulfide and Selenide Based Materials for Emerging Applications*; Dalapati, G., Shun Wong, T., Kundu, S., Chakraborty, A., Zhuk, S., Eds.; Elsevier, 2022; pp 645–678.

- [134] Haynes, W. *CRC Handbook of Chemistry and Physics*, 95th ed.; CRC press, 2014.
- [135] Vargel, C. *Corrosion of Aluminium*, 1st ed.; Oxford: Elsevier Science, 2004.
- [136] Gao, Y.; Hill, D. E.; Hao, W.; McNicholas, B. J.; Vantourout, J. C.; Hadt, R. G.; Reisman, S. E.; Blackmond, D. G.; Baran, P. S. Electrochemical Nozaki–Hiyama–Kishi Coupling: Scope, Applications, and Mechanism. *J. Am. Chem. Soc.* **2021**, *143*, 9478–9488.
- [137] Wang, Y.; Tang, S.; Yang, G.; Wang, S.; Ma, D.; Qiu, Y. Electrocarboxylation of Aryl Epoxides with CO₂ for the Facile and Selective Synthesis of β -Hydroxy Acids. *Angew. Chem. Int. Ed.* **2022**, *61*.
- [138] Zhang, B.; Gao, Y.; Hioki, Y.; Oderinde, M. S.; Qiao, J. X.; Rodriguez, K. X.; Zhang, H.-J.; Kawamata, Y.; Baran, P. S. Ni-Electrocatalytic Csp³–Csp³ Doubly Decarboxylative Coupling. *Nature* **2022**, *606*, 313–318.
- [139] Li, C.-H.; Song, X.-Z.; Tao, L.-M.; Li, Q.-G.; Xie, J.-Q.; Peng, M.-N.; Pan, L.; Jiang, C.; Peng, Z.-Y.; Xu, M.-F. Electrogenerated-Bases Promoted Electrochemical Synthesis of N-bromoamino Acids from Imines and Carbon Dioxide. *Tetrahedron* **2014**, *70*, 1855–1860.
- [140] Yuan, G.; Li, Z.; Jiang, H. Electrosyntheses of α -Hydroxycarboxylic Acids from Carbon Dioxide and Aromatic Ketones Using Nickel as the Cathode. *Chin. J. Chem.* **2009**, *27*, 1464–1470.
- [141] Yuan, G.; Li, L.; Jiang, H.; Qi, C.; Xie, F. Electrocarboxylation of Carbon Dioxide with Polycyclic Aromatic Hydrocarbons Using Ni as the Cathode. *Chin. J. Chem.* **2010**, *28*, 1983–1988.
- [142] Li, C.; Yuan, G.; Jiang, H. Electrocarboxylation of Alkynes with Carbon Dioxide in the Presence of Metal Salt Catalysts. *Chin. J. Chem.* **2010**, *28*, 1685–1689.
- [143] Yuan, G.-Q.; Jiang, H.-F.; Lin, C. Efficient Electrochemical Dicarboxylations of Arylacetylenes with Carbon Dioxide Using Nickel as the Cathode. *Tetrahedron* **2008**, *64*, 5866–5872.
- [144] Yuan, G.-Q.; Jiang, H.-F.; Lin, C.; Liao, S.-J. Efficient Electrochemical Synthesis of 2-Arylsuccinic Acids from CO₂ and Aryl-Substituted Alkenes with Nickel as the Cathode. *Electrochim. Acta* **2008**, *53*, 2170–2176.
- [145] Matthesen, R.; Fransaer, J.; Binnemans, K.; Vos, D. E. D. Electrochemical Dicarboxylation of Conjugated Fatty Acids as an Efficient Valorization of Carbon Dioxide. *RSC Adv.* **2013**, *3*, 4634.
- [146] Li, C.-H.; Yuan, G.-Q.; Ji, X.-C.; Wang, X.-J.; Ye, J.-S.; Jiang, H.-F. Highly Regioselective Electrochemical Synthesis of Dioic Acids from Dienes and Carbon Dioxide. *Electrochim. Acta* **2011**, *56*, 1529–1534.

- [147] Cannes, C.; Condon, S.; Durandetti, M.; Périchon, J.; Nédélec, J.-Y. Nickel-Catalyzed Electrochemical Couplings of Vinyl Halides: Synthetic and Stereochemical Aspects. *J. Org. Chem.* **2000**, *65*, 4575–4583.
- [148] Laza, C.; Duñach, E.; Serein-Spirau, F.; Moreau, J. J. E.; Vellutini, L. Novel Synthesis of Arylboronic Acids by Electroreduction of Aromatic Halides in the Presence of Trialkyl Borates. *New J. Chem.* **2002**, *26*, 373–375.
- [149] Orsini, M.; Feroci, M.; Sotgiu, G.; Inesi, A. Stereoselective Electrochemical Carboxylation: 2-Phenylsuccinates from Chiral Cinnamic Acid Derivatives. *Org. Biomol. Chem.* **2005**, *3*, 1202.
- [150] Peters, B. K. et al. Scalable and Safe Synthetic Organic Electroreduction Inspired by Li-ion Battery Chemistry. *Science* **2019**, *363*, 838–845.
- [151] Godeau, J.; Pintaric, C.; Olivero, S.; Duñach, E. Electrochemical Preparation of Pinacol Allylboronic Esters. *Electrochim. Acta* **2009**, *54*, 5116–5119.
- [152] Feroci, M.; Inesi, A.; Orsini, M.; Palombi, L. Electrochemical Carboxylation of *N*-(2-Bromopropionyl)-4*R*-Phenyloxazolidin-2-One: An Efficient Route to Unsymmetrical Methylmalonic Ester Derivatives. *Org. Lett.* **2002**, *4*, 2617–2620.
- [153] Feroci, M.; Orsini, M.; Palombi, L.; Sotgiu, G.; Colapietro, M.; Inesi, A. Diastereoselective Electrochemical Carboxylation of Chiral α -Bromocarboxylic Acid Derivatives: An Easy Access to Unsymmetrical Alkylmalonic Ester Derivatives¹. *J. Org. Chem.* **2004**, *69*, 487–494.
- [154] Okamoto, K.; Nagahara, S.; Imada, Y.; Narita, R.; Kitano, Y.; Chiba, K. Hydrosilane-Mediated Electrochemical Reduction of Amides. *J. Org. Chem.* **2021**, *86*, 15992–16000.
- [155] Manabe, S.; Wong, C. M.; Sevov, C. S. Direct and Scalable Electroreduction of Triphenylphosphine Oxide to Triphenylphosphine. *J. Am. Chem. Soc.* **2020**, *142*, 3024–3031.
- [156] You, Y.; Kanna, W.; Takano, H.; Hayashi, H.; Maeda, S.; Mita, T. Electrochemical Dearomative Dicarboxylation of Heterocycles with Highly Negative Reduction Potentials. *J. Am. Chem. Soc.* **2022**, *144*, 3685–3695.
- [157] Isse, A. A.; Gennaro, A. Electrocatalytic Carboxylation of Benzyl Chlorides at Silver Cathodes in Acetonitrile. *Chem. Commun.* **2002**, 2798–2799.
- [158] Burrows, C. J.; Harper, J. B.; Sander, W.; Tantillo, D. J. Solvation Effects in Organic Chemistry. *J. Org. Chem.* **2022**, *87*, 1599–1601.
- [159] Alfonsi, K.; Colberg, J.; Dunn, P. J.; Fevig, T.; Jennings, S.; Johnson, T. A.; Kleine, H. P.; Knight, C.; Nagy, M. A.; Perry, D. A.; Stefaniak, M. Green Chemistry Tools to Influence a Medicinal Chemistry and Research Chemistry Based Organisation. *Green Chem.* **2008**, *10*, 31–36.

- [160] Lu, L.; Siu, J. C.; Lai, Y.; Lin, S. An Electroreductive Approach to Radical Silylation via the Activation of Strong Si–Cl Bond. *J. Am. Chem. Soc.* **2020**, *142*, 21272–21278.
- [161] Guan, W.; Chang, Y.; Lin, S. Electrochemically Driven Deoxygenative Borylation of Alcohols and Carbonyl Compounds. *J. Am. Chem. Soc.* **2023**, *145*, 16966–16972.
- [162] Guan, W.; Lu, L.; Jiang, Q.; Gittens, A. F.; Wang, Y.; Novaes, L. F. T.; Klausen, R. S.; Lin, S. An Electrochemical Strategy to Synthesize Disilanes and Oligosilanes from Chlorosilanes**. *Angew Chem Int Ed* **2023**, *62*, e202303592.
- [163] Kim, Y.-C.; Park, H.-H.; Chun, J. S.; Lee, W.-J. Compositional and Structural Analysis of Aluminum Oxide Films Prepared by Plasma-Enhanced Chemical Vapor Deposition. *Thin Solid Films* **1994**, *237*, 57–65.
- [164] Hess, A.; Kemnitz, E.; Lippitz, A.; Unger, W.; Menz, D.-H. ESCA, XRD, and IR Characterization of Aluminium Oxide, Hydroxyfluoride, and Fluoride Surfaces in Correlation with Their Catalytic Activity in Heterogeneous Halogen Exchange Reactions. *J. Catal.* **1994**, *148*, 270–280.
- [165] Dürrwächter, M.; Indlekofer, G.; Boyen, H.-G.; Oelhafen, P.; Quitmann, D. Core Level Binding Energy Shifts in Liquid Binary Alloys: AuGa. *J. Non-Cryst.* **1993**, *156–158*, 241–245.
- [166] Elia, G. A.; Hasa, I.; Greco, G.; Diemant, T.; Marquardt, K.; Hoepfner, K.; Behm, R. J.; Hoell, A.; Passerini, S.; Hahn, R. Insights into the Reversibility of Aluminum Graphite Batteries. *J. Mater. Chem. A* **2017**, *5*, 9682–9690.
- [167] Cho, E.; Mun, J.; Chae, O. B.; Kwon, O. M.; Kim, H.-T.; Ryu, J. H.; Kim, Y. G.; Oh, S. M. Corrosion/Passivation of Aluminum Current Collector in Bis(Fluorosulfonyl)Imide-Based Ionic Liquid for Lithium-Ion Batteries. *Electrochemistry Communications* **2012**, *22*, 1–3.
- [168] Levy, N. R.; Auinat, M.; Ein-Eli, Y. Tetra-Butyl Ammonium Fluoride – An Advanced Activator of Aluminum Surfaces in Organic Electrolytes for Aluminum-Air Batteries. *Energy Stor. Mater.* **2018**, *15*, 465–474.
- [169] Rehim, S. S.; Hassan, H. H.; Amin, M. A. Corrosion and Corrosion Inhibition of Al and Some Alloys in Sulphate Solutions Containing Halide Ions Investigated by an Impedance Technique. *Appl. Surf. Sci.* **2002**, *187*, 279–290.
- [170] Mazhar, A.; Badawy, W.; Abou-Romia, M. Impedance Studies of Corrosion Resistance of Aluminium in Chloride Media. *Surf. Coat.* **1986**, *29*, 335–345.
- [171] Li, W.; Cochell, T.; Manthiram, A. Activation of Aluminum as an Effective Reducing Agent by Pitting Corrosion for Wet-chemical Synthesis. *Sci Rep* **2013**, *3*, 1229.

- [172] Natishan, P. M.; O'Grady, W. E. Chloride Ion Interactions with Oxide-Covered Aluminum Leading to Pitting Corrosion: A Review. *J. Electrochem. Soc.* **2014**, *161*, C421–C432.
- [173] Reese, A.; Voigt, N.; Zimmermann, T.; Irrgeher, J.; Pröfrock, D. Characterization of Alloying Components in Galvanic Anodes as Potential Environmental Tracers for Heavy Metal Emissions from Offshore Wind Structures. *Chemosphere* **2020**, *257*, 127182.
- [174] Skeldon, M.; Shimizu, K.; Skeldon, P.; Thompson, G.; Wood, G. The Migration of Cl⁻ and I⁻ Ions in Anodic Alumina. *Corros. Sci.* **1995**, *37*, 1473–1488.
- [175] Brown, F.; Mackintosh, W. D. The Use of Rutherford Backscattering to Study the Behavior of Ion-Implanted Atoms During Anodic Oxidation of Aluminum: Ar, Kr, Xe, K, Rb, Cs, Cl, Br, and I. *J. Electrochem. Soc.* **1973**, *120*, 1096.
- [176] Shimizu, K.; Brown, G. M.; Kobayashi, K.; Skeldon, P.; Thompson, G. E.; Wood, G. C. A Novel Approach for the Study of the Migration of Cl⁻ Ions in Anodic Alumina. *Corrosion Science* **1999**,
- [177] Vinogradov, N. A.; Simonov, K. A.; Zakharov, A. A.; Wells, J. W.; Generalov, A. V.; Vinogradov, A. S.; Mårtensson, N.; Preobrajenski, A. B. Hole Doping of Graphene Supported on Ir(111) by AlBr₃. *Appl. Phys. Lett.* **2013**, *102*, 061601.
- [178] Furumata, K.; Seri, O. An Estimation of Chloride Ion Concentration in Pitting Cavity for Aluminum 1100 Corroded in NaCl Solution. *J. Jpn. Inst. Met.* **2001**, *65*, 880–887.
- [179] Lewandowski, A.; Osińska, M.; Swiderska-Mocek, A.; Galinski, M. A Cryptate Reference Electrode for Ionic Liquids. *Electroanalysis* **2008**, *20*, 1903–1908.
- [180] Li, M.; Dincă, M. Reductive Electrosynthesis of Crystalline Metal–Organic Frameworks. *J. Am. Chem. Soc.* **2011**, *133*, 12926–12929.